

# A Measurement of Solar Neutrinos and the Development of Reconstruction Algorithms for the SNO+ Experiment

by

Jie Hu

A thesis submitted in partial fulfillment of the requirements for the degree of  
Doctor of Philosophy

Department of Physics  
University of Alberta

© Jie Hu, 2022

# Abstract

This thesis presents a measurement of the flux of Boron-8 ( ${}^8\text{B}$ ) solar neutrinos. The measurement is based on a dataset of 190.33 live days acquired during the SNO+ water physics commissioning. To analyze the data, an event reconstruction framework was developed to evaluate the orientation of the incoming neutrino's momentum vector and the position of the event it induces. A multivariate analysis was applied to reduce the number of background events in the analysis dataset. By analyzing the data within an energy range from 5 to 15 MeV, an observed elastic scattering flux assuming no neutrino flavor transformation is obtained as  $\Phi_{\text{ES}} = (2.07 \pm 0.206(\text{stat.})^{+0.0528}_{-0.0455}(\text{syst.})) \times 10^6 \text{ cm}^{-2}\text{s}^{-1}$  while the total  ${}^8\text{B}$  solar neutrino flux is evaluated as  $\Phi_{{}^8\text{B}} = (4.62 \pm 0.459(\text{stat.})^{+0.126}_{-0.105}(\text{syst.})) \times 10^6 \text{ cm}^{-2}\text{s}^{-1}$ . These fluxes are consistent with the previous measurement done by SNO+ [Anderson, M., et al. “Measurement of the  ${}^8\text{B}$  solar neutrino flux in SNO+ with very low backgrounds.” Physical Review D 99.1 (2019): 012012], and the measurements from Super Kamiokande [Abe, K., et al. “Solar neutrino measurements in Super-Kamiokande-IV.” Physical Review D 94.5 (2016): 052010] and Borexino [Agostini, M., et al. “Improved measurement of  ${}^8\text{B}$  solar neutrinos with 1.5 kt·y of Borexino exposure.” Physical Review D 101.6 (2020): 062001]. The systematics were obtained by reconstructing and analyzing the calibration datasets from a nitrogen-16 calibration source.

Currently, the SNO+ experiment has completed the water phase commission and is filled with the liquid scintillator. It turns from a water Cherenkov detector into a 780-tonne liquid scintillator detector. Tellurium-130 isotopes will be loaded into the detector to fulfill the ultimate physics goal of SNO+: to search for the neutrinoless double beta decay. The other parts of this thesis discuss the reconstruction framework for the partial-fill and scintillator phases. For the scintillator phase, the event reconstruction gives a high position resolution down to about 65 mm.

# Preface

Since the research in this thesis relates to the SNO+ experiment, the results described herein required the effort of many individuals from the multi-national SNO+ collaboration. While the thesis focuses on the original work performed by the author, some of the research was based on the ideas, methods, or tools provided by the SNO+ collaboration.

Usage of work other than the author's is appropriately cited in the text. The theoretical and experimental results and discussion presented in Chapter 2 are a review of the literature. Chapter 3 is an overview of the SNO+ detector based on the work of the collaboration, along with literature reviews. There is one exception in Chapter 3: the relative light yield measurements of the Te-loaded liquid scintillators were performed by the author, with the assistance of the author's supervisor, Dr. A. L. Hallin. Dr. M. Sharma and Prof. J. Veinot from the Chemistry Department at the University of Alberta provided the samples for the measurement.

Unless otherwise stated or cited in the text, the analyses of simulations and data from Chapters 4 to 6 are the author's own work, performed under the supervision of Drs. A. L. Hallin, J. P. Yáñez Garza, and C. B. Krauss.

The framework of the reconstruction algorithms presented in Chapter 4 was first developed by Dr. A. L. Hallin. Drs. K. Singh and D. J. Auty at the University of Alberta further developed and extended the framework for the SNO+ water phase. The SNO+ reconstruction and software working groups, as well as the Code Integrity Committee (CIC) helped to implement the framework into the SNO+ analysis software (**RAT**). The author was responsible for testing and optimizing the algorithms on simulations and data, as presented in this chapter. The author also extended the framework's usage for multiple SNO+ physics

phases, particularly for the SNO+ partial-fill phase. The algorithm requires the parameters which were measured and determined by the collaboration. To develop the reconstruction framework, the author performed simulations by using the RAT. The studies on the simulations of the wavelength-shifter were performed by the author, while the reconstruction algorithm was developed by Dr. K. Singh. The other reconstruction algorithms developed by the collaboration were also introduced briefly in Chapter 4.

The members of the SNO+ calibration working group deployed the  $^{16}\text{N}$  source for the calibration mentioned in Chapter 5. The data used in Chapters 5 and 6 were collected by the SNO+ detector during the operation, which requires a collaborative effort. The simulations used in these two chapters were mostly produced by the SNO+ calibration, background, and simulation working groups. The author applied the reconstruction algorithms (described in Chapter 4) to the data and simulations, and then evaluated the reconstruction systematics for the water physics in Chapter 5, following the routines and methods provided by the SNO+ water physics and analysis working groups.

In Chapter 6, the author analyzed the water physics data by using the reconstruction algorithms mentioned in Chapter 4. The separation of signal and background based on machine learning was performed by the author. The author evaluated the Boron-8 solar neutrino rates and the background rates from the dataset. The systematics and uncertainties from Chapter 5 were evaluated and included in the results by the author.

The author executed algorithms on data and simulation mentioned above by using the Compute Canada computing resources, that were allocated to Dr. C. B. Krauss. The author also received assistance from the technical support team at the University of Alberta.

# Acknowledgements

It takes several years for this thesis to come out, and it cannot be there without the support from numerous people. First, I would like to thank my supervisor Dr. Aksel Hallin. As an experienced experimental physicist, he is unique in mastering the art of particle physics experiments and is always on the front line of the research, which amazes people. He is a great teacher with insights and patience. Thanks to Dr. Carsten B. Krauss, who provided me with critical suggestions for my research and also a chance for working in the laboratory. Thanks to Dr. Juan Pablo Yáñez Garza, who shared his smart ideas for physics analysis, and extensive knowledge in neutrinos.

The research presented in this thesis cannot proceed without the SNO+ collaboration. I would like to thank the whole SNO+ collaboration as well as the staff in SNOLAB. I would like to thank Drs. Jeff Tseng, Edward Leming, and Nuno Barros for giving useful suggestions on the event reconstruction and their help in implementing the codes. I would like to thank Dr. Alex Wright and Brian Krar for their suggestions on the solar neutrino analysis. I am grateful to Drs. Christine Kraus, Erica Caden, Aleksandra Bialek, and Mrs. Nancy Brown, for their roles in arranging and helping my site work in SNOLAB.

Fellow researchers, postdocs, and staff in the Department of Physics at the University of Alberta offered me a lot of help during my Ph.D. study. I would like to thank Drs. Kalpana Singh, David J. Auty, Karin Gilje, Yang Zhang, Fady Shaker, and Munish Sharma for their invaluable help and suggestions. I am grateful to Kalpana, who gave me a hand when I was first involved in the SNO+ research. Though she was always busy, she generously offered her time to teach me a lot of research methods and shared her smart ideas on resolving problems. Karin and David kindly helped me in the experiment, analyses, and academic

English writing as well. I had a wonderful trip to Sudbury with David for my first summer visit to SNOLAB. Thanks to Prof. John Wilson, who helped me with my thesis writing. I am also amazed by his pure enthusiasm for physics. I would like to thank Dr. Richard Soluk, Paul Davis, and Len Wampler for their help in the laboratory. Jamie Rajewski provided technical support on the Compute Canada computing resources, and I am appreciative of his help. For my Ph.D. program, I also received valuable suggestions and help from the faculty and staff, and I would like to thank Drs. Erik Rosolowsky and Craig Heinke, Mrs. Rae Beaumont, Mrs. Suzette Chan, and Mrs. Sarah MacKinnon.

I would like to thank my office mates: Logan Sibley, Pawel Mekarski, Courtney Mielnichuk, Thomas McElroy, Jonathan Chalaturnyk, Joseph Willis, and Pooja Nolan. I spent a wonderful time with these smart and interesting people, who have great enthusiasm for science and life. Logan and Pawel were also my colleagues in SNO+. They kindly helped me to get familiar with the collaboration and research, gave me suggestions in studies and writing, and let me enjoy life in Edmonton.

I am grateful to my friends: Yu Chen, Xuemeng Chen, Jingyan Hao, Dinglian Kang, Jinyuan Luo, Youfang Luo, Yuxiu Lv, Chengyue Qian, Wenhui Ruan, Mingcheng Tang, Haifeng Xu, Wenqing Yu, Lingjun Zhou, and Gaofei Zhu. They have brought me countless insights and ideas about science and life.

When I first came to Edmonton, Prof. Keumhee Chough kindly provided me with accommodation, welcomed me at the airport, and helped me to get familiar with life in the city. I will never forget her kindness.

My parents highly encourage and support me to pursue a postgraduate education abroad. Raising a child is no easier than the Labours of Heracles. I am also grateful to my late grandma, who shared her love and always missed me when I was far away from home.

# Contents

<b>Abstract</b>	<b>ii</b>
<b>Preface</b>	<b>iv</b>
<b>Acknowledgements</b>	<b>vi</b>
<b>Contents</b>	<b>viii</b>
<b>List of Figures</b>	<b>xiii</b>
<b>List of Tables</b>	<b>xix</b>
<b>1 Introduction</b>	<b>1</b>
<b>2 Neutrino physics</b>	<b>4</b>
2.1 Overview . . . . .	4
2.2 Neutrino Interactions . . . . .	6
2.2.1 Neutrino-Electron Elastic Scattering . . . . .	7
2.3 Neutrino Flavor Transformation . . . . .	10
2.3.1 Vacuum Oscillation . . . . .	11
2.3.2 Matter Effect . . . . .	15
2.4 Solar Neutrinos . . . . .	17
2.4.1 Kamiokande and Super-Kamiokande . . . . .	20
2.4.2 SNO . . . . .	20
2.4.3 KamLAND . . . . .	21

2.4.4	Borexino . . . . .	22
2.4.5	More Studies on Solar Neutrino and Future Experiments . . . . .	23
2.5	Neutrinoless Double Beta Decay . . . . .	24
<b>3</b>	<b>The SNO+ Experiment</b>	<b>29</b>
3.1	Overview . . . . .	29
3.2	SNO+ Physics Phases . . . . .	30
3.2.1	Water Phase . . . . .	31
3.2.2	Scintillator Phase . . . . .	33
3.2.3	Partial-fill Phase . . . . .	33
3.2.4	Tellurium Phase . . . . .	34
3.3	Detection Media . . . . .	34
3.3.1	Cherenkov Radiation . . . . .	34
3.3.2	Scintillation Light from Organic Scintillator . . . . .	36
3.3.3	Liquid Scintillator for SNO+ . . . . .	38
3.3.4	Water-based Wavelength Shifter (Proposal) . . . . .	39
3.3.5	Unloaded Liquid Scintillator . . . . .	40
3.3.6	Tellurium-loaded Liquid Scintillator . . . . .	43
3.3.7	Relative Light Yield Measurements of the Te-loaded Liquid Scintillators	44
3.4	SNO+ Electronics . . . . .	54
3.5	Calibration . . . . .	56
3.5.1	The $^{16}\text{N}$ Calibration Source . . . . .	57
3.6	Monte Carlo Simulation and RAT Software . . . . .	59
<b>4</b>	<b>Event Reconstruction</b>	<b>61</b>
4.1	An Overview of the Reconstruction Algorithms in SNO+ . . . . .	61
4.2	Multi-Path Vertex and Direction Reconstructions for the Water Phase . . . . .	63
4.2.1	Vertex Reconstruction . . . . .	64
4.2.2	Direction Reconstruction . . . . .	67
4.2.3	Effective Group Velocity . . . . .	68
4.2.4	Fitter Pull and Drive Correction . . . . .	72

4.2.5	PMT Selectors for the Reconstruction . . . . .	75
4.2.6	Position Figure of Merit . . . . .	78
4.2.7	Performance of the Water Vertex Reconstruction . . . . .	78
4.2.8	Performances of the Direction Reconstruction in water . . . . .	82
4.2.9	Test on Gamma Events . . . . .	85
4.3	Vertex and Direction Reconstruction for the Water-based Wavelength-shifter	86
4.4	Vertex Reconstruction for the Partial-fill . . . . .	89
4.4.1	Partial-fill . . . . .	89
4.4.2	Creating the Timing PDFs . . . . .	94
4.4.3	Partial Fitter Performance . . . . .	97
4.4.4	Test on Bi-Po Simulations . . . . .	103
4.4.5	Discussions for the Partial Fitter . . . . .	104
4.5	Vertex Reconstruction for the Scintillator Phase . . . . .	106
4.5.1	Performance of the Vertex Reconstruction . . . . .	107
4.6	Multi-Path Fitter Structure for Multiple SNO+ Physics Phases . . . . .	107
4.7	Energy Reconstruction . . . . .	112
4.7.1	Energy Figure of Merit . . . . .	112
4.7.2	Energy Reconstruction in Partial-fill Phase . . . . .	113
4.8	Machine Learning and Deep Learning . . . . .	114
4.9	Conclusion . . . . .	115
<b>5</b>	<b>Calibration</b>	<b>116</b>
5.1	$^{16}\text{N}$ Calibration Scans in the Water Phase . . . . .	117
5.2	High Level Cuts for the Water Phase . . . . .	118
5.2.1	Effects of the High Level Cuts . . . . .	119
5.3	Quality of Event Reconstruction Judged by $^{16}\text{N}$ Calibration Scans in the Water Phase . . . . .	122
5.3.1	Position Reconstruction Evaluation . . . . .	122
5.3.2	Direction Reconstruction Evaluation . . . . .	134
5.3.3	$\beta_{14}$ and its Systematics . . . . .	139
5.3.4	Energy Reconstruction Evaluation . . . . .	141

<b>6 Solar Neutrino Analysis in the SNO+ Water Phase</b>	<b>152</b>
6.1 Backgrounds . . . . .	153
6.1.1 Internal backgrounds . . . . .	153
6.1.2 External backgrounds . . . . .	154
6.2 Solar Neutrino Analysis in Open Dataset . . . . .	154
6.3 Likelihood Fits for Solar Neutrino Candidate Events . . . . .	157
6.3.1 Maximum Likelihood Fit . . . . .	158
6.3.2 Ensemble Test . . . . .	159
6.3.3 Signal-background Discrimination Based on TMVA . . . . .	161
6.3.4 TMVA Outputs . . . . .	169
6.3.5 Discussions of TMVA Results . . . . .	172
6.3.6 Fitting Whole Low Background Dataset . . . . .	175
6.3.7 Evaluating $^8\text{B}$ Solar Neutrino Flux . . . . .	176
6.3.8 Systematics Evaluation . . . . .	180
6.3.9 Summary of Results . . . . .	184
6.3.10 Limitations of this Study . . . . .	185
<b>7 Conclusions</b>	<b>187</b>
<b>Bibliography</b>	<b>189</b>
<b>A Details for the Multi-Path Fitter</b>	<b>208</b>
A.1 Create a Random Vertex . . . . .	208
A.2 Levenberg-Marquardt Method . . . . .	209
A.3 Calculations of Derivatives of Likelihood Functions . . . . .	212
A.4 Inversion of Hessian Matrix . . . . .	213
A.5 Likelihood Surfaces . . . . .	214
A.6 Detailed Light Path Calculations in the Partial Fitter . . . . .	214
<b>B Information for <math>^{16}\text{N}</math> Scan Runs</b>	<b>219</b>
B.1 $^{16}\text{N}$ Source Positions in the Scan Runs . . . . .	219

<b>C Bi-Po Analysis</b>	<b>225</b>
C.1 Uranium chain and Bi-Po Analysis . . . . .	225

# List of Figures

2.1	Feynman diagrams for the elastic scattering interaction at tree level. . . . .	8
2.2	A diagram of the $\nu + e^-$ elastic scattering in the lab frame. . . . .	9
2.3	All reactions in the three PP chains. . . . .	17
2.4	All reactions in the CNO bicycle. . . . .	18
2.5	Solar neutrino energy spectrum. . . . .	19
2.6	Feynman diagrams for $2\nu\beta\beta$ and $0\nu\beta\beta$ . . . . .	25
2.7	Energy spectrum of the $^{130}\text{Te}$ $2\nu\beta\beta$ decay and the hypothetical $0\nu\beta\beta$ decay.	27
2.8	Natural abundance vs. Q-values for different $2\nu\beta\beta$ isotopes. . . . .	28
3.1	The SNO+ detector labeled with main structures. . . . .	31
3.2	A Jablonski diagram for the organic scintillator. . . . .	36
3.3	Structural formulae of LAB and PPO. . . . .	40
3.4	Spectral absorption length for SNO+ optical components. . . . .	41
3.5	Time profiles for liquid scintillators in different SNO+ phases. . . . .	43
3.6	Initial stages of the TeBD compound formation. . . . .	43
3.7	A vial filled with the test sample and the measurement setup. . . . .	45
3.8	A diagram shows the light yield measurement setup. . . . .	46
3.9	A typical triggered waveform. . . . .	49
3.10	Measured LAB-PPO energy spectrum with and without coincidence cut. . .	50
3.11	The 2D energy spectrum of the counting measurements. . . . .	51
3.12	The single <i>p.e.</i> peak fitted with an asymmetric Gaussian function. . . . .	52
3.13	Two dimensional spectrum of LAB-PPO sample with coincidence cut. . . .	53
3.14	The SNO+ Source Manipulator System. . . . .	58

3.15	$^{16}\text{N}$ calibration source geometry.	58
3.16	$^{16}\text{N}$ main decay scheme.	59
4.1	Straight light path calculation in the water geometry.	65
4.2	The PMT response time profile, used as the timing PDF for vertex reconstruction.	66
4.3	Cherenkov cone and straight line light paths (SNO+ water phase).	67
4.4	PMT angular distribution as the angular response PDF for direction reconstruction.	68
4.5	Refractive index of water vs wavelength.	69
4.6	A cartoon shows effects of tuning the effective group velocity.	70
4.7	Group velocity vs. radial bias for the <b>MPW fitter</b> .	70
4.8	$^{16}\text{N}$ central run for evaluating the average group velocity.	71
4.9	A cartoon shows fitter pull effect.	73
4.10	A diagram illustrating the drive correction.	73
4.11	Drive correction parameters as a function of electron energy.	74
4.12	Radial biases of simulated electron events as a function of energy.	75
4.13	PMTs are grouped by partitioning the PSUP sphere into intervals of latitude and longitude.	78
4.14	The position biases projected on the $x$ , $y$ and $z$ axes.	79
4.15	The position biases against the position FoMs.	80
4.16	The <b>MPW fitter</b> fit position biases ( $\mu_{x,y,z}$ ) as a function of energy.	81
4.17	The <b>MPW fitter</b> fit position resolutions ( $\sigma_{x,y,z}$ ) as a function of energy.	82
4.18	The <b>MPW fitter</b> fit position biases ( $\mu_{x,y,z}$ ) as a function of radius.	83
4.19	The <b>MPW fitter</b> fit position resolutions ( $\sigma_{x,y,z}$ ) as a function of radius.	83
4.20	The bias between the fitted and true (MC) direction.	84
4.21	Direction resolutions as a function of radius.	85
4.22	Position distribution of hit PMTs (zenith and azimuth angles).	86
4.23	The energies of simulated electrons as a function of mean NHits.	87
4.24	The timing PDF for the wbWLS.	88
4.25	A comparison of fitted $x$ positions.	88

4.26	Light path calculation for the MP <b>scint-water fitter</b> . . . . .	90
4.27	Line-sphere intersections. . . . .	92
4.28	Timing PDFs used by the MP <b>scint-water fitter</b> . . . . .	94
4.29	Timing PDFs built for various PPO concentrations based on the Oxford bench-top measurements. . . . .	96
4.30	Tuning the effective group velocities in the scintillator and water. . . . .	97
4.31	Reconstructed position and fit bias for simulated 3-MeV electron events in the scintillator region. . . . .	98
4.32	Effects of the <i>scaleLogL</i> cut on the reconstructed positions and fit biases. .	100
4.33	Reconstructed positions and fit biases of the 3-MeV $e^-$ events in the water region. . . . .	101
4.34	Fit position biases against the PPO concentrations. . . . .	102
4.35	Fit position resolutions against the PPO concentrations. . . . .	103
4.36	Distributions of NHits for the tagged $^{214}\text{Po}$ and $^{214}\text{Bi}$ events. . . . .	104
4.37	Fit position biases for tagged $^{214}\text{Bi}$ and $^{214}\text{Po}$ . . . . .	105
4.38	The fit position biases for 2.5-MeV $e^-$ events in full scintillator simulations.	108
4.39	The Gaussian means ( $\mu$ ) of the MP <b>scint fitter</b> fit position biases as a function of radius. . . . .	109
4.40	The Gaussian resolutions ( $\sigma$ ) of the MP <b>scint fitter</b> fit position biases as a function of radius. . . . .	109
4.41	The Gaussian means ( $\mu$ ) of the MP <b>scint fitter</b> fit position biases as a function of energy. . . . .	110
4.42	The Gaussian resolutions ( $\sigma$ ) of the MP <b>scint fitter</b> fit position biases as a function of energy. . . . .	110
5.1	The deployed source positions of the $^{16}\text{N}$ scan runs. . . . .	117
5.2	Position biases vs ITR and $\beta_{14}$ for the $^{16}\text{N}$ central run 107055. . . . .	120
5.3	$E_{fit}$ vs $\beta_{14}$ for the data and MC. . . . .	121
5.4	Position biases vs <i>scaleLogL</i> for the $^{16}\text{N}$ central run 107055. . . . .	123
5.5	Reconstructed energy vs <i>scaleLogL</i> for the $^{16}\text{N}$ central run 107055. . . . .	123
5.6	Schematic of the $^{16}\text{N}$ source. . . . .	125

5.7	Spatial distribution of $^{16}\text{N}$ $\gamma$ -ray's first interaction positions, projected onto the $x$ -axis. . . . .	125
5.8	Distributions of the reconstructed position projected onto the $x$ -axis. . . . .	126
5.9	The fitted values of $\mu_P$ and $\sigma_P$ along $x$ , $y$ and $z$ -scans. . . . .	128
5.10	Relative differences of $\sigma_P$ ( $\sigma_{p,\delta}$ ) as a function of the $^{16}\text{N}$ source position. . . . .	129
5.11	Smeared reconstructed positions of $^{16}\text{N}$ central run 107055 MC. . . . .	131
5.12	Vertex shifts of $\mu_P$ ( $\mu_{p,\delta}$ ) as a function of the $^{16}\text{N}$ source position. . . . .	132
5.13	Vertex shifts along $x$ , $y$ , $z$ axes and fitted with linear functions: $shift = p_0 + p_1 \cdot x_i$ , ( $x_i = x, y, z$ ). . . . .	133
5.14	Smeared reconstructed radius $r'$ spectrum of $^{16}\text{N}$ central run 107055 MC by radius scales. . . . .	135
5.15	Distributions of the angular error in direction reconstruction, from the data and from MC. . . . .	136
5.16	Fitted direction resolution parameters $\beta_M$ , $\beta_S$ for the source scans. . . . .	138
5.17	Relative differences of $\beta_M$ and $\beta_S$ as a function of the $^{16}\text{N}$ source position. . . . .	139
5.18	Distributions of $\beta_{14}$ for the $^{16}\text{N}$ central run 107055. . . . .	140
5.19	A comparison of the $\beta_{14}$ for the data and the MC in run 107055. . . . .	140
5.20	$\beta_{14}$ systematics along $(x, y, z)$ scans. . . . .	141
5.21	$^{16}\text{N}$ central-run 107055, $U_{test}$ vs. $E_{fit}/5.1$ MeV. . . . .	142
5.22	$^{16}\text{N}$ central-run 107055, $G_{test}$ vs. $E_{fit}/5.1$ MeV. . . . .	142
5.23	$^{16}\text{N}$ central-run 107055, $Z_{factor}$ vs. $E_{fit}/5.1$ MeV. . . . .	143
5.24	NHits spectra of the $^{16}\text{N}$ central run 107055. . . . .	144
5.25	Reconstructed energy spectra from the $^{16}\text{N}$ central run 107055 and 106925. . . . .	145
5.26	Simulated electron energy spectra for different processes. . . . .	146
5.27	Converting number of photons to effective electron spectrum. . . . .	147
5.28	The reconstructed energy spectrum fitted with resolution function. . . . .	148
5.29	Fitted energy scales as a function of the source manipulator's radial position. . . . .	149
5.30	Fitted energy resolutions ( $b$ ) as a function of the source manipulator's radial position. . . . .	149

5.31 Smeared reconstructed energy spectrum of $^{16}\text{N}$ central run 107055 MC by energy scales. . . . .	151
5.32 Smeared reconstructed energy spectrum of $^{16}\text{N}$ central run 107055 MC by the energy resolution. . . . .	151
6.1 Reconstruction results for the candidate events, projected onto PMT sinusoidal maps. . . . .	156
6.2 The $\cos \theta_{\text{sun}}$ distribution of solar $\nu_e$ used as a PDF function. . . . .	158
6.3 Real data from run 200004 to 203602, after the beforehand cuts. . . . .	160
6.4 An example of the $\cos \theta_{\text{sun}}$ distribution fitted with $(N_{\text{sig}}, N_{\text{bkg}})$ . . . . .	160
6.5 $N_{\text{sig}}$ fit biases for 5000 fake datasets. . . . .	161
6.6 $N_{\text{sig}}$ fit pulls for 5000 fake datasets. . . . .	162
6.7 The $-2 \ln L$ distribution of the best fit results from the 5000 fake datasets. . . . .	162
6.8 Energy spectrum of events from different simulations. . . . .	164
6.9 Multiple variables as the inputs for the TMVA analysis. . . . .	166
6.10 TMVA outputs for signal/background separations by different methods. . . . .	167
6.11 TMVA ROC outputs for signal/background separations by different methods. . . . .	168
6.12 MLP cut efficiency, with $5 < E_{\text{fit}} < 15$ MeV. . . . .	170
6.13 BDT cut efficiency, with $5 < E_{\text{fit}} < 15$ MeV. . . . .	170
6.14 BDT and MLP outputs for the $\cos \theta_{\text{sun}}$ ( $4 < E_{\text{fit}} < 15$ MeV). . . . .	171
6.15 MLP outputs from one random fake dataset ( $5 < E_{\text{fit}} < 15$ MeV). . . . .	171
6.16 Event count ratios from TMVA outputs on 5000 fake datasets. . . . .	173
6.17 The distributions of six variables from the simulated internal and external $^{208}\text{Tl}$ backgrounds. . . . .	174
6.18 Poisson fit results for the $5 < E_{\text{fit}} < 15$ MeV range. . . . .	176
6.19 The MSW survival probability curves as functions of MC energies. . . . .	177
6.20 The MC $\cos \theta_{\text{sun}}$ distributions used as PDFs for the flux calculations after the BDT selections ( $5 < E_{\text{fit}} < 15$ MeV). . . . .	178
6.21 A fit on the total $^8\text{B}$ flux. . . . .	179
6.22 Fitting with the spectrum of elastic scattering. . . . .	180
6.23 Smearing effects on the $\cos \theta_{\text{sun}}$ PDF. . . . .	183

6.24 A comparison of the ES flux measured recently by three independent experiments. . . . .	185
A.1 Likelihood surface of an $^{16}\text{N}$ event projected on planes. . . . .	215
A.2 Likelihood surface of an $^{16}\text{N}$ event projected on $x, y, z, t$ -axis respectively. .	216
A.3 Derivatives of the best-fit $\ln \mathcal{L}$ of an $^{16}\text{N}$ event projected on $x, y, z, t$ -axis respectively. . . . .	216
A.4 Layouts for the scintillator light paths inside the AV sphere. . . . .	217
A.5 Layouts of the scintillator light paths inside the neck cylinder. . . . .	218
C.1 A flow chart for Bi-Po tagging. . . . .	226

# List of Tables

2.1	Neutrino interactions in the $\mathcal{O}(0.1\text{-}10 \text{ MeV})$ energy region. . . . .	7
2.2	Neutrino experiments for studying flavor transformation. . . . .	14
2.3	The main reactions producing solar neutrinos. . . . .	18
3.1	Number of photons calculated by the charge weighted photon number method. . . . .	53
3.2	A list of SNO+ radioactive sources. . . . .	56
4.1	Direction resolutions for the reconstruction of 5 MeV $e^-$ events. . . . .	85
4.2	Reconstruction performances for the 2.2-MeV and 4.4-MeV $\gamma$ events. . . . .	85
4.3	A comparison of quantitative estimates for the angular resolution for the SNO heavy water, SNO+ wbWLS and the SNO+ pure water cases. . . . .	89
4.4	Time constants and amplitudes measured by Oxford. . . . .	95
4.5	Relative light yields with different PPO concentrations. . . . .	95
4.6	Tuned effective group velocities for different PPO concentrations. . . . .	96
4.7	Fit position biases and resolutions for the $^{214}\text{Bi}$ - $^{214}\text{Po}$ tagging. . . . .	105
5.1	Position resolution parameters for the <b>MPW fitter</b> ( $x$ -axis). . . . .	126
5.2	Systematic uncertainties of the <b>MPW fitter</b> for position on $(x, y, z)$ -axes. . . . .	130
5.3	Vertex shifts for the reconstructed positions on $(x, y, z)$ axes. Unit: mm. . . . .	130
5.4	Vertex scales for the reconstructed positions on $(x, y, z)$ axes. . . . .	134
5.5	Direction resolution of the <b>MPW</b> and <b>RAT</b> fitters. . . . .	136
6.1	Candidate events in the open dataset. . . . .	155
6.2	Candidate events in the open dataset found by the <b>MPW fitter</b> . . . . .	155

6.3	Datasets of MC simulations. . . . .	163
6.4	Ratios of the signal event numbers to the background event numbers. . . . .	164
6.5	Testing results from different TMVA methods. . . . .	169
6.6	Fit results for the whole dataset ( $5 < E < 15$ MeV). . . . .	175
6.7	Systematics for the solar $\nu_e$ analysis in the water phase. See Sect. 5.3.1.2, 5.3.2.2, 5.3.3 and 5.3.4.4 for details. The positive and negative values of a quantity $Q$ are denoted as $Q^+$ and $Q^-$ , respectively. . . . .	181
6.8	Systematics for the fitted flux scale $f_s$ . . . . .	182
6.9	Average results. . . . .	186
A.1	Optimized fitter setting parameters for different physics phases. . . . .	212
B.1	$^{16}\text{N}$ internal $z$ -axis scan runs. . . . .	220
B.2	$^{16}\text{N}$ internal $y$ -axis scan runs. . . . .	221
B.3	$^{16}\text{N}$ internal $x$ -axis scan runs. . . . .	222
B.4	$^{16}\text{N}$ corner scan runs. . . . .	223
B.5	$^{16}\text{N}$ external scan runs. . . . .	224

# Chapter 1

## Introduction

Among state-of-the-art neutrino experiments, SNO+ aims to search for an extremely rare process called neutrinoless double-beta decay ( $0\nu\beta\beta$ ). This search will explore and attempt to resolve a key question as to the nature of the neutrino: is it a Majorana or a Dirac particle. A discovery that the  $0\nu\beta\beta$  occurs would unravel the masses of neutrinos and test new physics theories.

Regarding its physics targets, the SNO+ experiment goes through three major stages, mainly determined by the working medium inside the SNO+ detector. First, the detector was filled with water and operated as a water Cherenkov detector. During this water phase, over 300 live days of data have been collected. Calibration sources were also deployed for measuring the detector properties. Based on the first 114.7 live days of data, SNO+ published a measurement of the fluxes of Boron-8 neutrinos from the Sun. The results are consistent with the other solar neutrino experiments and also demonstrate extremely low background levels for the analysis [1].

As of the time of writing this thesis, the water phase stage has been completed, and the liquid scintillator has replaced the water. During the scintillator filling, there were several long intervals during which the water/scintillator interface level remained stable at a fixed height ( $z$ ) inside the detector. Collectively these stable (albeit) transitional stages are named the “partial-fill phase”, during which detector data are used to analyze the properties and estimate the backgrounds of the liquid scintillator for the two physics phases to follow.

Once the detector is fully filled with the liquid scintillator, the detector will be operated during the “scintillator phase”. A 6-month data-taking interval is planned, to establish the background levels of the liquid scintillator and to measure solar neutrinos, reactor antineutrinos and geoneutrinos [2]. After this scintillator phase, tellurium isotopes will be loaded into the liquid scintillator and once the mixture (or “cocktail”) is stable, the search for the  $0\nu\beta\beta$  signal will commence.

The thesis is organized as follows. In Chapter 2, basic neutrino properties and the phenomena of neutrino flavor transformation and neutrinoless double beta decay are introduced, along with the relevant theories and experiments. Chapter 3 is an overview of the SNO+ experiment, covering how the SNO+ detector works and reads the physics data; optical properties of liquid scintillators and the detector calibrations, which are crucial to the reconstruction; and a bench-top light yield measurement for a tellurium-loaded liquid scintillator. The latter measurement shows a light yield shift due to the humidity content of the tellurium-loaded scintillator in addition to (an expected) light yield sensitivity to tellurium concentration. Since the light yield of the scintillator is crucial to event reconstruction, this study is helpful for the detector running in realistic situations.

Event reconstruction is crucial for the physics analyses in SNO+. In this thesis, a framework of reconstruction algorithm, called the “multiple-path fitter” (**MP fitter**), was developed for multiple SNO+ physics phases. This framework was first developed by Dr. A. L. Hallin, to reconstruct and investigate the data taken during the “partial-fill water”, which was an early stage of the experiment when the detector was only *partially* filled with water (the residual volume being air) in December 2014 [3]. Drs. K. Singh and D. J. Auty (U. Alberta) further developed this fitter to accommodate the wavelength shifter and analyze water events ([4, 5, 6, 7]), while Dr. J. Tseng (U. Oxford) restructured the framework using more flexible and efficient C++ code logic and implemented it into the SNO+ software [8]. I was first involved in testing and optimizing the **MP fitter** on simulations and data. Then I extended its usage by developing an **MP partial fitter** for the partial-fill phase and an **MP scint fitter** for both the scintillator phase and tellurium phase. With these extensions, the **MP fitter** framework is ready for multiple SNO+ physics phases. The principles, optimizations, and performances of these fitters are described in Chapter 4 and

Appendix A. The other reconstruction algorithms, for example, the energy reconstruction, are also introduced.

Chapter 5 focuses on the calibration during the SNO+ water phase. The **MP water fitter** was applied to the calibration data and simulations. Among the reconstructed quantities, the position and direction results were based on the **MP water fitter**, while the energy and classifier results were extracted using the SNO+ official algorithms. However, these results (energy, event type) depend on the position and direction results provided by **MP water fitter**. By comparing simulations and data, I obtained the reconstruction resolutions and uncertainties, following procedures suggested by the collaboration.

The results of Chapter 5 underpin an analysis (in Chapter 6) of solar neutrinos during the SNO+ water phase. The key research results presented in this thesis stem from the application of the **MP water fitter** to calibration data taken during the SNO+ water phase and to the 190.3 live days of water phase data. Based on these data, a measurement of the Boron-8 solar neutrino flux was performed. The **MP water fitter** was applied to the water phase physics data and simulations. Based on the simulations, I applied a machine learning analysis to optimize the signal and background separation. Then the optimized separation parameters were applied to the data to extract the solar neutrinos from the backgrounds. I evaluated the solar neutrino rates and the background rates from the dataset. The systematics and uncertainties from Chapter 5 were evaluated and included in the results. Finally, a  ${}^8\text{B}$  solar neutrino flux was evaluated and compared with the results from other experiments.

## Chapter 2

# Neutrino physics

This chapter introduces the properties of neutrinos and their interactions, focusing on the weak interactions, neutrino mass, and flavor transformations. The existence of the particle (or class of particles) now known as the neutrino was first proposed by Pauli, to explain the (otherwise incomprehensible) spread of the electron energy spectrum in radioactive beta decay. Since the first (indirect) *observations* of the neutrino, decades later in the 1950s, various types of neutrino experiments have measured and studied neutrinos produced from different sources: the core of the Sun, Earth's mantle and crust, the atmosphere, fission reactors, accelerator beams, and astrophysical objects such as supernovae. To state the obvious, these sources produce (in turn): solar neutrinos, geoneutrinos, atmospheric neutrinos, reactor antineutrinos, accelerator neutrinos, and supernova/astrophysical neutrinos. Experiments focused on solar neutrinos have unraveled the phenomenon of neutrino flavor transformation in the matter. The solar neutrino experiments relevant to the analysis presented in Chapter 6 are introduced. The last section of this chapter introduces the major physics goal for SNO+, i.e. neutrinoless double beta decay, and covers experiments relevant to that goal.

### 2.1 Overview

A neutrino is a neutral, spin-1/2 fermion that interacts (*with other fermions or fermionic fields*) only via the weak interaction and gravity. Its basic properties and interactions are

described by the Standard Model (SM), a theory describing the properties of all elementary particles currently observed and their interactions based on *three* fundamental forces: the strong, weak, and electromagnetic forces. Notably, the gravitational force, though equally deserving the adjective “fundamental”, is not included in the Standard Model, and a long-standing effort to unify the four forces is ongoing.

The SM has successfully explained and predicted phenomena in particle physics since the latter half of the 20th century. An important triumph achieved by the SM is the discovery of the predicted Higgs bosons in 2012. However, there are still open issues in the SM. Besides the question of accommodating gravity, some of the unsolved questions relate to the mysterious properties and behavior of neutrinos: What are the masses of neutrinos? How do neutrinos obtain their masses? Why are their masses so small compared to those of the other elementary particles? Are neutrinos their own antiparticles? Still, further questions about neutrinos are likely to emerge. Were any of these questions to be answered, a door would open to new physics theories beyond the SM.

Since neutrinos weakly interact with other particles and fields, they can penetrate through massive matter or travel a long way through space without being interrupted. Neutrinos produced in the core of the Sun, in Supernovae, or in the galactic core of the Milky Way can carry original information of these astrophysics objects and easily bring this information to the detectors on the Earth. This property enables neutrinos as a probe to study the status of astrophysics objects.

Therefore, studying neutrinos can provide us with a deeper knowledge of nature.

The existence of neutrinos was first put forward by Wolfgang Pauli in the 1930s to solve the observed contradiction in  $\beta$ -decay process. In 1914, James Chadwick found that the electrons emitted in  $\beta$ -decay (called the “ $\beta$ -electrons”) have a continuous energy spectrum [9]. However, since nuclei have discrete energy levels, the energy spectrum of  $\beta$ -electrons should be discrete and equal to the difference between the final and initial states of nuclei. This indicates that the energy and momentum are not conserved if only nuclei and  $\beta$ -electrons are present in the  $\beta$ -decay products. Pauli then introduced a charge-neutral, spin-1/2, and nearly massless particle to the  $\beta$ -decay products. This particle was later called “neutrino” (the small neutral one) by Enrico Fermi. The neutrinos take away a part

of the energy and then cause the broad energy spectrum of  $\beta$ -electrons, thus the problem was solved.

In 1934, Fermi developed the four-fermion vertex interaction theory to describe the weak interactions relating to neutrinos. Soon after that, Bethe and Peierls suggested direct neutrino detection can be made via a neutrino-induced interaction, called the inverse beta decay (IBD):  $\bar{\nu}_e + p \rightarrow e^+ + n$ . Their calculation showed that the IBD cross-section was the order of  $\mathcal{O}(10^{-44} \text{ cm}^2)$ , which was difficult for detection [10]. Though the task to detect neutrinos was difficult, in 1956 Fred Reines and Clyde Cowan made the first discovery of the antineutrinos from nuclear reactors. They measured the cross-section as  $6.3 \times 10^{-44} \text{ cm}^2$ , which was consistent with Bethe's calculation [11].

In 1962, Lederman, Schwartz, and Steinberger demonstrated that more than one type of neutrino exists by detecting the interactions of the muon neutrino ( $\nu_\mu$ ) [12]. The tau neutrino ( $\nu_\tau$ ) was proposed after the discovery of the  $\tau$  lepton and was observed in 2000 by the DONUT collaboration [13]. The decay width of the  $Z^0$  boson measured by the ALEPH collaboration implied that based on the SM, the number of light neutrino species is three [14].

Currently, there are three flavor neutrinos described in the SM. Neutrinos mostly participate in the weak interaction, while the other interactions are negligible. Via weak interaction, a neutrino  $\nu_x$  is generated with a definite leptonic flavor, accompanied by one of the three charged leptons: electron ( $e$ ), muon ( $\mu$ ) or tauon ( $\tau$ ), from which it is identified as an electron neutrino ( $\nu_e$ ), a muon neutrino ( $\nu_\mu$ ), or a tau neutrino ( $\nu_\tau$ ). By observing the produced secondary charged particles, neutrinos can be detected.

## 2.2 Neutrino Interactions

In the SM, the weak interaction is described by the electroweak theory based on the Glashow-Weinberg-Salam (GWS) model, as fermions exchanging three types of gauge bosons, the weak force carriers: the charged  $W^\pm$ , and the neutral  $Z^0$ . The theory requires the lepton number and lepton flavor conservation and allows only the chiral left-handed neutrino ( $\nu_L$ ) and right-handed antineutrino ( $\bar{\nu}_R$ ) to participate in weak interactions. Neutrino in-

Table 2.1: Neutrino interactions in the  $\mathcal{O}(0.1\text{-}10 \text{ MeV})$  energy region, modified from Ref. [16].

ES	IBD	Nuclear Interactions
$(-) \nu_x + e^- \rightarrow (-) \nu_x + e^-$	$\bar{\nu}_e + p \rightarrow n + e^+$	$\nu_e + (N, Z) \rightarrow (N - 1, Z + 1) + e^-$
$(-) \nu_x + p \rightarrow (-) \nu_x + p$		$\bar{\nu}_e + (N, Z) \rightarrow (N + 1, Z - 1) + e^+$

teractions include the neutrino-electron scattering, neutrino-nucleon scattering and hadron decays [15].

This thesis studies solar neutrinos in the energy range  $E_\nu \sim \mathcal{O}(0.1\text{-}10 \text{ MeV})$ , a range in which the most completely understood interactions are neutrino elastic scattering on electrons, protons and nuclei [16], see Table 2.1. Elastic scattering can proceed via the charged weak current (CC) process entailing an exchange of the  $W^\pm$  bosons, or via the neutral weak current (NC) process wherein the  $Z^0$  boson is exchanged. In particular the elastic scattering interaction  $\nu + e^-$  ES:  $\nu_x + e^- \rightarrow \nu_x + e^-$  ( $x = e, \mu, \tau$ ) plays an important role in the detection of solar neutrinos, and will be discussed in the next section.

### 2.2.1 Neutrino-Electron Elastic Scattering

The  $\nu + e^-$  ES process is a pure leptonic process and can be precisely described by the electroweak theory in the SM. This process has no energy threshold and is sensitive to all neutrino flavors. It is valid for both neutrino and antineutrino.

The amplitude for this process has contributions from both NC and CC interactions. Fig. 2.1 shows the tree-level Feynman diagrams (without radiative corrections) for the CC ES (Fig. 2.1(a)) and the NC ES (Fig. 2.1(b)) interactions.

It is a characteristic of the charged vertex that lepton generation does not change, thus, although the  $\nu_e$  can undergo both the CC ES and NC ES interactions, the  $\nu_\mu$  and  $\nu_\tau$  may interact only through the NC ES interaction <sup>1</sup>. In other words for the CC channel the charged lepton in the final state must belong to the same lepton generation as the

---

<sup>1</sup>For  $\bar{\nu}_e$ , the Feynman diagram of the CC ES is a  $s$ -channel diagram rather than the  $t$ -channel presented in Fig 2.1(a)

(incoming) neutrino, this being required by (the theory of) the weak interaction. In this case, since the rest masses of muon and tau leptons are much larger than the masses of solar neutrinos, specifically  $m_\mu \approx 105.6$  MeV and  $m_\tau \approx 1.78$  GeV [17], evaluation of the elastic scattering via the CC channel requires energy thresholds [18]

$$E_\nu \geq \frac{m_l^2 - m_e^2}{2m_e} \quad (l = \mu, \tau)$$

larger than 10.9 GeV for the  $\nu_\mu$  and 3089 GeV for the  $\nu_\tau$ , which is impossible for solar neutrinos due to their MeV-scale energies.

On the other hand, for the NC ES, the Feynman diagram is the same for all flavors  $\bar{\nu}_x$  [15, 19].

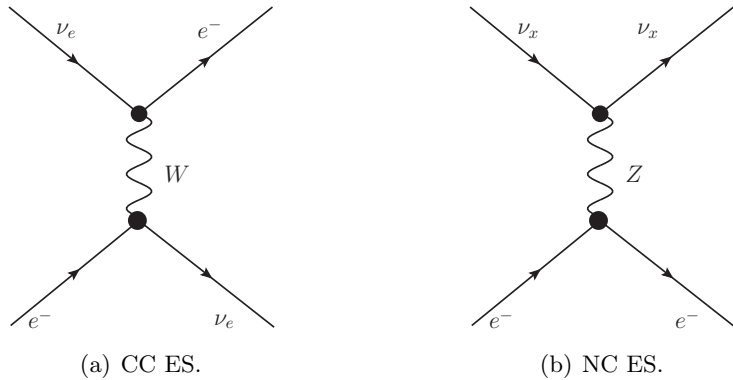


Figure 2.1: Feynman diagrams for the elastic scattering interaction in different channels at tree level. (a): CC ES for  $\nu_e$ ; (b): NC ES for all flavors  $\nu_x$  ( $x = e, \mu, \tau$ ).

In a particle detector, the “target” electron is normally an atomic electron of the detector medium and is considered to be at rest in the laboratory frame. The incoming solar neutrinos interact with these electrons via the  $\nu + e^-$  ES, and these electrons are scattered, as shown in Fig 2.2.

In the laboratory frame, the kinetic energy of a recoil electron from the  $\nu + e^-$  ES process is [15]:

$$T_e = \frac{2m_e c^2 E_\nu^2 \cos^2 \theta}{(m_e c^2 + E_\nu)^2 - E_\nu^2 \cos^2 \theta}, \quad (2.1)$$

where the scattering angle  $\theta$  is defined (Fig. 2.2) as the deviation of the outgoing (scattered) electron’s path and the path of the incoming neutrino (Eqn. 2.1 follows directly from conservation of relativistic 4-momentum, if one neglects the mass of the neutrinos). The recoil

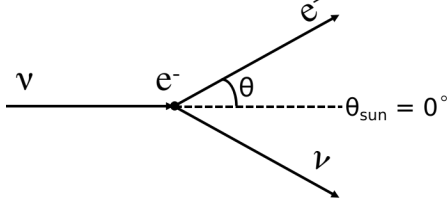


Figure 2.2: A diagram of the  $\nu + e^-$  elastic scattering in the lab frame, modified from Ref. [15].

electron has maximum energy

$$T_{max} = \frac{2E_\nu^2}{2E_\nu + m_e c^2} \quad (2.2)$$

when it scatters along the direction of the incident neutrino (i.e. when  $\theta = 0$  or  $\theta = \pi$ ).

The direction of the scattered electron is strongly correlated with the direction of the incident neutrino. For solar neutrinos, the scattering angle (relative to the axis between the SNO+ detector and the sun's position) is denoted as “solar angle” ( $\theta_{sun}$ ) in this thesis. It is one of the crucial parameters for measuring solar neutrinos, which will be discussed in Chapter 6 for analyzing solar neutrinos in the SNO+ water phase. By rearranging Eqn. (2.1) we obtain [15]

$$\begin{aligned} \cos \theta_{sun} &= \sqrt{\frac{T_e(m_e c^2 + E_\nu)^2}{2m_e c^2 E_\nu^2 + T_e E_\nu^2}}, \\ &= \left(1 + \frac{m_e c^2}{E_\nu}\right) \frac{1}{\sqrt{1 + \frac{2m_e c^2}{T_e}}}. \end{aligned} \quad (2.3)$$

The differential cross-section of the  $\nu + e^-$  ES in the lab frame (without radiative corrections) is given by [15, 19, 20]:

$$\frac{d}{dT_e} \sigma(E_\nu, T_e) = \frac{G_F^2 m_e}{2\pi} \left[ (c_V + c_A)^2 + (c_V - c_A)^2 \left(1 - \frac{T_e}{E_\nu}\right)^2 - (c_V^2 - c_A^2) \frac{m_e T_e}{E_\nu^2} \right], \quad (2.4)$$

where  $G_F$  is the Fermi coupling constant in the weak interaction; the coupling parameters  $c_V = 2 \sin^2 \theta_W \pm \frac{1}{2}$ ,  $c_A = \pm \frac{1}{2}$ , and the “+” sign is for the  $\nu_e + e^-$  case while “−” sign is for the  $\nu_{\mu,\tau} + e^-$  cases; the Weinberg angle  $\sin \theta_W$  is given by  $\sin^2 \theta_W = 0.23$ . The cross-section is  $\sigma^{ES}(\nu_e + e^-) = 9.52 \times 10^{-44} (E_\nu/10 \text{ MeV}) \text{ cm}^2$  and the expected solar neutrino rate is

(see [20]):

$$R = A \int_{T_{thresh}}^{T_{max}} \frac{d\sigma}{dE} \frac{dN}{dE_\nu} dE_\nu. \quad (2.5)$$

The shape of the recoil electron energy spectrum and the directionality are utilized by the experiments to tag solar neutrinos in real-time [20]. These experiments will be introduced in Sect. 2.4.

For the solar neutrino case,  $E_\nu \gg m_e c^2$ , the total cross-section of  $\nu_e + e^-$  ES and  $\nu_x + e^-$  ES ( $x = \mu$  or  $\tau$ ) can safely be approximated as [19]:

$$\sigma^{ES}(\nu_e + e^-) = \frac{2G_F^2}{\pi} m_e E_\nu \left[ (1 + c_L)^2 + \frac{1}{3}(c_R)^2 \right], \quad (2.6)$$

$$\sigma^{ES}(\nu_x + e^-) = \frac{2G_F^2}{\pi} m_e E_\nu \left[ (c_L)^2 + \frac{1}{3}(c_R)^2 \right], \quad (2.7)$$

where  $x = \mu$  or  $\tau$ ,  $c_L = \frac{(c_V+c_A)}{2}$  and  $c_R = \frac{(c_V-c_A)}{2}$ . Then the ratio of  $\sigma^{ES}(\nu_{\mu,\tau} + e^-)$  to  $\sigma^{ES}(\nu_e + e^-)$  is [19]:

$$\frac{\sigma^{ES}(\nu_x + e^-)}{\sigma^{ES}(\nu_e + e^-)} = \frac{3(c_L)^2 + (c_R)^2}{3(1 + c_L)^2 + (c_R)^2} \approx 0.155. \quad (2.8)$$

Thus the cross-section for CC ES is about 6.5 times larger than that for NC ES. It follows that *if* at the detector the fluxes of  $\nu_e$  ( $\Phi_{\nu_e}$ ) and of  $\nu_\mu$  **or**  $\nu_\tau$  ( $\Phi_{\nu_x}$ ) were equal, the expected number of  $\nu_e$  detected would be about 6.5 times greater than the sum of the  $\nu_\mu$  and  $\nu_\tau$  events. This theory-based expectation was an input in the solar neutrino simulations, which will be discussed in Sect. 6.3.7.

## 2.3 Neutrino Flavor Transformation

Neutrino flavor transformation is a quantum mechanical interference phenomenon [21]. It was first discovered in 1998, based on the analysis of atmospheric neutrino fluxes measured by the Super-Kamiokande (Super-K) experiment to solve the “atmospheric neutrino anomaly” [22]. It is the first direct evidence showing that neutrinos have finite masses and that the SM is incomplete.

### 2.3.1 Vacuum Oscillation

For neutrino flavor oscillation experiments, neutrinos are detected in certain flavor eigenstates via weak interaction. A neutrino flavor state vector can be taken as a linear superposition of the mass eigenstates. For three-flavor neutrino mixing, we have [17]:

$$|\nu_f\rangle = \sum_{j=1}^3 U_{fj}^* |\nu_j\rangle , \quad (2.9)$$

where  $f = (e, \mu, \tau)$  and  $j = (1, 2, 3)$ . The unitary matrix  $U_{fj}^*$ , known as the Pontecorvo–Maki– Nakagawa– Sakata (PMNS) matrix,  $U_{PMNS}$ , can be parameterized as <sup>2</sup> :

$$U_{PMNS} = \begin{pmatrix} 1 & 0 & 0 \\ 0 & c_{23} & s_{23} \\ 0 & -s_{23} & c_{23} \end{pmatrix} \begin{pmatrix} c_{13} & 0 & e^{-i\delta_{CP}} s_{13} \\ 0 & 1 & 0 \\ e^{-i\delta_{CP}} s_{13} & 0 & c_{13} \end{pmatrix} \begin{pmatrix} c_{12} & s_{12} & 0 \\ -s_{12} & c_{12} & 0 \\ 0 & 0 & 1 \end{pmatrix}, \quad (2.10)$$

where  $i$  is the imaginary unit ( $i^2 = -1$ ),  $c_{jk} \equiv \cos \theta_{jk}$  and  $s_{jk} \equiv \sin \theta_{jk}$  ( $j, k = 1, 2, 3$ ). In the PMNS matrix, there are four parameters: the three mixing angles  $\theta_{12}$ ,  $\theta_{13}$ ,  $\theta_{23}$  and the charge-parity (CP) violation parameter of the lepton sector,  $\delta_{CP}$ . The unknown value of  $\delta_{CP}$  is related to leptogenesis, the hypothetical physical process that produced an asymmetry between leptons and anti-leptons in the very early universe [23].

Now consider the propagation of a neutrino in the vacuum. Suppose that a neutrino is generated at time  $t_0 = 0$  (in the lab frame) by some mechanism (source), and that it is in flavor state

$$|\nu(0)\rangle = |\nu_\alpha\rangle = \sum_j U_{\alpha j}^* |\nu_j\rangle . \quad (2.11)$$

The energy of the initial state is a linear combination of the energies  $E_j = \sqrt{p_j^2 + (m_j c^2)^2}$  of the mass eigenstates (where  $p_j$  is the 3-momentum). The neutrino then propagates in vacuum with a speed close to the speed of light (ultra-relativistic) for a distance  $L$  and is finally detected at time  $t$  in a detector.

Now assume that the 3-momentum vector is oriented along the vector separating source and detector, with a single non-zero component. Via the 1D Schrödinger equation, the

---

<sup>2</sup>Here we ignore the Majorana CP violation phases, which cancel out and do not affect the calculation of flavor transformation probability. They will be introduced in Sect. 2.5.

amplitude for the flavor eigenstate  $|\nu_\beta\rangle$  in the detector at  $(L, t)$  is (using the natural units:  $\hbar = c = 1$ ) [24]:

$$\mathcal{A}(\nu_\alpha \rightarrow \nu_\beta; L, E) = \sum_j U_{\alpha j}^* e^{-iE_j t + ip_j L} \langle \nu_\beta | \nu_j, p_j \rangle = \sum_j U_{\alpha j}^* U_{\beta j} e^{-iE_j t + ip_j L}. \quad (2.12)$$

Then the probability that the neutrino  $\nu_\alpha$  at time  $t_0 = 0$  transforms into a  $\nu_\beta$  at time  $t$  is:

$$\begin{aligned} P(\nu_\alpha \rightarrow \nu_\beta; L, E) &= |\mathcal{A}|^2 = \mathcal{A} \mathcal{A}^* = \\ &= (U_{\alpha 1}^* U_{\beta 1} e^{-iE_1 t + ip_1 L} + U_{\alpha 2}^* U_{\beta 2} e^{-iE_2 t + ip_2 L} + \dots) (U_{\alpha 1} U_{\beta 1}^* e^{+iE_1 t - ip_1 L} + U_{\alpha 2} U_{\beta 2}^* e^{+iE_2 t - ip_2 L} + \dots) = \\ &= \sum_j |U_{\alpha j}|^2 |U_{\beta j}|^2 + \sum_{j>k} (U_{\alpha j}^* U_{\beta j} U_{\alpha k} U_{\beta k}^*) \exp\{-i(E_j - E_k)t + i(p_j - p_k)L\} + (j \leftrightarrow k), \end{aligned} \quad (2.13)$$

where  $(j \leftrightarrow k)$  stands for the second term exchanging the  $j, k$  indices.

For the second term in Eqn. 2.13, in the ultra-relativistic case,  $p_j \simeq p_k \equiv p \simeq E \gg m$ , where  $E$  is the average energy <sup>3</sup>. Then  $E_j = \sqrt{p_j^2 + m_j^2} \simeq p + \frac{m_j^2}{2E}$  and thus [17, 24]

$$E_j - E_k \simeq \frac{m_j^2 - m_k^2}{2E} \equiv \frac{\Delta m_{jk}^2}{2E}. \quad (2.14)$$

Here  $\Delta m_{jk}^2$  is a set of parameters called the “mass square differences”, and they feature in the flavor transition probability <sup>4</sup>. With the further simplification that  $L \simeq ct = t$  ( $c \equiv 1$ ), we obtain

$$\exp\{-i(E_j - E_k)t + i(p_j - p_k)L\} \simeq \exp\{-i\frac{\Delta m_{jk}^2}{2E} L\}.$$

In addition,

$$\begin{aligned} U_{\alpha k}^* U_{\beta j} U_{\alpha k} U_{\beta k}^* &= |U_{\alpha j}^* U_{\beta j} U_{\alpha k} U_{\beta k}^*| \exp\{i\phi_{\alpha\beta;jk}\}, \\ &= |U_{\alpha j}^* U_{\beta j} U_{\alpha k} U_{\beta k}^*| \{\cos \phi_{\alpha\beta;jk} + i \sin \phi_{\alpha\beta;jk}\} \end{aligned}$$

where

$$\begin{aligned} \phi_{\alpha\beta;jk} &= \text{Arg}(U_{\alpha j}^* U_{\beta j} U_{\alpha k} U_{\beta k}^*), \\ \phi_{\alpha\beta;jk} &= -\phi_{\alpha\beta;kj}. \end{aligned}$$

---

<sup>3</sup>Note: here and elsewhere in the thesis factors of  $c$  or  $c^2$  (etc.) will be dropped – but are understood to be necessary for dimensional homogeneity.

<sup>4</sup>Viewed as a matrix or rank-2 tensor, the quantity  $\frac{\Delta m_{jk}^2}{2E}$  has zeros along the diagonal. It is anti-symmetric in its indices.

Then combining the second term (of Eqn. 2.13) and the corresponding ( $j \leftrightarrow k$ ) term, Eqn. 2.13 can be written as [24]:

$$P_{\nu_\alpha \rightarrow \nu_\beta}(L, E) = \sum_j |U_{\alpha j}|^2 |U_{\beta j}|^2 + 2 \sum_{j>k} |U_{\alpha j}^* U_{\beta j} U_{\alpha k} U_{\beta k}^*| \cos\left(\frac{\Delta m_{jk}^2}{2E} L - \phi_{\alpha\beta;jk}\right), \quad (2.15)$$

where (recall)  $L$  is distance from source to detector, and  $E$  is the energy of the neutrino *averaged along the path*.

Because the matrix  $U$  is unitary the second term in Eqn. 2.15 expands as

$$\begin{aligned} & |U_{\alpha j}^* U_{\beta j} U_{\alpha k} U_{\beta k}^*| \{ \cos(\phi_{\alpha\beta;jk}) \cos\left(\frac{\Delta m_{jk}^2}{2E} L\right) + \sin(\phi_{\alpha\beta;jk}) \sin\left(\frac{\Delta m_{jk}^2}{2E} L\right) \} = \\ & \Re(U_{\alpha j}^* U_{\beta j} U_{\alpha k} U_{\beta k}^*) (1 - 2 \sin^2 \frac{\Delta m_{jk}^2 L}{4E}) + \Im(U_{\alpha j}^* U_{\beta j} U_{\alpha k} U_{\beta k}^*) \sin \frac{\Delta m_{jk}^2 L}{2E}, \end{aligned} \quad (2.16)$$

and when  $t = L = 0$ , Eqn. 2.15 becomes

$$P_{\nu_\alpha \rightarrow \nu_\beta} = \delta_{\alpha\beta} = \sum_j |U_{\alpha j}|^2 |U_{\beta j}|^2 + 2 \sum_{j>k} \Re(U_{\alpha j}^* U_{\beta j} U_{\alpha k} U_{\beta k}^*). \quad (2.17)$$

We can now eliminate the first term in Eqn. 2.15, and upon doing so we obtain the important and widely cited “vacuum neutrino oscillation equation” [17, 24]:

$$\begin{aligned} P_{\nu_\alpha \rightarrow \nu_\beta}(L, E) = \delta_{\alpha\beta} & - 4 \sum_{j>k} \Re[U_{\beta j} U_{\alpha j}^* U_{\alpha k} U_{\beta k}^*] \sin^2 \frac{\Delta m_{jk}^2 L}{4E} \\ & + 2 \sum_{j>k} \Im(U_{\beta j} U_{\alpha j}^* U_{\alpha k} U_{\beta k}^*) \sin \frac{\Delta m_{jk}^2 L}{2E}. \end{aligned} \quad (2.18)$$

Choosing a set of units commonly used by experiments and with dimensional transformation, we have [17]:

$$X_{jk} \equiv \frac{\Delta m_{jk}^2 L}{4E} = \frac{1.267 \Delta m_{jk}^2 [\text{eV}^2] L [\text{m}]}{E_\nu [\text{MeV}]} . \quad (2.19)$$

Maximum oscillation occurs when  $X_{jk} \sim \pi$ , which gives an effective length  $L^{osc}(\Delta m_{jk}, E_\nu) = 4\pi E / |\Delta m_{jk}^2|$ .

Currently, the four parameters in the PMNS matrix ( $\theta_{12}, \theta_{13}, \theta_{23}$  and  $\delta_{CP}$ ), as well as the two squared-mass differences:  $\Delta m_{21}^2 = m_2^2 - m_1^2$  and  $\Delta m_{32}^2 = m_3^2 - m_2^2$ , have been measured by neutrino oscillation experiments.

These experiments can be classified by the neutrino sources they use: the sun, nuclear reactors, muons generated in the atmosphere by cosmic rays, particle accelerators, and astronomical sources in deep space. Table 2.2 lists the energy scale of the neutrino source as well as the example experiments.

Table 2.2: Neutrino experiments for studying flavor transformation.

type	source	$E_\nu$	example
solar	the Sun	MeV scale	SNO
reactor	reactor	MeV scale	DayaBay
atmospheric	cosmic-ray	GeV scale	SuperK
accelerator	$\nu$ beam from accelerator	GeV scale	T2K
astronomical	astronomical objects	GeV-EeV scale	IceCube

Currently, the sign of  $\Delta m_{32}^2$  is still not determined. If it is positive, the neutrino masses are in a “normal hierarchy” (NH,  $m_3 > m_2 > m_1$ ); otherwise they are in an “inverted hierarchy” (IH,  $m_3 < m_1 < m_2$ ) [17].

For  $\Delta m_{21}^2$  and  $\theta_{12}$ , a combined analysis of the measurements from the reactor experiment KamLAND (Kamioka Liquid Scintillator Antineutrino Detector) and the solar neutrino experiment SNO (Sudbury Neutrino Observation) gave  $\Delta m_{21}^2 = 7.59_{-0.21}^{+0.21} \times 10^{-5}$  eV<sup>2</sup> and  $\tan^2 \theta_{21} = 0.47_{-0.05}^{+0.06}$  [25]. Details will be discussed in Sect. 2.4.

Accelerator neutrino experiments as well as atmospheric neutrino experiments have measured  $\Delta m_{32}^2$  and  $\theta_{23}$ . The most recent results from Super-K show that assuming a normal mass hierarchy,  $\Delta m_{32}^2 = 2.5_{-0.20}^{+0.13} \times 10^{-3}$  eV<sup>2</sup> and  $\sin^2 \theta_{23} = 0.588_{-0.064}^{+0.031}$  [26].

In 2012, the reactor neutrino experiment Daya Bay reported the discovery of non-zero  $\theta_{13}$  with a significance of  $5.2\sigma$ . In 2016, Daya Bay reported that  $\sin^2 2\theta_{13} = 0.0841 \pm 0.0027(\text{stat.}) \pm 0.0019(\text{syst.})$ . This high-precision result makes  $\sin^2 2\theta_{13}$  the best measured mixing angle [27, 28].

In the case of antineutrino flavor oscillation, we have  $|\bar{\nu}_\alpha\rangle = \sum_i U_{\alpha i} |\bar{\nu}_i, p_i\rangle$ . By a calculation analogous to that summarized above, a similar oscillation probability equation can

be obtained, but with the final term (in Eqn. 2.18) being negative [24]:

$$\begin{aligned} P_{\bar{\nu}_\alpha \rightarrow \bar{\nu}_\beta}(L, E) = \delta_{\alpha\beta} & - 4 \sum_{j>k} \Re[U_{\beta j} U_{\alpha j}^* U_{\alpha k} U_{\beta k}^*] \sin^2 \frac{\Delta m_{jk}^2 L}{4E} \\ & - 2 \sum_{j>k} \Im(U_{\beta j} U_{\alpha j}^* U_{\alpha k} U_{\beta k}^*) \sin \frac{\Delta m_{jk}^2 L}{2E}. \end{aligned} \quad (2.20)$$

This provides a measure of CP violation [24],

$$\mathcal{A}_{CP} = P_{\nu_\alpha \rightarrow \nu_\beta}(L, E) - P_{\bar{\nu}_\alpha \rightarrow \bar{\nu}_\beta}(L, E) = 4 \sum_{j>k} \Im(U_{\beta j} U_{\alpha j}^* U_{\alpha k} U_{\beta k}^*) \sin \frac{\Delta m_{jk}^2 L}{2E}, \quad (2.21)$$

where  $\delta_{CP}$  is examined by the experiments which measure the difference between neutrino and antineutrino oscillation probabilities  $P(\bar{\nu}_\alpha \rightarrow \bar{\nu}_\beta)$  and  $P(\nu_\alpha \rightarrow \nu_\beta)$  [19]. In 2019, the Tokai-to-Kamioka (T2K) experiment in Japan claimed confidence intervals for  $\delta_{CP}$  with three standard deviations ( $3\sigma$ ): [-3.41,-0.03] (NH) or [-2.54,-0.32] (IH). This result indicates that leptons exhibit CP violation [29].

### 2.3.2 Matter Effect

The matter effect is caused by neutrinos interacting with ambient electrons and nucleons in the dense matter such as the Sun or the Earth. In this case, at the MeV energy scale, the  $\nu + e^-$  ES is dominant. As explained in Sect. 2.2.1, a  $\nu_e$  may interact with electrons via either the charged current (CC) or the neutral current (NC) mechanism, while  $\nu_\mu$  and  $\nu_\tau$  interact only by the NC. Thus the  $\nu_e + e^-$  ES has an additional potential,  $V_{CC} = \sqrt{2} G_F n_e$ , where  $n_e$  is the number density of electrons in the matter encountered. This term alters the oscillation probabilities for neutrinos propagating in matter relative to the situation in the vacuum, an effect which is called the Mikheyev-Smirnov-Wolfenstein (MSW) mechanism [30, 31].

In vacuum two-flavor mixing, the Schrödinger equation can be written (in natural units) [19]:

$$i \frac{d}{dt} \begin{pmatrix} \nu_e \\ \nu_\mu \end{pmatrix} = H_0^f \begin{pmatrix} \nu_e \\ \nu_\mu \end{pmatrix}, \quad (2.22)$$

where

$$\begin{aligned} H_0^f &= \frac{1}{2E} \begin{pmatrix} m_1^2 \cos^2 \theta + m_2^2 \sin^2 \theta & (m_2^2 - m_1^2) \sin \theta \cos \theta \\ (m_2^2 - m_1^2) \sin \theta \cos \theta & m_1^2 \sin 2\theta + m_2^2 \cos^2 \theta \end{pmatrix} = \\ &\quad \frac{\Delta m_{21}^2}{4E} \begin{pmatrix} -\cos 2\theta & \sin 2\theta \\ \sin 2\theta & \cos 2\theta \end{pmatrix} + \frac{(m_1^2 + m_2^2)}{4E} \begin{pmatrix} 1 & 0 \\ 0 & 1 \end{pmatrix}, \end{aligned} \quad (2.23)$$

and  $\Delta m_{21}^2 = (m_2^2 - m_1^2)$ .

To simplify the calculation, we can drop the second unitary term of  $H_0^f$  that is irrelevant to the neutrino flavor transformation. Then including the matter effect term,  $H_0^f$  is changed to:

$$H_m = \begin{pmatrix} -\frac{\Delta m_{21}^2}{4E} \cos 2\theta + \sqrt{2}G_F n_e & \frac{\Delta m_{21}^2}{4E} \sin 2\theta \\ \frac{\Delta m_{21}^2}{4E} \sin 2\theta & \frac{\Delta m_{21}^2}{4E} \cos 2\theta \end{pmatrix}. \quad (2.24)$$

By analogy with mixing in vacuum, a mixing angle in matter,  $\theta_m$  is defined as

$$\tan 2\theta_m = \frac{\Delta m^2 \sin 2\theta}{\Delta m^2 \cos 2\theta - 2\sqrt{2}EG_F n_e}, \quad (2.25)$$

and an effective squared-mass difference in matter,  $\Delta m_m^2$  is defined as:

$$\Delta m_m^2 = \sqrt{(\Delta m^2 \cos 2\theta - 2\sqrt{2}EG_F n_e)^2 + (\Delta m^2 \sin 2\theta)^2}. \quad (2.26)$$

Thus we can write the mixing equation relating the energy eigenstates in matter ( $\nu_{1m}, \nu_{2m}$ ) to the flavor eigenstates by a unitary matrix:

$$\begin{pmatrix} \nu_e \\ \nu_\mu \end{pmatrix} = \begin{pmatrix} \cos \theta_m & \sin \theta_m \\ -\sin \theta_m & \cos \theta_m \end{pmatrix} \begin{pmatrix} \nu_{1m} \\ \nu_{2m} \end{pmatrix}. \quad (2.27)$$

The probability of flavor transformation in matter is:

$$P_{\nu_e \rightarrow \nu_\mu} = \sin^2(2\theta_m) \sin^2 \left( \frac{\Delta m_m^2 L}{4E} \right). \quad (2.28)$$

The denominator in Eqn. 2.25 implies a resonance condition:

$$V(n_e) = \sqrt{2}G_F n_e = \frac{\Delta m^2 \cos 2\theta}{2E}. \quad (2.29)$$

From this condition, for a given  $E$ , there is a resonance density  $n_e^{\text{res}}$  while for a given  $n_e$ , there is a resonance energy  $E^{\text{res}}$ . When the resonance condition is satisfied,  $\theta_m = \frac{\pi}{4}$  and two flavor neutrinos are maximally mixed, even if the vacuum mixing angle  $\theta$  is small. This is called matter enhanced neutrino oscillation [30, 32]. The matter effect was first observed by measuring the solar neutrino fluxes, which will be discussed in the next section.

## 2.4 Solar Neutrinos

In the 1930s, Gamow, von Weizsäcker and Bethe et al. explained that the Sun's energy is derived from a series of nuclear reactions [33]. Our current knowledge of these nuclear reactions has been summarized in the Standard Solar Model (SSM).

The SSM is a modern and broadly accepted theory for tracing the evolution of the Sun from its beginning, which is based on contemporary data from theories and experimental measurements, including an equation of state describing the balance between the gravitational and pressure forces; the cross-sections of the nuclear reactions; and the modern Sun's mass, age, radius, luminosity, etc. [34]. According to the SSM, the energy in the Sun is mainly produced by two sets of reactions: the proton-proton (pp) chain, which is dominant and contributes  $\sim 98.6\%$  of the energy released, and the Carbon-Nitrogen-Oxygen (CNO) cycle, which contributes  $\sim 1.4\%$  [16]. Fig. 2.3 shows all the reactions in the pp chain, and Fig. 2.4 shows the reactions in the CNO cycle.



Figure 2.3: All reactions in the three PP chains: PP-I, PP-II, PP-III. The reactions producing neutrinos are labeled in the solid frames. Modified from [35].

Via these nuclear reactions, hydrogen is eventually fused into helium, and the net nuclear transformation is  $4p + 2e^- \rightarrow {}^4He + 2\nu_e + Q$ , where the released energy  $Q = 26.73$  MeV is

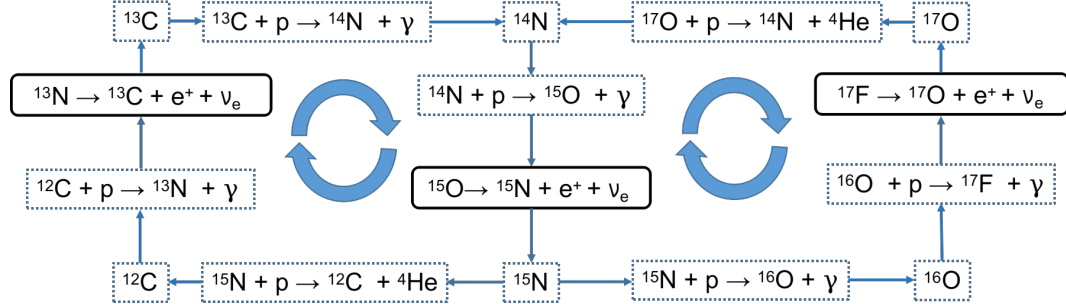


Figure 2.4: All reactions in the CNO bicycle. The reactions producing neutrinos are labeled in the solid frames. Modified from [35].

mostly released in the form of the kinetic energy of the photons, with a small fraction carried by neutrinos [16, 36].

The electron neutrinos  $\nu_e$  produced in the solar nuclear reactions are called “solar neutrinos” and can be detected on the Earth. Due to the branching ratios and unterminated chains in the pp chain and CNO cycle, the solar neutrinos come from different reactions, as shown in Fig. 2.3 and Fig. 2.4. They are named after the corresponding reactions, as shown in Table 2.3.

Table 2.3: The main reactions producing solar neutrinos in pp chain (a) and CNO cycle (b).

(a) pp chain		(b) CNO cycle	
solar $\nu_e$	reaction	solar $\nu_e$	reaction
pp	$p + p \rightarrow ^2\text{H} + e^+ + \nu_e$	CNO	$^{13}\text{N} \rightarrow ^{13}\text{C} + e^+ + \nu_e$
pep	$p + e^- + p \rightarrow ^2\text{H} + \nu_e$		$^{15}\text{O} \rightarrow ^{15}\text{N} + e^+ + \nu_e$
hep	$^3\text{He} + p \rightarrow ^4\text{He} + e^+ + \nu_e$		$^{17}\text{F} \rightarrow ^{17}\text{O} + e^+ + \nu_e$
$^7\text{Be}$	$^7\text{Be} + e^- \rightarrow ^7\text{Li} + \nu_e$		
$^8\text{B}$	$^8\text{B} \rightarrow ^8\text{Be}^* + e^+ + \nu_e$		

The average energy of a solar electron neutrino ( $\nu_e$ ) is calculated by summing over the energies  $E_{\nu_e}^i$  from the  $i^{th}$  reaction chain with a flux of  $\Phi_{\nu_e}^i$  and dividing by  $\Phi_{\nu_e}^{tot}$  [16]:

$$\langle E_{\nu_e} \rangle = \sum_i E_{\nu_e}^i \frac{\Phi_{\nu_e}^i}{\Phi_{\nu_e}^{tot}} \approx 0.265 \text{ MeV}. \quad (2.30)$$

For every MeV of released energy, there are about two  $\nu_e$  generated. Then the solar  $\nu_e$  flux at the Earth’s surface can be estimated via the measured solar radiation energy on the

Earth surface:

$$\Phi_{\nu_e} \simeq \frac{\mathcal{L}_\odot}{4\pi D_\odot^2} \frac{2}{Q - 2\langle E_{\nu_e} \rangle} \simeq 6.40 \times 10^{10} \text{ } \nu_e/\text{cm}^2/\text{s}, \quad (2.31)$$

where the solar constant  $G_{sc} = \mathcal{L}_\odot/(4\pi D_\odot^2) \simeq 0.136 \text{ W/cm}^2$  [37].

The SSM can predict the fluxes and energies of the solar neutrinos coming from different reactions, as shown in Fig. 2.5 [34].



Figure 2.5: Solar neutrino energy spectrum ( $E_\nu$  vs. flux) along with the SSM uncertainties, from Ref. [34].

In 1964, J. Bahcall and R. Davis proposed the first experiment to detect solar neutrinos [38, 39]. Davis designed an experiment that used a  $380 \text{ m}^3$  tank filled with Perchloroethylene ( $\text{C}_2\text{Cl}_4$ ), a dry-cleaning fluid rich in chlorine. Solar neutrinos were expected to change  $^{37}\text{Cl}$  to  $^{37}\text{Ar}$  via the endothermic reaction:  $\nu_e + ^{37}\text{Cl} \rightarrow ^{37}\text{Ar} + e^-$ , and the resulting  $^{37}\text{Ar}$  atoms were extracted and counted (a “radiochemical” method). The neutrino energy threshold ( $E_{\min}$ ) of the experiment was 0.814 MeV, which allowed a measurement mostly of the  $^8\text{B}$  solar  $\nu_e$  flux but also included some lower-energy neutrinos [39]. Their first results, announced in 1968, showed that only about one-third of the predicted radioactive argon atoms were measured [40]. This pioneering experiment raised a problem of the “missing”

solar neutrinos, the “solar neutrino problem.” In the middle of 1990s, by using the similar radiochemical method, two gallium experiments, SAGE [41] and GALLEX [42], measured the solar neutrinos via  $\nu_e + {}^{71}\text{Ga} \rightarrow e^- + {}^{71}\text{Ge}$  at an energy threshold of 233 keV [20]. They provided the first observation of  $pp$  neutrinos which verified the nuclear fusions happening in the Sun, and also confirmed the solar neutrino problem [20, 43].

#### 2.4.1 Kamiokande and Super-Kamiokande

The Kamiokande-II experiment in 1988 demonstrated *real-time* solar neutrino measurements by using a water Cherenkov detector [44]. As the successor of the Kamiokande experiment, Super-K uses a 50-kilotonne water Cherenkov detector to measure the solar neutrinos via the  $\nu + e^-$  elastic scattering. By utilizing the pattern of Cherenkov light produced by the recoil electrons (see Sect. 3.3.1), the direction of the incoming neutrino can be traced and thus neutrinos produced specifically by the sun can be selected. Unlike the radiochemical method, this enables real-time measurements of the solar neutrinos.

In 2000, Super-K reported the observed solar neutrino flux to be only about 45% of the flux expected according to the SSM, and with more than a 99.9% confidence level. This suggests there had been a flavor transformation of solar neutrinos, and limited the oscillation parameters ( $\Delta m_{21}^2$ ,  $\theta_{12}$ ) [44].

Super-K continues to measure solar neutrinos with more precision and higher statistical accuracy, and the energy threshold has been lowered to 3.5 MeV to enable a search for  ${}^8\text{B}$  solar neutrinos. The fourth phase of Super-K (Super-K-IV) took data from 2008 to 2014, and by utilizing this 1664 live-day data, Super-K-IV reported a measurement of the elastic scattering flux as:  $\Phi_{ES} = (2.308 \pm 0.020(\text{stat.})^{+0.039}_{-0.040}(\text{syst.})) \times 10^6 \text{ cm}^{-2}\text{s}^{-1}$  [45]. Combined with the previous three phases, it gives  $\Phi_{ES} = (2.345 \pm 0.014(\text{stat.}) \pm 0.036(\text{syst.})) \times 10^6 \text{ cm}^{-2}\text{s}^{-1}$  [45]. In Chapter 6 these values will be compared to the SNO+ measurements of this thesis.

#### 2.4.2 SNO

The Sudbury Neutrino Observatory (SNO) experiment finally resolved the solar neutrino problem and first confirmed that the missing solar neutrinos are due to the neutrino flavor

transformation  $\nu_e \rightarrow \nu_{\mu,\tau}$ , along with the matter effect mentioned in Sect. 2.3.2.

SNO used a 1-kilotonne heavy water ( $D_2O$ ) Cherenkov detector to distinguish the flavors of solar neutrinos. The SNO detector was sensitive to the  $^8B$  solar neutrinos via three interactions: (1) the charged current (CC) on deuteron ( $d$ ):  $\nu_e + d \rightarrow p + p + e^-$ , (2) the neutral current (NC):  $\nu_x + d \rightarrow p + n + \nu_x$ , and (3) the elastic scattering (ES):  $\nu_x + e^- \rightarrow \nu_x + e^-$ . The CC channel was sensitive only to  $\nu_e$  while the NC channel was independent of the neutrino type (“flavor-blind”), which provided a measurement of the total solar neutrino flux regardless of neutrino flavors. The ES channel was also sensitive to all flavors but with reduced sensitivities to  $\nu_\mu$  and  $\nu_\tau$  [46]. As mentioned in Sect. 2.2.1, from Eqn. 2.8 the ES cross-section of  $\nu_e$  is 6.5 times larger than that of  $\nu_{\mu,\tau}$  (combined).

In 2002, SNO reported that the measured total  $^8B$  solar neutrino flux via the NC channel ( $\Phi_{NC}$ ) was consistent with the SSM while the  $\nu_e$  component of the flux ( $\Phi_e$ ) was about one-third of the total flux [46]:

$$R = \Phi_{CC}/\Phi_{NC} = \Phi_e/\Phi_{tot} = 0.34 \pm 0.04 . \quad (2.32)$$

A combined analysis of SNO data acquired from 1999 to 2006 gave the measured total flux of  $^8B$  solar neutrinos as  $\Phi_{^8B} = 5.25 \pm 0.16(stat.)^{+0.11}_{-0.13}(syst.) \text{ cm}^{-2}\text{s}^{-1}$ . Based on a two-flavor neutrino oscillation analysis, SNO implied that  $\Delta m_{21}^2 = (5.6^{+1.9}_{-1.4}) \times 10^{-5} \text{ eV}^2$  and  $\tan^2 \theta_{12} = 0.427^{+0.033}_{-0.029}$  [47].

### 2.4.3 KamLAND

As mentioned in Sect. 2.3.1, reactor antineutrino experiments study the neutrino flavor transformation by measuring  $\mathcal{O}(\text{MeV}) \bar{\nu}_e$  produced by nuclear reactors. If the distance between the reactor and the detector is long enough (according to Eqn. 2.19,  $L \sim \mathcal{O}(100 \text{ km})$ ), such experiments can probe the  $\Delta m_{12}^2$  and  $\theta_{12}$  parameters, or the flavor transformation parameters in the solar sector. KamLAND is able to study the solar sector due to its long baseline of 180 kilometers (the average value of the distances to the various reactors). It is a 1-kilotonne liquid scintillator detector, located in Gifu Prefecture, Japan, under Mount Ikenoyama at a depth of about 2700 metres water equivalent (*m.w.e*) [25]. KamLAND measures the  $\bar{\nu}_e$  via the inverse beta decay (IBD) process  $\bar{\nu}_e + p \rightarrow n + e^+$ , utilizing the

prompt (light) signal produced by annihilation of the positron  $e^+$ , along with the delayed coincidence with the signal due to the  $\gamma$  emitted by neutron capture on a nucleus after thermalization [17]. KamLAND provided best fit values of [48]:  $\Delta m_{21}^2 = 7.50_{-0.20}^{+0.19} \times 10^{-5}$  eV $^2$  and  $\tan^2 \theta_{12} = 0.452_{-0.033}^{+0.035}$ . This value for  $\tan^2 \theta_{12}$  matches well with the solar neutrino measurements, but for the  $\Delta m_{21}^2$  there is a  $< 2\sigma$  level tension, which may be attributable to statistical fluctuation or some minor effect, such as the day/night matter effect.

Assuming CPT invariance, the KamLAND and solar neutrino data can be combined by including solar  $\nu_e$  and reactor  $\bar{\nu}_e$  data to obtain the oscillation parameters. These values have been given in Sect. 2.3.1.

#### 2.4.4 Borexino

Borexino is a liquid scintillator neutrino detector with a target mass of about 300 tonnes. It is located at the Gran Sasso National Laboratory (LNGS) in central Italy, under an overburden of rock with 3800 water equivalent meters (*m.w.e*) to suppress the cosmogenic backgrounds. It is the first experiment to have made real-time measurements of low energy ( $< 1$  MeV) solar neutrinos, thanks to the high light yield of the liquid scintillator [49].

Unlike a water Cherenkov detector, although a liquid scintillator provides more (detectable) photons per unit of neutrino energy deposited, it cannot be used to measure the event direction (see Sect. 3.3.2). Borexino mainly measures the energy spectrum of the recoil electrons from the  $\nu + e^-$  ES, a method that is termed “spectroscopic” [49]. Precise measurements of the energy spectrum can identify different types of solar neutrinos and separate backgrounds.

Borexino has measured the  ${}^7\text{Be}$ , *pep*, *pp* and  ${}^8\text{B}$  solar neutrino fluxes [50]. In 2020 it reported the first observation of CNO neutrinos with an interaction rate of  $7.2_{-1.7}^{+3.0}$  counts per day per 100 tonnes of target at 68% C.L., and this result gives an estimate of the CNO neutrino flux at the Earth as  $7.0_{-2.0}^{+3.0} \times 10^8$  cm $^{-2}$  s $^{-1}$  [51]. An improved measurement of the  ${}^8\text{B}$  solar neutrino was reported in 2020, with the elastic scattering flux (integrated over energy range  $3.2 < E_\nu < 17$  MeV) determined as  $\Phi_{ES} = (2.57_{-0.18}^{+0.17}(\text{stat.}) \pm 0.07(\text{syst.})) \times 10^6$  cm $^{-2}$  s $^{-1}$  [49].

#### 2.4.5 More Studies on Solar Neutrino and Future Experiments

There are at least the following three avenues for future solar neutrino research: (1) precision measurements of solar neutrino fluxes, (2) sub-leading-order effects on the phenomenology from both standard and nonstandard physics, and (3) new detection techniques [16].

Currently, *hep* neutrinos have not been measured yet due to the weakness of their flux. On the other hand, although most “species” of low energy solar neutrinos have been discovered (i.e. measured), more precise measurements would help to probe the details of matter effects, measure the oscillation parameters in the solar sector more precisely to resolve the tensions between reactor- and solar-source experiments, and could unveil new physics such as nonstandard neutrino interactions (NSI) by observing sub-leading effects [52]. Among the low energy neutrinos, *pep* neutrinos enjoy the distinction of being mono-energetic (with  $E_\nu=1.442$  MeV), and their flux is well predicted by the Standard Solar Model [53]. A precise measurement of the *pep* neutrinos will give more information on the matter effect in neutrino oscillations.

Solar metallicity ( $Z$ ) is the abundance of elements heavier than  ${}^4\text{He}$  (called “metal” elements in the context of astronomy). It is poorly constrained and the predictions from different solar models vary [54]. Since the sub-dominant CNO neutrino flux depends linearly on the metallicity of the solar core, a precise measurement of the CNO neutrinos can determine the abundance of  ${}^{12}\text{C}$ ,  ${}^{13}\text{N}$  and  ${}^{15}\text{O}$  in the Sun and thus determine the solar metallicity [55].

Several new experiments using various detection techniques are being planned, to precisely measure the solar neutrinos in the near future. These experiments include:

Large-scale water Cherenkov detectors, such as Hyper-Kamiokande (Hyper-K) [56]. Hyper-K is the next generation of Super-K, and it is designed to have a fiducial mass of 187 kilotonnes, about 8× larger than that of Super-K. With a 4.5-MeV energy threshold, it will measure the  ${}^8\text{B}$  solar neutrinos, and it expects to observe 130  $\nu + e^-$  elastic scattering events per day. With such a high count rate, the oscillation parameters in the solar sector can be precisely measured. Hyper-K also has the potential to detect the *hep* neutrinos [57].

A liquid argon neutrino detector, such as DUNE (Deep Underground Neutrino Experiment) [58], can provide two channels for detecting solar neutrinos:  $\nu_e + {}^{40}\text{Ar} \rightarrow e^- + {}^{40}\text{K}^*$

and the  $\nu + e^-$  ES process:  $\nu_x + e^- \rightarrow \nu_x + e^-$ . Similar to Hyper-K, DUNE aims for precise measurements of  ${}^8\text{B}$  neutrinos, and also searches for *hep* neutrinos [59].

Large-scale liquid scintillator detectors with  $\mathcal{O}(10)$  kilotonne fiducial mass, such as ASDC (Advanced Scintillation Detector Concept)-THEIA [60], JUNO (Jiangmen Underground) [61], Jinping (Jinping Neutrino Experiment) [62], and LENA (Low Energy Neutrino Astronomy) [63], are expected to be built to measure low energy solar neutrinos. Some new liquid scintillator techniques (such as water-based liquid scintillator) will be implemented to precisely measure neutrino energy and incoming direction.

Ton-scale dark matter direct search experiments, such as the DARWIN experiment (DARk matter WImp search with liquid xenon) can also measure low-energy solar neutrinos. With an energy threshold down to several keV and ultra-low background levels, DARWIN will be able to measure the *pp* and  ${}^7\text{Be}$  solar neutrinos [64, 65, 66].

SNO+, one of the operating large-scale liquid scintillator detectors, has measured the  ${}^8\text{B}$  solar neutrino flux during its initial water phase [1]. In the following (scintillator) phase, SNO+ is able to measure low energy solar neutrinos ( $E_\nu < 2$  MeV), and specifically the CNO and *pep* neutrinos. Due to the depth of SNOLAB, SNO+ is expected to have much lower cosmogenic backgrounds than did Borexino, and thus may obtain more precise measurements [2]. More details will be discussed in Sect. 3.2.2.

## 2.5 Neutrinoless Double Beta Decay

The neutrino flavor transformation experiments proved that neutrinos are not massless. However in these experiments mass *differences* rather than absolute masses are measured, so we cannot from these results know the absolute scale of neutrino mass. Currently, there are three main approaches to probing the neutrino masses [36]: (1) Cosmological measurements [67, 68, 69]; (2) Direct measurements of the  $\beta$ -decay spectrum [70]; and (3) A search for the neutrinoless double beta decay ( $0\nu\beta\beta$ ) process [71, 72], which relates to SNO+ and will be discussed below.

For middle-heavy to heavy radioactive isotopes whose nuclei have even neutron number and even proton number (“even-even” nuclei), the  $\beta$ -decay is energetically forbidden due

to large binding energies [32]. In 1935, M. Goeppert-Mayer pointed out that these isotopes can still decay through a *double* beta decay process:  $(Z, A) \rightarrow (Z + 2, A) + 2e^- + 2\bar{\nu}_e + Q_{\beta\beta}$ , where  $Q_{\beta\beta}$  is the released energy. This is called ordinary double beta decay or  $2\nu\beta\beta$ , which is allowed within the SM. Typically the half-life for isotopes subject to  $2\nu\beta\beta$   $T_{1/2} > 10^{19}$  years (yr) [73, 74].

In the SM, neutrinos are neutral (charge 0) fermions. As such, there is no apparent quantum number to distinguish a neutrino and an antineutrino [75]. A neutral fermion that *is* its own antiparticle is named a “Majorana” particle, in honor of E. Majorana who developed a mathematical modification of the Dirac equation [76].

In 1939 W. H. Furry [71] proposed that *if* neutrinos are Majorana particles (Majorana neutrinos), then a process called neutrinoless double beta decay ( $0\nu\beta\beta$ ) will also be expected to occur:  $(Z, A) \rightarrow (Z + 2, A) + 2e^- + Q_{\beta\beta}$ . In this process, evidently the *lepton number changes* 2, which within the scope of the SM is not allowed. Should such a decay be observed, a new paradigm for elementary particle physics will be required. The Feynman diagrams for  $2\nu\beta\beta$  and  $0\nu\beta\beta$  are compared in Fig. 2.6.

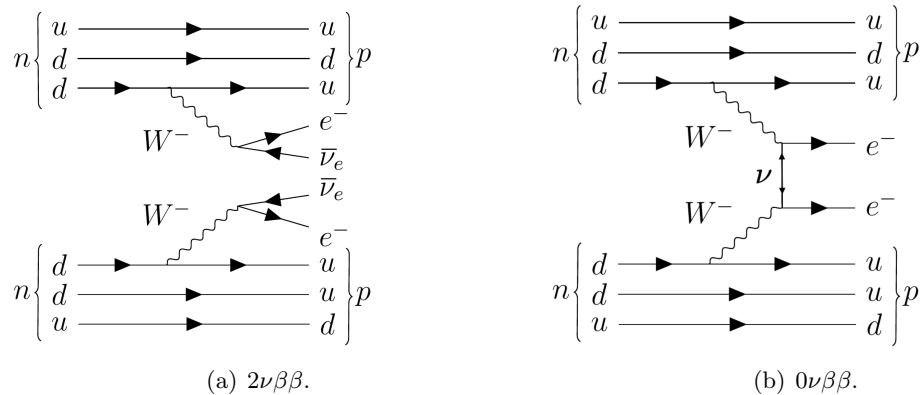


Figure 2.6: Feynman diagrams for  $2\nu\beta\beta$  (a) and  $0\nu\beta\beta$  (b).

For the Majorana neutrino, an effective Majorana mass  $\langle m_{ee} \rangle$  is defined as [37, 43]:

$$\langle m_{ee} \rangle = \left| \sum_{i=1}^3 U_{ei}^2 m_i \right| = |c_{13}^2 c_{12}^2 m_1 + c_{13}^2 s_{12}^2 e^{i\alpha_1} m_2 + s_{13}^2 e^{i\alpha_2} m_3| , \quad (2.33)$$

where the values of  $U_{ei}$  are the elements of the neutrino mixing matrix for the flavor state  $\nu_e$ , and  $m_i$  are the mass eigenvalues of the mass eigenstates, according to Enq. 2.9;  $\alpha_1, \alpha_2$

are two Majorana CP-violation phase factors ranging from 0 to  $\pi$ , and  $\alpha_2$  can also be taken as  $\alpha_2 - \delta_{CP}$ .

The neutrino mass eigenvalues  $m_i$  can be expressed as the lightest neutrino mass  $m_{\nu\min}$  and mass square differences  $\Delta m_{ij}^2$  [37]. For the normal hierarchy (NH),

$$\begin{aligned} m_{\nu\min} &= m_1, \\ m_2 &= \sqrt{m_{\nu\min}^2 + \Delta m_{21}^2}, \\ m_3 &= \sqrt{m_{\nu\min}^2 + |\Delta m_{31}^2|}, \end{aligned}$$

while for the IH,

$$\begin{aligned} m_{\nu\min} &= m_3, \\ m_1 &= \sqrt{m_{\nu\min}^2 + |\Delta m_{31}^2|}, \\ m_2 &= \sqrt{m_{\nu\min}^2 + |\Delta m_{31}^2| + \Delta m_{21}^2}. \end{aligned}$$

In this case, the effective Majorana mass can be derived from  $m_{\nu\min}$  and neutrino flavor transformation parameters  $\theta_{ij}$  and  $\Delta m_{ij}^2$ . A probe of the effective Majorana mass  $\langle m_{ee} \rangle$  can thus determine  $m_{\nu\min}$  and (in turn) the absolute neutrino masses.

The decay width and the half-life of the  $0\nu\beta\beta$  process are calculated as [37, 43]:

$$\Gamma = (T_{1/2}^{0\nu})^{-1} = G_{PS}(Q, Z) |M_{Nuc}|^2 \langle m_{ee} \rangle^2, \quad (2.34)$$

where  $G_{PS}(Q, Z)$  is a phase space corresponding to the effective coupling constant, which depends on the endpoint energy  $Q$  and the atomic number  $Z$ , while  $|M_{Nuc}|$  is the nuclear matrix element describing the nuclear transition. The latter can be calculated theoretically, albeit using *approximate methods* based on many-body nuclear models, such as the Nuclear Shell Model (NSM), interacting Boson Model (IBM), etc. Since  $G_{PS}$  and  $|M_{Nuc}|^2$  can be calculated theoretically in certain physics cases, a  $0\nu\beta\beta$  experiment can measure  $T_{1/2}^{0\nu}$  to quantify  $\langle m_{ee} \rangle$  [43, 77].

Similar to the  $\beta$ -decay case, the  $2\nu\beta\beta$  process will cause a continuous spectrum in the detector. However very significantly, the (hypothetical)  $0\nu\beta\beta$  process only has *two electrons in the final state* and so the *sum of the energies of these two electrons is constrained*. These electrons must carry away the total energy released by the decay (the energy from the

nuclear recoil is negligible here), and so a spectrum of the (summed) energy released to the outgoing electrons must show a distinct energy peak at the Q-value ( $Q_{\beta\beta}$ ). Taking the isotope  $^{130}\text{Te}$  as an example, Fig. 2.7 illustrates the shapes of the energy spectrum from the  $2\nu\beta\beta$  and the  $0\nu\beta\beta$  decay processes.

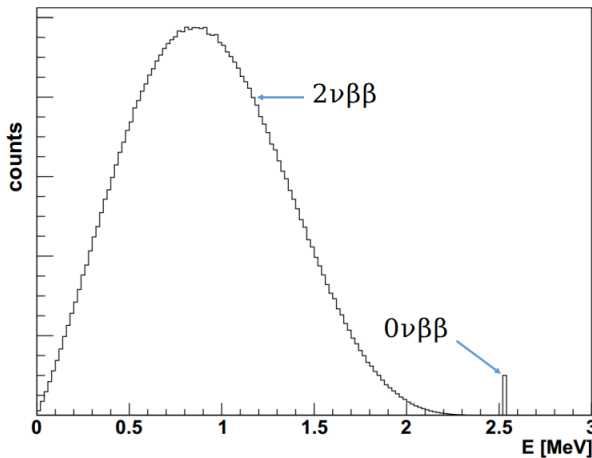


Figure 2.7: Energy spectrum of the  $^{130}\text{Te}$   $2\nu\beta\beta$  decay and the hypothetical  $0\nu\beta\beta$  decay (sum of the energies of the two outgoing electrons). The SNO+ software package (RAT) was used to produce the simulations for the plot. The package is described in Sect. 3.6.

To determine  $T_{1/2}^{0\nu}$ , experiments search for events in which the total energy deposited is close to  $Q_{\beta\beta}$ . For a candidate isotope, the observed number of events in expectation is [43]:

$$N_{event} = \ln 2 \frac{N_A}{M_A} \frac{\alpha \cdot \epsilon \cdot m \cdot t}{T_{1/2}^{0\nu}}, \quad (2.35)$$

where  $N_A$  is the Avogadro's number,  $\alpha$  is the abundance of the isotope in the element,  $M_A$  is the molar mass of the isotope,  $m$  is the target isotope mass in the detector, and  $t$  is the measurement time of total exposure.

There are 35 candidate isotopes that can undergo the  $2\nu\beta\beta$  decay process, but only a few of them are suitable for the application in direct  $0\nu\beta\beta$  search experiments [15]. From the experimental viewpoint, the candidate isotopes are required to have relatively high natural abundances and high Q-values, be deployable in a large amount with low cost, be atoxic and unharful to the environment, etc. However, in a realistic situation, no isotope fulfills all these criteria, and trade-offs have to be made for contemporary experiments [77]. Fig. 2.8 shows the Q-values and natural abundances of the candidate isotopes currently selected by

the  $0\nu\beta\beta$  experiments.

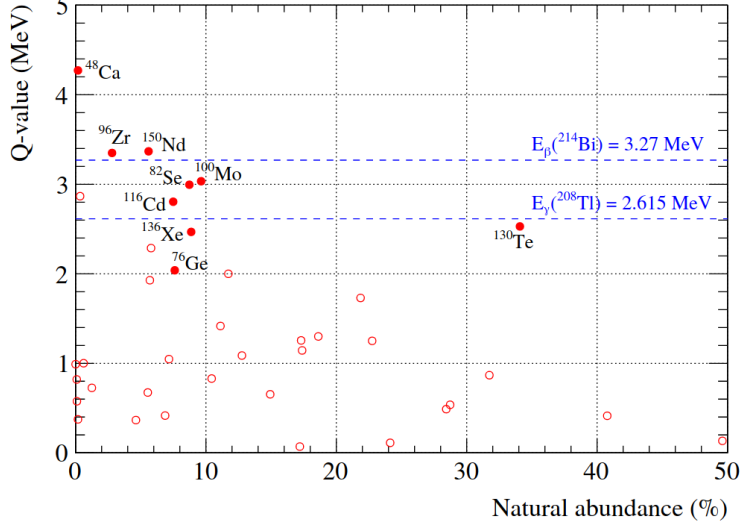


Figure 2.8: Natural abundance vs. Q-values for different  $2\nu\beta\beta$  isotopes, from Ref. [78].

Among the isotopes under consideration,  $^{130}\text{Te}$  has the highest natural abundance of 34% and thus can provide a higher target isotope mass. SNO+ will use a Te-loaded liquid scintillator to search for  $0\nu\beta\beta$ , which will be discussed in Chapter 3.

At the time of this writing, no experiment has found the signal of  $0\nu\beta\beta$ , while limits on  $T_{1/2}^{0\nu}$  and  $\langle m_{ee} \rangle$  for various candidate isotopes have been set. Currently, the best limit on  $T_{1/2}^{0\nu}$  reported by the experiments is obtained from the KamLAND-Zen experiment, searching for the signal from the  $^{136}\text{Xe}$ . Their 2016 results gave a lower limit of  $T_{1/2}^{0\nu}(^{136}\text{Xe}) > 1.07 \times 10^{26}$  yr at 90% C.L., and a corresponding upper limit on the effective Majorana mass:  $\langle m_{ee} \rangle < (61 - 165)$  meV [79].

For  $^{130}\text{Te}$ , the current best limit is from the CUORE experiment (Cryogenic Underground Observatory for Rare Events). In 2018, CUORE placed a lower limit of  $T_{1/2}^{0\nu}(^{130}\text{Te}) > 1.5 \times 10^{25}$  yr at 90% C.L., with  $\langle m_{ee} \rangle < (110 - 520)$  meV [80].

For  $^{76}\text{Ge}$ , the current best limit is from the GERDA experiment (GERmanium Detector Array). In 2019, GERDA reported a lower limit half-life of  $T_{1/2}^{0\nu}(^{76}\text{Ge}) > 1.8 \times 10^{26}$  years at 90% C.L. with  $\langle m_{ee} \rangle < (79 - 180)$  meV [81].

Future experiments such as the KamLAND2-Zen, LEGEND-1000 and nEXO, coming to fruition within about a decade, are required to reach  $T_{1/2}^{0\nu}$  at  $\mathcal{O}(10^{27} - 10^{28})$  years [77].

## Chapter 3

# The SNO+ Experiment

### 3.1 Overview

The SNOLAB facility is located at Vale’s Creighton mine in Sudbury, Ontario, Canada (coordinates:  $46^{\circ}28'19.6''\text{N}$ ,  $81^{\circ}11'12.4''\text{W}$ ), and in particular the SNO+ detector sits deep underground in the mine, beneath a  $2092 \pm 6$  m overburden of rock [78, 82]. This ensures an environment with extremely low cosmic ray backgrounds. At sea level, the average cosmic muon ( $\mu$ ) flux is about  $1.44 \times 10^7 \mu/\text{m}^2/\text{day}$  [83]. Cosmic muons with high energies (mostly  $\mathcal{O}(\text{GeV})$ ) can induce spallation backgrounds, such as fast neutrons and lasting isotopes, which are harmful to experiments of this type because they increase the background count rate, and therefore can obscure “signal” events in the sense of widening the confidence intervals on physics findings [62]. The rock overburden above the SNO+ detector reduces the cosmic muon ( $\mu$ ) flux to as low as  $0.286 \pm 0.009 \mu/\text{m}^2/\text{day}$ , corresponding to 6010 water equivalent meters (*m.w.e*) [78]. Accordingly in each hour, the number of muons passing through the SNO+ detector is of  $\mathcal{O}(1)$ .

The SNO+ detector is a refurbishment of the SNO detector. The SNO+ collaboration makes use of the SNO infrastructure and upgraded it to be a liquid scintillator (as opposed to heavy water) detector. As shown in Fig. 3.1, the detector is inside a barrel-like rock cavity with a diameter of 22 m at its waist and a height of 34 m. The cavity is filled with 7000 tonnes of ultrapure water (UPW) to provide buoyancy for the detector vessel, and shield radiation backgrounds from the environment, such as the cosmic rays and isotope

decays from the rock.

The detector consists of an acrylic vessel (AV) sphere of 12.01 m diameter and 5.5 cm thickness. The AV contains the detection medium (i.e. target material) and is held in place by a rope net system including hold-up and hold-down Tensylon ropes. This spherical structure is simple in geometry which reduces the complexity of simulation and event reconstruction. Furthermore, this geometry allows for spherical fiducial volume cuts from the center of the AV to reduce the external background count, which makes the SNO+ a “graded-shield” type of detector [84]. Joined to the top of the AV sphere is an acrylic “neck”, specifically a cylinder 6.8 m high and 1.46 m in inner diameter. The neck connects the AV sphere to facilities on the deck above. Through the neck, pipes can introduce the detector medium into the AV and recirculate it for purification. Calibration sources for internal scans can also be lowered down into the AV through the neck.

The AV sphere is concentric with, and lies within, a stainless steel geodesic dome having an average radius of 8.4 m, this being the photomultiplier support structure (PSUP). A total of 9394 Hamamatsu R1408 8-inch photomultipliers (PMTs) are mounted on the PSUP, looking inward to the AV. To increase the light collection efficiency of these PMTs and thus to obtain an extensive photocathode coverage of the detector, each of these PMTs was fitted into a 27 cm diameter reflective bucket (called the “concentrator”), which consists of aluminum-coated reflective petals. The effective photocathode coverage<sup>1</sup> of the detector is about 54% [85]. In addition to the inward-looking PMTs, a further 90 PMTs look outward, serving as muon vetos. Four Hamamatsu R5912 High Quantum Efficiency (HQE) PMTs were also installed, in order to test their performance for a potential further phase of the SNO+ experiment [86].

### 3.2 SNO+ Physics Phases

The SNO+ experiment is designed for multi-purpose measurements of neutrino physics, and the detector has been in operation since December 2016. There are three physics phases of the experiment, each phase having a different detection medium inside the AV: the water

---

<sup>1</sup>Defined as the fraction of a large sample of photons, emitted isotropically at the origin, that enter a PMT.



Figure 3.1: The SNO+ detector labeled with main structures, modified from Ref. [87].

phase, the scintillator phase, and the tellurium phase [85].

### 3.2.1 Water Phase

In this initial phase, about 905 tonnes of ultrapure water were contained in the AV. The detector collected water physics data from May 2017 to July 2019.

During the data-taking, different types of calibration runs were performed. The detector timing and energy response, systematics, and backgrounds were studied. Numerous analyses, e.g. of invisible nucleon decay, solar neutrinos, and reactor antineutrinos, are ongoing, and related findings have been published [88, 1, 89, 90]. The external backgrounds<sup>2</sup> were also measured, and these are expected to be unchanged over the subsequent two phases.

In this first phase, i.e. the water phase, the main physics goal is to search for invisible nucleon decay, whose occurrence is predicted by Grand Unified Theory (GUT) and would violate the baryon number conservation rule of the SM. In the putative “invisible” decay mode, a proton or a bound neutron decays without releasing charged particles, in contrast

---

<sup>2</sup>That is, event types and rates due to radioactive sources other than those producing the signals of interest, in particular, decays occurring outside the detector in the rock mass and the water cavity, as well as those due to low-level radioactive contamination of the acrylic AV wall, and so forth.

to the (again, putative) “visible” decay channels<sup>3</sup> of  $p \rightarrow e^+ \pi^0$  and  $p \rightarrow \nu K^+$ , for which the Super-K experiment searched and set limits. In the SNO+ water detector, a  $^{16}\text{O}$  nucleus may decay into a  $^{15}\text{O}^*$  (bound neutron invisible decay) or a  $^{15}\text{N}^*$  (proton invisible decay) excited state. The  $^{15}\text{O}^*$  has 44% chance to de-excite to produce a 6.18-MeV  $\gamma$  ray and a 2% chance to produce 7.03-MeV  $\gamma$ ; while  $^{15}\text{N}^*$  has a 41% probability to release a 6.32 MeV  $\gamma$  and a (2%, 2%, 3%) probability to release (respectively) a (7.01, 7.03, 9.93) MeV  $\gamma$ . The SNO+ experiment has searched for these  $\gamma$  signals and published world-leading limits of  $\mathcal{O}(10^{29})$  years for both the proton and the neutron invisible decay lifetime at 90% Bayesian credibility level [88].

The  $^8\text{B}$  solar neutrinos were measured with a 69.2 kilo-tonnes·day dataset. By analyzing solar neutrino elastic scattering events based on the dataset (Chapter 6 will discuss the method in detail), the number of the solar neutrino events were counted in different energy regions. In the first publication [1], by fitting to the *non-oscillating* solar neutrino model the data provided an estimate  $2.53_{-0.28}^{+0.31}(\text{stat.})_{-0.10}^{+0.13}(\text{syst.}) \times 10^6 \text{ cm}^{-2}\text{s}^{-1}$  for the flux of  $^8\text{B}$  solar neutrinos having energies larger than 5 MeV. In the energy region larger than 6 MeV, the dataset has a background rate of  $0.25_{-0.07}^{+0.09}$  events/kilo-tonne·day[1], which is extremely low for a water Cherenkov detector to measure solar neutrinos in that energy region. Currently, this background rate is the lowest among the class of water Cherenkov detectors [1].

Reactor antineutrinos can be captured by the SNO+ detector and measured. 40% of these antineutrinos are from one nearby reactor complex in Canada at a distance of 240 km; 20% are from two Canadian complexes at around 350 km; the remainder arrives from the USA and elsewhere with longer baselines [85]. Though the detectable antineutrino event rate in pure water is much lower than in the scintillator, during the water phase, SNO+ still has the potential to detect reactor antineutrinos due to the low background dataset and relatively high detection efficiency. An americium-beryllium (AmBe) calibration source was deployed during the water phase to evaluate the sensitivity for detecting reactor antineutrinos. This source provides neutrons along with 4.4 MeV  $\gamma$  photons. The neutrons are captured by hydrogen, emitting 2.2 MeV  $\gamma$  photons. An analysis of delayed coincidence between 4.4 MeV and 2.2 MeV photons can help tag neutrons, which is crucial for tagging

---

<sup>3</sup>Whether visible or invisible, these hypothesized events lie outside the SM, because they violate baryon number conservation.

the reactor antineutrinos since they are measured by the inverse  $\beta$ -decay process, which also produces neutrons with a similar energy scale. In the first publication for the SNO+ water phase, a neutron detection efficiency of 50% was obtained when the AmBe source was deployed at the center of the detector; the neutron-hydrogen capture time constant  $\tau$  was measured to be  $202.35^{+0.87}_{-0.76} \mu\text{s}$ , and from  $\tau$ , a thermal capture cross-section was calculated to be  $336.3^{+1.2}_{-1.5}$  milli-barn (mb) [89].

### 3.2.2 Scintillator Phase

In this phase, the AV will be filled with 780 tonnes of liquid scintillator, which is a mixture of linear alkylbenzene (LAB) serving as solvent and 2,5-diphenyloxazole (PPO) serving as fluor, with a concentration of 2 gram PPO per liter LAB (2 g/L in short). This LAB-based organic liquid scintillator is denoted as the “unloaded” liquid scintillator (more details in Sect. 3.3.5).

As mentioned in Sect. 2.4.5, the main physics goal of the scintillator phase is to measure low energy solar neutrinos: the CNO, *pep*, and low energy  $^8\text{B}$  neutrinos. Three kinds of antineutrinos will also be measured: reactor antineutrinos (mentioned before), geoneutrinos (from natural radioactivity in the Earth); and supernova neutrinos. SNO+ is intended to join the SuperNova Early Warning System (SNEWS), which is an international network of experiments with the ability to provide an early warning of a galactic supernova [78].

### 3.2.3 Partial-fill Phase

Between the water phase and the scintillator phase, the liquid scintillator occupied a gradually increasing proportion of the AV volume, as it progressively replaced the water. The liquid scintillator, being insoluble in and having a lower density than water, formed a layer standing above the water. Over certain intervals during the fill, the level of the scintillator/water interface the mixing ratio of PPO in the LAB were stable, and these stable stages were sustained for a few weeks in order to take data under steady conditions. These transition stages were denoted as the “partial-fill phase”. At these stages, the mechanical stability of the detector (specifically, the function of the rope net system) and the chemical compatibility between the liquid scintillator and the detector materials were monitored.

Analyses on the partial-fill phase data are mainly aimed to demonstrate in a trial setting the techniques to be used with liquid scintillator before arriving at that (scintillator) phase, and to test the physical properties of the liquid scintillator, such as the light yield, the background levels, etc. Due to the COVID-19 pandemic, the duration of the partial-fill phase proved to be longer than had been planned, accidentally providing more data for some of the intended physics studies, such as measuring solar neutrinos.

### 3.2.4 Tellurium Phase

In the final, “Te-loaded scintillator” phase, 1.3 tonnes of  $^{130}\text{Te}$  will be loaded into the scintillator to achieve a planned mixing ratio of 0.5% natural tellurium (Te) by mass (more details in Sect. 3.3.6). Higher loading concentrations would be possible for a further loading plan [91]. The main purpose of this phase is to search for the  $0\nu\beta\beta$  signals in  $^{130}\text{Te}$ .

## 3.3 Detection Media

In the SNO+ detector, charged particles interact with the detection medium and create Cherenkov light and scintillation light.

### 3.3.1 Cherenkov Radiation

For any charged particle traveling in a transparent medium at an ultra-relativistic speed (a speed greater than the local phase speed of light in the medium), a type of electromagnetic radiation, called Cherenkov radiation, can be emitted from the coherent response of the medium under the action of the field of the moving particle [92, 93].

Suppose a charged particle moves in a transparent, isotropic, and non-magnetic medium and creates an electromagnetic wave. The electromagnetic wave propagates with a wavenumber  $k = \omega/v_p \equiv n\omega/c$ , where  $c$  is the speed of light in vacuum,  $\omega$  is the frequency,  $n = n(\omega)$  is the real-valued refractive index and  $v_p = c/n(\omega)$  is the phase velocity in the medium. If the particle travels uniformly along the  $x$ -axis with speed  $v > v_p$ , Cherenkov radiation of frequency  $\omega$  is emitted [93]. The “Cherenkov angle”,  $\theta_{\text{Ch}}$ , is the angle between the direction

of motion of the particle and the direction of Cherenkov emission, and it is given by

$$\cos \theta_{\text{Ch}}(\omega) = \frac{c}{n(\omega)v} . \quad (3.1)$$

The radiation is distributed over the surface of a cone with the half-opening angle  $\theta_{\text{Ch}}$ .

Now consider the case of an electron traveling in a water detector: what threshold speed and energy must the electron possess, in order to promote Cherenkov radiation? Taking  $n_{\text{water}} \simeq 1.33$  [17], i.e. neglecting the dependence of  $n$  on  $\omega$ , we obtain a threshold speed  $v^{\min} = v_p \simeq 2.254 \times 10^8$  m/s. This corresponds to a kinetic energy:

$$E_k = (\gamma - 1)mc^2 = 0.264 \text{ MeV} ,$$

where  $\gamma = 1/\sqrt{1 - v_p^2/c^2}$ . This is the lowest kinetic energy to create Cherenkov radiation in water, and is referred to as the Cherenkov threshold ( $E_{\text{thresh}}$ ). The corresponding Cherenkov angle is  $\theta_{\text{Ch}} \simeq 41.25^\circ$ . For the LAB-PPO (scintillator) medium,  $n \simeq 1.50$  [94], giving a threshold electron (kinetic) energy  $E_{\text{thresh}} \simeq 0.175$  MeV and  $\theta_{\text{Ch}} \simeq 48.19^\circ$ . For a particle with a charge of  $ze$ , the number of photons produced by Cherenkov radiation per unit path length and per unit frequency of the photons is given by [95]

$$\frac{d^2N}{d\omega dx} = \frac{\alpha(ze)^2}{c} \sin^2 \theta_{\text{Ch}} = \frac{\alpha(ze)^2}{c} \left(1 - \frac{1}{\beta^2 n^2(\omega)}\right) , \quad (3.2)$$

where  $\alpha$  is the fine structure constant and  $\beta = v/c$ . Substituting  $\omega = (2\pi c)/\lambda$  and integrating over a wavelength band  $\lambda_1 \leq \lambda \leq \lambda_2$ , the number of photons produced per unit of distance along the  $x$ -axis (i.e. particle path) within that waveband is [95]:

$$\frac{dN}{dx} = 2\pi\alpha(ze)^2 \sin^2 \theta_{\text{Ch}} \int_{\lambda_1}^{\lambda_2} \frac{d\lambda}{\lambda^2} . \quad (3.3)$$

For optical photons with wavelengths ranging from 350 to 550 nm (a typical PMT sensitivity range), the above formula evaluates to [95]:

$$\frac{dN}{dx} = 476(ze)^2 \sin^2 \theta_{\text{Ch}} \text{ photons/cm} . \quad (3.4)$$

For Cherenkov radiation caused by electron motion in a water detector,  $dN/dx \simeq 207$  photons/cm; while in the LAB-PPO case,  $dN/dx \simeq 264$  photons/cm. In more detailed accounting, PMT coverage and detection efficiency need to be admitted into the derivation.

### 3.3.2 Scintillation Light from Organic Scintillator

When charged particles travel through an organic scintillator the importance of Cherenkov radiation is much reduced, relative to “scintillation photons”<sup>4</sup>, which are produced as follows.

An organic liquid scintillator is composed of aromatic hydrocarbon compounds with benzene-ring structures, and ionizing radiation may excite the free valence electrons of the molecules into the  $\pi$ -molecular orbitals with the benzene rings. These highly delocalized electrons can occupy a series of energy levels, as shown on a Jablonski diagram (Fig. 3.2) which represents these  $\pi$ -electronic energy levels [95, 97]. In the diagram,  $S_{0,1,2,3,\dots}$  are the

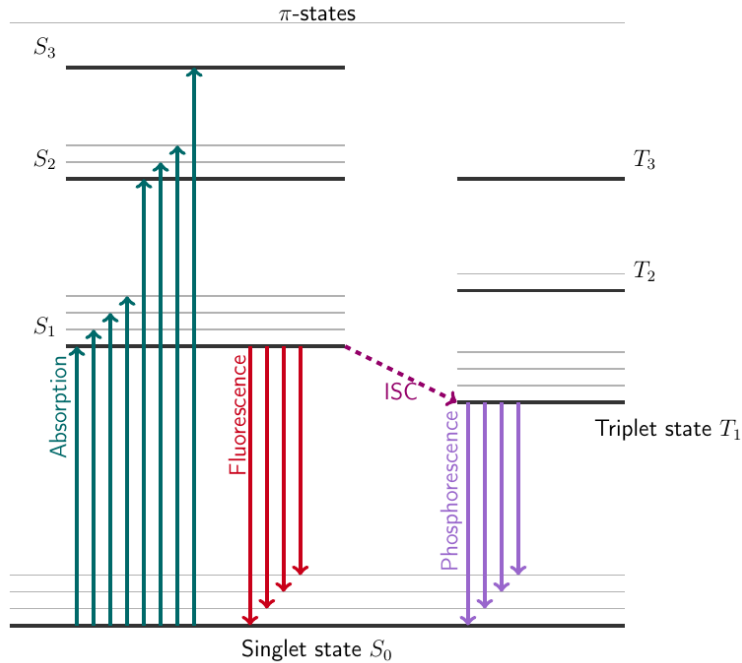


Figure 3.2: A Jablonski diagram for the organic scintillator, modified from Refs. [97, 98].

energy levels of the spin-0 singlet states, where  $S_0$  is the ground state and  $S^* = S_{1,2,3,\dots}$  are the excited singlet states. Above the ground state  $S_0$ , there is also a set of spin-1 triplet states  $T_{1,2,3,\dots}$ , where  $T_1$  is the lowest triplet state. These electron energy levels are labeled with thick black lines. The energy spacings between these levels are  $\mathcal{O}(\text{eV})$ . In

---

<sup>4</sup>For the liquid scintillator used in the SNO+ scintillator phase, the number of scintillation photons emitted from an event is about two orders of magnitude higher than the number of Cherenkov photons [96].

each level, there are also fine structure levels that correspond to excited vibration modes of the molecule (labeled with gray lines and typically labeled as  $S_{10}, S_{11}, \dots, S_{20}, S_{21}, \dots$ ). The energy spacings between these fine levels are  $\mathcal{O}(0.15)$  eV [95, 97].

The ionizing radiation transfers energy to the molecules and excites the electron levels as well as the vibrational levels, labeled as the absorption lines (in green). The decays between the excited singlet states (not to the ground state) are almost immediate ( $\leq 10$  ps), and occur without emission of photons, a process called internal degradation. The decays from the excited singlet state  $S_1$  (as well as from the vibrational states  $S_{10}, S_{11}, S_{12}, \dots$ ) to the ground state (or to the vibrational excitations of it, i.e. to  $S_{01}, S_{02}, \dots$ ) happen promptly ( $\mathcal{O}(\text{ns})$ ) and emit light (these transitions are shown as red lines): this is the *fluorescence* process, which contributes the prompt component of the emitted scintillation light. The probability that an  $S_1$  state decays to one of the vibrational states  $S_1 \rightarrow S_{01}, S_{02}, \dots$  exceeds the probability of a decay to the ground state  $S_0$ . Since the (photon) energy absorbed to enable the  $S_0 \rightarrow S_1$  transition is larger than the emitted photon energy of the decays  $S_1 \rightarrow S_{01}, S_{02}, \dots$ , organic scintillators exhibit very little self-absorption of (their own) fluorescence light, and so are effectively transparent to their own radiation. The effect of Stokes shift, which refers to the overlap between the optical absorption and emission spectra, is small [95, 97].

Transitions between the singlet and triplet states are highly forbidden, as electron spin-flip is involved [99, 100], leaving the question: how are the triplet states populated? There does exist a relatively rare process called intersystem crossing (ISC), which converts excited singlet states into triplet states. But most often (with 75% probability) triplet states are produced by ionization-recombination [99, 101].

As to the de-excitation of triplet states, there are again similar processes of internal degradation taking states  $T_{2,3,\dots}$  to state  $T_1$ .  $T_1$  however is a relatively stable state, as indicated by the fact that the mean lifetime of a molecule in the triplet state is  $\mathcal{O}(10^{-4} - 10)$  s [102]. This stability owes to the fact that the direct transition  $T_1 \rightarrow S_0$  is highly forbidden. However, the  $T_1$  state can undergo an indirect decay process by interacting with another excited  $T_1$  molecule to form an excited singlet state:

$$T_1 + T_1 \rightarrow S^* + S_0 + \text{phonons} . \quad (3.5)$$

The  $S^*$  state will then de-excite, emitting delayed scintillation light. This process is called “delayed fluorescence” or (perhaps more commonly) “phosphorescence” [95], and contributes to the delayed component of scintillation light.

For a typical scintillator detector, the time scale of detector response is  $\mathcal{O}(1 - 100)$  ns. In this time region, the emission of the scintillation light contains the primary fluorescence from the de-excitation of the singlet states (prompt component) and the delayed fluorescence from the de-excitation of the indirect triplet states (delayed component) [101]. The time profile of the scintillation light is a mixture of prompt and delayed components.

Different types of charged particles can cause different ionization densities when they deposit energy into the scintillator molecules. The ionization density affects the relative populations of the excited singlet and triplet states. Compared to an electron, an  $\alpha$ -particle causes a high ionization density, producing a higher ratio of triplet states to singlet states. Therefore, the time profile for the  $\alpha$ -particle has more delayed light (or longer tails) than that of the electron. This enables the organic scintillator detector to distinguish an  $\alpha$  particle from an electron or other lighter charged particle [101, 103]. An empirical formula, Birk’s law [98, 104], describes the photon yield per unit distance produced by the incident particle:

$$\frac{dY}{dx} = A \frac{dE/dx}{1 + k_B dE/dx}, \quad (3.6)$$

where  $A$  is a normalization constant and  $k_B$  is the Birk’s constant of the scintillator, which in practice is obtained by fitting the formula to measured data.

### 3.3.3 Liquid Scintillator for SNO+

Organic scintillators can offer a high light yield at wavelengths in the sensitive wavelength band of the detector’s PMTs and (as seen above) have characteristics that are useful in the context of particle identification. In addition, since organic liquids are non-polar media, the solubility of ionic impurities within them is low. This leads to lower contamination levels of uranium (U), thorium (Th), and potassium (K) in organic liquid scintillators. Among the organic scintillators, aromatic organic liquid scintillators have high electron densities and thus provide sufficiently numerous targets for particle interactions [105]. Due to these advantages, aromatic organic liquid scintillators have been extensively developed

as detection media for large particle detectors, especially for neutrino experiments, such as KamLAND, Borexino, Day Bay, and JUNO [103].

The SNO+ project has developed such liquid scintillators, compatible with the detector components and notably with the acrylic material of the AV sphere. Two kinds of SNO+ liquid scintillators are discussed in the following sub-sections: the unloaded liquid scintillator for the scintillator phase and the Tellurium-loaded liquid scintillator (TeLS) for the tellurium phase.

### 3.3.4 Water-based Wavelength Shifter (Proposal)

X. Dai et al. [106] proposed adding wavelength shifter (WLS) into a water Cherenkov detector like SNO. A WLS is a fluorescent organic chemical containing polycyclic aromatic hydrocarbons or heterocycles in their molecules which absorb photons and re-emit them at longer wavelengths [106, 107]. Relative to a water Cherenkov detector, a detector using a water-based wavelength shifter (wbWLS) has a higher light yield (about threefold higher than SNO [106]) and thus has a lower energy threshold for particle detection, i.e. low energy events. At the same time, such a detector retains the directionality characteristic of the Cherenkov signal, in contrast to the case of a *pure* liquid scintillator detector. For studying directional signals such as solar neutrinos, this directionality helps to suppress the background events. This concept of keeping the directionality is also the purpose of developing the water-based liquid scintillator (mentioned in Sect. 2.4.5) for future neutrino experiments, such as the ASDC-THEIA [108], the WATCHMAN experiment [109] and the Jinping experiment [62].

The U. Alberta group made a proposal of adding WLS into the SNO+ detector in the middle of the water phase. The specific wavelength shifter we considered is PPO, which is a well-studied ingredient of the liquid scintillator used in the SNO+ scintillator phase and tellurium phase. It can be dissolved into the water by mixing with a suitable water surfactant. Although this proposal was not adopted due to the experiment schedule, it is still worthwhile for a conceptual study of a SNO+-like detector that uses wbWLS as the detection medium. In Sect. 4.3, an event reconstruction algorithm based on the use of wbWLS is discussed. This algorithm that relative to an ordinary water-Cherenkov detector,

the energy threshold can be lowered and the resolution of the reconstructed event position improved, while still retaining the directionality response (i.e. permitting to reconstruct the direction of the incoming particle’s path from the Cherenkov light). This feature will help for measuring low-energy solar neutrinos.

### 3.3.5 Unloaded Liquid Scintillator

SNO+ adopted a liquid scintillator cocktail containing two primary components: LAB as solvent and PPO as solute. The LAB will be doped with PPO to a concentration of 2 g/L. This mixture of the LAB and 2 g/L PPO is denoted as the unloaded liquid scintillator in the text. Fig. 3.3 shows the chemical structural formulae of LAB and PPO [103].

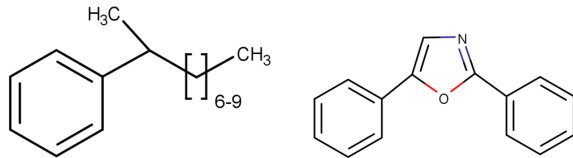


Figure 3.3: Structural formulae of LAB (left) and PPO (right).

LAB is a family of alkylated aromatic organic compounds with a phenyl group attached to a long carbon chain varying from 9 to 14 carbons [103, 110]. It has been used as a biodegradable surfactant to detergent since the 1960s and is known to be relatively non-toxic, and carry a very low risk for the environment and for human health [110]. Due to the long carbon chain, LAB is an effective energy absorber to transfer the energy deposited by a passing charged particle into light. It also has a long attenuation length of  $(72 \pm 14)$  m at 546 nm and thus has good optical transparency [78]. Fig. 3.4 shows the absorption lengths of SNO+ optical components, comparing the LAB, PPO to the water (plot from the data based on the SNO+ optical calibrations).

As discussed above, PPO is dissolved into the LAB so it may function as a wavelength shifting fluor [111]. Energy is transferred from LAB to PPO via non-radiative Förster resonant energy transfer, bypassing or short-circuiting the other de-excitation modes of the LAB. The outcome is that radiant de-excitation of the PPO (fluor) occurs at scintillation photon wavelengths in a range of 300-550 nm, better suited to the PMT’s sensitivity range.

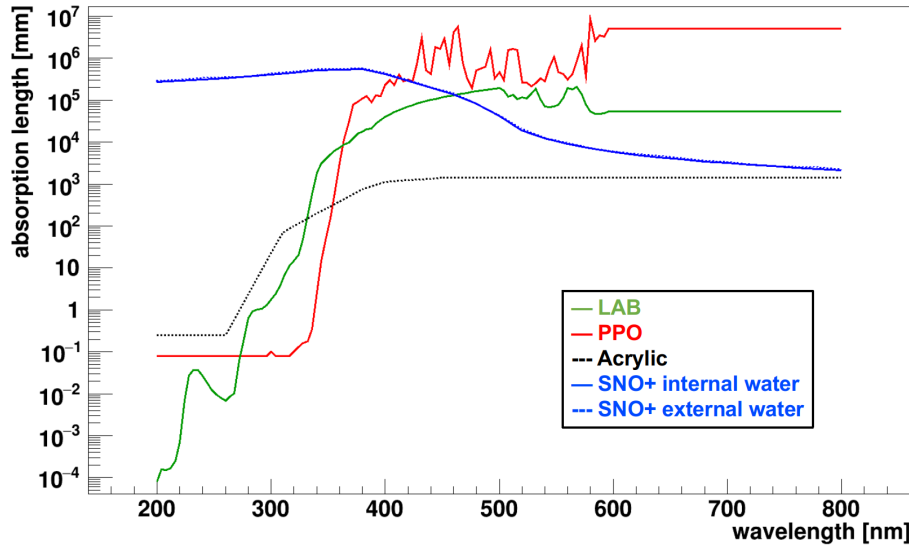


Figure 3.4: Spectral absorption length for individual SNO+ optical components. The internal (solid blue line) and external water (dashed blue line) absorption curves are based on the measurements of the laserball scans in July 2018 during the SNO+ water phase (optical calibrations). The horizontal lines are a conservative extrapolation to wavelengths at which measurements are lacking.

In addition, the PPO-doped cocktail results in reduced self-absorption of scintillation light (better optical transparency).

The 2 g/L PPO concentration in LAB is considered optimal for the purposes of SNO+ [85]. The absolute light yield of the LAB+ 2g/L PPO mixture has been well-measured from large particle physics experiments [50, 112], as well as bench-top measurements [112, 113, 114]. The value determined by SNO+ is  $11900 \pm 60$  photons/MeV, and this is expected to be increased by over 15% after an extensive purification process [78, 115]. At the 2 g/L PPO concentration, the emission decay time is about 5 ns, which is good enough for event vertex reconstruction, and this fast timing ensures distinct timing spectra for  $\alpha$  and  $\beta$  events, which is crucial for  $\alpha/\beta$  discrimination and reducing the backgrounds [78].

During the SNO+ partial-fill phase, intervals of detector operation are available with steady values of PPO mixing ratio at 0.25 g/L, 0.5 g/L, and 1 g/L concentrations. When the PPO concentration increases, the PPO transfer efficiency will increase, which can increase the light yield of the liquid scintillator, and also cause a faster scintillation timing response. However it was found that there is little to be gained by allowing the PPO concentration to

exceed 2 g/L, due to an increase in self-absorption (such that light yield reaches a plateau) and a slightly accelerated timing response (see Sect. 4.4.2.1, Chapter 4 for more details) [78, 103]. In Sect. 4.4.3.1, Chapter 4, I show the effects of the PPO concentration on event position reconstruction. As PPO concentration increases from 0.25 g/L to 2 g/L, the resolution in the reconstructed event position (for 3-MeV electron events) is refined by about 9 cm. However, as PPO concentration increases from 2 g/L to 6 g/L, there is almost no change in light yield, demonstrating that 2 g/L PPO concentration is for all intents and purposes optimal.

Scintillator light emission time profiles were obtained from bench-top measurements. An empirical model for the response, consisting of  $n$  ( $n=3$  or 4) exponential decays with a common rise time, is used to describe (i.e. fit) the time profiles [116], viz.

$$\sum_{i=1}^n A_i \cdot \frac{e^{-\frac{t}{\tau_i}} - e^{-\frac{t}{\tau_r}}}{\tau_i - \tau_r}, \quad (3.7)$$

where the rise time ( $\tau_r$ ), timing parameters  $t_i$ , and amplitude  $A_i$  of any given liquid scintillator must be determined by measurements. Fig. 3.5 plots the time profiles based on the measured parameters from the collaboration [117, 118, 119, 120]. It shows the time profiles of four different liquid scintillator cocktails planned for SNO+, including the LAB+0.5g/L PPO for the partial-fill phase, which will be discussed in Chapter 4; the LAB+2g/L PPO for the scintillator phase; the LAB+2g/L PPO+0.5% molar concentrations DDA, which will be a transient state before loading of the Te; and the LAB+2g/L PPO+0.5% molar concentrations Te+0.5% molar DDA for the tellurium phase. For each liquid scintillator, the timing responses to  $\alpha$ - (dashed lines) and  $\beta^-$  (solid lines) particles are shown. This figure shows that with 2 g/L PPO there is obvious difference between the  $\alpha$  and  $\beta^-$  timing, while for the 0.5 g/L PPO, such difference is not obvious. However, some recent SNO+ *in-situ* data analyses (relating to the “Berkeley AlphaBeta Classifiers”) based on the partial-fill data still show some ability to distinguish  $\alpha$ - and  $\beta^-$  particles by their time profiles [121].

The LAB and the PPO used by SNO+ are ultrapure, with very low levels of natural radioactive contaminants such as U, Th, and K. The target background levels for the SNO+ LAB are expected to be  $\mathcal{O}(10^{-17})$  gram of  $^{238}\text{U}$  per gram LAB (g $^{238}\text{U}/\text{gLAB}$ ), which taking account of the detector volume equates to  $\mathcal{O}[10^3]$  events per year. The  $^{232}\text{Th}$  and  $^{40}\text{K}$

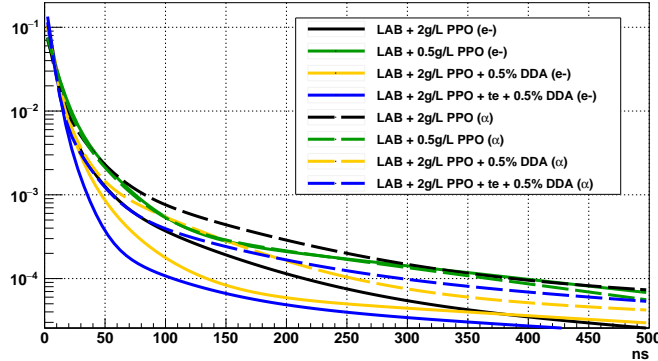


Figure 3.5: Time profiles for liquid scintillators in different SNO+ phases.

contamination levels are equally low, i.e.  $\mathcal{O}(10^{-17})$  g/gLAB, but due to their longer half-lives their event rates in the detector are  $\mathcal{O}[10^2]$  events per year [78, 122]. A liquid scintillator purification plant has been implemented to maintain the optical clarity and radiopurity of the scintillator [78].

### 3.3.6 Tellurium-loaded Liquid Scintillator

To load the  $^{130}\text{Te}$  into the liquid scintillator, an organo-metallic compound, called “Tellurium Butanediol (TeBD)”, is formed by condensation (or “deiolization”) reactions between telluric acid (TeA) and 1,2-butanediol (BD) [91]. A tertiary amine “DDA” (for N, N-Dimethyldodecylamine) is added during the reaction to stabilize TeBD compounds and avoid any phase separation [123]. Fig. 3.6 shows initial stages of the process. This compound is then loaded into the liquid scintillator.

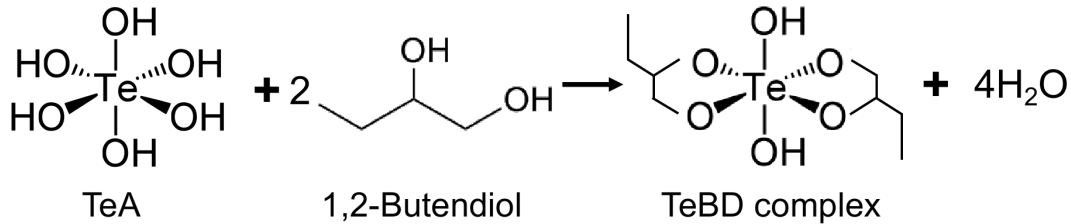


Figure 3.6: Initial stages of the TeBD compound formation, modified from Ref. [91].

Two special synthesis procedures, called the “DDA” and “SOP” procedures (see Refs. [124, 125, 126] for details) are being developed by the SNO+ Te-loading working groups. These

methods achieve retention of the optical transparency of the unloaded scintillator after the loading and ensure that the mixture will be stable for a decade. To meet the low background requirement of the  $0\nu\beta\beta$  analysis, it is aimed to achieve mixing ratios as low as  $\mathcal{O}(10^{-15})$  g/g for the contaminants U and Th.

For the  $^{130}\text{Te}$   $0\nu\beta\beta$ -decay process, the signature energy peak is around 2.5 MeV [85]. This peak is relatively small and can be drowned out by the ubiquitous radioactive decays from natural sources, such as isotopes along the natural uranium and thorium decay chains existing (as low-level contaminants) in the materials [85]. Therefore, the  $0\nu\beta\beta$ -decay experiments require a fine energy resolution <sup>5</sup> to distinguish the signal from the backgrounds. This in turn demands that the light yield (i.e. number of photons produced per MeV of energy deposited) of the liquid scintillator induced by a particle interaction be as large as can feasibly be arranged. The total light yield of the full cocktail (0.5% Te-loaded LAB) is expected to be about 400 PMT hits (NHits) per MeV, which is about 65% of the unloaded scintillator's light yield [124].

### 3.3.7 Relative Light Yield Measurements of the Te-loaded Liquid Scintillators

As mentioned in the previous section, the light yield of the TeLS is crucial for the  $0\nu\beta\beta$ -decay experiments since it determines the energy resolution of the detector and sensitivity for studying the  $0\nu\beta\beta$  process from the  $^{130}\text{Te}$ . With tellurium being loaded into the LAB, the light yield of the liquid scintillator will go down since the light output is quenched by the TeBD complex. A few efforts are aimed to develop high light yield Tellurium-loaded scintillators [124].

Here I measured the light yield of 0.5% Te-loaded LAB samples relative to the LAB-PPO scintillator (called “relative light yield”). These measurements help to understand the light yields of the TeLS samples made by different Te-loading methods, and it is also useful for preparing the quality control of the TeLS during the SNO+ tellurium phase.

---

<sup>5</sup>For the SNO+ 0.3% Te-loaded cocktail, the energy resolution at 2.5 MeV is about 270 keV for the full width at half maximum (FWHM) [85].

### 3.3.7.1 Measurement Setup and Data Acquisition

We<sup>6</sup> first prepared LAB+2 g/L PPO by dissolving PPO into the pure LAB. The LAB-PPO mixture was fully mixed by an electromagnetic stirrer. During the stirring, the mixture was distilled by heating to 75 °C<sup>7</sup> and flowing with pure and dry nitrogen gas for 48 hours to remove dissolved water (humidity) and oxygen in the scintillator, both of which can reduce the light yield. The distilled LAB-PPO was added into the original Te-butanediol samples which contain 16.5% Te by weight, and these samples were diluted into 0.5% TeLS samples.

The two original Te-butanediol samples were synthesized from the DDA and SOP synthesis procedures (described in Ref. [123]). The diluted 0.5% TeLS samples were tagged as the TeDDA and TeSOP samples, respectively. The TeDDA and TeSOP samples were transferred into scintillation vials to be used for the measurements, as shown in the left picture of Fig. 3.7. The vials have PTFE caps sealed on the top of the glass cylinders to prevent humidity exposure from the air. The liquid level for each sample was kept at 30 mm from the bottom of the vial to avoid air bubbles and contamination created by squeezing the vial cap into the liquid.

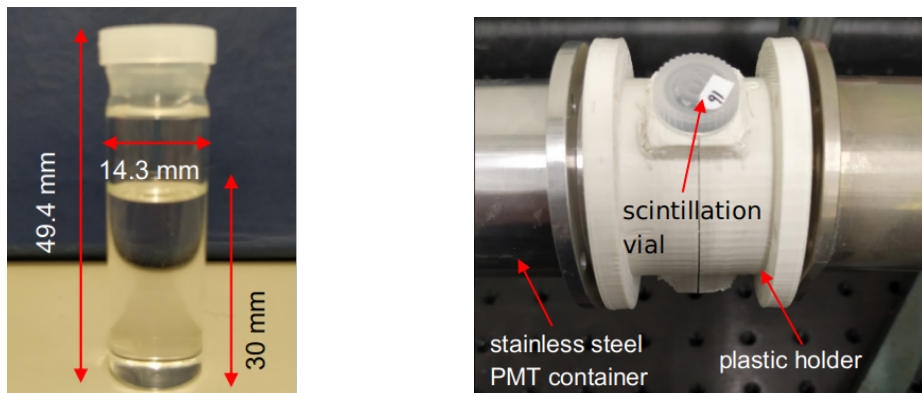


Figure 3.7: A vial filled with the test sample (left) and the measurement setup (right). Left: The samples were filled into scintillation vials. The dimensions are shown in the picture. Right: two PMTs were aligned by a coupling to face the scintillation vial from each side.

Two Hamamatsu R580 PMTs (see Hamamatsu R580 manual [127] for details) were

<sup>6</sup>Dr. M. Sharma, who worked in Prof. Veinot's lab at the Department of Chemistry at U. Alberta, performed the tellurium synthesis procedures and helped with the sample preparations.

<sup>7</sup>This temperature is far below the flashpoints of the LAB (140 °C) and the PPO (335 °C). Data from the Material Safety Data Sheet (MSDS).

used for detecting the light. The diameter of the PMT round surface is 38.71 mm. These PMTs were housed in stainless steel cylinders (PMT holders), set face to face, looking at the scintillation vial from each side. The PMTs and the vial were aligned by a plastic coupling, as shown in the right picture in Fig. 3.7. The plastic coupling is cylindrical, with a hole on the top into which the scintillation vial is seated, and a slot at the bottom to attach a radioactive source. Inside the cylindrical coupling, there is a button-shaped groove at the bottom, to secure the vial upright. At the bottom of the coupling, the center of the groove from inside is aligned with the center of the slot from outside. A 2-mm-diameter hole was drilled through the bottom center to allow the radiation rays to pass through the vial from the bottom. The surface inside the coupling was polished to be smooth to reduce its absorptivity. The coupling piece is made of plant-based and biodegradable polylactide (PLA) filament, and was fabricated by the 3D printing facility at U. Alberta<sup>8</sup>.



Figure 3.8: A diagram shows the light yield measurement setup. See the text for details.

Fig. 3.8 shows a diagram of the whole measurement setup. The plastic coupling piece held the radioactive source and the scintillation vial. It also aligned two PMTs to face the scintillation vial from each side and shielded the vial from outside light. The apparatus was placed in a dark box to prevent light from the lab. Two RG59/U-type high voltage (HV) cables connected the PMTs to an HV supply outside the dark box. The HV cables were

<sup>8</sup>Shengzhao Yu, who was an undergraduate student at the Department of Physics, helped with the machining.

connected to two signal/HV split boxes to separate the HV current and electrical signals. Due to the resistance of the split box, the HV supply was set to 2200 Volts (V) for PMT operation, instead of the 1800 V operation voltage suggested by Ref. [127].

The signal cables from the split box were connected to a two-channel Hewlett Packard (HP) amplifier, which inverted the signals and amplified them by 26 dB. The amplified signals were then input to a two-channel digitizer whence they were recorded on a desktop computer.

To obtain and analyze the data, I used a desktop Waveform Digitizer, the DT5751 module provided by the Costruzioni Apparecchiature Elettroniche Nucleari (CAEN). Running in a digital pulse processing mode, the module records the digitized PMT waveforms with a data-taking rate of 1 GHz for each channel. For each channel, the digitizer provides an input voltage up to 1 V with a 10-bit resolution (about 0.98 mV) [128].

This module was controlled by the CoMPASS software provided by CAEN. The software set up the threshold and trigger parameters. Once the triggered event passed the threshold, the software recorded event time, trigger flag, and waveform histograms from the two channels. By integrating the waveforms, the energy of a triggered event was calculated [129].

Each channel recorded the signals from each PMT individually. With the two-PMT setup, I applied coincidence time mode measurements. In the coincidence mode, a coincidence time window between two channels was set to 48 ns, based on checking the recorded waveforms from two channels. For a certain event, the CoMPASS software compares the event time difference between two channels and only records the waveforms from the two channels if the event time difference is less than 48 ns. A smaller window of 10 ns was further applied for analysis.

### **3.3.7.2 Measurement**

The liquid scintillator samples I have measured are LAB-PPO, TeDDA, and TeSOP. The unloaded LAB-PPO sample served as a standard candle.

A cesium-137 ( $^{137}\text{Cs}$ ) radioactive source was always placed at the bottom of the scintillation vials. The source was made by Radiochemical Centre Amersham. The radioactivity

measured on 1st April 1974 was 11.09 microCurie ( $\mu\text{Ci}$ ) on record, with an accuracy of 3.7%. Then the activity was expected to be  $11.09 \times (\frac{1}{2})^{\frac{46}{30.08}} = 3.84 \mu\text{Ci}$  in 2020, accounting for the 30.08 year half-life of  $^{137}\text{Cs}$  [130].

Upon decay, the  $^{137}\text{Cs}$  isotope has an 85.10% chance to emit 0.661 MeV  $\gamma$ -particles [130]. These  $\gamma$ -particles can travel into the liquid scintillator sample in the vial, interact with the samples, and create scintillation photons.

For each sample, measurements were taken for a one-minute time duration. Waveforms from the PMT photo-current signals were digitized in a 252 ns time window. Shown in Fig. 3.9 is a typical waveform caused by  $\gamma$ -particles interacting with the LAB-PPO sample. The photo-electron (*p.e.*) signals triggered PMT pulses, and the pulses were digitized as waveforms. For each waveform, the digitizer firmware dynamically calculated the baseline as the mean value of 256 data points inside a moving time window of 252 ns width. A threshold was set as 100 LSB (Least-significant bit) units above the baseline. The data point at 90% of peak height on the leading edge of the pulse was taken as the trigger time (*trig*) tag.

After the occurrence of this *trig* tag to avoid introducing another pulse, in the subsequent 80 ns window the digitizer did not produce another trigger (trigger hold-off). Also, from the *trig* tag, a pre-gate of 8 ns was set to allow the waveform to shape properly. The waveform was integrated across the time interval [*trig* − 8, *trig* + 72] ns. This time interval was selected to include the peak region caused by a possible event. It was based on checking the average waveform which was obtained by summing up thousands of waveforms recorded during the measurement with the same setup. The integral of the waveform gives the integrated charge, which was provided (i.e. output) in one of the A/D convertor's (output) channels.

If the measurement system were to be calibrated, the ADC channel number could be converted exactly into the energy of the particle interaction. However, since only the photon count was interested here, I used the ADC channel number as the energy without further scaling. Once the pulse in the waveform passed the threshold and a triggered time tag was found, the digitizer considered it as a triggered event. A time flow started when the measurement began. Timestamps were recorded as event time when the triggered event happened. The waveform was recorded, and the ADC channel number (nominally, the

energy) of this event was calculated.

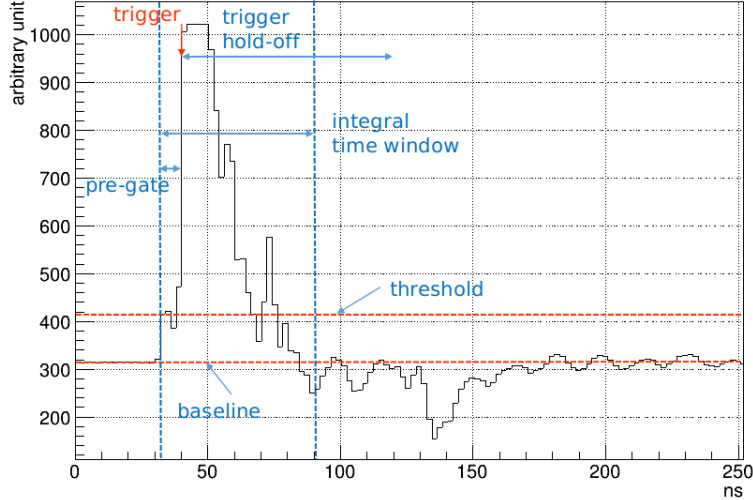


Figure 3.9: A typical waveform triggered by scintillation photons from  $^{137}\text{Cs}$   $\gamma$ -particles interacting with LAB-PPO in the scintillation vial.

In a coincidence time measurement, the event times of the events recorded by each of the two PMTs were compared. If the event time differences between two events from each PMTs were too long, those events were considered to be random noise rather than the physics events and were not recorded. I optimized a coincidence time cut as 40 ns and set that cut during the digitizer data-taking based on checking the recorded waveforms. If the coincidence time was set too long, more waveforms from background noises with multiple small peaks fluctuating around the baseline were recorded; on the other hand, if the time was set too short, waveforms from physics events were cut off and too few events were recorded. Multiple one-minute measurements were tested to obtain the optimized coincidence time cut.

Fig. 3.10 shows the measured LAB-PPO energy spectrum with and without coincidence time cut (10 ns) on a single ADC channel (here using channel 0). Without the coincidence time cut, there is a zero peak caused by the pulses from random electronic noise or fluctuations of the digitized waveforms. The peak on the left is the single *p.e.* peak. It is mainly caused by light sources (events) that are so weak that the captured photons produce at most one single photo-electron inside the PMT [95]. The peak on the right is the multiple *p.e.* peak, in our case, which is mainly caused by scintillation photons produced

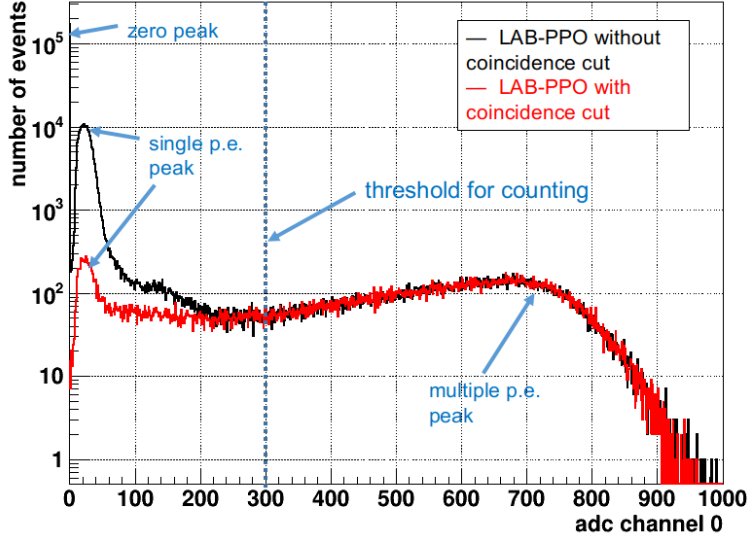


Figure 3.10: Measured LAB-PPO energy spectrum with and without a coincidence cut on the ADC channel 0. A threshold for counting is set by comparing the two spectra.

by the (<sup>137</sup>Cs) 0.661 MeV  $\gamma$ -ray interacting with the LAB-PPO. In the coincidence time measurement mode, the sampling system only records photons detected by the two PMTs almost simultaneously. Therefore, the zero peaks are removed and the single *p.e.* peak is suppressed. The multiple *p.e.* peak is consistent with the non-coincidence measurement. A threshold in energy, shown in Fig. 3.10 as 300 (nominal energy units) can be set to count only the scintillation photons emitted from LAB-PPO.

Fig. 3.11 (a) shows the result of a one-minute measurement for the LAB-PPO sample. The data points in the 2D plot represent the triggered events read by the ADC channel 0 and 1 simultaneously. A 10 ns coincidence window cut was applied to cut down noise, single *p.e.*, and background events. The events in the 0 ADC channel, which represent noise, were totally cut off after applying the coincidence cut. Fig. 3.11 (b) and (c) show corresponding results for the TeSOP and TeDDA samples respectively. Compared to the LAB-PPO sample, a shift of the multiple *p.e.* peak due to the different light yields can be observed clearly.

The 2D plots were projected onto a single channel, as shown in Fig. 3.11 (d). I used an empty vial and let  $\gamma$ -particles from the <sup>137</sup>Cs source pass through it as a background run (without imposing the coincidence cut). This was to verify the single *p.e.* peak and



Figure 3.11: The 2D energy spectrum of the counting measurements of LAB-PPO (a), TeSOP (b), and TeDDA (c) samples, projected the 2D plots into one channel (d). The single *p.e.* peak is mainly caused by backgrounds while the multiple *p.e.* peak is from scintillation photons.

noise region, shown as the black background spectrum. From this plot, the single *p.e.* peaks for all the samples and the background match together. The several different multiple *p.e.* peaks indicate the different light yields of the scintillator samples. Here it shows that the multiple *p.e.* peak of the LAB-PPO occupies the largest ADC channel number, while the channels of TeSOP are slightly larger than the TeDDA.

To quantify the light yield differences between different samples, an analysis method of charge weighted photon number has been applied as the following:

First, from the energy spectrum, the single *p.e.* peak was fitted with an asymmetric Gaussian function ( $f_{asym}$ )<sup>9</sup>:

$$f_{asym} = c \exp \left[ -\frac{(x - \mu)^2}{2\sigma^2} \right] \text{Erfc}(\xi), \quad (3.8)$$

where  $\xi = -\frac{\alpha(x-\mu)}{\sqrt{2}\sigma}$ , as shown in Fig. 3.12. The mean value of the asymmetric Gaussian ( $p_0$ ) represents the ADC channel number corresponding to the single *p.e.* peak for the weighting.

Then in the multiple *p.e.* region, weighting (dividing) the counts of the event in each channel with the single *p.e.* ADC channel number to calculate the total number of the photons.

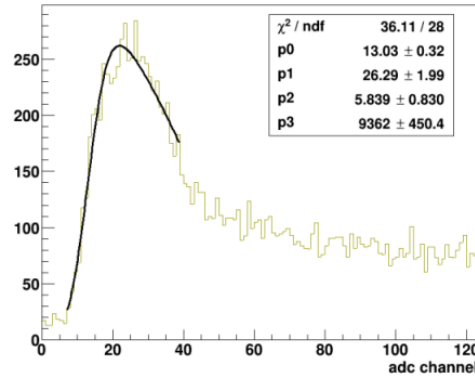


Figure 3.12: The single *p.e.* peak is fitted with an asymmetric Gaussian function ( $f_{asym}$ ) to obtain the ADC channel for weighting. Here the parameters ( $p_0, p_1, p_2, p_3$ ) represent ( $\mu, \sigma, \alpha, c$ ) in Eqn. 3.8, respectively. The mean value of  $p_0$  (or  $\mu$ ) is used as the ADC channel number relative to a single *p.e.* peak.

To define the multiple *p.e.* region for the counting, the spectrum projected on each

---

<sup>9</sup>This fitting is suggested by Ref. [131], which allows for non-zero skewness due to contributions from background peaks.

channel with and without coincidence cut were compared to define a threshold of the ADC channel for counting. By integrating from this threshold, the total numbers of events between the two spectra were close to each other. From two channels, I got two thresholds and then define a box cut in the 2D coincidence plot. I weighed the events in the box to obtain the total number of photons.

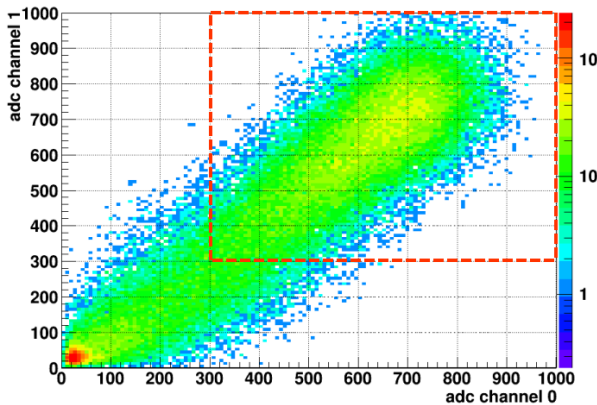


Figure 3.13: Two dimensional spectrum of LAB-PPO sample with coincidence cut. A box cut is defined for multiple *p.e.* counting.

Two dimensional (2D) spectrum of LAB-PPO with coincidence cut is shown in Fig. 3.13. A box cut is defined for multiple *p.e.* counting.

Once the total number of photons for a certain sample is counted, we can calculate its ratio to the LAB-PPO sample to obtain the relative light yield (RLY).

### 3.3.7.3 Results

Table 3.1: Number of photons calculated by the charge weighted photon number method.

Sample	Number of photons ( $\times 10^6$ )	RLY
LAB-PPO	2.0811	1
TeDDA	1.2652	0.61
TeSOP	1.3976	0.67

Table 3.1 shows the number of photons calculated by the charge weighted photon number method. Then the RLY of the samples were obtained. The RLY of the 0.5% Te by SOP synthesis procedure (TeSOP) is 0.67 and the one of the 0.5% Te by DDA procedure is 0.61.

The RLY of TeSOP is slightly larger than the TeDDA. These results are close to the RLY of  $\sim 0.65$  for the 0.5% Te loading samples reported by Ref. [124].

### 3.4 SNO+ Electronics

In this section, the SNO+ electronics system is introduced. The system includes the trigger and readout systems. As mentioned in Sect. 3.1, the PMTs as photon sensors are the basic detection elements for the SNO+ detector. The signals from the PMTs are sent to the SNO+ electronics system, which records the PMT time and charge information and then transfers the digitized data to offsite computing systems for data analysis. These steps are detailed in the following.

The photons created from particle interactions in the detector propagate to the PMT sphere and may hit a certain PMT and strike on its photo-cathode, which is a thin cesium bialkali film coated on the inner surface of PMT glass. The photocathode then produces a photo-electron (*p.e.*) through a photoelectric effect. The photocathode is held at ground voltage, while the anode is at a high voltage ranging from +1700 to +2100 V [101, 132]. This potential difference establishes strong electric fields inside the PMT. The *p.e.* is accelerated and focused by the electric field in the PMT and travels through a volume that is under vacuum until it reaches the region of a series of secondary emission electrodes, called dynodes. When the *p.e.* transfers its energy to the material in the dynodes, a number of secondary electrons escape and form a measurable current, which is collected by a custom-made operating circuit (called “PMT base”) at the anode [133].

The anode pulse produced from the PMT travels along 35 m long RG59/U type coaxial cable (with a resistance of  $75 \Omega$ ) to the front-end electronics, which are located on the deck above the detector. The coaxial cable also carries the high-voltage [132].

To tidily manage the more than 9000 PMTs in the SNO+ detector, the coaxial cables connected to the PMTs are grouped into bundles. Each bundle is connected to a Paddle Card, which is linked to a PMT Interface Card (PMTIC). The PMTIC supplies the high voltages and receives the signals from the PMTs. 32 channels (for 32 PMTs) in the PMTIC are plugged into a Front End Card (FEC) that processes, digitizes, and stores those 32

PMT signals. There are in total over 300 of the Front End Cards, distributed (or organized) across 19 “crates” to energize and monitor the 9728 PMT channels in total. Of that total, 32 channels are reserved for calibration inputs and labeled as FEC Diagnostic (FECD) channels. These FECD channels are mainly used to tag calibration events. The triggered PMTs can be labeled by the logical channel number (lcn) using the map of the PMT to the crates and cards [78, 86]:

$$\text{lcn} = 512 \times \text{crate} + 32 \times \text{FEC} + \text{channel} . \quad (3.9)$$

A 10-MHz and a 50-MHz clock are used to record the time of the triggered event. The universal time of the triggered event is calculated as the time elapsed from a predefined origin *zero*, namely midnight on January 1, 2010 (GMT), until the moment when the event happens. A 10-MHz clock used for counting the absolute time started at *zero*. It has a 53-bit register and can run for 28.5 years. Its accuracy is maintained by a GPS system. The 50-MHz clock gives more accurate timing. It limits the best time resolution of the global trigger time (GT) to 20 ns. This clock has a 43-bit register and rolls over every 2.04 days. The relative time between the events can be used for analyzing specific physics processes, such as radioactive decays [86, 134].

The recorded hit information of the triggered event, including the time and charge information of hit PMTs and the trigger settings, are sent to a Crate Controller Card (XL3) in each crate. These cards were installed for SNO+ to handle higher data transfer rates compared to SNO, with a maximum rate of 14 MB/s, which is sufficient for typical data-taking rates of 2.5 MB/s [135, 136]. The XL3 cards read the recorded data, wrap them as Ethernet packets, and send them to the Data Acquisition System (DAQ) and Event Builder system [137]. The Event Builder system writes information into event records based on their GT identification number (GTID) and saves them on storage disk [78]. These raw data are written to the disc and are further processed into ROOT format by high-performance computing clusters.

The SNO+ electronic system can measure signals with a nanosecond-level timing resolution and a single-photon level charge resolution. It can handle a “routine” event rate of several kHz, and when called for can handle much higher rates for cases such as the burst events from a galactic supernova [78].

### 3.5 Calibration

Calibration sources with known physics parameters are operated frequently to determine the detector’s response to well-understood events, and calibrations are essential steps for making accurate measurements. Two kinds of calibration sources are used by SNO+: (1) optical sources to measure the *in-situ* optical properties of the detector medium and to calibrate the PMT responses [78, 90]; and (2) radioactive sources to test the detector energy response, check the performance of event reconstruction algorithms for reconstructing event position, direction and energy, and determine the systematic uncertainties in event reconstruction. The various radioactive sources designed for SNO+ cover the energy range from 0.1 MeV to about 10 MeV, as listed in Table 3.2 [78]. All the calibration sources have been designed to meet the radiopurity required by SNO+, and their materials are compatible with the detection media [78].

Table 3.2: A list of SNO+ radioactive sources for detector calibration. The energy cited is given the total  $\gamma$  energy, modified from Ref. [78]. The half-life ( $T_{1/2}$ ) values of the isotopes are also shown [130].

source	total $\gamma$ energy [MeV]	$T_{1/2}$ for main decay
$^{16}\text{N}$	6.1	7.13 s
AmBe	4.4	432 years for $\alpha$ -decay from $^{214}\text{Am}$
$^{46}\text{Sc}$	2.0	83.79 days
$^{48}\text{Sc}$	3.3	43.67 hours
$^{137}\text{Cs}$	0.66	30.08 years
$^{57}\text{Co}$	0.14	271.74 days

Amongst these radioactive sources, the nitrogen-16 ( $^{16}\text{N}$ ) calibration source and the AmBe sources have been deployed in the water phase and the partial-fill phase. The  $^{16}\text{N}$  source was used to test and optimize the reconstruction algorithm discussed in Chapter 4. It was also used to obtain the reconstruction uncertainties in the water phase, which is the topic of Chapter 5. A detailed description of the  $^{16}\text{N}$  source is given in Sect. 3.5.1.

The  $^{46}\text{Sc}$ ,  $^{48}\text{Sc}$ ,  $^{137}\text{Cs}$  and  $^{57}\text{Co}$  sources are newly designed by SNO+ to calibrate the energy scale in the scintillator and tellurium-loading phases, especially for the energy region of interest (ROI) in the  $0\nu\beta\beta$  study [78].

The detector geometry is not perfectly symmetric due to the presence of the AV neck, ropes, gaps between the PMTs, and the differences between individual PMTs [78]. The deployment of calibration sources at different positions in the detector can help to understand the asymmetries in the detector response. To achieve this, several fixed optical sources were mounted at different positions on the PSUP. To provide a wider range in calibration source positions a source manipulator system (SMS) was installed, as shown in Fig. 3.14 [78]. Sources are attached temporarily to (and removed from) the SMS via the Universal Interface (UI), which is a sealed, cylinder-shaped glove box on the top of the AV: this prevents Radon-bearing air in the lab from leaking into the detector [78]. The motion of the deployed sources along the central vertical axis inside the AV is controlled by the Umbilical Retrieval Mechanism (URM) through an umbilical and a central rope, and the off-axis motion is controlled by the side rope manipulator system. The motion of the sources in the external water region between the AV and PSUP is along the calibration guide tubes [78].

The position of the deployed source in the detector can be evaluated by the manipulator system. In addition, a camera system with six underwater cameras already mounted on the PSUP can take photographs of the source and then triangulate its position. Positional uncertainty of only a few centimeters is achieved. This system is also used to monitor the physical state of the detector, such as the offset of the AV center with respect to the PSUP, the movement of the rope net, the height of the water-scintillator interface during the partial-fill, etc [78, 138].

### 3.5.1 The $^{16}\text{N}$ Calibration Source

The  $^{16}\text{N}$  calibration source was inherited from the SNO experiment, and is well-understood [139, 140, 141]. Fig. 3.15 shows the geometry of the  $^{16}\text{N}$  source chamber. The chamber is a stainless steel cylinder mainly containing a small PMT and a gas decay chamber. The chamber was designed to confine the electrons from  $^{16}\text{N}$  decay within the chamber and let them be detected by the PMT inside [139].

Since the  $^{16}\text{N}$  isotope has a short half-life of 7.13 s, it must be produced on-site during the calibration runs. A commercial deuterium-tritium (DT) generator was installed (underground) at SNOLAB to produce neutrons through the reaction:  $D + T \rightarrow n + {}^4\text{He}$ ; then the



Figure 3.14: The SNO+ Source Manipulator System, from Ref. [78].



Figure 3.15:  $^{16}\text{N}$  calibration source geometry. Left: a detailed diagram of  $^{16}\text{N}$  source geometry, modified from Refs. [142, 143]; middle: source geometry implemented in RAT, modified from Ref. [144]; right: a picture of the  $^{16}\text{N}$  source, taken from Ref. [145].

produced 14 MeV neutrons that interact with CO<sub>2</sub> gas streaming through small diameter capillary tubing and produce the <sup>16</sup>N isotope via the (*n, p*) reaction:  $n + ^{16}\text{O} \rightarrow ^{16}\text{N} + p$ . These <sup>16</sup>N nuclei are transferred into the cavity or detector via the CO<sub>2</sub> gas tubing [140].

The <sup>16</sup>N isotope mainly decays by  $\beta$ -decay process:  $^{16}\text{N} \rightarrow ^{16}\text{O} + e^- + \bar{\nu}_e$ . In doing so it has a 66.2% probability of emitting an electron with  $E_{\text{end point}} = 4.29$  MeV and a 22.8% probability of emitting an electron with  $E_{\text{end point}} = 10.42$  MeV; furthermore the resulting <sup>16</sup>O daughter nucleus de-excites, producing a cascade of  $\gamma$ -photons. These are mainly 6.13 MeV  $\gamma$ -photons with a probability of 67.0% and 7.12 MeV  $\gamma$ -photons with a probability of 4.9%. The probabilities of the  $\gamma$ -photons with other energies are all below 1% [130]. A simplified decay scheme is shown in Fig. 3.16.

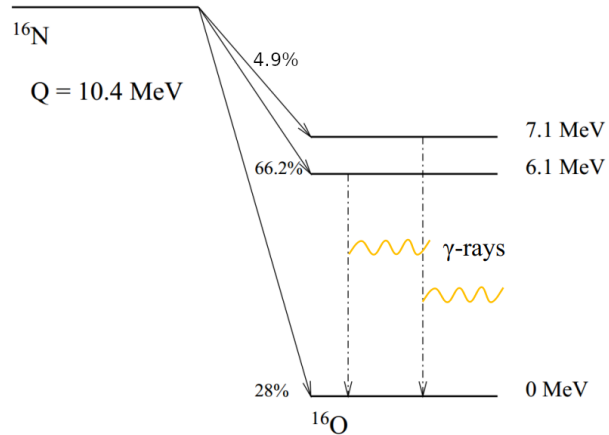


Figure 3.16: <sup>16</sup>N main decay scheme, modified from Ref. [140].

Calibrations using the <sup>16</sup>N source are crucial for the quality of the reconstruction algorithms. Chapter 4 will cover how this source was used to test and optimize the reconstruction algorithms. Chapter 5 will show how the source is used to estimate the reconstruction uncertainties.

### 3.6 Monte Carlo Simulation and RAT Software

The SNO+ collaboration uses a software package called the Reactor Analysis Tool (RAT) for Monte Carlo simulation as well as event-based analysis offline and online. To accomplish these two tasks, RAT integrates the Geant4 simulation toolkit [146] and ROOT data analysis

framework [147] for processing and analyzing data. This feature makes it easy to analyze Monte Carlo-generated events and real data in the same framework and data structure.

The software was originally developed by Stan Seibert from the Braidwood Collaboration to simulate a generic KamLAND-like detector [148]. A simulation package called Generic Liquid Scintillator **Geant4** simulation (**GLG4sim**) was developed and implemented in **RAT** [149]. It simulates the scintillation physics, i.e. generation of scintillation photons and their propagation, reflections, refraction, scattering, and absorption [101].

The SNO+ version of **RAT** links the existing **ROOT**, **Geant4** and **GLG4sim** packages to minimize code duplication. The SNO+ **RAT** is being developed by the whole collaboration and evolves with the experiment's progress to precisely simulate the SNO+ detector in its different physics phases, as well as being applied for many analysis tasks. The relatively flexible code structure of **RAT** allows the user to introduce their own code into the simulation or analysis process [148]. It can be updated and optimized with the measured parameters from detector calibration; it can be equipped with more precise descriptions of the physical processes in the detector; it can also be introduced with more advanced analysis tools. Users can perform different analysis tasks, such as using different reconstruction algorithms on the same set of events [148]. Therefore, different versions of **RAT** appropriate to and serving different SNO+ physics phases may give different outputs. For the work in this thesis, multiple **RAT** versions were used, mainly the versions for the water phase and the partial-fill phase. In this case, I will specify the **RAT** version when I discuss a specific analysis.

**RAT** is also used by other astroparticle physics experiments, such as DEAP [150].

## Chapter 4

# Event Reconstruction

### 4.1 An Overview of the Reconstruction Algorithms in SNO+

A particle interaction that happens in the SNO+ detector can produce Cherenkov or scintillation photons or both. These photons propagate through the detector and may trigger PMTs when they reach the PSUP. As described in the last chapter, if sufficiently many PMTs are triggered within a defined time window, an “event” is determined by the trigger system to have occurred, and the time and charge information measured by the hit PMTs are recorded.

By utilizing the recorded time and charge information, reconstruction algorithms attempt to calculate the physical quantities, including the event position and time (the “vertex”), the direction of motion of the charged particle that prompted the primary light emission, and its energy. Several reconstruction algorithms (called “fitters”) have been implemented in the SNO+ RAT software, or are still being developed. These fitters are based on different methods and can be coordinated and optimized for different detector situations or physics phases.

According to the physics quantities they determine, the SNO+ fitters can be generally classified as:

- Vertex fitter. A vertex fitter reconstructs the event position and time by utilizing the positions and timing information of the hit PMTs. Currently, vertex fitters have been

used to process the data and simulations for the water and partial-fill phases. They are also ready for the scintillator and tellurium-loading phases.

On the other hand, some types of events, such as radioactive background events that emit  $\gamma$ -photons, can create multiple correlated vertices. A multi-site or multi-vertex fitter will be helpful in tagging and removing such types of events during the  $0\nu\beta\beta$  search. This kind of fitter is being developed.

- Direction fitter. A direction fitter reconstructs the event direction by using the information encoded in the spatial distribution of the detected Cherenkov photons, which cause ring-like patterns of hit PMT positions. The direction fitter has been used in the water phase analysis. However during the scintillator and tellurium-loading phases, the Cherenkov patterns will be submerged in scintillation photons, so that direction reconstruction requires a different approach, which is being developed currently.
- Energy fitter. An energy fitter generally translates the number of photons created from an event to kinetic energy. Similar to the vertex fitters, the energy fitters have been used in the water and partial-fill phases at the time of this writing, and they are ready for the scintillator and tellurium-loading phases.
- Muon track fitter. This fitter is used to reconstruct the tracks of cosmic muons. Each muon track is treated as a straight line, and by dividing the SNO+ detector into several  $XY$ -slices along  $Z$ , the fitter reconstructs the path’s intersection point on each slice by utilizing the position and timing information of the set of hit PMTs [151]. The muon track fitter is currently being developed for the scintillator and tellurium phases and will help to tag and reduce the cosmogenic backgrounds, especially the  $^{11}\text{C}$  backgrounds induced by muon spallation on the liquid scintillators [100].

A fitter’s performance is first tested on Monte Carlo simulations of specific physics processes, then on both simulations and data from the calibration runs. Once the algorithm has been proven to give good results and is approved by the SNO+ collaboration, it is implemented into the SNO+ `RAT` software to process the SNO+ simulations and data files.

For a specific SNO+ physics phase, the fitters for reconstructing different physics quantities of an event are integrated. Currently, there are three integrated fitters: the `Water`

**Fitter** for the water phase, the **Partial Fitter** for the partial-fill phase, and the **Scint Fitter** for the scintillator phase and the tellurium phase. The fitter parameters, such as the optical parameters, fitter optimization parameters, are coordinated and optimized based on simulations and calibration data from that specific physics phase. In addition, PMT selectors and classifiers are also included in the integrated fitters. The PMT selectors are used to remove the outliers of the hit PMTs for a specific fitter, such as PMTs whose hit(s) probably were triggered by noise. These selectors can help to make the fitter more accurate or to boost fitter speed. The classifiers mainly use the reconstructed results to calculate specific quantities which describe the probability of determining an event as an expected signal or background.

In this chapter, a Multi-Path (MP) reconstruction framework and its principles are discussed. It was developed by the University of Alberta group as an additional fitter to provide event vertex and direction reconstructions. In this framework, the fitters can be adapted for all the SNO+ physics phases by switching light path calculations, input parameters such as the optical parameters, and the detector state. That is the reason why it is called “multiple paths”. It was applied in the water phase to provide an alternative diagnosis of event position and direction; it also works as the vertex reconstruction algorithm for the **Partial Fitter**. After re-coordination for the scintillator and tellurium phases, I also show the potential of the vertex fitter for application in these two future phases.

## 4.2 Multi-Path Vertex and Direction Reconstructions for the Water Phase

In the SNO+ water phase, both the cavity and the AV were filled with ultra-pure water. In this case, the detector geometry is simple since everything inside the PSUP sphere can be simplified as water (if one neglects the effects of the plexiglass AV shell). Therefore to explain the reconstruction concepts, I will start with the **MP water fitter** (the **MPW fitter**).

The **MPW fitter** determines the vertex and direction of a triggered event in the SNO+ water phase. It first fits for the event vertex and then uses that result (reconstructed

position) to fit for the event direction.

#### 4.2.1 Vertex Reconstruction

The vertex is defined by four parameters, namely  $x, y, z$  and  $t$ . The fitter first creates a randomly-generated position inside a sphere of radius 8.39 m (i.e. the PSUP radius  $r_{\text{PSUP}}$ )<sup>1</sup>. Meanwhile, a random event time  $t_0$  (relating to the global trigger time) is also generated from a uniform distribution in the range of [100, 300] ns. The Class Library for High Energy Physics (**CLHEP**) is used for creating pseudo-random numbers. The random position and the random time are combined to form a random event vertex as the trial event vertex ( $\vec{X}_0, t_0$ ). Details are given in the Appendix. A.1.

For each triggered event, photons created around the event position propagate to the hit PMTs. In a simplified detector geometry model that neglects the effects of scattering, reflection, and refraction, these photons are considered as propagating along straight lines that connect the trial event vertex to the hit PMTs. Thus the fitter evaluates a timing parameter, called the time residual ( $t_{\text{res}}$ ), which is defined as [152]:

$$t_{\text{res}} = t_{\text{PMT}} - t_{\text{transit}} - t_{\text{event}}, \quad (4.1)$$

where  $t_{\text{PMT}}$  is the PMT trigger time recorded by the detector,  $t_{\text{event}}$  is the time when an event occurs (event time), and  $t_{\text{transit}}$  is the total transit time (or time of flight, TOF) taken by a photon traveling from the event position ( $\vec{X}_{\text{event}}$ ) to the hit PMT ( $\vec{X}_{\text{PMT}}$ ) and crossing different materials in the detector.

To calculate  $t_{\text{transit}}$ , the fitter uses Cherenkov photons in a prompt time window (called the “prompt light”), chosen as  $-10 < t_{\text{res}} < 10$  ns for the **MPW fitter**, and the photons are assumed to propagate in straight lines (straight light paths). By assuming straight light paths, or rather, by neglecting that they are *not* perfectly straight, complicated aspects of photon propagation are neglected, including refraction and reflection when photons cross boundaries between different detector materials, absorption, and scattering by the detector

---

<sup>1</sup>In this case, the fitter prefers a “PSUP coordination”, the origin of which is at the center of the PSUP. While in the physics analysis for the events inside the AV, an “AV coordination” is preferred. As mentioned in Chapter 3, there is an offset of the AV center with respect to the PSUP. In the water phase, the AV center was 108 mm higher, so the AV center in the PSUP coordination is at (0,0,108) mm. A correction in z must be applied when doing transformations between these two coordinates.

medium, and the lensing effects caused by the spherical structure of the acrylic vessel. In this case, the TOF can be simply calculated as

$$t_{\text{transit}} = \frac{|\vec{X}_{\text{event}} - \vec{X}_{\text{PMT}}|}{v_{\text{water}}} ,$$

where  $v_{\text{water}}$  is an effective average photon group velocity obtained by tuning on Monte Carlo simulations. Sect. 4.2.3 will show the details of this tuning. Based on reconstruction experience from the SNO experiment, it is found that even without the detailed tuning of  $v_{\text{water}}$  the fitter still produces results that are rather consistent with the outcome that *does* use a more detailed calculation [87, 152]. Fig. 4.1 shows straight light paths from the event position to the hit PMT positions.

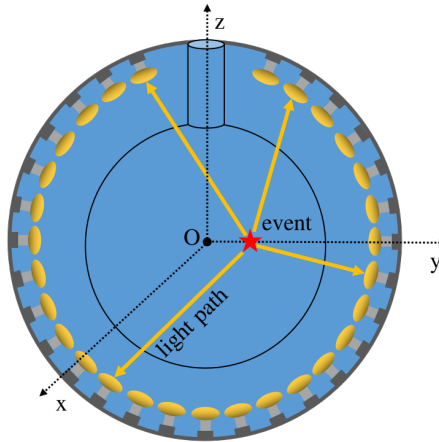


Figure 4.1: A diagram of straight light paths for event position reconstruction in the SNO+ water phase geometry.

A one-dimensional (1D) probability density function (PDF) is used for fitting the timing model, as shown in Fig. 4.2. This PDF serves as a model of the timing responses of the triggered PMTs to the event being fitted. It was taken from the bench-top measurements of the individual PMT time profile from SNO [153] and was further tuned according to the measured *in-situ* SNO+ detector response to the calibration sources [90].

For a trial vertex  $(\vec{X}_0, t_0)$ , the fitter calculates a  $t_{\text{res}}$  value with respect to each hit PMT. Looping over all the hit PMTs, a likelihood function is built as:

$$\ln \mathcal{L}(\vec{X}_0, t_0) = \sum_{i=1}^{\text{NHits}} \ln P(t_{\text{res}}^i) , \quad (4.2)$$

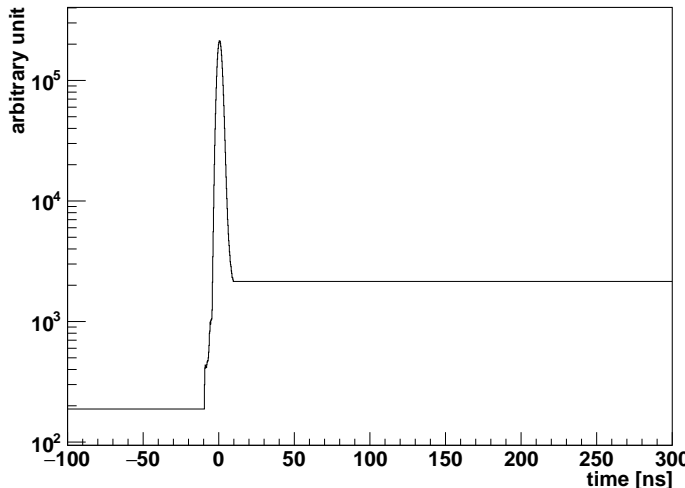


Figure 4.2: The PMT response time profile, used as the timing PDF for vertex reconstruction.

where  $t_{\text{res}}^i$  is the time residual calculated from the  $i^{\text{th}}$  hit PMT; NHits is the total number of PMTs triggered by an event and  $P(t_{\text{res}}^i)$  is the probability returned by reading the PDF when given a  $t_{\text{res}}^i$  for the  $i^{\text{th}}$  hit PMT.

In summary, the likelihood function starts with a random  $(\vec{X}_0, t_0)$  as a seed and calculates the likelihoods and their derivatives for various paths, assuming straight-line paths of the prompt Cherenkov light from the trial vertex  $(\vec{X}_0, t_0)$  to each of the hit PMTs. The trial vertex is varied until the likelihood function reaches the global maximum, which corresponds to the best-fit vertex. This fitting scheme implements the Levenberg-Marquardt (MRQ) method, which is commonly used for fitting a nonlinear model with multiple parameters. In Sect. A.2 this method is described in detail, along with its application for the **MP fitter** (also see Refs. [154, 155] for details).

As will be shown in the sections to follow, one of the main tasks for the fitter is to calculate  $t_{\text{transit}}$  by evaluating light paths. As mentioned earlier, the water phase geometry is the simplest case compared to the other situations when the AV is filled with the wavelength shifter or scintillator. Such materials, with properties quite distinct from the cavity water, make the light path calculations more complicated.

### 4.2.2 Direction Reconstruction

A unit vector  $\vec{u}$  with prescribed orientation can be defined by two parameters, the zenith angle  $\theta$  and the azimuth angle  $\phi$ . In the Cartesian coordinate system, we have:

$$\vec{u} = (\cos \phi \sin \theta, \sin \phi \sin \theta, \cos \theta) , \quad (4.3)$$

which is easily seen to have unit magnitude.

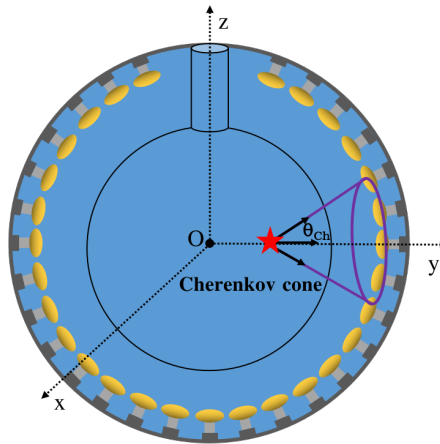


Figure 4.3: Cherenkov cone and straight line light paths, in the SNO+ water phase geometry.

To fit for the direction with its two parameters  $(\theta, \phi)$ , as for the vertex reconstruction a random trial direction  $\vec{u}_0(\phi_0, \theta_0)$  is first generated using CLHEP (see Sect. A.1). The direction fitter then evaluates an angular parameter,  $\cos \theta_{\text{Ch}}$ , which is the angle between  $\vec{u}_0$  and  $\vec{X}_{\text{diff}} \equiv \vec{X}_{\text{event}} - \vec{X}_{\text{PMT}}$ . Therefore, the direction fitter requires an event position as input and necessarily runs after the vertex fitter <sup>2</sup>.

A 1D PDF, serving as a model of the angular distribution of the triggered PMTs and shown in Fig. 4.4, is used for fitting the angular model. It was obtained from 10000 MC simulations of 5-MeV  $e^-$  events generated at the detector center ( $\vec{X}_{MC} = (0, 0, 0)$ ), and traveling along the positive side of the  $x$ -axis, i.e., the orientation of the momentum vector is  $\vec{u}_{MC} = (1, 0, 0)$ <sup>3</sup>.

<sup>2</sup>It has been discussed that, instead of fitting in two steps, the vertex and direction can be fitted simultaneously by utilizing the MRQ algorithm for fitting six parameters  $(x, y, z, t, \theta, \phi)$ . However, results were worse by using this method, because the likelihood function with more parameters becomes more complicated, which makes the fitter more difficult to find a global maximum.

<sup>3</sup>Here 5 MeV is a typical energy for the SNO+ water phase analysis. No obvious changes in fitter performances by using PDFs generated with alternative values for electron energy.



Figure 4.4: PMT angular distribution as the angular response PDF for direction reconstruction.

For the  $i^{th}$  hit PMT,  $\cos \theta_{\text{Ch}}^i = \vec{u}_0 \cdot \frac{\vec{X}_{\text{diff}}^i}{|\vec{X}_{\text{diff}}^i|}$ , then the likelihood function is built as:

$$\ln \mathcal{L}(\vec{u}_0) = \sum_{i=1}^{\text{NHits}} \mathcal{L}_i(\cos \theta_{\text{Ch}}^i), \quad (4.4)$$

Finally, the fitter fits for the angular PDF by using the MRQ method to obtain the best-fit direction. There are several optimizations for improving the fitter performance. First, the group velocity used in the  $t_{\text{transit}}$  calculation is tuned, as shown in Sect. 4.2.3. In Sect. 4.2.4, a drive correction for compensating the pulls in the reconstructed position is discussed. In Sect. 4.2.5, PMT selectors for sending proper PMT information to the fitter are discussed.

### 4.2.3 Effective Group Velocity

When photons travel through the detector, their group velocities ( $v_{\text{gr}}$ ) change in accordance with the different refractive indices of different detector materials. The group velocities also depend on the wavelengths of the photons:  $v_{\text{gr}} = c/n(\lambda)$ . Fig. 4.5 shows the measured refractive index ( $n$ ) of water as a function of wavelength, obtained from the measurements of the laserball scans in the SNO+ water phase [156].

To simplify reconstruction, a tuned value (of  $v_{\text{gr}}$ ) is used in the straight line light path calculation. As mentioned in Sect. 4.2, the water vertex fitter calculates  $t_{\text{transit}}$  by evaluating

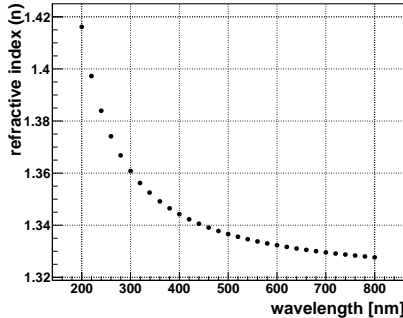


Figure 4.5: Refractive index of water vs wavelength, reproduced from RAT. These values are based on the measurements from laserball calibration scans in the SNO+ water phase [156].

the distances from the trial vertex to the hit PMTs:  $t_{\text{transit}} = |\vec{X}_{\text{event}} - \vec{X}_{\text{PMT}}|/v_{\text{gr,eff}}$ , where the  $v_{\text{water}}$  is replaced by the effective group velocity  $v_{\text{gr,eff}}$ . The value of  $v_{\text{gr,eff}}$  set in the fitter can introduce bias in the reconstructed position, mainly due to a “complementary” effect of the fitter. Setting a large value of  $v_{\text{gr,eff}}$  (a fast effective group velocity) will decrease  $t_{\text{transit}}$ , while according to Eqn. 4.1,  $t_{\text{res}}$  will increase. During the reconstruction, when the fitter compares the large  $t_{\text{res}}$  with the timing PDF, it will attempt to place the trial vertex further away from the hit PMTs to increase  $t_{\text{transit}}$  and then decrease  $t_{\text{res}}$ , as illustrated in Fig. 4.6. On the other hand, if  $v_{\text{gr,eff}}$  is set too small (i.e. too slow),  $t_{\text{transit}}$  will increase while  $t_{\text{res}}$  will decrease, and the fitter will place the trial vertex closer to the hit PMTs to increase  $t_{\text{res}}$ . These effects can be quantified as radial bias ( $r_{\text{bias}}$ ), which is the difference between the reconstructed and true (MC) positions ( $\vec{X}_{\text{fit}} - \vec{X}_{\text{MC}}$ ), projected along the radial component of the true position (the unit vector  $\hat{\vec{X}}_{\text{MC}}$ ) [157]:

$$r_{\text{bias}} \equiv (\vec{X}_{\text{fit}} - \vec{X}_{\text{MC}}) \cdot \hat{\vec{X}}_{\text{MC}} . \quad (4.5)$$

An overestimated  $v_{\text{gr,eff}}$  (too fast) results in a positive radial bias to the true event position while an underestimated one (too slow) brings a negative radial bias.

In practice,  $v_{\text{gr,eff}}$  is calculated by an effective refractive index  $n_{\text{eff}}$  (or “RI value”):  $v_{\text{gr,eff}} = c/n_{\text{eff}}$ . To obtain a reasonable  $v_{\text{gr,eff}}$  for the water-phase vertex fitter, my initial approach was to obtain the value by a linear interpolation based on MC simulations. First, 500 simulations of 5-MeV electrons were generated uniformly inside the AV, with isotropic



Figure 4.6: A cartoon shows effects of tuning the effective group velocity. In this case, the effective group velocity is faster than expected, and the fitted position is dragged back along the direction to increase  $t_{\text{transit}}$ .

momentum directions. Then the **MPW fitter** reconstructed the same MC simulations by using seven different values of  $v_{\text{gr}}$ , from 200 to 230 mm/ns (such that  $n_{\text{eff}}$  ranged from 1.50 to 1.30), with a step of 5 mm/ns. The distributions of radial bias from each reconstruction result were calculated and fitted with Gaussian functions. The mean values of these Gaussian fits were taken as the values of  $r_{\text{bias}}$ , and they were plotted against  $v_{\text{gr}}$ , as shown in Fig. 4.7. A linear fit was applied on these points, giving  $v_{\text{gr,eff}} = 215.868 \pm 5.585$  mm/ns ( $n_{\text{eff}} = 1.3888$ ) at the point where  $r_{\text{bias}} = 0$ .

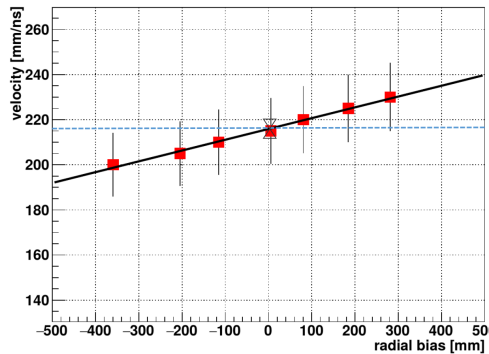


Figure 4.7: Group velocity vs. radial bias for the **MPW fitter**.

Later I turned to a more data-driven approach. This approach is to tune the average group velocity based on the analysis of the  $^{16}\text{N}$  calibration source data. As shown in Fig. 4.8, for the  $^{16}\text{N}$  central run 100934 and run 107055, the source was deployed almost at the PSUP

center, and the optical photons propagated to reach PMTs on the PSUP.

For each event, suppose the triggered PMTs were found within a solid angle

$$\Omega = \frac{\pi(L/2)^2}{r_{\text{PSUP}}^2},$$

where  $L$  is the line segment and  $r_{\text{PSUP}} = 8390$  mm is the radius of the PSUP, as shown in Fig. 4.8. Since the diameter of the PMT concentrator is 27 cm, the line segment is chosen as  $L = 50$  cm ( $\theta = \arcsin(\frac{1}{2}L/r_{\text{PSUP}}) \approx 0.17^\circ$ ) to let roughly 2 triggered PMTs be within the  $\Omega$  (these PMTs are denoted by “PMTin $\Omega$ ”). Then the arrival time  $T_1$  was found by calculating  $|\vec{X}_{\text{source}} - \vec{X}_{\text{PMTin}\Omega}|/v_{\text{water}}$ , where  $v_{\text{water}} = 217.554$  mm/ns is an effective velocity obtained by the SNO+ collaboration for light in water [157].

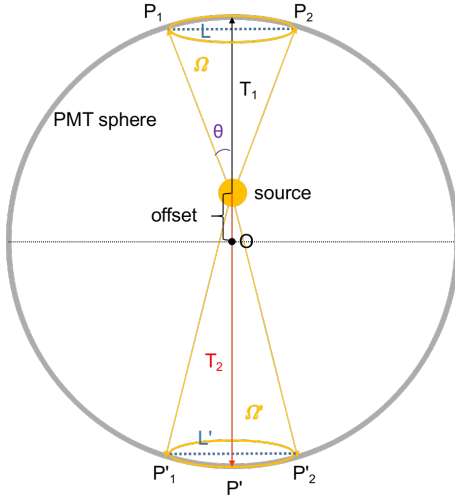


Figure 4.8:  $^{16}\text{N}$  central run for evaluating the average group velocity.

On the other hand, a solid angle  $\Omega'$  is calculated as opposed to the solid angle  $\Omega$  subtended at the source position. Similarly, the triggered PMTs within the  $\Omega'$  were found, and then the arrival time  $T_2$  was calculated. An average group velocity was then calculated as:

$$v_{\text{gr}} = \frac{2r_{\text{PSUP}}}{(T_1 + T_2)}. \quad (4.6)$$

The final estimate for  $v_{\text{gr}}$  was calculated by averaging the  $v_{\text{gr}}$  values obtained from all the events and triggered PMTs in both run 100934 and run 107055. It was found that  $v_{\text{gr}} = c/n_{\text{water,eff}} = 216.478$  mm/ns, where  $n_{\text{water,eff}} = 1.38486$ .

The SNO+ collaboration used a more complicated approach to measure actual group velocities in the SNO+ water detector by analyzing a set of laserball calibration runs [90, 158]. That analysis can give more accurate values of  $v_{\text{gr}}$  as a function of wavelength (see Figure 14 in Ref. [90]), but it was not applied here.

For the vertex fitters used in the partial-fill and scintillator phases, since no internal calibration was performed, I adopted the linear interpolation method, which will be discussed in Sect. 4.5.

#### 4.2.4 Fitter Pull and Drive Correction

An effect of “fitter pull” in the event vertex reconstruction utilizing the Cherenkov light was observed in the SNO experiment. The distribution of  $\vec{u}_{\text{fit}} \cdot (\vec{X}_{\text{fit}} - \vec{X}_{\text{MC}}) / |\vec{X}_{\text{fit}} - \vec{X}_{\text{MC}}|$  shows a large peak at +1, which indicates that the fitted position  $\vec{X}_{\text{fit}}$  is prone to be pulled forward from the true position systematically along the event direction  $\vec{u}$  [157, 159, 160].

Similar to the SNO heavy water case, in the SNO+ ultrapure water, Cherenkov photons created by an event trigger most of the PMT hits with early timing, and these hits are located within the Cherenkov cone; for the same event, there are also a few PMT-hits with later timing. These later PMT hits can be caused by scattered or reflected photons, and the positions of the hit PMTs are randomly distributed on the PSUP. A random PMT hit is more likely to be placed outside the Cherenkov cone, due to the detector geometry. This can be understood as follows. Consider an event at the center of the PSUP: the Cherenkov cone it produces will intersect the PSUP over an area of  $2\pi R_{\text{PSUP}}^2(1 - \cos 41^\circ)$ , equivalent to about 12% of the total area of the PSUP sphere. Therefore a random PMT-hit on the PSUP sphere has more than an 88% likelihood of *not* lying within the Cherenkov cone.

For these later timing PMT hits, a “complementary” effect similar to that mentioned in Sect. 4.2.3 can also happen. When the fitter deduces a large  $t_{\text{res}}$  value caused by the later timing hits, it pulls the trial position away from the later timing hits to increase  $t_{\text{transit}}$  and decrease  $t_{\text{res}}$ , as illustrated in Fig. 4.9. In Ref. [159] this effect was referred to as the “straightening out of delayed photons” by the timing fitter. Furthermore, the major early hits can also cause small  $t_{\text{res}}$  values and thus the fitter pulls the trial position closer towards the early hits to decrease  $t_{\text{transit}}$  and increase  $t_{\text{res}}$ . Recall that the early hits are located on

or around the Cherenkov cone, therefore an overall effect of this “fitter pull” is that the fitted position will be pulled along the axis of the Cherenkov cone and towards the PSUP sphere. This pull direction is coincident with the event direction.



Figure 4.9: This schematic illustrates the fitter pull effect, modified from Fig. C.2 in Ref. [160] and Fig. 2, 3, 4 in Ref. [159].

A simple way to eliminate this “fitter pull” effect is to pull back the fitted event position against the event direction. This is called “drive correction”. Once the **MPW fitter** obtains the fitted position and direction, the drive correction  $\vec{X}_{\text{corrected}} = p_0 \vec{X}_{\text{fit}} + p_1 \vec{u}_{\text{fit}}$  is applied on the fitted position, where  $p_0$  and  $p_1$  are the correction parameters (see Fig. 4.10).

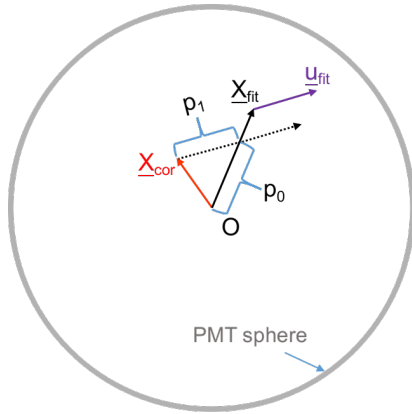


Figure 4.10: A diagram illustrating the drive correction.

To obtain the values of  $p_0$  and  $p_1$ , I generated electron events uniformly distributed inside the AV, with energies ranging from 2 to 10 MeV with a 1 MeV step. The **MPW fitter** was applied on each simulation and returned  $\vec{X}_{\text{fit}}$  and  $\vec{u}_{\text{fit}}$ . Taking the Monte Carlo generated

positions  $\vec{X}_{MC}$  as the true positions, for all the fitted events, a  $\chi^2$  function was calculated as:

$$\chi^2 = \sum_{i=1}^{N_{\text{events}}} [\vec{X}_{MC}^i - (p_0 \vec{X}_{fit}^i + p_1 \vec{u}_{fit}^i)]^2, \quad (4.7)$$

and the parameters  $(p_0, p_1)$  were obtained by minimizing the  $\chi^2$  function. When calculating  $\chi^2$ , fitted events having  $|\vec{X}_{fit} - \vec{X}_{MC}| > 3$  m were rejected to improve the  $\chi^2$  minimization results.

For the 2 to 10 MeV  $e^-$  event simulations (using RAT version 6.17.6), the values obtained for  $(p_0, p_1)$  are energy- (or NHit-) dependent, as shown in Fig. 4.11. However using NHit-dependent functions  $p_0(\text{NHits}), p_1(\text{NHits})$  as drive corrections does not improve the results. Finally I take average values from the 5 to 10 MeV electron simulations and find the optimal drive correction is:

$$\vec{X}_{\text{corrected}} = 0.9868 \vec{X}_{fit} - 78.417 \vec{u}_{fit} [\text{mm}]. \quad (4.8)$$

Note that these drive correction parameters were obtained from simulations, and so changes of the simulation model, and especially changes to the optical model of the detector, can affect the  $n_{\text{gr,eff}}$ , mode cut and time residual cut, and thereby affect the drive correction parameters. If needed, however, the drive correction parameters can be re-coordinated with the changes in the simulation.



Figure 4.11: Drive correction parameters  $p_0$  (left) and  $p_1$  (right) as a function of electron energy.

To check the effects of the drive correction, 1000 simulations of 5 MeV electrons were generated at the detector center, with their momentum vector oriented along  $(1, 0, 0)$ . It

was found that the drive effect in the reconstruction caused about +50 mm bias away from the detector center and along the  $x$ -axis (i.e., the pull towards positive  $x$ ). The drive correction reduced this pull down to about +0.2 mm along the  $x$ -axis. The resolution of the  $r_{\text{bias}}$  distribution was also improved by  $\sim 20$  mm. With the same simulation settings, various electron energies from 2 to 10 MeV (with a 1 MeV step) were generated to check the effects before and after the drive correction, with the outcome shown in Fig. 4.12. The pull is quantified by the radial bias mentioned in Sect. 4.2.3. The distributions of the  $r_{\text{bias}}$  in each simulation were fitted with Gaussian functions, and the Gaussian means were used as the pull. It can be seen that the pull effect is larger at higher electron energy. The drive corrections improve the radial biases by about 55 mm. The drive correction is also applied in the **Rat water fitter**, and those results are also shown.



Figure 4.12: Radial biases of simulated electron events before (unfilled triangles) and after the application of a drive correction (filled triangles), as a function of energy. The results from the official **RAT water fitter** are also shown, with the unfilled blue squares for biases before the correction and filled blue square after the correction.

#### 4.2.5 PMT Selectors for the Reconstruction

PMT selectors were developed to optimally select a set of hit PMTs for the reconstruction algorithm, from all the PMTs triggered by an event. The purpose was to optimize the fitter results and boost the fit speed. The PMT selectors used by the **MP fitter** are:

- Straight Light Path Time Residual Cut Selector

This selector is used for the direction reconstruction for the SNO+ water phase and was first developed by K. Singh [7]. The time residual ( $t_{\text{res}}$ ) is calculated for each hit PMT, and PMTs returning a  $t_{\text{res}}$  value within the prompt time window  $[-10.0, 120.0]$  ns are selected for the fitter. The calculation of  $t_{\text{res}}$  is based on using straight-line light paths, as in the case of the **MPW fitter**. The selector mostly removes PMTs that had been triggered by late-arriving photons, such as those reflected off the detector elements (called “late light”), and thereby keeps the possible Cherenkov ring hit pattern clear for the direction reconstruction. Removing irrelevant PMTs can potentially boost the fit speed.

- Mode Cut Selector

This selector was developed by the SNO+ collaboration for all fitters. It checks the hit time ( $t_{\text{PMT}}$ ) distributions of all the hit PMTs and finds the mode of the hit time ( $t_{\text{mode}}$ ). Here the  $t_{\text{mode}}$  is required to be a unique number and is found by looking for the peak of the  $t_{\text{PMT}}$  distribution. If it fails to get  $t_{\text{mode}}$ , it instead calculates the median ( $t_{\text{median}}$ ) [161]. Then it selects PMTs for which  $t_{\text{PMT}} \in [t_{\text{mode}} + t_{\text{low}}, t_{\text{mode}} + t_{\text{high}}]$  ns. This selector is used to remove the PMTs triggered by noise, or reflected light. The values of  $t_{\text{low}}$  and  $t_{\text{high}}$  are optimized for different detection media. For the **MPW fitter**, the optimized window is found to be  $[t_{\text{mode}} - 50, t_{\text{mode}} + 100]$  ns by checking with the fit biases and resolutions for the  $^{16}\text{N}$  central run data in the water phase, while for the **MP partial fitter** and **MP scint fitter**, the optimized window is  $[t_{\text{mode}} - 100, t_{\text{mode}} + 100]$  ns based on tuning with the simulations.

- Uniform PMT Selector

I implemented this selector and the Earliest Hit Selector mentioned below for the partial-fill and scintillator phases, when a single event can trigger many PMTs due to the high light yields of the liquid scintillator. In this case, the fit speed for each event becomes slow, which can present a difficulty for the data processing. These selectors can reduce the number of the hit PMTs to a designated number ( $n_{\text{select}}$ ) to boost the fit speed, while still providing acceptable values for fit bias and resolution.

For the Uniform PMT Selector, when an event triggers  $N$  calibrated PMTs, the selector goes through these recorded PMTs and uniformly picks one PMT per interval of  $\lceil N/n_{\text{select}} \rceil$ . If  $N \leq n_{\text{select}}$ , the selector does nothing. This way, the selector uniformly reduces the number of the PMTs for the fitter, without introducing an obvious bias.

- Earliest Hit PMT Selector

This selector first groups the PMTs by their positions on the PSUP sphere. Taking the center of the sphere as the origin of the coordinate, the sphere is decomposed into intervals of azimuth angle  $\phi$  (longitude) and zenith angle  $\theta$  (latitude). The PMT positions are projected to  $\phi \in [-\pi, \pi]$  and  $\cos \theta \in [-1, 1]$  on the sphere, each range being uniformly divided into  $n$  intervals, where  $n$  is an integer. The whole PSUP sphere is thus decomposed into  $N' = n \times n$  panels by  $\phi$  and  $\cos \theta$ , and the PMTs are grouped into these panels:  $\text{PMT}(\phi_i, \cos \theta_j) \in [i \cdot \phi/n, j \cdot \cos \theta/n]$ , ( $i, j = 1, 2, \dots, n$ ), see Fig. 4.13.

In each panel, the selector first removes the hit PMTs which are triggered too early ( $t_{\text{PMT}} < 100$  ns, where 100 ns is set as a default threshold). These PMTs could be triggered by noises, such as the pre-pulsing from thermal noises. Then in the rest of the hit PMTs, the selector picks up one PMT which has the earliest  $t_{\text{PMT}}$  in the panel. In each of the  $N'$  panels, 1 PMT (or no PMT<sup>4</sup>) is selected, thus the number of the hit PMTs is reduced to  $n_{\text{select}}$  for the fitter, and  $n_{\text{select}} \leq N' = n \times n$ . If  $\text{NHits} \leq n_{\text{select}}$ , the selector does nothing.

Other timing parameters can also be used for selecting the PMT in each panel, such as  $t_{\text{mode}}$  or  $t_{\text{median}}$ . However, tests on the simulations for the scintillator phase showed that using the earliest hit time  $t_{\text{PMT}}$  gave smaller fit bias and better fit resolution. Tests on the 10 MeV  $e^-$  simulations in the scintillator phase showed that by applying this selector with  $n_{\text{select}} = 16 \times 16$ , the fit speed was reduced from 1.2 s/event to 0.4 s/event.

---

<sup>4</sup>If all the hit PMTs in a panel are triggered too early and are removed by  $t_{\text{PMT}} < 100$  ns, there would be no PMT in that panel.



Figure 4.13: PMTs are grouped by partitioning the PSUP sphere into intervals of latitude and longitude.

#### 4.2.6 Position Figure of Merit

A quantity called scaled log  $L$  (*scaleLogL*) is used as the position reconstruction figure of merit (*posFoM*):  $scaleLogL = \ln \mathcal{L} / \text{NHits}_{\text{selected}}$ . This quantity utilizes the best log-likelihood returned by the **MP fitter** for a successfully reconstructed event vertex, and then it is scaled by the “selected” NHits ( $\text{NHits}_{\text{selected}}$ ), which is the number of the PMTs actually used by the fitter for the event vertex reconstruction, after the PMT selection mentioned in Sect. 4.2.5. This *posFoM* quantity can remove a few mis-reconstruct events and thereby improve the results of the reconstruction.

#### 4.2.7 Performance of the Water Vertex Reconstruction

Using the **RAT** (version 6.17.6) package, MC simulations were performed in which 10,000 electron events were generated at the detector center (in the PSUP coordinate frame) with isotropic direction, i.e. the orientation of the momentum vector was generated randomly and uniformly over the entire solid angle ( $4\pi$ ). The default detector trigger settings of the SNO+ water phase were **N100Hi**=21.0, **N100Med**=16.0 and **N100Lo**=11.0 and with those settings some events, especially those with lower energies ( $E < 3$  MeV), may fail to trigger the detector. Since the fitters only reconstruct triggered events, the number of events reconstructed by the fitter may be lower than the number simulated.

The average fit speed of the event vertex reconstruction for the 5 MeV  $e^-$  simulations was 0.005 s/event and for the direction reconstruction, the fit speed was 0.002 s/event, figures that are very fast and certainly acceptable for the data processing in the SNO+ water phase. Fig. 4.14 shows the position reconstruction results and performance for the

5 MeV  $e^-$  events. The bias between the fitted and MC positions,  $\vec{X}_{fit} - \vec{X}_{mc} = (x_{fit} - x_{MC}, y_{fit} - y_{MC}, z_{fit} - z_{MC})$ , was projected onto the  $(x, y, z)$  axes respectively and its distribution was fitted with Gaussian functions. The mean of the fitted Gaussian ( $\mu$ ) is taken as the fit position bias while the standard deviation ( $\sigma$ ) is taken as the fit position resolution.



Figure 4.14: The position biases projected on the  $x$ ,  $y$  and  $z$  axes. The distributions were fitted with Gaussian functions. The MC generated 10000 5-MeV  $e^-$  particles at the detector center with isotropic directions.

In Fig. 4.14 there are a few events with position biases larger than 2000 mm, and these are interpreted as being mis-reconstructed events. Some of these events are due to relatively lower log-likelihood values and can be tagged by the *posFoM* mentioned in Sect. 4.2.6. As

shown in Fig. 4.15, a cut requiring  $scaleLogL > 10$  can remove some mis-reconstructed events. The remainder may have resulted from the “straight-light path” approximation used by the MP **fitter**, since this calculation misrepresents refracted and/or reflected light paths from event to PMT, as mentioned in Sect. 4.2.1. However, the fraction of these mis-reconstructed events is low, about 0.1% and thus it is tolerable.

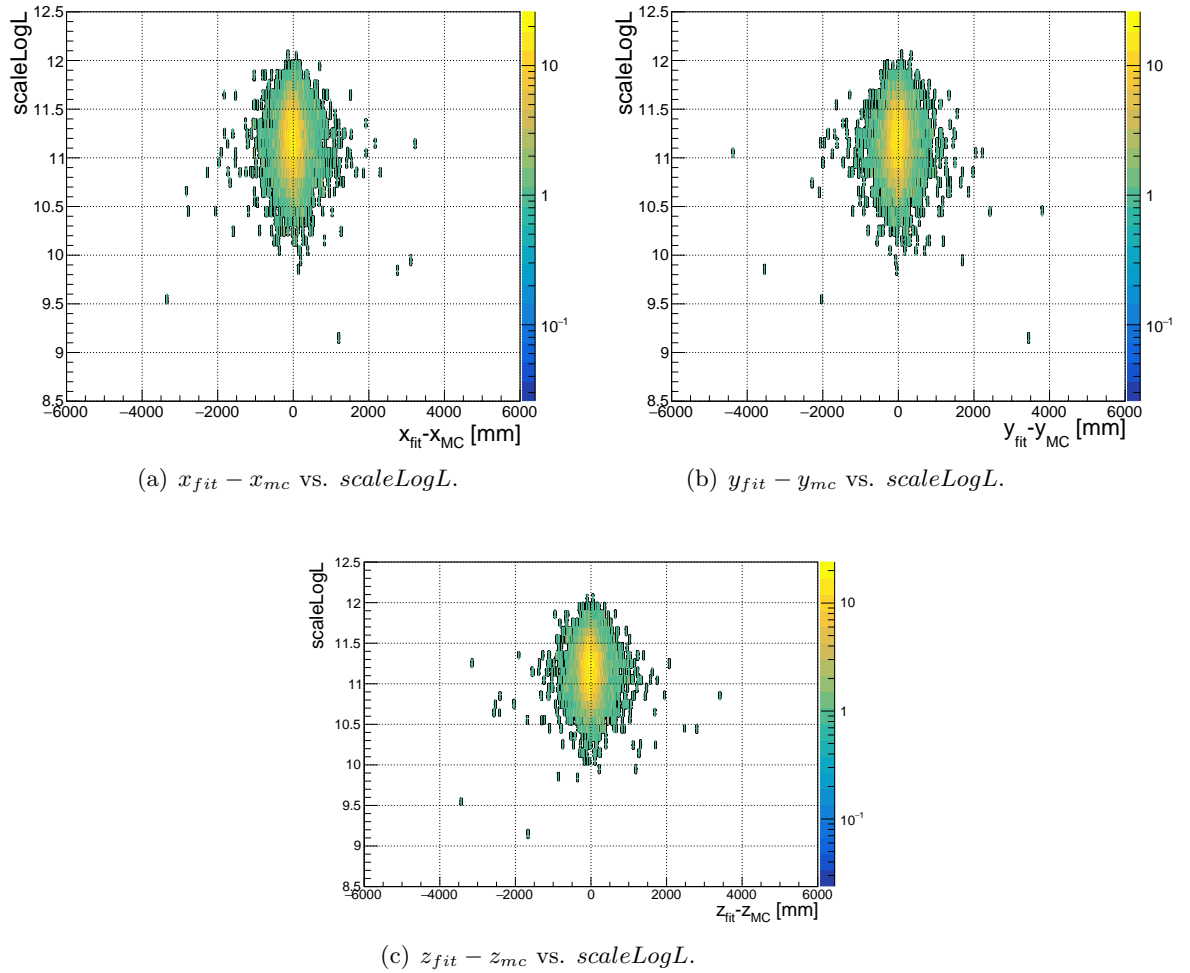


Figure 4.15: The position biases against the position FoMs. The MC generated 10000 5-MeV  $e^-$  particles at the detector center with isotropic directions.

The above results pertain to electron events at the center of the PSUP, but a more realistic analysis must permit events to happen anywhere and everywhere inside the AV. To simulate this, electron events were generated at random positions uniformly distributed

inside the AV volume, and (again) with isotropic directions. Simulations were performed for a range of  $e^-$  energies covering 2 to 15 MeV, with a 1 MeV interval. Fig. 4.16 and Fig. 4.17 show the fit position bias ( $\mu_{x,y,z}$ ) and resolution ( $\sigma_{x,y,z}$ ) respectively.

These results show that the fit position biases  $\mu_{x,y,z}$  are stable across different energies and (with two exceptions) smaller than 10 mm in magnitude. The resolutions  $\sigma_{x,y,z}$  improve (i.e. the  $\sigma$ 's decrease) with increasing event energy, from about 350 mm at 2 MeV to about 120 mm at 15 MeV, and the average value is 180 mm. Of course, more photons are produced by higher-energy  $e^-$  events, thus triggering more PMTs, and events having a larger NHit value provide more information for the fitter: this explains the trend in resolution given by Fig. 4.17. As will be shown in the following section, the position resolution can also be improved by using a detection medium that produces more photons for the same event.



Figure 4.16: The MPW fitter fit position biases in  $x$ -(red circle),  $y$ -(green square), and  $z$ -(black triangle) axes as a function of energy.

To check the radial dependence of reconstruction performance, the volume inside the AV sphere was divided into eleven concentric shells. The centers of these fictitious shells were at the AV center, and their inner and outer radii were at  $r, r+0.001$  m, where  $r$  ranged from 0.5 m to 5.5 m with a step of 0.5 m. Simulations were performed with 5 MeV electrons generated (with an isotropic orientation, and uniformly in azimuth and elevation angles) within each of eleven concentric shells. Fig. 4.18 and Fig. 4.19 show the fit position bias



Figure 4.17: The MPW `fitter` fit position resolutions in  $x$ -(red circle),  $y$ -(green square), and  $z$ -(black triangle) axes as a function of energy.

and resolution respectively. Evidently fit position bias is rather stable across the differing radii, but resolution deteriorates for events close to the AV wall, or  $R > 5$  m. This is called the “near AV effect”, and it was observed in the SNO experiment. For events that occur close to the AV wall, the plexiglass can serve as a lens that distorts the light path [160]. A complicated calculation to encompass this complication, and a technique called the “Near AV cut”, are discussed in Refs. [87, 157], but they are not applied in this thesis.

#### 4.2.8 Performances of the Direction Reconstruction in water

The bias between the true event direction (unit vector  $\vec{u}_{MC}$ ) and the reconstructed direction (unit vector  $\vec{u}_{fit}$ ) is described by the angle “ $\theta_e$ ”, defined as  $\cos \theta_e \equiv \vec{u}_{fit} \cdot \vec{u}_{MC}$ . To describe the distribution of  $\cos \theta_e$ , an empirical function for the angular resolution was adopted by SNO [152] and it is defined as a combination of two exponential components,

$$P(\cos \theta_e) = \alpha_M \frac{\beta_M \exp[-\beta_M(1 - \cos \theta_e)]}{1 - \exp(-2\beta_M)} + (1 - \alpha_M) \frac{\beta_s \exp[-\beta_s(1 - \cos \theta_e)]}{1 - \exp(-2\beta_s)}, \quad (4.9)$$

where the parameters  $\beta_M$  and  $\beta_s$  are the “decay” constants or the “slopes” of the two exponential components, and  $\alpha_M$  adjusts the relative weighting (or blending) of the two exponential components. The first component is due to single scattering of the electrons and represents the true angular resolution of the detector, while the second component,



Figure 4.18: The MPW fitter fit position biases of  $x$ -(red circle),  $y$ -(green square), and  $z$ -(black triangle) axes as a function of radius.



Figure 4.19: The MPW fitter fit position resolutions of  $x$ -(red circle),  $y$ -(green square), and  $z$ -(black triangle) axes as a function of radius.

which has a broad tail, is mainly due to the multiple scattering of electrons; this broad tail also includes back-scattering on detector components and poorly reconstructed events [152]. Fig. 4.20 shows the  $\cos \theta_e$  distribution for 5 MeV  $e^-$  particles generated at the detector center, with isotropic directions.

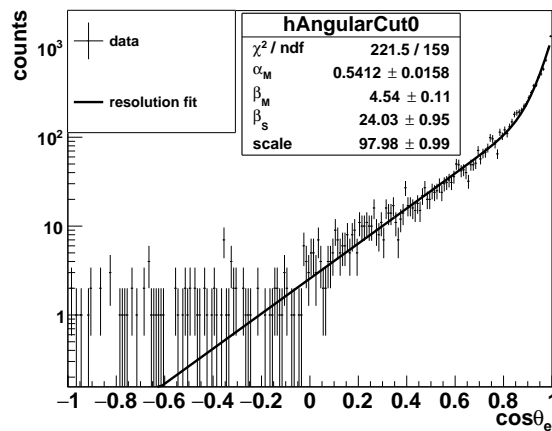


Figure 4.20: The bias between fitted and true (MC) direction, fitted with the resolution function  $P(\cos \theta_e)$ . The MC simulation generated  $10^4$  5 MeV electrons at the detector's center.

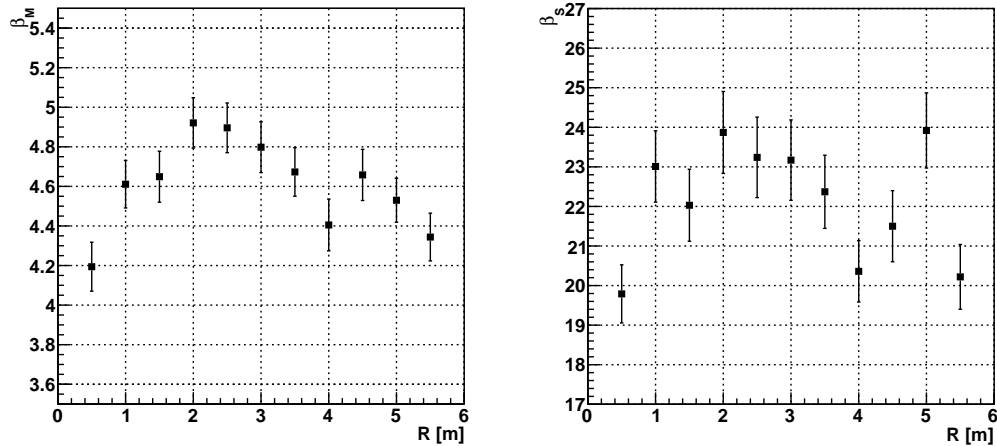
Another way to quantify the performance of the reconstruction is to calculate the angles that contain 50%, 80% or 90% of the reconstructed events, denoted by  $\cos \theta_{0.5}$ ,  $\cos \theta_{0.8}$  and  $\cos \theta_{0.9}$  respectively [157]. Their values (represented in Eqn. 4.10 by the abstract  $\cos \theta_a$ ) are obtained by solving:

$$\frac{\int_{\cos \theta_a}^1 P(\cos \theta_e) d \cos \theta_e}{\int_{-1}^1 P(\cos \theta_e) d \cos \theta_e} = a \times 100\% , \quad (4.10)$$

where  $P(\cos \theta_e)$  is the direction resolution function with the best fit parameters. A larger  $\cos \theta_a$  means the  $\cos \theta_e$  distribution is more peaked around +1, and implies a better direction reconstruction. The results of this analysis for direction resolution, listed in Table 4.1, are slightly better than those obtained from the SNO fitter results for the 5-MeV  $e^-$  in heavy water, for which Ref. [152] lists ( $\beta_M = 3.348 \pm 0.08119$ ,  $\beta_S = 19.30 \pm 0.6929$ ). Fig. 4.21 shows the direction resolution parameters  $\beta_M$  (left plot) and  $\beta_S$  (right plot) as a function of event radial position, based on the simulations described in Sect. 4.2.7

Table 4.1: Direction resolutions for the reconstruction of 5 MeV  $e^-$  events.

$\beta_M$	$\beta_S$	$\cos \theta_{0.5}$	$\cos \theta_{0.8}$	$\cos \theta_{0.9}$
$4.47 \pm 0.12$	$21.54 \pm 0.91$	0.978	0.777	0.624

Figure 4.21: Direction resolutions as a function of radius. The MC generated 10000 5-MeV  $e^-$  inside the AV with isotropic directions.

#### 4.2.9 Test on Gamma Events

For analyzing the AmBe calibration data, reconstructing  $\gamma$ -events with energies of 2.2 MeV and 4.4 MeV is crucial. When a realistic trigger setting for the antineutrino analysis (taken as that of run 106904) is adopted in simulations, only about 53% of the (simulated) low energy 2.2-MeV  $\gamma$  events triggered a detector response. The event count for simulations was, therefore, doubled to  $2 \times 10^4$ . Table 4.2 shows the performance (bias and resolution on each axis) of the event position reconstruction for these important gamma events.

Table 4.2: Reconstruction performances for the 2.2-MeV and 4.4-MeV  $\gamma$  events.

simulation	$\Delta x \pm \sigma_x$ [mm]	$\Delta y \pm \sigma_y$ [mm]	$\Delta z \pm \sigma_z$ [mm]
2.2-MeV	$2.278 \pm 626.927$	$-5.663 \pm 608.182$	$-10.523 \pm 626.034$
4.4-MeV	$-6.964 \pm 364.725$	$-2.804 \pm 368.752$	$-1.342 \pm 368.398$

#### 4.2.9.1 Test on $^{16}\text{N}$ Calibration Source Events

In a more realistic situation, the data collected from the calibration runs were used to evaluate the fitter performance as well as the reconstruction uncertainties. Chapter 5 will discuss the analyses of the  $^{16}\text{N}$  calibration source in detail. For these analyses, rather than the simple Gaussian function used here, a more specific position resolution function was used. It is constructed by the distributions of the initial interaction positions of the particles emitted from the source, convolved with a Gaussian resolution function. On the other hand, the same direction resolution function was used in Chapter 5.

### 4.3 Vertex and Direction Reconstruction for the Water-based Wavelength-shifter

A reconstruction algorithm was developed to investigate the proposal, mentioned in Sect. 3.3.4, for incorporating in the detector a water-based wavelength-shifter. Fig. 4.22 shows the position distribution of hit PMTs for MC simulated 5 MeV electrons traveling along the positive  $x$  direction in the AV. The left panel shows the case when the detector is filled with pure water while the right panel is for water into which is mixed with the wavelength shifter PPO at a concentration of 0.1 ppm (“wbWLS”). For the same set of electron events, the number of hit PMTs (NHits) in wbWLS is about 2.4 times greater than in pure water. Although in the wbWLS medium extra isotropic light is emitted, the Cherenkov ring can still be clearly distinguished, allowing reconstruction of the directionality of events.

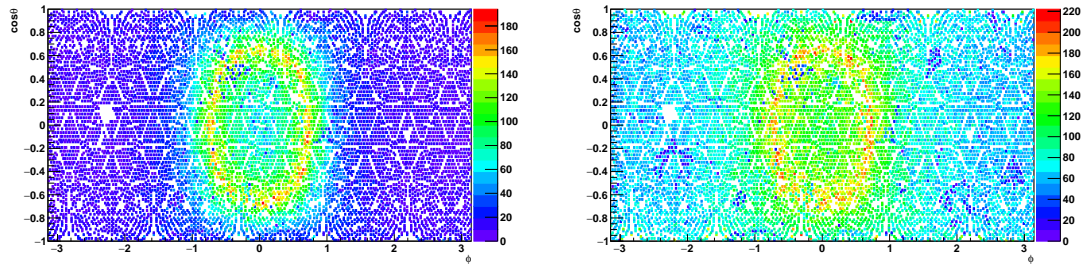


Figure 4.22: Position distribution of hit PMTs (zenith and azimuth angles) for 5 MeV electrons traveling along the  $+x$  direction in pure water (left) and water bearing 0.1 ppm PPO (right).

Fig. 4.23 shows the energies of simulated electrons as a function of the mean value of the NHits distribution (mean NHits). In pure water, a 1 MeV electron may cause about 7 PMT hits (but below the detector trigger threshold), while in the wbWLS case the 1 MeV electron simulation results (on average) detect an event with NHits = 20.



Figure 4.23: The energies of simulated electrons as a function of mean NHits. The values in the 0.1 ppm PPO (solid line with inverted triangle) are compared with the water (dashed line with star).

In the wbWLS case, since the WLS absorbs and re-emits photons, the reconstruction mentioned in Sect. 4.2 is slightly modified to build the **MP WLS fitter**. Given the optical properties of PPO, the prompt light emitted from an event has a probability of  $\sim 0.6$  to be absorbed by the WLS and then re-emitted at a vertex that is *shifted* along the direction of motion ( $\hat{n}$ ) of the event-originating charged particle. Accordingly the fitter returns a shifted vertex,  $\vec{X}_{0,\text{shifted}} = \vec{X}_0 + \text{offset} \cdot \hat{n}$ . The offset specified in the fitter, obtained from simulations, is 100 mm. Fig. 4.24 shows the timing PDF for the wbWLS, which is the PMT response time modified for photon propagation time in the wbWLS.

To reconstruct event direction, in addition to the angular distribution of Cherenkov photons,  $\cos\theta_{Ch}$ , we also consider the fraction of the re-emitted and wavelength-shifted photons that cause a flat (i.e. uniform) angular distribution.

To test the performance of the **MP WLS fitter**, a simulation was performed with 5 MeV electrons released at the center of the wbWLS-filled AV and traveling along  $+x$  direction; and for comparison, the equivalent simulation was also done for the pure water-filled AV, in which case the simulated events were reconstructed by the water fitter. Fig. 4.25 shows the



Figure 4.24: The timing PDF for the wbWLS.

performance of the WLS fitter reconstructed positions of the MC simulations, in comparison with the pure water case. For the fit position distribution of 5 MeV  $e^-$  in the wbWLS medium, we obtained a root mean square (RMS) position error (i.e position resolution) of 201 mm, and a bias towards the AV center (the mean of the histogram) of 29 mm. Compared to the pure water case, the RMS is a 188 mm improvement, and the fit bias is about 19 mm better.

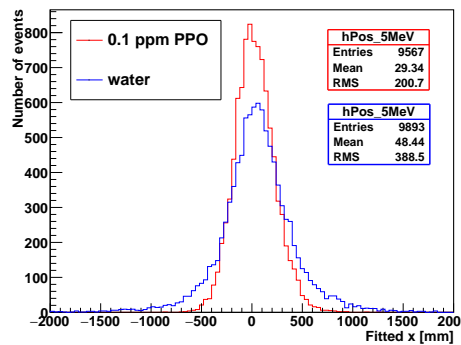


Figure 4.25: A comparison of fitted  $x$  positions. The MP WLS fitter reconstructed  $x$  positions of the 5-MeV  $e^-$  events in the wbWLS (red) are compared to those in the pure water (blue).

As it had been in Sect. 4.2.8, again here  $\cos \theta_a$  in Eqn. 4.10 was used to characterize the performance of the direction reconstruction. Table 4.3 compares the MP WLS Fitter's  $\cos \theta_a$  values when applied to SNO heavy water data [152], and to simulations for both

SNO+ pure water and SNO+ wbWLS. The best direction reconstruction is obtained for the SNO+ pure water case, with results for the wbWLS case proving less satisfactory (e.g. by about 30% for  $\cos \theta_{0.9}$ ).

Table 4.3: A comparison of quantitative estimates for the angular resolution for the SNO heavy water, SNO+ wbWLS and the SNO+ pure water cases.

medium	$\cos \theta_{0.9}$	$\cos \theta_{0.8}$	$\cos \theta_{0.5}$
SNO heavy water	0.50	0.71	0.92
SNO+ water	0.62	0.78	0.98
wbWLS	0.37	0.63	0.90

Comparing a pure water SNO+ detector and the wbWLS one, using the **MP WLS fitter** for physics events gives a better position resolution without significant loss in performance of the direction reconstruction. This **MP WLS fitter** was also applied in a study of the potential for measuring reactor antineutrinos in the wbWLS-filled SNO+ detector, see Ref. [162] for details.

## 4.4 Vertex Reconstruction for the Partial-fill

The following two sections discuss the vertex reconstruction in liquid scintillators. The vertex reconstructions for the partial-fill and scintillator phases are very similar. Both must accommodate two detection media, water, and scintillator, and calculate the light paths in these two regions. I will first describe the calculations in the partial-fill case since its geometry is more complex, relative to which the full scintillator case can be considered a simplification.

### 4.4.1 Partial-fill

In the partial-fill geometry, the SNO+ detector can be described as being composed of three parts: the neck cylinder filled with scintillator; the AV sphere, which contains scintillator above and water below the water-scintillator interface (plane); and the water-filled PSUP sphere lying outside the neck and the AV.

If we neglect complications related to the acrylic and other solid parts of the detector,

then photons travel in only two media: water and scintillator (see Fig. 4.26). By definition the length of the straight light path from a vertex to a hit PMT position is  $|\vec{l}_p| = |\vec{X}_{\text{PMT}} - \vec{X}_0|$ . The MP `scint-water fitter` evaluates the portion  $d_{sp}$  of the total path travelled in scintillator, and length of the path travelled in water obviously is  $|\vec{l}_p| - d_{sp}$ . Since photons travel at different speeds ( $v_{\text{gr,scint}}$ ,  $v_{\text{gr,water}}$ ) in these two media, the MP `scint-water fitter` evaluates the time of flight, as:

$$t_{\text{transit}} = \frac{|\vec{l}_p| - d_{sp}}{v_{\text{gr,water}}} + \frac{d_{sp}}{v_{\text{gr,scint}}} . \quad (4.11)$$

Once having computed  $t_{\text{transit}}$  the time residual  $t_{\text{res}}$  can be calculated, and the balance of the fitting procedure is the same as in the `MPW fitter`.



Figure 4.26: Light path calculation for the MP `scint-water fitter`. In the figure, a light path intersects with the neck cylinder surface, the AV sphere as well as the water-scintillator interface. The total length of the path in the scintillator region (scintillator path,  $d_{sp}$ ) includes the paths in the neck ( $d_{sp,\text{neck}}$ ) and in the AV ( $d_{sp,\text{AV}}$ ). Calculations of the ray-cylinder, ray-plane and ray-sphere intersections are applied.

It follows that the crucial part of the calculation is obtaining  $d_{sp}$ . The light path vector  $\vec{l}_p$ , encoding length and direction, may intersect and one or more of three geometrical objects: the neck cylinder, the AV sphere, and the water-scintillator interface plane. As illustrated in Fig. 4.26, a detailed calculation of  $d_{sp}$  includes evaluation of (1)  $\vec{l}_p$  and neck

(ray-cylinder) intersection; (2)  $\vec{l}_p$  and the AV (ray-sphere) intersection and (3)  $\vec{l}_p$  and the water-scintillator interface (ray-plane) intersection. The distance  $d_{sp}$  is further separated into path segments within the neck ( $d_{sp,\text{neck}}$ ) and within the AV ( $d_{sp,\text{AV}}$ ).

For a trial position  $\vec{X}_0 = (x_0, y_0, z_0)$  and a hit PMT position  $\vec{X}_{\text{PMT}} = (x_{\text{PMT}}, y_{\text{PMT}}, z_{\text{PMT}})$ , define the ray vector as  $\vec{l}_0 \equiv \vec{X}_0 + a \cdot \vec{u}$ , where  $a$  is the distance between the vertex and the PMT intersection point, i.e. the parameter to be determined, and  $\vec{u} = (\vec{X}_{\text{PMT}} - \vec{X}_0)/|\vec{X}_{\text{PMT}} - \vec{X}_0|$  is the direction of the ray vector, i.e. is a unit vector pointing from  $\vec{X}_0$  to  $\vec{X}_{\text{PMT}}$ . The following three types of intersection occur:

- Ray-sphere intersection

In the ray-sphere intersection case (ray vector passes through the AV sphere), the intersection points ( $\vec{X}$ ) on  $\vec{l}_0$  must satisfy the equation  $|(\vec{X} - \vec{O}_{\text{AV}})|^2 = r_{\text{AV}}^2$ , where  $r_{\text{AV}} = 6005$  mm is the radius of the AV sphere and  $\vec{O}_{\text{AV}}$  its origin, with the value  $\vec{O}_{\text{AV}} = (0, 0, 108)$  mm in the PSUP coordinate system (the AV center is 108 mm higher than the PSUP center). Thus the intersection equation is:  $(\vec{l}_0 - \vec{O}_{\text{AV}})^2 = r_{\text{AV}}^2$ .

Now define

$$\Delta \equiv [(\vec{X}_0 - \vec{O}_{\text{AV}}) \cdot \vec{u}]^2 - (\vec{X}_0 - \vec{O}_{\text{AV}})^2 + r_{\text{AV}}^2. \quad (4.12)$$

If  $\Delta > 0$ , one may solve to evaluate two roots,

$$a_{\pm} = -(\vec{X}_0 - \vec{O}_{\text{AV}}) \cdot \vec{u} \pm \sqrt{\Delta}. \quad (4.13)$$

In this case, both  $a_+$  and  $a_-$  exist and their values are distinct. If  $a_+ > a_- > 0$ , the length of the path inside the sphere is  $a_+ - a_-$ , as illustrated in Fig. 4.27 (a). Due to this geometry, the event position should be outside the AV, the condition  $|\vec{X}_0| \geq r_{\text{AV}}$  is automatically met. If  $a_+ > 0 > a_-$ , then  $a_-$  determines an intersection point along the opposite direction of the ray vector. Thus the ray vector actually does not pass that point<sup>5</sup>, and then the length of the path inside the sphere is  $a_+$ , as illustrated in Fig. 4.27 (b). Also, the condition  $|\vec{X}_0| < r_{\text{AV}}$  is automatically met.

If  $\Delta \leq 0$ , there is either **no** intersection point (Fig. 4.27 (c)) or there is **one** intersection point (Fig. 4.27 (d)). In either case, the ray vector never passes through the AV sphere.

---

<sup>5</sup>The line intersection with no direction can pass two points.



Figure 4.27: Line-sphere intersections. (a) the ray vector intersects the sphere with 2 points; (b) the ray vector intersects the sphere with 1 point; (c) and (d): the ray vector never passes through the sphere.

- Ray-plane intersection

For a “ray-plane” intersection, the  $z$  components of the intersection points on  $\vec{l}_0$  satisfy the plane equation  $z = Z_{\text{split}}$ , where  $Z_{\text{split}}$  is the water level, i.e., the  $z$  position of the water-scintillator intersection. Thus the intersection equation is:  $l_{0,z} = Z_{\text{split}}$ , where  $l_{0,z} = z_0 + a \cdot u_z$ .

If  $u_z = z_{\text{PMT}} - z_0 = 0$ , the ray is parallel to the plane and never intersects the plane.

If  $u_z \neq 0$ , solve the intersection equation  $l_{0,z} = Z_{\text{split}}$ , we have:  $a = (Z_{\text{split}} - z_0)/u_z$ .

Let:

$$a_3 \equiv a = \frac{(Z_{\text{split}} - z_0)|\vec{X}_{\text{PMT}} - \vec{X}_0|}{z_{\text{PMT}} - z_0} \quad (\text{if } z_{\text{PMT}} - z_0 \neq 0), \quad (4.14)$$

Similar to the case of ray-sphere intersection, if  $a_3 < 0$ , the ray-plane intersection point is on the extended line along the opposite direction to the ray;  $a_3 \geq 0$  ensures the ray hits the interface. Note that here we consider the plane to be infinitely large: later we will combine with further logic to correct this fallacy.

- Ray-cylinder intersection

For a ray-cylinder intersection, the  $x$  and  $y$  components of the intersection points on  $\vec{l}_0$  satisfy the intersection equation  $l_{0,x}^2 + l_{0,y}^2 = r_{\text{neck}}^2$ , where  $r_{\text{neck}}$  is the radius of the neck cylinder ( $r_{\text{neck}} = 785$  mm).

To solve the intersection equation, let

$$\Delta' \equiv [x_0 \cdot (x_{\text{PMT}} - x_0) + y_0 \cdot (y_{\text{PMT}} - y_0)]^2 - (x_0^2 + y_0^2 - r_{\text{neck}}^2) \cdot [(x_{\text{PMT}} - x_0)^2 + (y_{\text{PMT}} - y_0)^2].$$

Then if  $\Delta' > 0$  we can solve for two roots,

$$a'_{\pm} = |\vec{X}_{\text{PMT}} - \vec{X}_0| \cdot \frac{-[x_0 \cdot (x_{\text{PMT}} - x_0) + y_0 \cdot (y_{\text{PMT}} - y_0)] \pm \sqrt{\Delta'}}{(x_{\text{PMT}} - x_0)^2 + (y_{\text{PMT}} - y_0)^2}. \quad (4.15)$$

Similar to the ray-sphere case, if  $a'_+ > a'_- > 0$ , the length of the path inside the cylinder is  $a'_+ - a'_-$ . In this case, the event position should be outside the cylinder, and the condition  $(x_0^2 + y_0^2) \geq r_{\text{neck}}^2$  is automatically met. If  $a'_+ > 0 > a'_-$ , the event position should be inside the cylinder and the ray-vector intersects the cylinder with one point (while the other point is along the opposite direction). Therefore, in this case, the length of the path inside the cylinder is  $a'_+$ . If  $\Delta' \leq 0$ , the ray vector never passes through the neck cylinder. Note that the calculations mentioned here assume that the cylinder is infinitely long ( $-\infty < z < +\infty$ ). However, since the geometrical boundaries of the AV and PSUP are considered in the calculations, the fitter calculation in the neck region is only valid if  $6000 < z < 8390$  mm (in the PSUP coordinates).

To evaluate the length ( $d_{sp}$ ) of  $|\vec{l}_p|$  that lies in the scintillator region, the above three geometrical criteria need to be combined carefully. The following two procedures go through all possible situations. First combine the evaluations of the ray-sphere and the ray-plane intersections to calculate the light path in the AV scintillator region ( $d_{sp,\text{AV}}$ ). Then combine the evaluations of the ray-sphere and the ray-cylinder intersections to calculate the light path in the neck scintillator region ( $d_{sp,\text{neck}}$ ). Detailed algorithms are shown in Appendix A.6.

Since a valid fit requires events to lie inside the PSUP sphere, only the part of the neck region that lies inside the PSUP sphere (with  $6108 < z_{\text{neck}} < 8390$  mm) needs to be considered. There is an option to turn off the neck path calculation, but if doing so a worse fit result is expected. Detailed calculations are shown in Appendix A.6.

If  $d_{sp} = 0$ , the light path is entirely in water. In this case, the fitter is equivalent to the MPW fitter, and fits the vertex with the MPW fitter PDF. Once the light path passes through the scintillator region, the fitter fits with a scintillator timing PDF, in which the

PMT time response is adjusted to account for photon propagation time in the scintillator, as shown in Fig. 4.28.



Figure 4.28: Timing PDFs used by the MP scint-water fitter. Blue: the timing PDF used by the MPW fitter; red: the scintillator timing PDF.

The next section will discuss the timing PDFs used by the fitter.

#### 4.4.2 Creating the Timing PDFs

##### 4.4.2.1 Evolving PPO Concentration during the Filling

During the partial-fill phase, the water level and the concentration of the PPO were unsteady. PPO was gradually added into and mixed with the LAB, and during the relatively stable partial-fill stages, which (by virtue of that stability) were suitable for obtaining meaningful data to be analyzed, the PPO concentrations dissolved in the LAB were 0.25 g/L (earlier stage from 2019 to 2020) or 0.5 g/L (later stage from 2020 to 2021). The planned eventual concentration of the PPO in the scintillator phase is 2 g/L.

An understanding of the characteristic photon emission response is crucial for building the timing PDF for event reconstruction. The Oxford group from the SNO+ collaboration carried out bench-top measurements to obtain the time constants and relative light yields of an LAB sample carrying dissolved PPO at the following concentrations: 0.25, 0.5, 1.0, 2.0 and 6.0 g/L [163, 164].

The model used by the Oxford group to fit the emission time profile is [164]:

$$f_{\text{optics}}(t) = A' \frac{e^{-\frac{t}{\tau_{\text{rise}}}}}{\tau_{\text{rise}}} + \sum_{i=1}^3 (A_i \frac{e^{-\frac{t}{\tau_i}} - e^{-\frac{t}{\tau_{\text{rise}}}}}{\tau_i - \tau_{\text{rise}}}) , \quad (4.16)$$

where  $A_i$  is the fraction of scintillation light emitted in the  $i^{th}$  component of the detector medium,  $A'$  is a small additional component with an instantaneous rise time and a fall time equivalent to the rise time of the primary fluor to improve the fit quality with the measured data,  $\tau_i$  is the corresponding decay constant, and  $\tau_{rise}$  is the rise time of scintillator. The parameter values determined by the Oxford group from the bench-top experiments are listed in Table 4.4 and Table 4.5.

Table 4.4: Time constants and amplitudes measured by Ref. [164]. Here the relative light yield is with respect to the LAB+2 g/L PPO case (11900 photons/MeV).

PPO [g/L]	$\tau_{rise}$ [ns]	$\tau_1$ [ns]	$\tau_2$ [ns]	$\tau_3$ [ns]	$A_1$ [%]	$A_2$ [%]	$A_3$ [%]	$A'$ [%]
0.25	1.25	8.1	25.0	68.2	29.2	53.1	13.9	3.8
0.5	1.12	7.2	18.7	49.1	43.5	40.4	12.6	3.5
1.0	1.18	5.5	13.3	40.9	45.6	37.5	13.3	3.6
2.0	1.06	4.2	11.7	48.9	57.9	27.8	8.9	5.4
6.0	0.94	2.5	9.3	46.0	63.7	17.0	8.6	10.7

Table 4.5: Relative light yields (RLY) with different PPO concentrations measured by Ref. [164].

PPO [g/L]	RLY
0.25	0.57
0.5	0.65
1.0	0.9
2.0	1.0
6.0	0.93

These Oxford-measured time profiles were convolved with the PMT time response profile discussed in Sect. 4.2.1, Fig. 4.2, to obtain a timing PDF

$$f(t)_{PDF} = f_{optics}(t) \otimes f_{PMT\ response}(t - t') \quad (4.17)$$

for vertex reconstruction during the partial-fill. I wrote a python tool to create the timing PDFs to re-coordinate the partial fitter for the different PPO concentration cases [165], as shown in Fig. 4.29<sup>6</sup>.

Following the same method as was used for tuning  $v_{gr,eff}$  (see Sect. 4.2.3), the effective group velocity in scintillator ( $v_{gr,scint}$ ) was obtained on the basis of simulations of 500 3 MeV

<sup>6</sup>For other potential phases, the PDF can be built by using the timing spectrum described in Sect. 3.3.5.

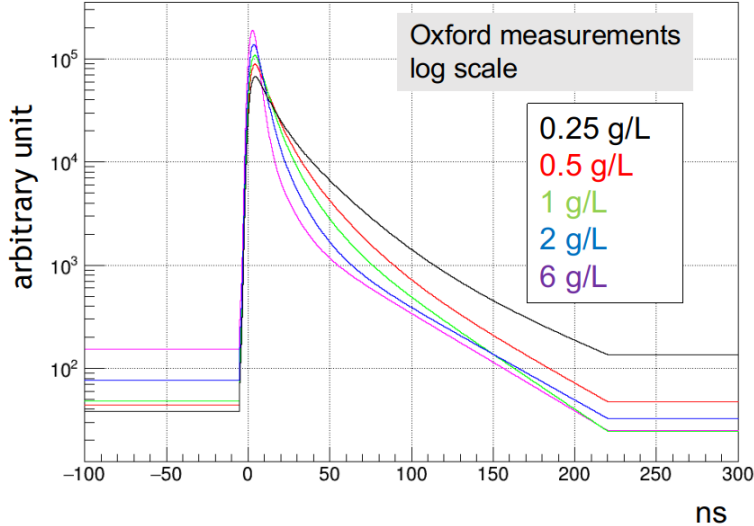


Figure 4.29: Timing PDFs built for various PPO concentrations based on the Oxford bench-top measurements.

electrons generated uniformly and with isotropic direction in the full scintillator geometry. The **MP scint fitter**, which will be discussed in Sect. 4.5, was used to reconstruct the same simulation data with different values of  $v_{\text{gr}}$ . Once  $v_{\text{gr,scint}}$  was obtained, it was fixed in the **MP scint-water fitter**. Then  $v_{\text{gr,water}}$  was tuned by simulating five hundred 3 MeV electron events in the water region of the partial-fill geometry, with the water level set at  $z = 3000$  mm in the AV coordinate. Fig. 4.30 shows the convergence of the values of (a)  $v_{\text{gr,scint}}$  and (b)  $v_{\text{gr,water}}$  to their optimal values, from a linear interpolation in the LAB+0.5 g/L PPO scintillator case. Table 4.6 lists the effective group velocities and refractive indices ( $n_{\text{eff}}$ ) for the liquid scintillator with different PPO concentrations.

Table 4.6: Tuned effective group velocities for different PPO concentrations.

PPO [g/L]	$V_{\text{gr,scint}}$ [mm/ns]	$n_{\text{eff,scint}}$	$V_{\text{gr,water}}$ [mm/ns]	$n_{\text{eff,water}}$
0.25	$184.068 \pm 5.153$	1.629	$211.871 \pm 5.731$	1.415
0.5	$183.467 \pm 5.159$	1.634	$211.587 \pm 5.773$	1.417
1.0	$182.93 \pm 5.193$	1.639	$211.393 \pm 5.805$	1.418
2.0	$183.045 \pm 5.184$	1.638	$211.629 \pm 5.767$	1.417
6.0	$184.218 \pm 5.135$	1.627	$211.173 \pm 5.843$	1.420

Figure 4.30: Tuning the effective group velocities in the scintillator (a) and water (b).



#### 4.4.3 Partial Fitter Performance

The performance of the MP `scint-water fitter` was studied with MC simulations. During the partial-fill phase, the filling and mixing of the liquid scintillator were stable at several water levels for data taking and data analysis. A typical water level is 3 m from the AV bottom, and a typical PPO concentration is 0.5 g/L. With these two settings in the partial-fill geometry, to test the partial fitter's performance 5000 electron events (3 MeV, uniform in position, isotropic in direction) were simulated in each of the regions, i.e. scintillator region and water region.

The average fit speed for vertex reconstruction of events in the scintillator region proved to be 0.2 s/event, which is acceptable for the data processing during the partial-fill phase. For the events in the water region, the average fit speed was 0.05 s/event, which is similar to the value yielded by the `MPW fitter`. Fig. 4.31 and Fig. 4.33 show the results of the MP `scint-water fitter` reconstructed positions in the scintillator and water regions respectively. The subfigures (a) are the reconstructed positions projected onto the  $(\sqrt{x^2 + y^2}, z)$  plane while the subfigures (b), (c), and (d) are the position biases between the reconstruction and MC truth, projected onto the  $(x, y, z)$ -axes respectively. The distributions of the position bias were fitted with Gaussian functions and the values of the Gaussian mean ( $\mu_{x,y,z}$ ) and standard deviation ( $\sigma_{x,y,z}$ ) quantify fit bias and resolution.

Fig. 4.31 shows that for events in the scintillator region, the resolutions  $\sigma_{x,y,z}$  are all better than 150 mm. The biases on  $x$  and  $y$  axes ( $\mu_{x,y}$ ) are smaller than 1.5 mm, while

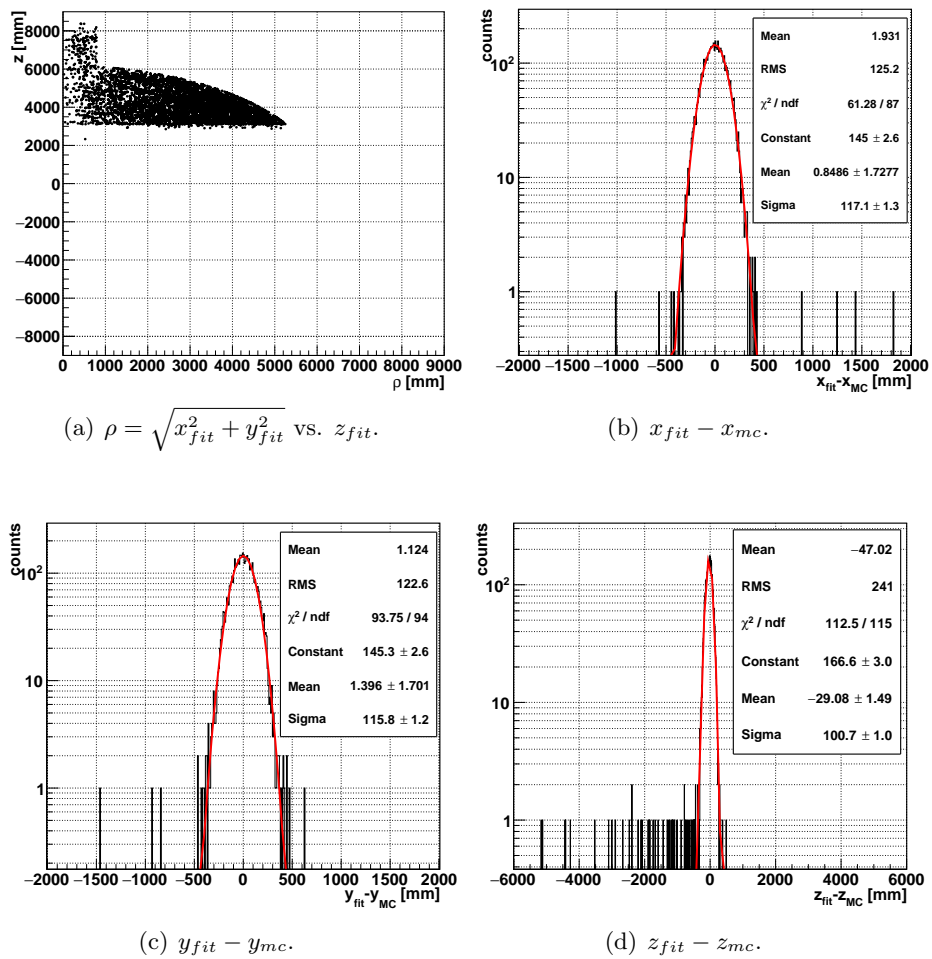


Figure 4.31: Reconstructed position and fit bias for simulated 3-MeV electron events in the scintillator region.

the bias  $\mu_z$  along  $z$  is significantly larger, about -29 mm. The larger bias in  $z$  is mostly caused by events that are mis-reconstructed in the water region. The main reason for that mis-reconstruction is caused by the fitter omitting the calculations relating to reflection and refraction of light paths happening at the water-scintillator interface or at AV boundaries, as earlier mentioned<sup>7</sup>. Since the refractive index of the liquid scintillator exceeds that of water, some photons are reflected off the water-scintillator interface. The reflection results in a light path with a longer  $t_{\text{transit}}$ , but the event is still created in the scintillator region. While the fitter does properly handle the reflected light path, it will pull the event into the water region a little further from the actual position to “explain” the longer  $t_{\text{transit}}$ , causing the event to be mis-reconstructed in the water region. This explains the mis-reconstructed events with  $z_{\text{fit}} - z_{MC} < 0$  in Fig. 4.31(d). Sect. 4.4.5 will discuss improving the fitter. Some of these mis-reconstructed events can be removed by applying the *posFOM* cut.

Fig. 4.32(a) shows the (vertical) fit error  $z_{\text{fit}} - z_{MC}$  versus the *posFOM* quantity *scaleLogL* mentioned in Sect. 4.2.6. Application of a  $\text{scaleLogL} > 9.8$  cut removes more than a third of the mis-reconstructed events with  $|\vec{X}_{\text{fit}} - \vec{X}_{MC}| > 1000$  mm. In Fig. 4.32(b), the fit position bias in  $z$  ( $z_{\text{fit}} - z_{MC}$ ) after the cut is plotted in red, overlaid with the distribution before the cut in black. By fitting with the Gaussian function, it is evident that the cut removes some mis-reconstructed events on the tail of the distribution, improving the resolution by about 1.5 mm and reducing the bias by about 1.9 mm compared to the plot in Fig. 4.31(d). As shown in Fig. 4.32(c), this cut removes most of the outliers observed in the  $\rho$  vs  $z$  plot in Fig. 4.31(a).

For events in the water region, the fit position biases in  $x$  and  $y$  ( $\mu_{x,y}$ ) are comparable to the results of the MPW **fitter** shown in Sect. 4.2.7, while  $\mu_z$  is about 50 mm worse and the resolutions  $\sigma_{x,y,z}$  are about 100 mm worse. This is due to the previously mentioned effects of the water-scintillator interface and boundaries. These boundary effects are more obvious (more severe) for events in the water than for those in the scintillator region, as shown by the  $\rho$  vs.  $z$  plot in Fig. 4.33(a). This is due to the lower NHits (fewer triggered PMTs) of events in the water, providing less information for the fitter. However, the poorer reconstruction performance for water events is not significant for the partial-fill analysis:

---

<sup>7</sup>The reflection and transmission of light are described by the Fresnel equations, and the refraction of light is described by the Snell’s law. These functions are not implemented in this thesis.



Figure 4.32: Effects of the  $scaleLogL$  cut on the reconstructed positions and fit biases.

since the analysis is focused on studying the liquid scintillator, events in the water region are less interesting and are mostly removed by the NHits and fiducial volume cuts ( $\text{NHits} > 40$  was applied on the data processing during the partial-fill phase).

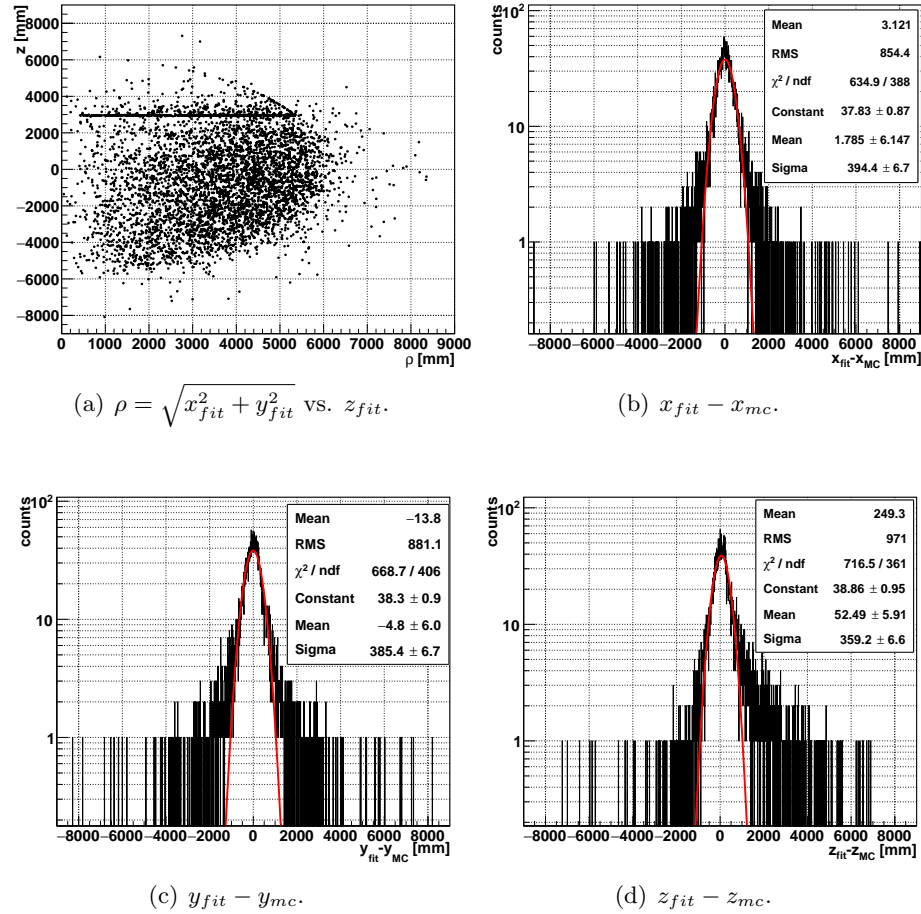


Figure 4.33: Reconstructed positions and fit biases of the 3-MeV  $e^-$  events in the water region.

#### 4.4.3.1 Test on Different PPO Concentrations

To study the effects of different PPO concentrations, in the partial-fill geometry, the water level was set at 3 m from the AV bottom, and the PPO concentrations were set to 0.25, 0.5, 1, 2, and 6 g/L respectively. Simulations of 5000 3-MeV  $e^-$  were generated in the scintillator region with uniformly distributed positions and isotropic directions. The MP scint-water

**fitter** uses the effective velocities and PDFs re-coordinated to the simulation geometries with corresponding PPO concentrations. The distributions of the position biases between the reconstruction and MC in x, y, and z axes were fitted with Gaussians to obtain the fit position biases ( $\mu_{x,y,z}$ ) and resolutions ( $\sigma_{x,y,z}$ ).

Fig. 4.34 and Fig. 4.35 show the  $\mu_{x,y,z}$  and  $\sigma_{x,y,z}$  against PPO concentrations. Biases  $\mu_{x,y,z}$  are stable in the [-10,16] mm region, while the resolutions ( $\sigma_{x,y,z}$ ) improve (i.e. decrease) from about 150 mm to about 60 mm as the PPO concentration increases. The cause of this improvement in resolution is the higher light yield of the liquid scintillator with increasing PPO concentration, resulting in events causing larger NHits values and thus more information for the fitter. However, the improvement from the 2 g/L case to the 6 g/L case is small, indicating a saturation effect for the PPO concentration above 2 g/L.

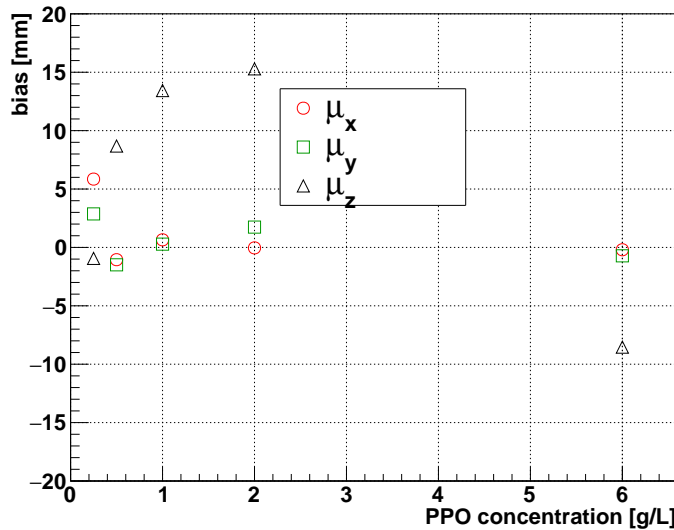


Figure 4.34: Fit position biases against the PPO concentrations.

If using a timing PDF with the wrong PPO concentration for the reconstruction, the effect on reconstruction is small [166]. I simulated 3-MeV  $e^-$  uniformly distributed in the LAB+0.25 g/L PPO scintillator with isotropic directions and then reconstructed the events by using the timing PDFs for 0.5, 1, and 2 g/L PPO (higher concentrations) respectively. All of these reconstructions gave fitted positions close to the correct reconstruction using the 0.25 g/L timing PDF, with fit biases of about 5 mm on the three axes. On the other hand,



Figure 4.35: Fit position resolutions against the PPO concentrations.

by repeating the simulations but with LAB+2 g/L PPO and then reconstructing using the timing PDFs of 0.25, 0.5, and 1 g/L PPO (lower concentrations) respectively, I found the fit biases were still around 5 mm. This indicates that the fit provided by the MP `scint-water fitter` is indifferent to changes in PPO concentration. The implication is that if the true PPO concentration in the detector were slightly different from the nominal value assumed for reconstruction, the effect on the reconstruction would not be very significant.

#### 4.4.4 Test on Bi-Po Simulations

Thorium-232 ( $^{232}\text{Th}$ ) and Uranium-238 ( $^{238}\text{U}$ ) are the two major internal contaminating isotopes (backgrounds) in the liquid scintillator. The amounts of these two backgrounds can be evaluated by a technique called “Bi-Po analysis”, which hinges on tagging the  $^{212}\text{Bi}$ - $^{212}\text{Po}$  event pairs from the  $^{232}\text{Th}$  decay chain and the  $^{214}\text{Bi}$ - $^{214}\text{Po}$  event pairs from the  $^{238}\text{U}$  decay chain. This analysis is one of the crucial physics studies during the partial-fill phase. Here I tested the MP `scint-water fitter` on simulations of  $^{214}\text{Bi}$ - $^{214}\text{Po}$  events in the detector with the LAB+0.5 g/L PPO and the interface at 4.5 m. In the  $^{238}\text{U}$  decay chain,  $^{214}\text{Bi}$  undergoes a  $\beta^-$  decay, which can trigger a prompt event [130]; its daughter  $^{214}\text{Po}$ , with a half-life of 164.3  $\mu\text{s}$ , goes through  $\alpha$  decay, and this can trigger a delayed

event. Applying proper cuts on the position and time differences between the prompt and delayed events can effectively tag (identify) these  $\beta - \alpha$  event pairs due to the  $^{214}\text{Bi}$ - $^{214}\text{Po}$  decay sequence, allowing to evaluate the  $^{238}\text{U}$  level. An optimized algorithm was developed by the collaboration [120], and a flowchart for picking the event pairs is shown in Fig. C.1 in Appendix. C.1.

This tagging algorithm was applied to reconstructed event vertices. Fig. 4.36 shows the distributions of NHits for the tagged  $^{214}\text{Po}$  and  $^{214}\text{Bi}$  events. A clear and relatively narrow single peak shows the  $\alpha$  events from the  $^{214}\text{Po}$  alpha-decay, and a wider and continuous spectrum shows the  $e^-$  events from the  $^{214}\text{Bi}$  decay. Fig. 4.37 shows the biases between the MC and the reconstructed positions, projected onto the  $z$ -axis. Fit errors on the three axes were fitted with Gaussians to obtain the biases and resolutions, which are listed in Table 4.7. These results indicate that the fitter's performance is acceptable for the Bi-Po analysis in the partial-fill.

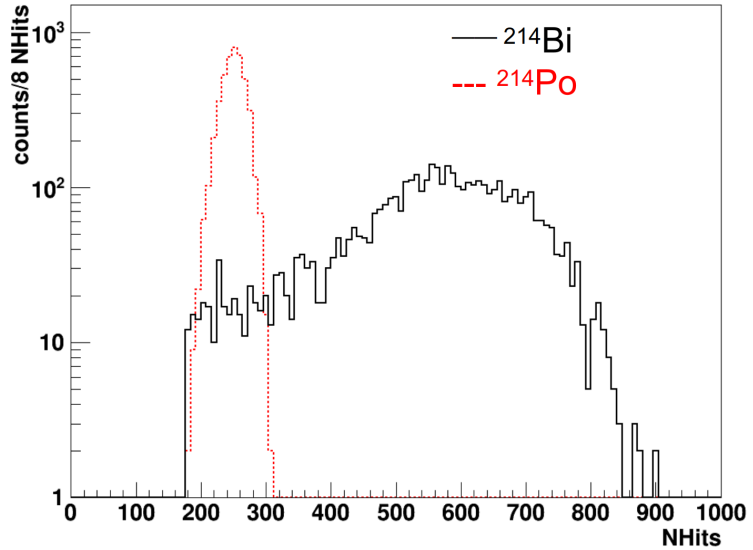


Figure 4.36: Distributions of NHits for the tagged  $^{214}\text{Po}$  (dashed red line) and  $^{214}\text{Bi}$  (solid black line) events.

#### 4.4.5 Discussions for the Partial Fitter

It was suggested by the SNO+ collaboration that I attempt to use the `MP scint-water fitter` to determine the water/scintillator interface level [167]. For this purpose the water

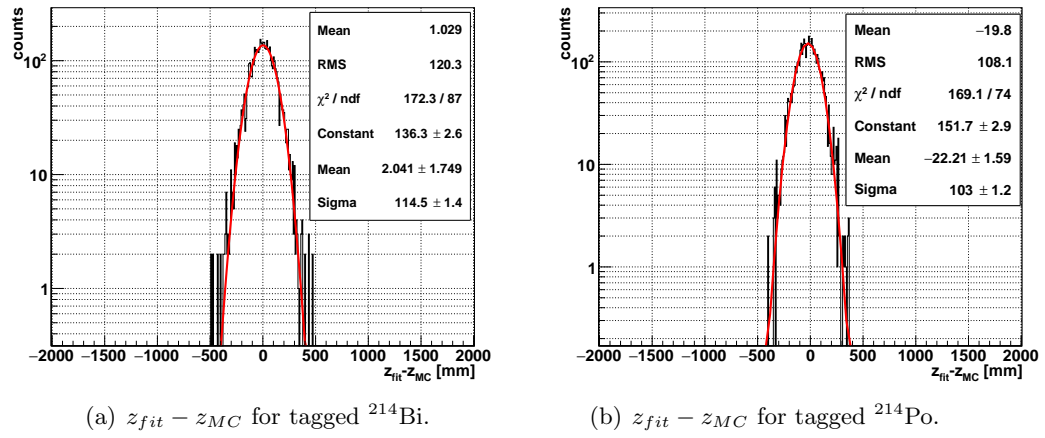


Figure 4.37: Fit position biases for tagged  $^{214}\text{Bi}$  (left) and  $^{214}\text{Po}$  (right).

Table 4.7: Fit position biases and resolutions for the  $^{214}\text{Bi}$ - $^{214}\text{Po}$  tagging. Unit: mm.

Tagged isotope	$\mu_x \pm \sigma_x$	$\mu_y \pm \sigma_y$	$\mu_z \pm \sigma_z$
$^{214}\text{Bi}$	$-7.657 \pm 127.2$	$-2.071 \pm 129.6$	$2.041 \pm 114.5$
$^{214}\text{Po}$	$-0.695 \pm 128.5$	$-0.1355 \pm 129.3$	$-22.21 \pm 103.0$

level ( $Z_{\text{water}}$ ) is considered as an additional fit parameter so that the **MP fitter** fits for *five* parameters:  $(x, y, z, t, Z_{\text{water}})$ . The bias between the true  $Z_{\text{water}}$  and the reconstructed value was fitted with a Gaussian, from which a bias of 40 mm and a resolution of 492 mm were deduced. The fit resolution for  $Z_{\text{water}}$  is much larger than the event position resolution, so this method is not good enough to be applied to the analysis.

The reconstructed vertices of certain events, such as the  $^{214}\text{Bi}$ - $^{214}\text{Po}$  event pairs, can be used to calculate the time residual distribution, which is taken as the time profile caused by the  $e^-$  or  $\alpha$  particles in the liquid scintillator. By extracting the characteristic time constants from the time profile, the quality and optical properties of the liquid scintillator can be obtained. This analysis has been applied by the collaboration on the partial-fill data [168, 169].

To process the partial-fill data, the water level set in the **MP scint-water fitter** is intentionally moved down by 150 mm (a few centimeters larger than the resolution at 3 MeV) from the nominal water level. This was done to include some events mis-reconstructed in the water region, and then to include more events for a conservative background estimation

for the liquid scintillator.

To improve the performance of the `MP scint-water fitter`, two points have been suggested by the collaboration. They have not been applied or tested in this thesis, but they are worth future investigation:

- The timing PDFs used by the `MP scint-water fitter` were obtained from bench-top measurements and the derivatives of the PDFs are calculated numerically. However, the PDFs can be expanded and fitted with suitable (e.g. Chebyshev) polynomials to obtain an analytic approximation function to describe the PDF [155]. Then the analytical function can give proper and smooth analytical derivatives, which may reduce the time cost of calculating the likelihoods using the numerical methods.
- To refine the reconstruction algorithms by accounting for refracted and reflected light paths. Currently, possible event-PMT paths that entail refraction and/or reflection *are neglected*, to simplify the calculations, and the `MP scint-water fitter` (also the `MP scint fitter` to be discussed in the next section) simply uses the straight-line light paths from the event position to the hit PMTs. However, it obviously would be more realistic to account for the refracted and reflected light paths, since such paths necessarily exist due to the interface between the two different optical media, the water, and the liquid scintillator. The Fresnel equations can be used for calculating the possibilities of these light paths [3], although such calculations are complicated. Also, the influence on photon paths of the 5-cm thick AV, which is another optical medium, is totally neglected by the fitter. To take this into account, three different boundaries of optical media would have to be considered in calculations for refracted and/or reflected light paths, which is a complicated proposition. In this case, a trade-off between the accuracy & precision of the reconstruction versus CPU time consumption comes into play.

## 4.5 Vertex Reconstruction for the Scintillator Phase

As mentioned in the previous section, the procedure for vertex reconstruction for the scintillator phase is similar to that for the partial-fill case, while no water-scintillator interface

is considered here since the AV is fully filled with liquid scintillator. Only the ray-sphere and ray-cylinder intersections are calculated and thus the major code of the **MP scint fitter** was modified directly from the **MP scint-water fitter** by removing the ray-plane intersection calculations.

#### 4.5.1 Performance of the Vertex Reconstruction

Since a 2.5 MeV event is the signal of major interest in the scintillator and tellurium-loading phases, a few tests were focused on this energy. Simulations of 10,000 2.5 MeV  $e^-$  events were generated at random positions inside the AV, and with isotropic directions. Fig. 4.38 shows the distributions of the position biases between the reconstruction and the MC truth. These distributions were fitted with Gaussians to obtain the mean error or bias ( $\mu$ ) and resolution ( $\sigma$ ). It can be seen that the fit position biases lie within the region of  $[-2, 2]$  mm, while the resolutions are better than 70 mm on all axes:  $\mu_{x,y,z} \in (-2, 2)$  mm and  $\sigma_{x,y,z} < 70$  mm.

A test of the quality of vertex reconstruction versus event radial position was performed, and this was similar to the tests in the Sect. 4.2.7. In simulations, 2.5 MeV  $e^-$  were generated within each of eleven thin concentric shells. Fig. 4.39 and Fig. 4.40 respectively show the biases ( $\mu$ ) and resolutions ( $\sigma$ ) as a function of radius: for all values of event radial position ( $R$ ),  $\mu_{x,y,z} \in (-10, 5)$  mm and  $\sigma_{x,y,z} < 70$  mm.

For other energies (from 1 to 10 MeV), the Gaussian means and resolutions of the fit position biases are shown in Fig. 4.41 and Fig. 4.42. For the 1 MeV  $e^-$  event, the  $\sigma_{x,y,z}$  are below 85 mm. These resolutions are slightly better than the Borexino spatial resolution of  $\sigma_{x,y,z} \sim 110$  mm for a 1 MeV electron at the detector center [51].

### 4.6 Multi-Path Fitter Structure for Multiple SNO+ Physics Phases

The **MP fitter** has already been implemented into the **RAT** software for data processing and analysis. Following the **RAT** event reconstruction structure, the **MP fitter** is suitable for multiple SNO+ physics phases.



Figure 4.38: The fit position biases projected on the  $x$ ,  $y$  and  $z$  axes, for 2.5-MeV  $e^-$  events in full scintillator simulations. The distributions were fitted with Gaussian functions.



Figure 4.39: The Gaussian biases ( $\mu$ ) of the MP `scint fitter` fit position biases as a function of radius, for the  $x$ -(red circle),  $y$ -(green square), and  $z$ -(black triangle) axes.



Figure 4.40: The Gaussian resolutions ( $\sigma$ ) of the MP `scint fitter` fit position biases as a function of radius, for the  $x$ -(red circle),  $y$ -(green square), and  $z$ -(black triangle) axes.

The MP `fitter` first loads the fitter database, which contains the parameters used by the fitter. Parameters include the physical constants (e.g., speed of light); geometrical parameters of the detector (e.g.,  $r_{PSUP}$ , length of neck, water level); fitter setting parameters



Figure 4.41: The Gaussian means ( $\mu$ ) of the MP scint fitter fit position biases as a function of energy, for the  $x$ -(red circle),  $y$ -(green square), and  $z$ -(black triangle) axes.



Figure 4.42: The Gaussian resolutions ( $\sigma$ ) of the MP scint fitter fit position biases as a function of energy, for the  $x$ -(red circle),  $y$ -(green square), and  $z$ -(black triangle) axes.

(e.g., the effective group velocity, fitter iteration number, etc.); and various optimized PDFs. This collection of parameters (and others not mentioned) is known as the **RAT** database (ratdb), stored in a JSON format [170], and contains tables which are structured by different

indices to indicate specific physics phases or detection media. For example, for the partial-fill phase with a PPO concentration of 0.5 g/L, the fitter extracts the PDFs and fitter setting parameters under the index of “`labppo_0p5_scintillator`”. These fitter setting parameters and PDFs were optimized for the 0.5 g/L PPO partial-fill geometry.

After loading the database the `MP fitter` goes through the event-by-event reconstruction. For a triggered event, it calls PMT selectors and sends the timing and charge information of the selected PMTs to a `Likelihood Calculation Class`. Sect. 4.2.5 will give the details about the PMT selectors. In the `Likelihood Calculation Class`, there are four main likelihood calculation functions <sup>8</sup>: the `WaterVertex` and `WaterDirection` for the event vertex and direction reconstruction in the water phase; the `ScintWaterVertex` for vertex reconstruction in the partial-fill phase; and the `ScintVertex` for vertex reconstruction in the scintillator and tellurium-loading phases.

Reading the detector geometry settings and the assigned index of detection medium, the fitter selects proper likelihood functions to construct the likelihood functions and to calculate the likelihoods and their derivatives by evaluating fit parameters based on different light path calculations in different detector geometries. The calculated likelihoods and derivatives are sent to the MRQ method class to maximize the likelihood and find the best-fit values. The MRQ method class does not “care” about how the likelihood functions had been constructed nor how the likelihoods and derivatives had been calculated.

A `Dump Likelihood Class` stores the trial fit parameters with respect to their likelihoods and derivatives for interesting events, by registering their event GTIDs in the database. For the MRQ method, it is important that the initial estimates lead the results to be somewhere in the neighborhood of the global maximum [154]. A badly fitted result could be caused by the fitter being stuck in a local maximum. By looking at the likelihood surfaces and derivatives of the event of interest, the fit performance for that event can be checked to see whether the fitter finds the global or local maximum. Sect. A.5 shows an example of the dumped likelihood surfaces and derivatives for an  $^{16}\text{N}$  event vertex reconstruction.

---

<sup>8</sup>The `AirWaterVertex` for the early partial water fill test in 2014 and the `WavelengthShifterVertex` for the conceptual wavelength-shifter test, as mentioned in the previous sections, were not included in the current version of `RAT` since they are not used in actual physics phases.

Once the reconstructed results are obtained, the fitter will send them to the classifiers for further analysis, which will be discussed in Chapters 5.

## 4.7 Energy Reconstruction

The SNO+ energy reconstruction algorithms (energy fitters) were based on SNO [152, 171] and have been further developed and optimized [87, 137, 172].

The energy fitters mainly use lookup tables to convert the NHits value of a triggered event into reconstructed energy. The energy fitters used in the water phase are mainly the energy response processor (**EnergyRSP fitter**) [137, 152, 171] and the energy Lookup fitter (**EnergyLookup fitter**) [87, 173]. The **EnergyRSP fitter** is used to reconstruct the events inside the AV (internal events). It considers detailed detector effects, such as the asymmetric geometry of the detector, the optical response of each PMT (including the PMT detection efficiency, transmission probability, attenuation, etc.), and utilizes the reconstructed event positions, directions, and time residuals as inputs to convert the corresponding value of NHits to estimated energy based on simulation models and calibration data. The **EnergyLookup fitter** is simpler and is mainly used to reconstruct events in the cavity water (external events). It mainly uses the lookup table of the NHits dependence on the event reconstructed position from simulations to calculate the energy of the event [87]. For the scintillator phase, a method using a functional form based on simulations was developed by Ref. [173, 174] and is currently used in the **EnergyRThetaFunctional fitter**. All these fitters adapt to the true number of online PMTs for a particular physics run (or called “channel efficiency”).

The resolutions and scales of the reconstructed energies in the water phase were derived from the  $^{16}\text{N}$  calibration scans at certain detector points, a topic that will be covered in Chapter 5.

### 4.7.1 Energy Figure of Merit

The SNO+ Antineutrino working group developed three figure of merit (FoM) quantities for the energy fitters in the water phase to identify poorly reconstructed results which have

significant biases to the truth energy values, especially for the low energy region around 2.2 MeV, which helps the analysis of neutron capture [175, 176]. The following energy FoMs were applied to the energy reconstruction results during the water phase, which will be discussed in the next chapter. Brief descriptions are presented below, while more details can be found in Ref. [176].

- $U$ -test ( $U_{test}$ ): a Mann-Whitney score uses the channel hit probabilities calculated by `EnergyRSP` which are ordered and ranked. `EnergyRSP` calculates the  $N$  as the prompt NHits, and  $N_{active}$  as the total number of active channels. For each active channel, the smallest hit probability assigned rank 1 and largest  $N_{active}$ .  $S$  is a sum of assigned ranks for hit PMTs and  $S \equiv \sum_i^N \text{rank}_i$ .

$$U_{test} \equiv \frac{S - N(N + 1)/2}{N(N_{active} - N)} , \quad (4.18)$$

- $G$ -test ( $G_{test}$ ): a score that uses the hit probabilities from `EnergyRSP` ( $E_i$ ), which are normalized to the number of observed hits ( $N$ ):

$$G_{test} \equiv \frac{1}{N} \sum_{i=1}^N \log\left(\frac{1}{E_i}\right) , \quad (4.19)$$

- $Z$ -factor ( $Z_{factor}$ ): a score that uses the medians and median absolute deviations of hit probabilities from `EnergyRSP`:

$$Z' \equiv 1 - \frac{3(\sigma_p + \sigma_n)}{\mu_p - \mu_n} , \quad (4.20)$$

where  $\mu_p$  is the median probability of all active PMT channels with hits;  $\mu_n$  is the median probability of all active PMT channels;  $\sigma_p$  is the median absolute deviation of hit PMT probability distribution; and  $\sigma_n$  is median absolute deviation of PMT probability distribution.

#### 4.7.2 Energy Reconstruction in Partial-fill Phase

At the time this thesis was written, no suitable energy fitter had yet been provided for the partial-fill phase. Below I will describe two methods that I have investigated for energy reconstruction in the partial-fill phase: the NHits-scale method, based on Ref. [177] and

the NHits-ratio method, based on Ref. [178]. Both methods use look-up tables produced by simulations of  $e^-$  events in the partial-fill geometry, then compare with the case in the full-fill geometry, and scale the energy. Both, however, will need further effort if they are to produce well-defined results [179, 180].

In the NHits-scale method, for an  $e^-$  event at  $(0,0,z)$  with a fixed energy (values of 1 MeV and 2.5 MeV were tested), a scaling factor ( $S$ ) between its NHits value in the partial-fill ( $\text{NHits}_{\text{partial}}$ ) with a water level  $Z_{\text{water}}$  set in the simulation and the NHits value in the full-fill ( $\text{NHits}_{\text{full}}$ ) is defined as

$$S = \frac{\text{NHits}_{\text{partial}} - \text{NHits}_{\text{full}}}{\text{NHits}_{\text{full}}} = 0.33 a_0 (Z_{\text{water}} + 6005)^{2.76} , \quad (4.21)$$

where the final term is an empirical function and the fit parameter  $a_0$  depends on the different event  $z$  positions in the simulations. Then the energy in the partial-fill is found by  $E_{\text{partial}} = E/(1 + S)$  [177, 179].

In the NHits-ratio method, the NHits value of an  $e^-$  event at  $(0,0,0)$  mm in the full scintillator geometry was used as a reference ( $\text{NHits}_{\text{ref}}$ ). By simulating 1 to 10 MeV  $e^-$  events (with a 1 MeV step) in the full-fill geometry with 0.5 g/L PPO, and fitting the NHits to the energies, a converting function between the energy and NHits was found [180]:

$$E_{\text{full}} = f(\text{NHits}) = 0.051 + 0.003 \cdot \text{NHits} + 2.49 \times 10^{-7} \cdot \text{NHits} . \quad (4.22)$$

Then for the partial-fill geometry with a given  $Z_{\text{water}}$ ,  $e^-$  events were simulated at different  $(\rho = \sqrt{x^2 + y^2}, z)$  positions in the AV, with  $\rho$  ranging from 0 to 5500 mm with a step of 500 mm, and  $z$  ranging from -5500 to 5500 with a step of 500 mm (these ranges cover the AV volume of interest). The value of scaled NHits for an event at  $(\rho_0, z_0)$  is found by

$$\text{NHits}' = \text{NHits}_{\text{partial}} / (\text{NHits}(\rho_0, z_0) / \text{NHits}_{\text{ref}}) , \quad (4.23)$$

and finally the partial energy is found as  $E_{\text{partial}} = f(\text{NHits}')$  [180].

## 4.8 Machine Learning and Deep Learning

Nowadays, the vast amount of data available to particle experiments make it feasible to implement machine learning and deep learning methods for data analysis. Chapter 6 will

describe a machine learning method applied to solar neutrino analysis. At the time of writing, a deep learning framework is being developed for reconstruction [181, 182, 183]. This method investigates the relation between the hit PMT distributions and the event reconstruction, currently for the position and direction. It trains neural networks based on information from MC simulation datasets (with  $\mathcal{O}(10^6)$  events) and from calibration datasets, to yield an algorithm that predicts event position and direction [182]. A few physics-based loss functions (or called “cost-functions”), such as the loss function checking the  $t_{\text{res}}$ , can be added to improve the reconstruction performance [182].

Once the neural networks are trained, the reconstruction speed is expected to be from 100 to 1000 times faster than the traditional likelihood-fit method when running on the CPU (Central Processing Unit). In addition, since the deep learning method can utilize the computing power of the GPU (Graphics Processing Unit), it is expected to be  $10^4$  times faster [182, 183]. Such a rapid reconstruction is hoped to be applied in the scintillator phase, for which the existing likelihood-based fitters will be very time-consuming owing to the higher NHits events. The deep learning framework is expected also to aid the data analysis.

## 4.9 Conclusion

The Multi-Path Fitter framework for event vertex reconstruction was developed for multiple SNO+ physics phases. Under this framework, the **MPW fitter** works as an alternative fitter to provide additional reconstruction information for water data, and it gives good position and direction resolution for the water analysis. The **MP scint-water fitter** works as the prime vertex fitter for the SNO+ partial-fill phase, which is crucial to the physics analyses during the partial-fill phase.

## Chapter 5

# Calibration

A detailed description of the SNO+ detector has been implemented in the `RAT` software package for Monte Carlo (MC) simulations, as mentioned in Chapter 3. However, when the simulations are compared to the real world, there always exist discrepancies. To make precise measurements, calibration sources were implemented in the SNO+ detector during the water phase and the partial-fill phase. During the water phase, the  $^{16}\text{N}$  source (described in Sect. 3.5.1) was used for the primary detector calibration. The  $^{16}\text{N}$  calibration data ( $^{16}\text{N}$  runs) were mainly used to check the performance of the reconstruction algorithms for event position, direction, and energy.

In this chapter, the `MPW fitter` (described in Sect. 4.2) was applied to both the experimental data from, and simulations of, the  $^{16}\text{N}$  runs in the water phase. By analyzing the differences between the  $^{16}\text{N}$  data and corresponding MC simulations, systematics of the position and direction reconstruction were extracted, and these were used in the solar neutrino analysis of Chapter 6. The event energy was reconstructed by the SNO+ energy fitter for the water phase (described in Sect. 4.7), which utilizes the `MPW fitter`'s event vertex and direction. Also, based on the `MPW fitter`'s reconstructed vertex and direction, other parameters, such as the in-time ratio (ITR) and the isotropy parameter ( $\beta_{14}$ ) were calculated.

## 5.1 $^{16}\text{N}$ Calibration Scans in the Water Phase

During the water phase, in June and in November 2017 the  $^{16}\text{N}$  source was deployed at different positions inside the AV to perform internal calibration scans, and in March 2018 it was deployed at various positions in the external water region between the AV and the PSUP to perform external scans. For each  $^{16}\text{N}$  run, the source was placed at a fixed position, and data were collected for about 20 minutes (with the exception of run 107055 with the source at PSUP center, for which run time was 1 hour). For some of the internal scans, the source was moved along  $(x, y, z)$ -axes (these scans being named “ $X, Y, Z$  scans” in this thesis), and in other internal scans, it was moved diagonally across the AV and placed at the corners of the inner AV (“corner scans”). For the external scans, the source was placed in the external water region outside the AV. The source was moved along the  $z$ -axis with a fixed  $(x, y)$  position close to the AV, at  $(-5861.0, -2524.0)$  mm. Fig. 5.1 shows the different positions of the source deployment. In this thesis, 79 internal scan runs were used. Details of the calibration runs are listed in the tables in Appendix. B.1.

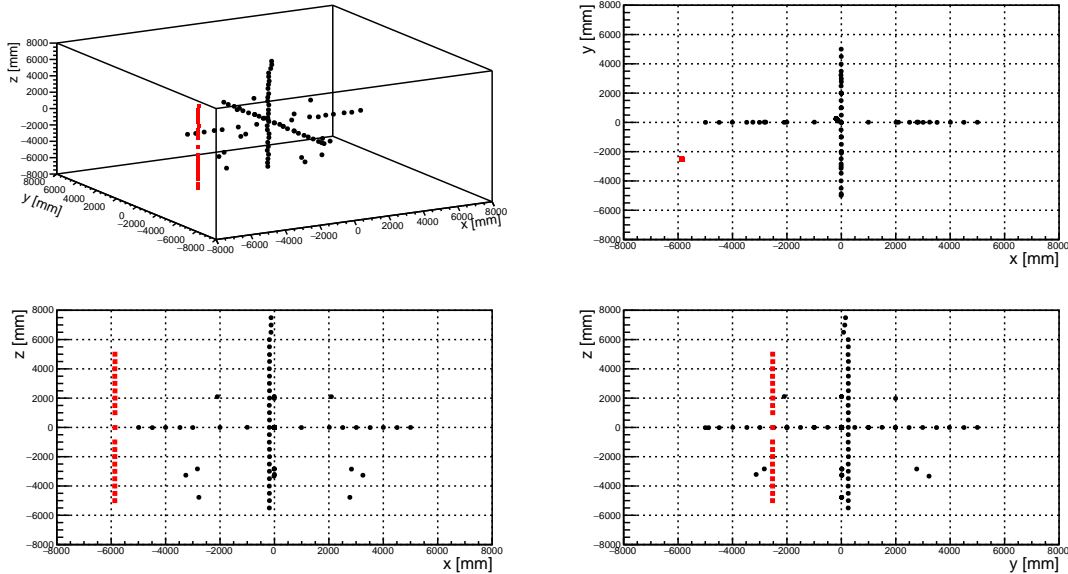


Figure 5.1: The deployed source positions of the  $^{16}\text{N}$  scan runs used by this thesis. The black dots are internal runs while the red squares are external runs.

The  $^{16}\text{N}$  calibration runs provide an ideal test of fitter performance. From a comparison

of reconstructions for data and MC, we can extract the resolution and bias of the fitter. Here I determined the performance of both the `RAT water fitter` and the `MPW fitter` for vertex and direction reconstruction, characterizing that performance in terms of statistics pertaining to vertex shift (or offset), and uncertainty.

When analyzing  $^{16}\text{N}$  run data and simulations, an FECD tag cut (FECD== 9188) was applied during data processing, to save the events only when the source trigger fired. A reconstruction threshold ( $\text{NHits} > 5$ ) was applied to the MC and data. In addition to these cuts, high level cuts based on classifiers were used.

## 5.2 High Level Cuts for the Water Phase

A set of (event-) classifiers, developed originally for the SNO analysis, have been adjusted and optimized for the SNO+ water phase analysis [184]. These event classifiers utilize reconstructed quantities, so they always require a valid reconstruction.

- In-time ratio (ITR) classifier

For each event, this classifier loops through the triggered PMTs (hits), calculates  $t_{res}$  for each, and determines the fraction of hit PMTs for which  $t_{res}$  falls within an optimized “prompt time window”. In the water phase, the time window was  $[-2.5, 5.0]$  ns. If the ITR is too low for an event, a large proportion of the hit PMTs was not triggered prompt light, suggesting that the event probably did not originate from Cherenkov light; it could be instrumental noise or caused by a large amount of light reflecting off detector components (called “late light”).

- $\theta_{ij}$  isotropy classifier

This classifier describes the angle subtended at an event vertex by PMT #i and PMT #j, as defined by:

$$\cos \theta_{ij} = \frac{(\vec{X}_{PMT\#i} - \vec{X}_{\text{event}}) \cdot (\vec{X}_{PMT\#j} - \vec{X}_{\text{event}})}{|\vec{X}_{PMT\#i} - \vec{X}_{\text{event}}| |\vec{X}_{PMT\#j} - \vec{X}_{\text{event}}|}. \quad (5.1)$$

- $\beta_{14}$  isotropy classifier

This classifier is derived from the event’s *set* of angles  $\theta_{ij}$ . The first ( $\beta_1$ ) and the fourth ( $\beta_4$ ) spherical harmonics of an event are determined from

$$\beta_l = \frac{2}{N(N-1)} \sum_{i=1}^{N-1} \sum_{j=i+1}^N P_l(\cos \theta_{ij}), \quad (5.2)$$

where  $N$  is the selected NHit used by the reconstruction (see Sect. 4.2.6), and the  $P_l(\cos \theta_{ij})$  are Legendre polynomials, and (following the precedent of the SNO collaboration) the linear combination  $\beta_{14} = \beta_1 + 4\beta_4$  is taken. For a set of events produced by Cherenkov light, the corresponding set of values of  $\beta_{14}$  has a Gaussian-like distribution [185]. In principle, any systematic deviation of  $\beta_{14}$  from zero suggests some polarity or a deviation from a totally isotropic pattern.

### 5.2.1 Effects of the High Level Cuts

As described above, the classifiers can help to distinguish the physical events from Cherenkov events and nonphysical events from non-Cherenkov events, such as instrumental noises. To remove the non-Cherenkov background events such as instrumental noises, cuts of  $ITR > 0.55$  and  $-0.12 < \beta_{14} < 0.95$  (termed “high level cuts”) were suggested by the collaboration [176]. These cuts are based on the analysis of simulated physics events, as well as the experience gathered by the SNO collaboration [176, 185, 186].

The  ${}^{16}\text{N}$  central run 107055 data and (corresponding) MC simulation, both reconstructed by the **MPW fitter** and the energy fitter, were used to check the effects of the high level cuts. For the MC (data), the cut  $ITR > 0.55$  removed 0.69% (0.79%) of the total events and the cut  $-0.12 < \beta_{14} < 0.95$  removed 1.11% (0.93%) of the total events. Combining the  $ITR$  and  $\beta_{14}$  cuts, 1.69% (1.62%) of the total events were removed.

Poorly reconstructed events with large position bias ( $> 6000$  mm) were counted as “outlier events”. For the MC case, the position biases were taken as the distance between the reconstructed position and the true (MC) position,  $|\vec{X}_{fit} - \vec{X}_{MC}|$ . For the data, however, the bias was taken as the difference between the reconstructed position and the source manipulator position,  $|\vec{X}_{fit} - \vec{X}_{src}|$ <sup>1</sup>. The outlier events with (so-defined) bias exceeding

---

<sup>1</sup>The source manipulator position is mainly measured by the ropes in the source manipulator system described in Sect. 3.5.



Figure 5.2: Position biases vs ITR (top) and  $\beta_{14}$  (bottom) for the  $^{16}\text{N}$  central run 107055. Left panels are data and right are MC. For the data, the offset of a reconstructed vertex was defined relative to the source position ( $\vec{X}_{src}$ ).

6000 mm made up 0.13% of the total event count, both in the MC and experimental calibration data. The high level cuts removed 73.12% (66.82%) of these outliers from the population of MC (data) events. In summary, the high level cuts remove more than half of the events having large (reconstructed) position offset, while removing only about 1.6% of the total events.

Fig. 5.2 shows the relations between the position biases and the ITR,  $\beta_{14}$  respectively, for the MPW results from the data and MC.

Fig. 5.3 shows the relations between the reconstructed energies ( $E_{fit}$ ) and  $\beta_{14}$  values from  $^{16}\text{N}$  central run 107055, comparing the MPW and RAT results from the data and MC, respectively<sup>2</sup>.

<sup>2</sup>Note that the MPW and the RAT results used the same energy fitter, while there are still differences in the reconstructed energies since the energy fitter utilizes the different reconstruction results of vertex and direction.

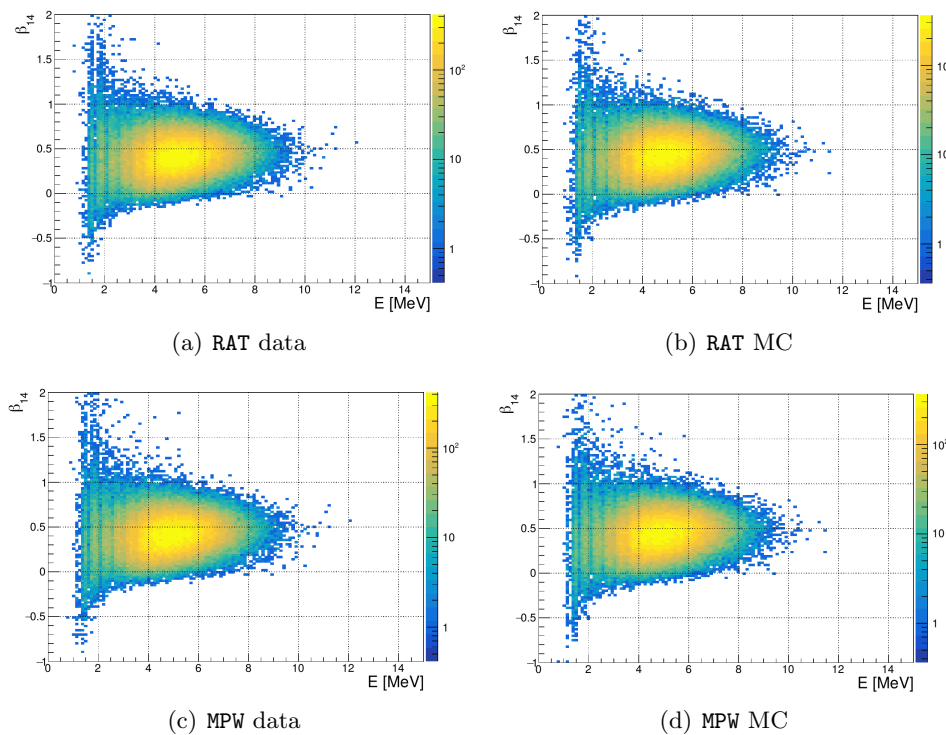


Figure 5.3:  $E_{fit}$  vs  $\beta_{14}$  for the data and MC. Both the RAT (a, b) and the MPW (c, d) results are shown.

## 5.3 Quality of Event Reconstruction Judged by $^{16}\text{N}$ Calibration Scans in the Water Phase

In this section, by analyzing the  $^{16}\text{N}$  data and corresponding simulations in the water phase, I extracted the resolution of the reconstruction algorithm for event position, direction, and energy. Then by comparing the data with the MC, the reconstruction systematics were evaluated.

To do these evaluations, a few cuts were applied to both the data and MC. Firstly, the high level cuts ( $\text{ITR} > 0.55$ ,  $-0.12 < \beta_{14} < 0.95$ ) were applied. For events having valid position, direction, and energy reconstructions, further cuts on the reconstruction figure of merit (FoM) and source geometry (to be described in detail below) were applied, to ensure that the analyzed events were nicely reconstructed physics events caused by  $\gamma$  photons (that originated in the source) interacting with the detector water.

### 5.3.1 Position Reconstruction Evaluation

The position figure of merit (posFoM) cuts mentioned in Sect. 4.2.6 were applied to the reconstruction results. Fig. 5.4 shows the  $\text{scaleLogL}$  with the position biases for the reconstructed events in the  $^{16}\text{N}$  central calibration run 107055. Results from both the data and the MC simulations are shown. For the MC case, the position biases are between the reconstructed positions and the true positions generated by the MC,  $|\vec{X}_{\text{fit}} - \vec{X}_{\text{MC}}|$ , while for the data, the biases are between the reconstructed positions and the source manipulator position,  $|\vec{X}_{\text{fit}} - \vec{X}_{\text{src}}|$ .

For the MC (data) case, about 0.035% (0.043%) of the total reconstructed events have large biases ( $|\vec{X}_{\text{fit}} - \vec{X}_{\text{MC}}| > 6000$  mm). A cut of  $\text{scaleLogL} > 10$  removes 96.0% (97.3%) of the events which have biases over 6000 mm, with a sacrifice of removing 0.012% (0.016%) of the total events.

Fig. 5.5 shows a relation between the  $\text{scaleLogL}$  and the reconstructed energy ( $E_{\text{fit}}$ ). Events with reconstructed energies below the water solar neutrino analysis threshold of 3.5 MeV ( $E_{\text{fit}} < 3.5$  MeV) are mostly coming from the U/Th isotopes, decays of Potassium, and instrument noise [176]. Their lower energy (or NHits) negatively impacts the quality

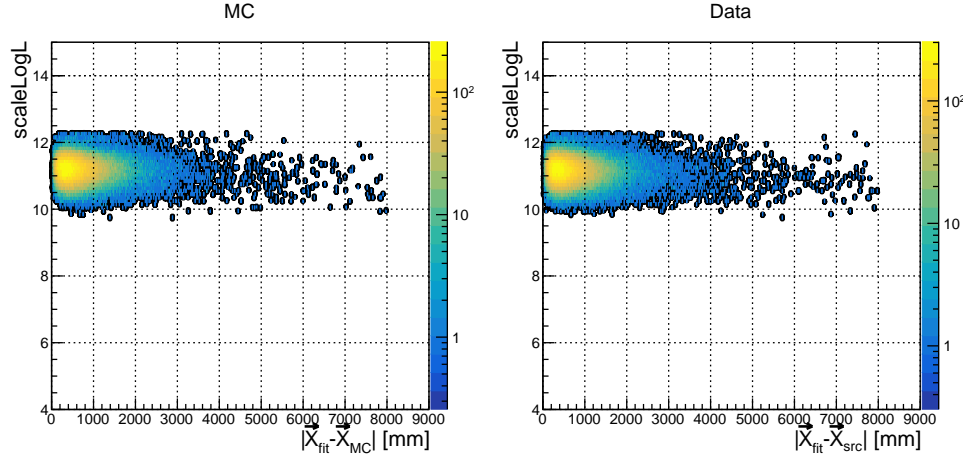


Figure 5.4: Position biases ( $|\vec{X}_{fit} - \vec{X}_{MC}|$ ) vs  $scaleLogL$  for the  $^{16}\text{N}$  central run 107055. Left is MC and right is data. For the data, the offset of a reconstructed vertex was defined relative to the source position ( $\vec{X}_{src}$ ).

of position reconstruction because there are fewer hit PMTs providing information, so it is not unexpected that their *posFoM* would be worse. In the MC (data) case, about 13.04 % (12.89%) of the events had  $E_{fit} < 3.5$  MeV. By applying a  $scaleLogL > 10$  cut, proportions of 0.10% (0.09%) of such events were removed.

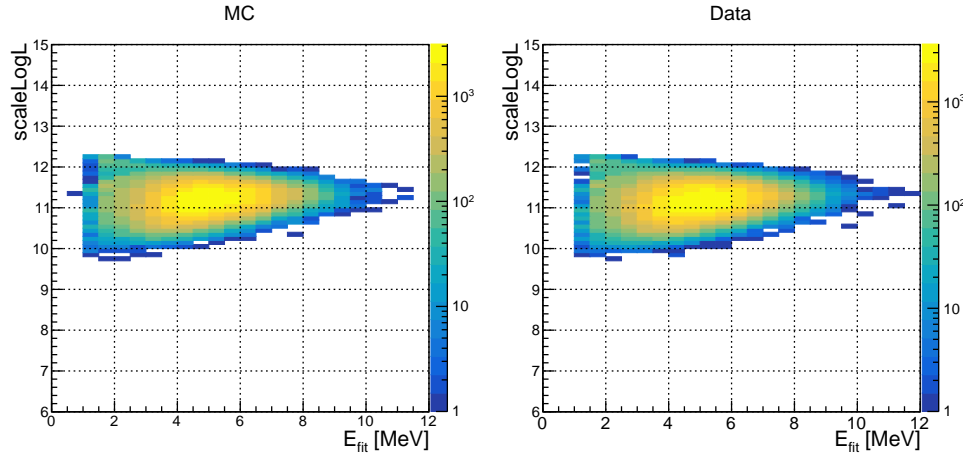


Figure 5.5: Reconstructed energy vs  $scaleLogL$  for the  $^{16}\text{N}$  central run 107055. Left is MC and right is data.

As a summary, about 0.04% of the events were poorly reconstructed (i.e. were misreconstructed) by the MPW fitter, resulting in a position error of over 6 meters. Applying

a cut to *posFoM* with *scaleLogL* > 10 can remove over 96% mis-reconstructed events. This *posFoM* cut was used in the following direction and energy reconstruction evaluations.

### 5.3.1.1 Position Resolution

A position resolution function is defined for the reconstructed electron position distribution [152]:

$$R(x) = \frac{1 - \alpha_e}{\sqrt{2\pi}\sigma_p} \exp\left[-\frac{1}{2}\left(\frac{x - \mu_p}{\sigma_p}\right)^2\right] + \frac{\alpha_e}{2\tau_p} \exp\left[\frac{-|x - \mu_p|}{\tau_p}\right], \quad (5.3)$$

where  $\alpha_e$  is the fractional exponential component,  $\sigma_p$  is the Gaussian width (corresponding to the position resolution),  $\mu_p$  is the Gaussian shift (corresponding to the position bias) and  $\tau_p$  is the exponential slope (corresponding to the position distributions in tails).

The  $\gamma$ -rays emitted from the  $^{16}\text{N}$  source interact with the water in the detector mainly via Compton scattering, as shown in Fig. 5.6. The position distribution of the  $\gamma$  interaction vertices (i.e. locations where electrons undergo scattering and are set in motion, producing Cherenkov light) encircles the source container and extends out to a radius of about 2 meters. Fig. 5.7, obtained from MC simulation, shows the spatial distribution  $S(x)$  of the *first*  $\gamma$ -ray interaction positions (first Compton scatter) projected onto the  $x$ -axis. Therefore, the  $^{16}\text{N}$  source can be treated as an *electron* source having a known spatial distribution [152]. For simplicity, in the following, we always discuss the  $x$  component of the position vector  $\vec{X}$ .

The spatial distribution function  $N_R(x)$  for electrons from the  $^{16}\text{N}$  calibration source can be described by the convolution of the position resolution function with  $S(x)$  [152],

$$N_R(x) = \int_{-\infty}^{+\infty} S(x) R(x_{fit} - x) dx. \quad (5.4)$$

The values of  $N_R(x)$  can be calculated bin by bin from histograms of  $S(x)$  and  $R(x)$  extracted from the MC or data,

$$N_R(x_i) = \sum_{x_i=-\infty}^{+\infty} S(x_i) R(x_{fit}^i - x_i). \quad (5.5)$$

Then the  $\chi^2$  statistic is calculated,

$$\chi^2 = \sum_{i=0}^{N_{bins}} \left[ \frac{N_R(x_{fit}^i) - N_R^{fit}(x_{fit}^i)}{\sigma_i} \right]^2, \quad (5.6)$$

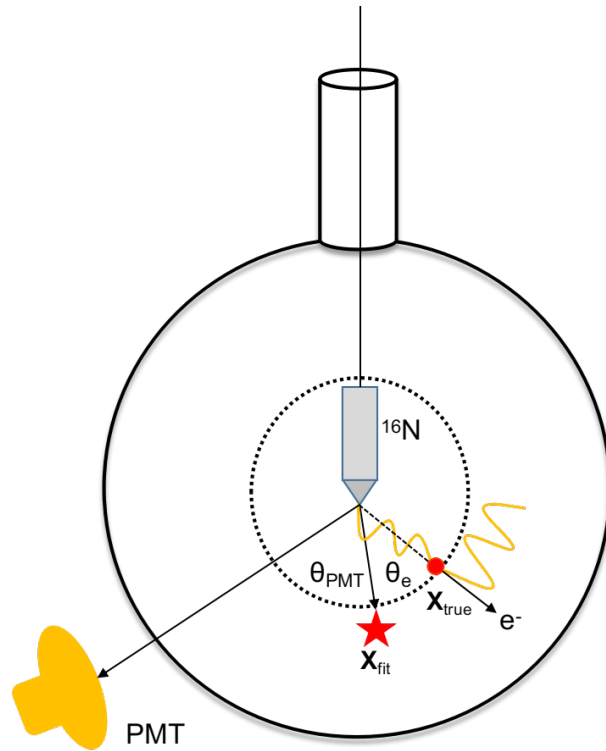


Figure 5.6: Schematic of the  $^{16}\text{N}$  source (not drawn to scale), showing the Compton scattering of a  $\gamma$  emanating from the source. The radius of the dashed circle is about 2 m.



Figure 5.7: Spatial distributions of  $^{16}\text{N}$   $\gamma$ -ray's first interaction position, projected onto the  $x$ -axis, obtained from the RAT simulations. The double-peak structure is due to the wall of the stainless steel container of the  $^{16}\text{N}$  source.

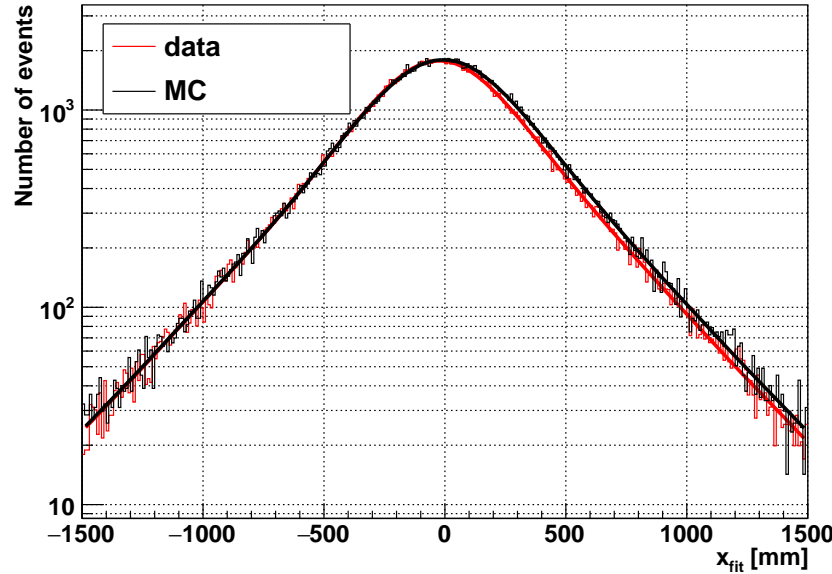


Figure 5.8: Distributions of the reconstructed position projected onto the  $x$ -axis, obtained from the SNO+  $^{16}\text{N}$  central run data (red) and MC (black). The distributions are fitted with  $N_R^{\text{fit}}$  (red and black lines).

where  $N_R^{\text{fit}}$  is a trial fit to the  $N_R$  obtained by tuning  $(\alpha_e, \mu_p, \sigma_p, \tau_p)$ , and  $\sigma_i$  is obtained from the bin width of the histograms. By minimizing  $\chi^2$ , the parameters  $(\alpha_e, \mu_p, \sigma_p, \tau_p)$  of the resolution function, and a best  $N_R^{\text{fit}}$ , were obtained. Fig. 5.8 shows a comparison of the reconstructed  $x$  position of  $^{16}\text{N}$  events between data and MC. The reconstructed position distributions were fitted with  $N_R^{\text{fit}}$ .

Table 5.1 summarizes the values of position resolution parameters (for the  $x$ -axis) obtained from data and MC of  $^{16}\text{N}$  calibration runs at the detector center.

Table 5.1: Position resolution parameters for the MPW fitter ( $x$ -axis).

MPW fitter	$\alpha_e$	$\sigma_P$ (mm)	$\tau_P$ (mm)	$\mu_P$ (mm)
data	$0.58 \pm 0.04$	$175.8 \pm 3.8$	$288.0 \pm 5.7$	$-28.8 \pm 1.0$
MC	$0.51 \pm 0.05$	$195.2 \pm 3.3$	$298.4 \pm 6.1$	$-10.9 \pm 1.0$

### 5.3.1.2 Position Systematics

To evaluate the position uncertainties, the MC and data runs of the  $^{16}\text{N}$  internal scans along  $(x, y, z)$  axes were taken to evaluate the  $(x, y, z)$  position uncertainties respectively (the runs are listed in Table B.1 to B.3. Three neck runs in the  $z$ -scan were not used). The high level cuts mentioned earlier, as well as the  $E_{fit} > 3.5$  MeV and  $scaleLogL > 10$  cuts, were applied. The fit range was set as  $[X_{\text{source}} - 2000, X_{\text{source}} + 2000]$  mm, where  $X = (x, y, z)$  for the scans along  $(x, y, z)$  axes respectively. This is because, recall, most of the source  $\gamma$ 's have their first Compton scatter – knocking an  $e^-$  into motion – within that distance from the source. If the value of  $(X - 2000)$  mm was smaller than -6000 mm, it was set to -6000 mm; if the  $(X + 2000)$  mm was larger than 6000 mm, it was set to +6000 mm. This was used to remove the AV effects, mainly the AV lensing and the material boundaries which distort the reconstruction performances, as mentioned in Chapter 4.

The position resolution function was first fitted with four free parameters,  $(\alpha_e, \mu_p, \sigma_p, \tau_p)$ . The average values of  $\alpha_e$  and  $\tau_p$  were calculated from all the scan runs used here and then, to simplify the calculation in propagating systematics, those average values<sup>3</sup> were assigned as constant values:  $\alpha_e = 0.5288$  (0.5375) for the MC (data) and  $\tau_p = 271.738$  (263.735) for the MC (data). With the fixed values of  $\alpha_e$  and  $\tau_p$ , both the data and the MC were refitted to optimize  $\mu_p$  and  $\sigma_p$  only.

Fig. 5.9 shows the fitted results for  $\mu_P$  and  $\sigma_P$  along the  $(x, y, z)$ -axes scans respectively. For the sake of simplicity, for the  $x$ -scan case, only the  $x$ -axis results  $(\mu_{P,x}, \sigma_{P,x})$  are shown here. Similarly, only the  $\mu_{P,y}$  and  $\sigma_{P,y}$  ( $\mu_{P,z}$  and  $\sigma_{P,z}$ ) are shown for the  $y$ -scan ( $z$ -scan). The relative differences discussed later consider all three axes.

Fig. 5.9 shows that the resolution for vertex reconstruction is generally better for the MC simulations than for the detector data. This is not unexpected, because of the non-uniformities of the detector in realistic situations (as opposed to the idealizations inherent in the MC simulation) [176]. Also, when the source is close to the AV or at the ends of the axes, the Gaussian shift  $\mu_P$  becomes large and the resolution worsens, which causes the difference between the MC and data to become large.

---

<sup>3</sup>Using fixed values for  $(\alpha_e, \tau_p)$  is justified by the fact that these parameters in principle can be viewed as corrections to the spatial distribution of the  $\gamma$ 's ( $S(x)$ ) that would not depend on position [176].



Figure 5.9: The fitted values of  $\mu_P$  (top) and  $\sigma_P$  (bottom) along  $x$  (left),  $y$  (middle) and  $z$  (right) scans. The source positions in each set of scans are projected onto  $(x, y, z)$  axes respectively. The MC results (red circles) are compared with the data (black boxes).

To quantify the discrepancies between the MC and data, a relative difference of  $\sigma_p$  between the MC and data is defined as [176]

$$\sigma_{p,\delta} \equiv \sqrt{\sum_i |(\sigma_{P,i}^{data})^2 - (\sigma_{P,i}^{MC})^2|} \quad (i = x, y, z), \quad (5.7)$$

Fig. 5.10 shows that  $\sigma_{p,\delta}$  varies along the internal  $(x, y, z)$ -axis scans. All the  $\sigma_p$  values are smaller than 190 mm, except for that with the source at  $z = 4973.567$  mm (run 106979) and (therefore) in proximity to the neck of the AV, whose presence probably is responsible for the anomaly. Looking at the pattern in Fig. 5.10 we see that  $\sigma_p$  is larger (worse) when the source is close to the AV (i.e. at the end of the position axes) and that when the source is close to the *center* of the AV, the differences are below 100 mm.

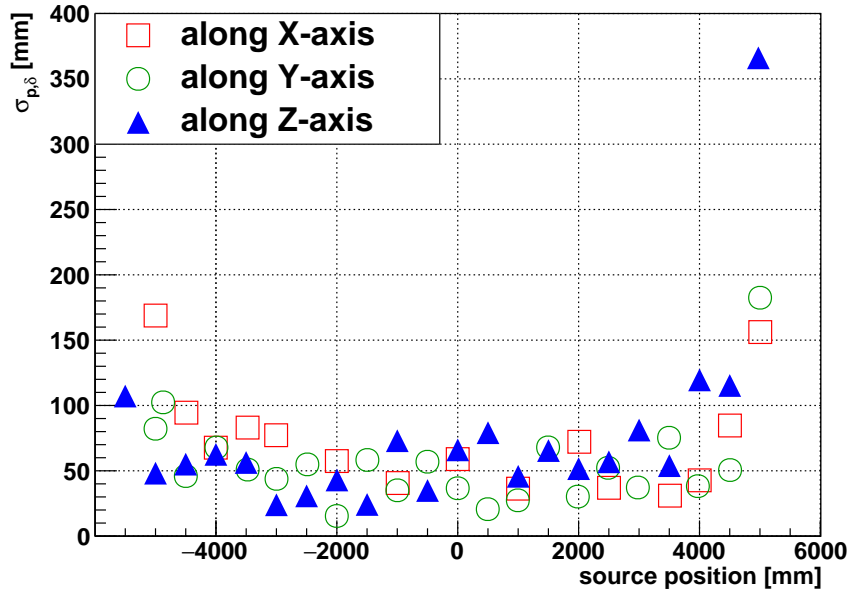


Figure 5.10: Relative differences of  $\sigma_P$  ( $\sigma_{p,\delta}$ ) as a function of the  $^{16}\text{N}$  source position. For simplicity, the corner scans are not shown in this figure. The red squares represent the results from the  $x$ -scan runs; green circles represent the  $y$ -scan runs and the blue triangles represent the  $z$ -scan runs.

As listed in Table 5.2, the averages and the standard deviations of  $\sigma_{p,\delta}$  were taken as the resolution systematics for the  $(x, y, z)$ -axes respectively. To smear the position results, a Gaussian distribution  $\mathcal{N}(0, \sigma)$  was convolved with positions. The listed values for the

standard deviation ( $\sigma$ ) of this Gaussian were used to smear the positions.

Table 5.2: Systematic uncertainties of the MPW **fitter** for position on  $(x, y, z)$ -axes. Unit: mm.

axis	systematic uncertainties	systematic to be applied ( $\sigma$ )	smearing
$x$	$73.89 \pm 39.71$	113.6	$x + \mathcal{N}(0, \sigma)$
$y$	$56.03 \pm 34.96$	90.99	$y + \mathcal{N}(0, \sigma)$
$z$	$75.47 \pm 70.09$	145.56	$z + \mathcal{N}(0, \sigma)$

Fig. 5.11 shows the effects of smearing the reconstructed positions of  $^{16}\text{N}$  central run 107055 MC smeared by the resolution systematic uncertainties. It shows that smearing with the additional resolutions coming from the uncertainties widens the reconstructed distributions. Since there is no unfolding procedure to improve or narrow the position resolutions, these position resolution systematics are one-sided. Therefore, in the analysis in Chapter 6, I simply took symmetric uncertainties with different signs.

To quantify the vertex shifts between the MC and data, values of vertex shifts:  $\mu_{P,\delta} \equiv \mu_P(\text{data}) - \mu_P(\text{MC})$  were calculated for the  $(x, y, z)$  scans. Fig. 5.12 shows these results.

In Table 5.3, the averages and the standard deviations of  $\mu_{P,\delta}$  were taken as the vertex shifts for  $(x, y, z)$ -axes. To smear the position results, the  $(x, y, z)$  values were shifted up or down by adding positive or negative values. The values on each axis were shifted independently. For example, the  $x$  shift-up is  $(x, y, z) \rightarrow (x + 6.48, y, z)$  mm; the  $z$  shift-down is  $(x, y, z) \rightarrow (x, y, z - 4.82)$  mm.

Table 5.3: Vertex shifts for the reconstructed positions on  $(x, y, z)$  axes. Unit: mm.

axis	vertex shift	systematics to be applied ( $\Delta$ )	smearing
$x$ shift	$0.50 \pm 5.98$	$+6.48/-5.98$	$x + \Delta x$
$y$ shift	$2.02 \pm 4.11$	$+6.13/-4.11$	$y + \Delta y$
$z$ shift	$1.89 \pm 4.82$	$+6.71/-4.82$	$z + \Delta z$

### 5.3.1.3 Vertex Scale Uncertainties

In addition to the vertex shifts mentioned previously, the vertex scale is defined as a linear scale factor between the fitted positions of the data and the MC,

$$x_{\text{fit}}^{\text{data}} - x_{\text{fit}}^{\text{MC}} = \mu_{P,x}^{\text{data}} - \mu_{P,x}^{\text{MC}} = \Delta + \beta x_{\text{fit}}^{\text{MC}} . \quad (5.8)$$

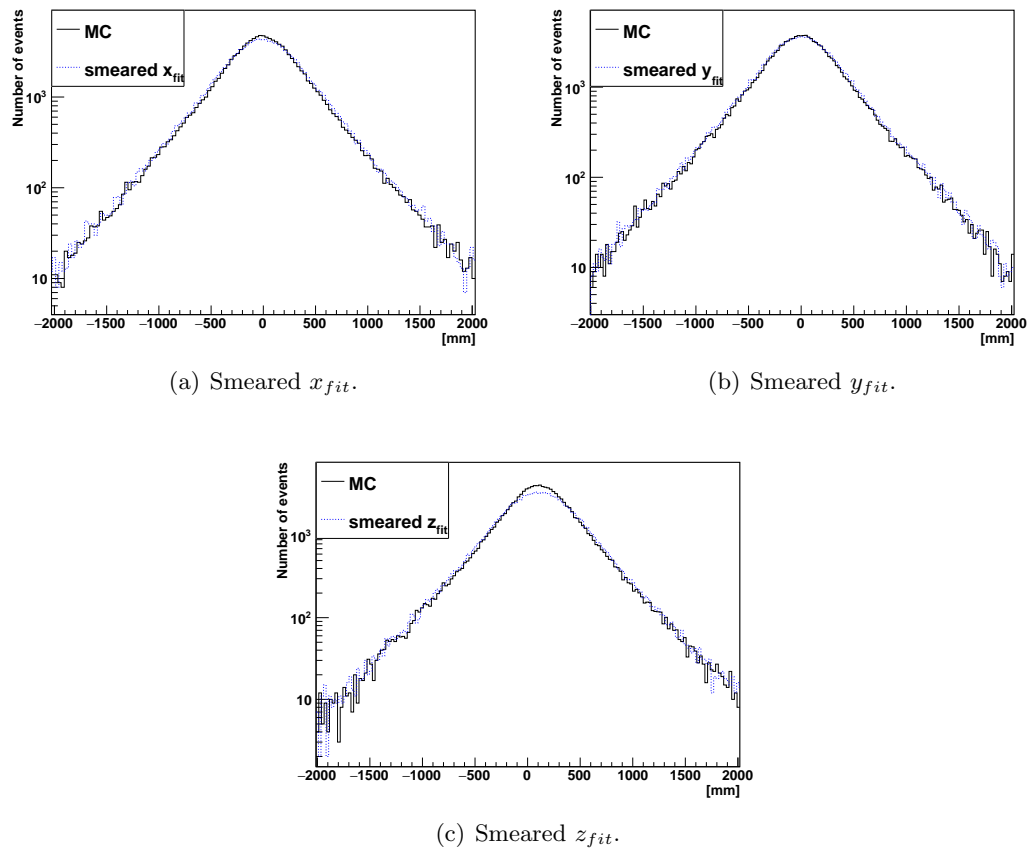


Figure 5.11: Smeared reconstructed positions ( $x_{fit}, y_{fit}, z_{fit}$ ) of  $^{16}\text{N}$  central run 107055 MC by the position resolution systematics.

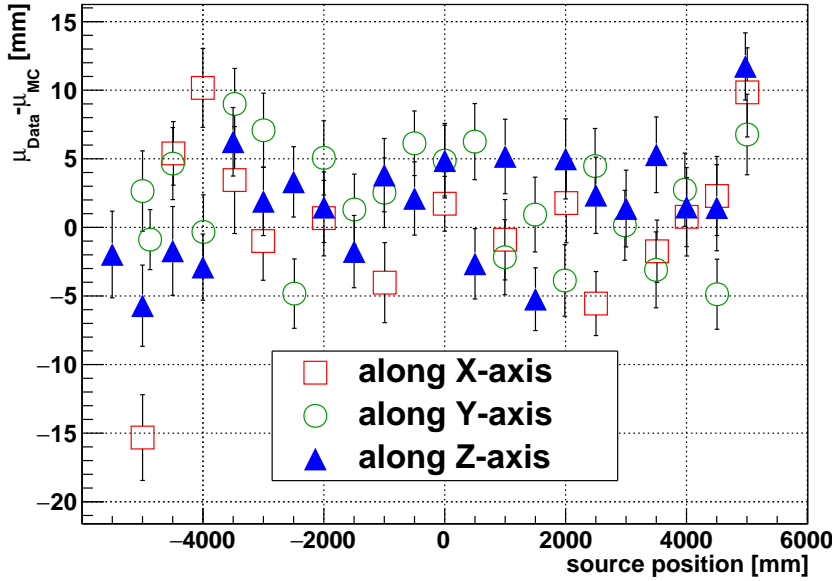


Figure 5.12: Vertex shifts of  $\mu_P$  ( $\mu_{p,\delta}$ ) as a function of the  $^{16}\text{N}$  source position. For simplicity, the corner scans are not shown in this figure. The red squares represent the results from the  $x$ -scan runs; green circles represent the  $y$ -scan runs and the blue triangles represent the  $z$ -scan runs.

Since  $x_{fit}^{data} = \Delta + (1 + \beta) x_{fit}^{MC}$ , if the vertex scale factor is defined  $\alpha \equiv 1 + \beta$  then  $x_{data} = \alpha x_{MC}$ .

To obtain  $\alpha$ , the results in Fig. 5.12 were fitted with linear functions:  $shifts = p_0 + p_1 x_{src}$  (where  $x_{src}$  is the source position), as shown in Fig. 5.13.

From the linear fits, the values of vertex shifts were obtained and listed in Table 5.4. Since the  $\chi^2/\text{ndf}$  values here were large, according to Refs. [17, 176], inflated errors were calculated as  $S \times (\text{slope errors})$ , where the error scale factor  $S = \sqrt{\chi^2/(\text{ndf} - 1)}$ . The downward systematic was calculated as the slope minus the slope error as well as the inflated error. In contrast, the upward systematic was taken as the slope plus the slope error as well as the inflated error, as suggested by [176]. For the  $z$  scan, the position at  $(-185.037, 247.24, 4973.567)$  mm pulls the slope results to the positive, possibly due to the bias in simulation from the neck geometry effects. This point was not used in the linear fit.

The vertex scale systematics were then transformed, e.g.  $x' = (1 + \delta_x/100)x$  with

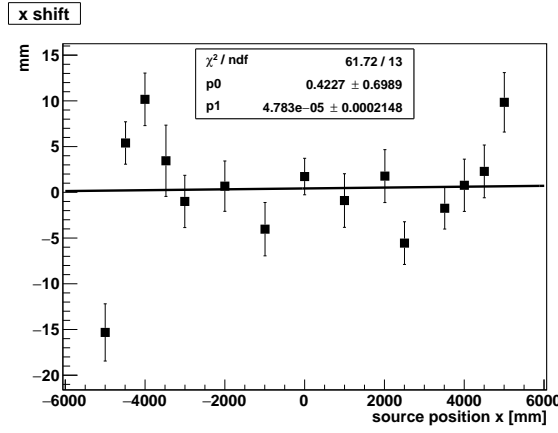
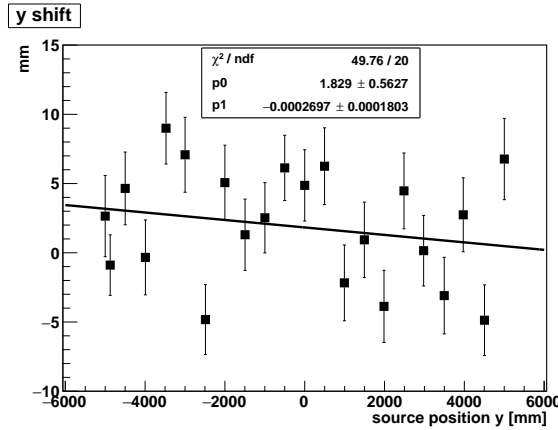
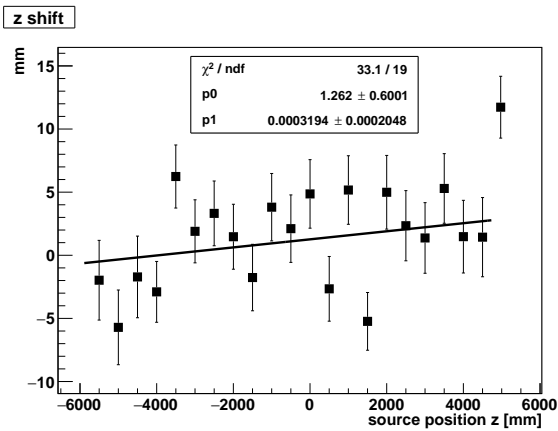
(a)  $^{16}\text{N}$  x-scan runs.(b)  $^{16}\text{N}$  y-scan runs.(c)  $^{16}\text{N}$  z-scan runs.

Figure 5.13: Vertex shifts along  $x, y, z$  axes and fitted with linear functions:  $\text{shift} = p_0 + p_1 \cdot x_i$ , ( $x_i = x, y, z$ ).

Table 5.4: Vertex scales for the reconstructed positions on  $(x, y, z)$  axes.

axis	fitted slope (%)	inflated error	systematics ( $\delta^+/\delta^-$ ) (%)
$x$ scale ( $\delta_x$ )	$0.005 \pm 0.021$	0.048	+0.07/-0.06
$y$ scale ( $\delta_y$ )	$-0.027 \pm 0.018$	0.030	+0.02/-0.07
$z$ scale ( $\delta_z$ )	$0.032 \pm 0.020$	0.027	+0.08/-0.01

equivalent formulae for the  $(y, z)$  axes.

The scale systematics also depend on the radius  $r = \sqrt{x^2 + y^2 + z^2}$  [176]. The reconstructed radius is always used for defining the fiducial volume inside the AV. In this case, due to the AV offset mentioned in Chapter 3 and Chapter 4, a correction in  $z$  with  $z' = z - 108$  (mm) should be applied, and then  $r$  is changed to  $r' = \sqrt{x^2 + y^2 + (z - 108)^2}$ . By the usual logic for calculating error propagation, for an event position  $(x, y, z)$ ,  $\delta_{r'}'$  is calculated as [176]:

$$\delta_{r'}' = \sqrt{\sum_{i=1}^3 \left(\frac{\partial r'}{\partial x_i}\right)^2 \delta_{x_i}^2} = \sqrt{\frac{x^2 \delta_x^2 + y^2 \delta_y^2 + (z - 108)^2 \delta_z^2}{r'^2}}. \quad (5.9)$$

Using the  $\delta^+$  and  $\delta^-$  for  $(x, y, z)$  scales in Table 5.4, the  $\delta_{r'}^+$  and  $\delta_{r'}^-$  are calculated, respectively. Then the two-sided bounds for the confidence interval of  $r'$  are calculated by as  $r'^+ = (1 + \delta_{r'}^+/100) r'$  and  $r'^- = (1 - \delta_{r'}^-/100) r'$ .

Fig. 5.14 shows the effects of smearing the radius scales on the reconstructed  $r'$  radius of the  $^{16}\text{N}$  central run 107055 MC.

### 5.3.2 Direction Reconstruction Evaluation

#### 5.3.2.1 Direction Resolution

For reconstructed  $^{16}\text{N}$  calibration events, on the assumption that a  $\gamma$  photon emitted by the source interacted with an electron at the reconstructed position, the “true” direction of an event is defined as the direction pointing from the source manipulator position to the reconstructed position,

$$\vec{u}_{\text{true}} = \frac{\vec{X}_{\text{fit}} - \vec{X}_{\text{src}}}{|\vec{X}_{\text{fit}} - \vec{X}_{\text{src}}|}. \quad (5.10)$$

Now define  $\theta$  as the angular difference between the “true” and the reconstructed event orientations, viz.  $\cos \theta = \vec{u}_{\text{true}} \cdot \vec{u}_{\text{fit}}$ .

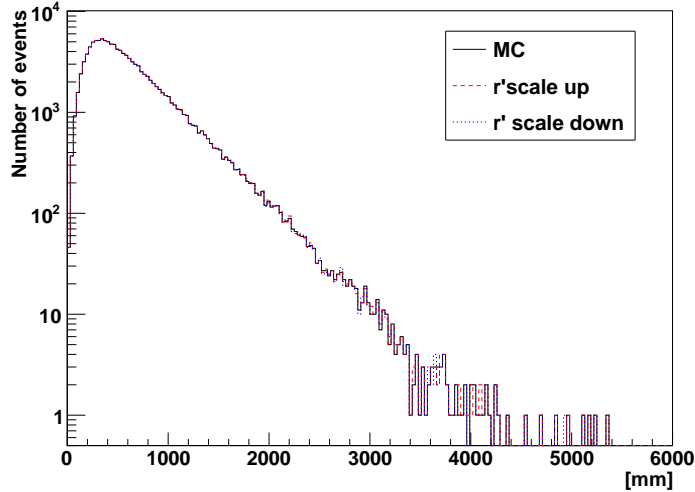


Figure 5.14: Smeared reconstructed radius  $r'$  of  $^{16}\text{N}$  central run 107055 by radius scales. The solid black line is for unsmeared MC; the red dash line is for scaling up the  $r'$  in MC; the blue dot line is for scaling down the  $r'_{fit}$  in MC.

The distribution of  $\cos\theta$  was fitted with the direction resolution function (Eqn. 4.9) mentioned in Sect. 4.2.8. Before the fitting, a few cuts relating to the position and energy reconstructions were applied to the data or simulation results. As mentioned in Chapter 4, the direction reconstruction relies on the position. Therefore, the *posFoM* cut ( $scaleLogL > 10$ ) was applied before evaluating the direction reconstruction. Other cuts were suggested by the SNO+ collaboration to remove instrumental backgrounds and poor reconstructions for events close to the source container or far away from the source. To remove instrumental backgrounds, the cuts

- $E_{fit} > 3.5 \text{ MeV}$ ,
- $\text{ITR} > 0.55$ ,
- $-0.12 < \beta_{14} < 0.95$ ,

were used. To remove poorly reconstructed events which were close to the source container due to its shadow effect, and also the events far away from the source, a distance cut,  $1000 < |\vec{X}_{fit} - \vec{X}_{src}| < 2300 \text{ mm}$ , was applied. For the internal scans, a radius cut  $R' < 5850 \text{ mm}$  was also applied. This radial cut was not applied on the external and neck scans [176].

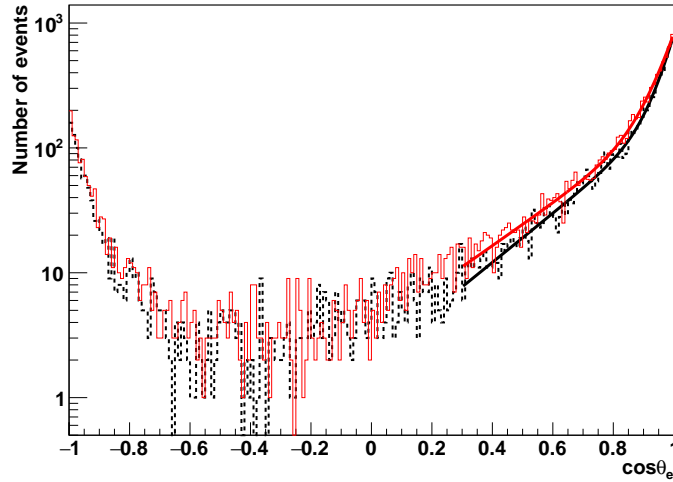


Figure 5.15: Distributions of the angular error in direction reconstruction, from the data (red solid line) and MC (black dashed line); both are reconstructed by the **MPW fitter**. These distributions are fitted with the angular resolution functions over the range [0.3,1].

Fig. 5.15 shows the fitted results of the angular distributions over a fit range (in  $\cos \theta_e$ ) of [0.3,1], after the cuts mentioned, and the resolution parameters are shown in Table 5.5. Direction resolution for the MC is better than for the data, due to the idealized (simpler) configuration modelled in the simulations. The reconstruction performances of the **MPW fitter** and the **RAT water fitter** are similar, while for both the detector data and MC,  $\beta_M$  values yielded by MPW are about 10% higher than those from RAT. In short, direction resolution of the MPW is slightly better than that of the RAT.

Table 5.5: Direction resolution of the MPW and RAT fitters, when applied to  $^{16}\text{N}$  calibration data and when applied to MC simulations of the calibration process.

	$\beta_M$	$\beta_S$	$\alpha_M$	$\chi^2/\text{ndf}$	$\cos \theta_{0.5}$	$\cos \theta_{0.8}$	$\cos \theta_{0.9}$
107055							
MPW data	$4.15 \pm 0.18$	$19.08 \pm 0.94$	$0.58 \pm 0.02$	$77.1/66$	0.964	0.744	0.410
MPW MC	$4.42 \pm 0.19$	$20.41 \pm 1.01$	$0.56 \pm 0.02$	$83.8/66$	0.974	0.768	0.454
RAT data	$3.76 \pm 0.18$	$17.90 \pm 0.82$	$0.55 \pm 0.02$	$70.5/66$	0.974	0.731	0.364
RAT MC	$4.02 \pm 0.18$	$20.89 \pm 0.92$	$0.54 \pm 0.03$	$94.9/66$	0.979	0.753	0.409

### 5.3.2.2 Direction Systematics

For all the internal  $^{16}\text{N}$  scans, the cuts mentioned in the previous section were applied to both the data and simulations. In a manner similar to that when evaluating the positional uncertainties, the angular resolution function was first fitted with three free parameters:  $\alpha_M$ ,  $\beta_S$ , and  $\beta_M$ . To simplify the calculation in propagating systematics, an average value of the fitted  $\alpha_M$  was calculated from all the internal scans (except the three neck scans), namely  $\alpha_M = 0.613$  for data and  $\alpha_M = 0.585$  for MC. With these fixed values for  $\alpha_M$ , both the data and the MC were refitted to extract  $\beta_S$  and  $\beta_M$  only. The default fit range (in  $\cos \theta_e$ ) was  $[0.3, 1]$ , however for some scans when the source was close to the AV the event count, after the cuts, was too low. For those situations, to ensure more than 5000 events were fitted, the fit range was enlarged by moving a 0.1 step leftward, until the negative-most value reached -0.5:  $[0.3 - 0.1 \cdot \text{step}, 1]$ .

Fig. 5.16 shows the results for the fitted  $\beta_M$  and  $\beta_S$  values for the internal  $^{16}\text{N}$  ( $x, y, z$ )-axis scans. For *most* scans, the MC results are better than the data. The three  $Z$  scans in the neck provided the least satisfactory direction resolutions, due to the asymmetry of the detector geometry.

The relative difference between data and MC of a fitted resolution quantity  $q \pm \delta_q$  is defined as

$$(\Delta q)_{\text{rel}} = \frac{q_{\text{data}} - q_{\text{MC}}}{q_{\text{MC}}} \times 100\% , \quad (5.11)$$

and the error of the relative difference is defined as

$$\delta_{(\Delta q)_{\text{rel}}} = \sqrt{\left(\frac{\delta_{q_{\text{data}}}}{q_{\text{data}}}\right)^2 + \left(\frac{\delta_{q_{\text{MC}}}}{q_{\text{MC}}}\right)^2} \times 100\% . \quad (5.12)$$

Fig. 5.17 shows the relative differences for the internal ( $x, y, z$ ) scans (excluding the neck scans). Based on those scans (i.e. the internal scans barring those with the source in the neck, leaving 77 runs in total) the means and standard deviations of the relative differences are  $\Delta(\beta_M)_{\text{rel}} = (-6.09 \pm 4.01)\%$  and  $\Delta(\beta_S)_{\text{rel}} = (-3.09 \pm 4.39)\%$ .

To be conservative, taking the largest and smallest values of the  $\Delta(\beta_M)_{\text{rel}}$  and  $\Delta(\beta_S)_{\text{rel}}$ , the negative and positive values of the direction systematics ( $\delta_\theta$ ) are obtained as  $\delta_\theta = +0.013 / -0.101$ .



Figure 5.16: Fitted direction resolution parameters  $\beta_M$ ,  $\beta_S$  for the source scans on  $(x, y, z)$ -axes respectively. Solid squares, MC; Open circles, data.

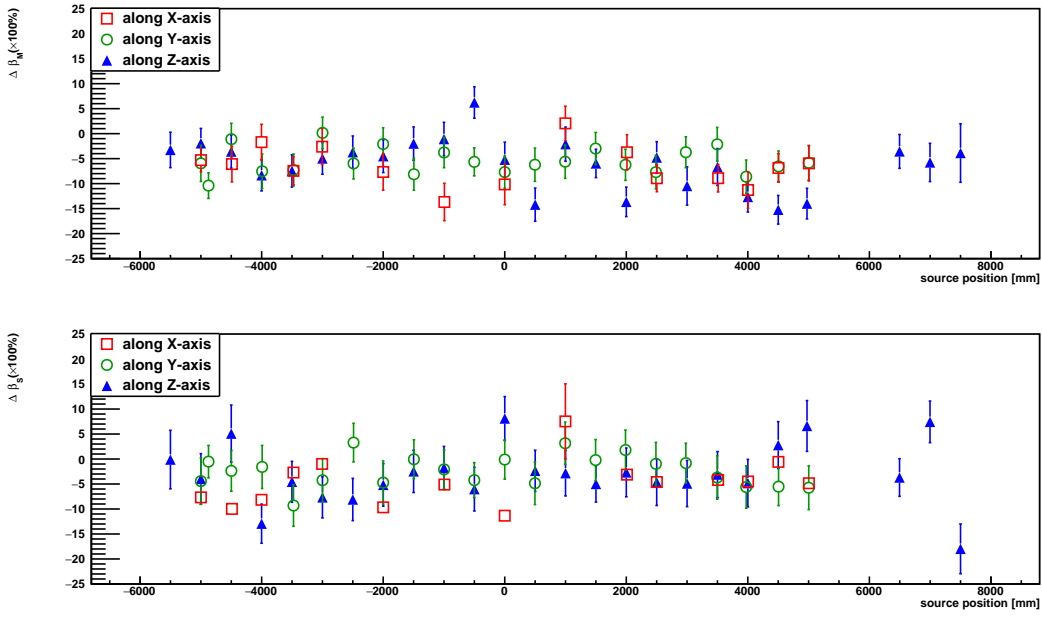


Figure 5.17: Relative differences of  $\beta_M$  and  $\beta_S$  as a function of the  $^{16}\text{N}$  source position. For simplicity, the corner scans are not shown in this figure. The red squares represent the results from the  $x$ -scan runs; green circles represent the  $y$ -scan runs and the blue triangles represent the  $z$ -scan runs.

To propagate the uncertainties in  $\beta_M$  and  $\beta_S$  to the direction resolution, a first-order approximation function was derived by the SNO collaboration [187]:

$$\cos \theta' = 1 + (\cos \theta - 1)(1 + \delta_\theta). \quad (5.13)$$

This angular remapping function was used to smear the angular distributions for systematic studies. In the next chapter, it will be applied to the angular distribution of solar neutrino data.

### 5.3.3 $\beta_{14}$ and its Systematics

Since  $\beta_{14}$  itself is used as the high level cut, only the cuts  $\text{ITR} > 0.55$  and  $\text{NHits} > 5$  were applied on the data and MC to extract the  $\beta_{14}$  distributions. Fig. 5.18 shows the  $\beta_{14}$  distributions of the central run 107055 data and MC, reconstructed by the **MPW fitter** and the official **RAT fitter** respectively. The  $\beta_{14}$  is calculated based on the reconstructed position,

time, and direction of an event, and the  $\beta_{14}$  distributions from the MPW and RAT fitter results are consistent. However, both fitters show a discrepancy between the data and the MC, a discrepancy that may be caused by inaccurate modeling of the Cherenkov process in the Geant4 simulation [185, 188]. Fig. 5.19 compares the  $\beta_{14}$  values from the data and the MC of run 107055. Both of the distributions are the MPW processed results and are fitted with Gaussian distributions over the range  $-0.5 \leq \beta_{14} \leq 1.5$ . The data shows a slightly smaller Gaussian mean value,  $\mu_{data} = 0.4157$ , compared to  $\mu_{MC} = 0.4388$ .

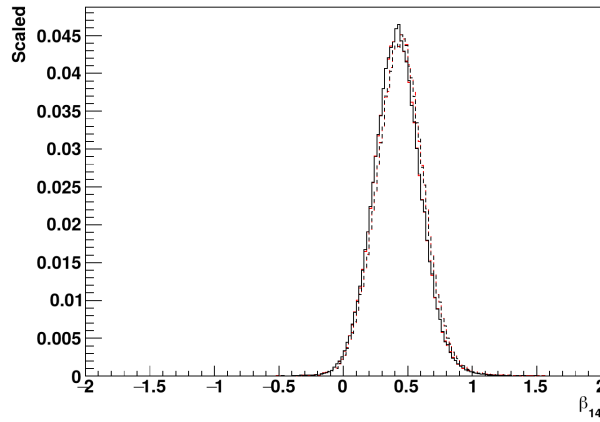


Figure 5.18: Distributions of  $\beta_{14}$  for the  $^{16}\text{N}$  central run 107055. Dashed lines for the MC and solid lines for data; red for the MPW fitter processed results and black for the RAT results.

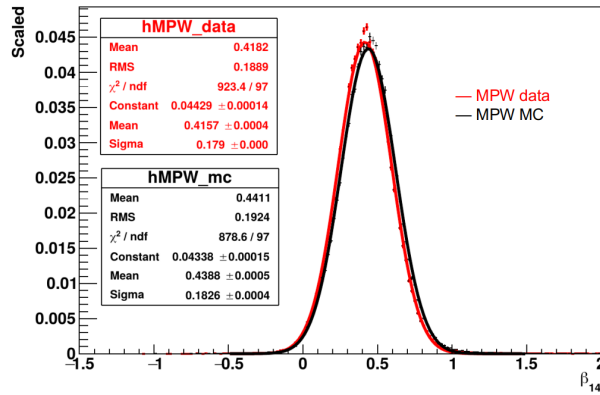


Figure 5.19: A comparison of the  $\beta_{14}$  for the data and the MC in run 107055.

Fig. 5.20 shows the effects on  $\beta_{14}$  when source position is moved along the  $(x, y, z)$  axes.  $\Delta\beta_{14} \equiv \mu_{data} - \mu_{MC}$  was calculated for each of the 80 internal runs (i.e. including neck

runs), and the mean and standard deviation of these  $\Delta\beta_{14}$  values were taken as the shift in  $\beta_{14}$ :  $-0.026 \pm 0.010$ . Following the suggestion in Ref. [176], an asymmetric uncertainty was taken: the upward shift was taken as  $+0.010$  while the downward shift was taken as  $-0.026 - 0.01 = -0.036$ . Thus the shifts  $+0.010 / -0.036$  were taken as the  $\beta_{14}$  systematics, and will be applied to the solar neutrino analysis in the next chapter.

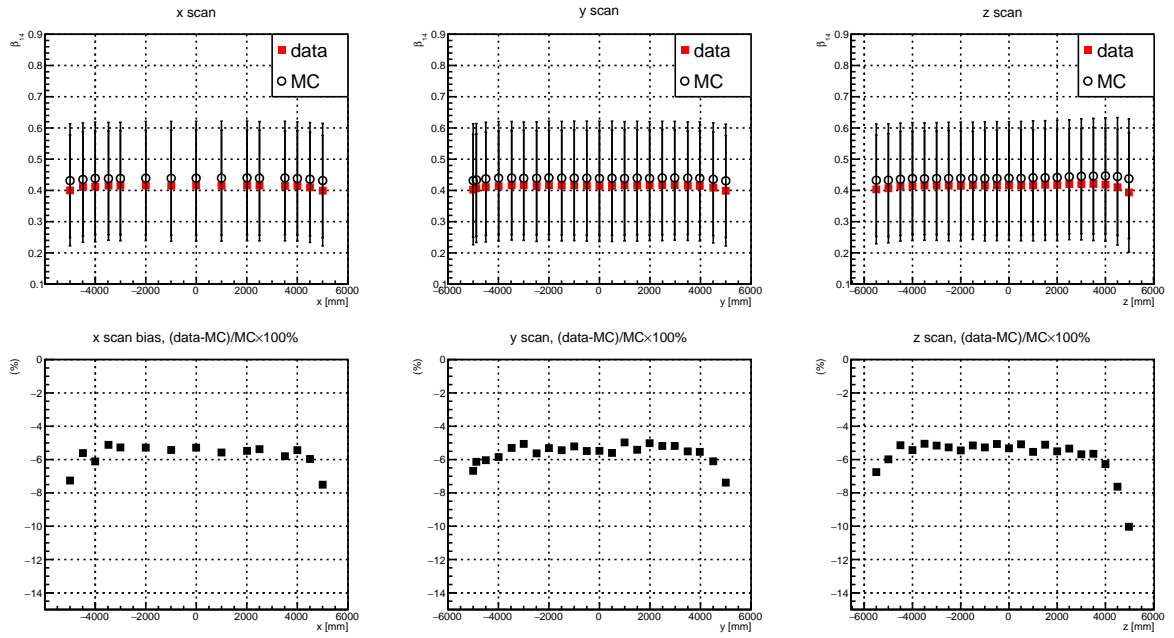


Figure 5.20:  $\beta_{14}$  systematics along  $(x, y, z)$  scans.

### 5.3.4 Energy Reconstruction Evaluation

#### 5.3.4.1 Energy Figure of Merits

Three energy FoM quantities, namely  $G_{test}$ ,  $U_{test}$  and  $Z_{factor}$ , were introduced in Sect. 4.7.1. Here I used the MC simulations as well as the data of the  $^{16}\text{N}$  central run 107055 to check the effects of the cuts on the FoM quantities which can reduce the energy biases. The sacrifices of the events were also calculated.

- $U_{test}$ : Fig. 5.21 shows  $U_{test}$  vs. energy biases. A cut of  $0.61 < U_{test} < 0.95$  was suggested by the collaboration, to remove events mostly caused by the source encapsulation.

sulation. This cut removes 0.38% of MC events and 0.34% of data events.

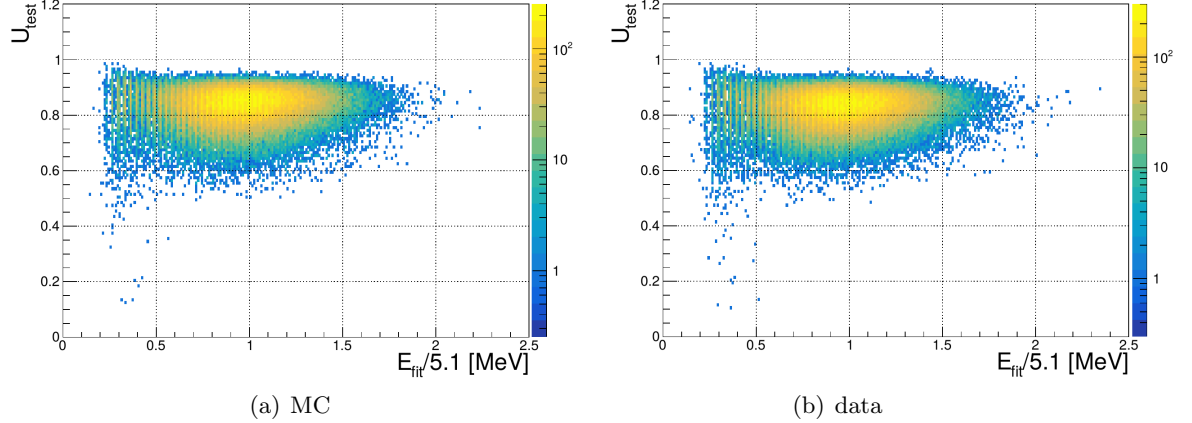


Figure 5.21:  $^{16}\text{N}$  central-run 107055,  $U_{test}$  vs.  $E_{fit}/5.1$  MeV.

- $G_{test}$ : Fig. 5.22 shows  $G_{test}$  vs. energy biases. A cut of  $0 < G_{test} < 1.9$  was suggested by the collaboration, which removes 0.01% events for both MC and data.

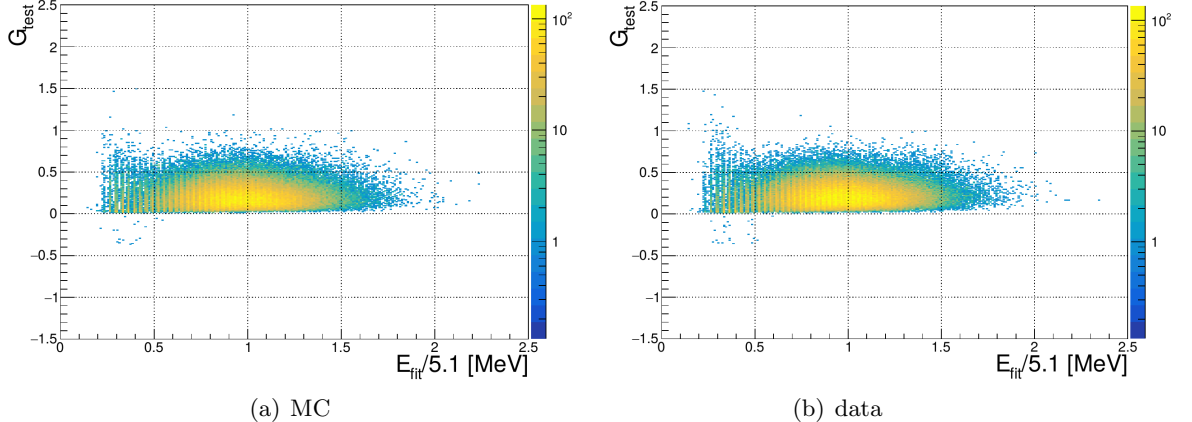


Figure 5.22:  $^{16}\text{N}$  central-run 107055,  $G_{test}$  vs.  $E_{fit}/5.1$  MeV.

- $Z_{factor}$ : Fig. 5.23 shows  $Z_{factor}$  vs. energy biases. A cut of  $-11 < Z_{factor} < 1$  was suggested by the collaboration, which removes 0.13% events for both MC and data.

All the cuts on the three energy FoM quantities remove 0.40% events from MC and 0.37% events from data. These cuts were also used in the water phase analysis in Chapter 6.

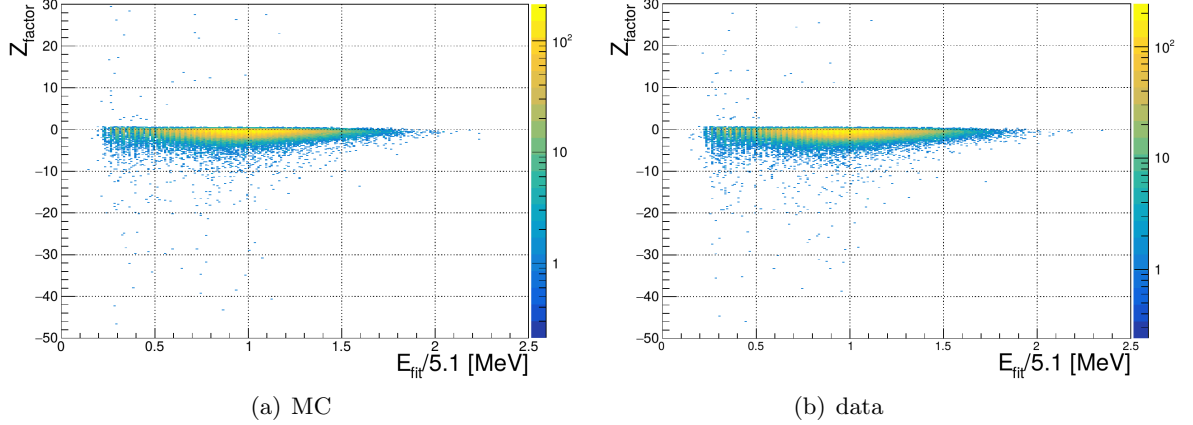


Figure 5.23:  $^{16}\text{N}$  central-run 107055,  $Z_{factor}$  vs.  $E_{fit}/5.1$  MeV.

### 5.3.4.2 Energy Resolution and Systematics

The energy fitters for the water phase were applied to the  $^{16}\text{N}$  MC simulations and data. As described in Sect. 4.7, the energy fitters utilize the reconstructed vertex and direction of an event to convert the NHits value into the reconstructed energy. Before the energy reconstruction, a reconstruction threshold cut  $\text{NHits} > 5$  was applied to both of the RAT and MPW fitters during the vertex and direction reconstructions. Then the energy fitters were applied to the results of the two fitters respectively. Fig. 5.24 shows the spectra of the NHits of the  $^{16}\text{N}$  events in the central run 107055, comparing results from the MC and data. An  $\text{ITR} > 0.55$  cut was also applied. The figure shows that the MPW fitter has more events in the  $5 < \text{NHits} \leq 10$  region. In the region of  $\text{NHits} > 10$ , the two fitters generally match with each other, while the number of events of the MC is slightly less than the data, which is due to the biases in simulation models.

Fig. 5.25 shows two examples for the reconstructed energy spectra of the  $^{16}\text{N}$  events. Cuts of  $\text{NHits} > 5$  and  $\text{ITR} > 0.55$  were applied. The upper plot shows the reconstructed energies of the  $^{16}\text{N}$  events in the central run 107055, comparing results from the MC and data. The reconstructed energies based on the results of the **RAT** and **MPW** fitters are also compared. The plot shows that the shapes of the spectra are very similar to the  $\text{NHits}$  case in Fig. 5.24, and the **MPW** fitter has more events around the  $0.5 < E < 2$  MeV region. The lower plot shows the reconstructed energies for the run 106025 when the source position

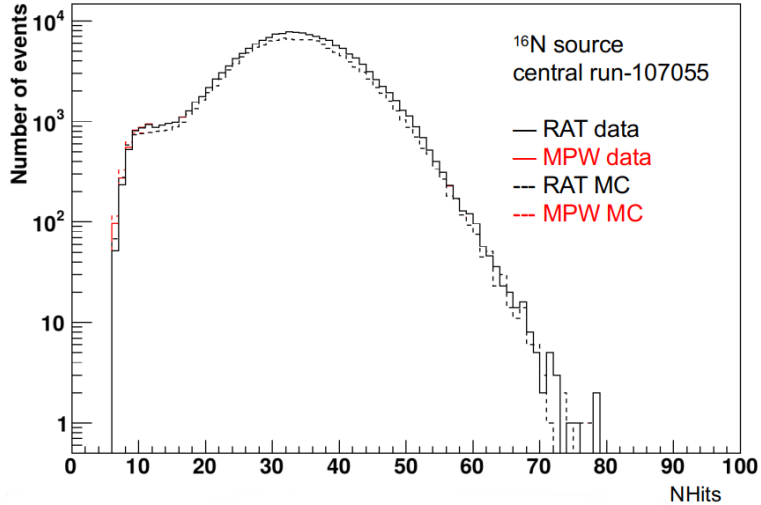


Figure 5.24: NHits spectra of the  $^{16}\text{N}$  central run 107055. Dashed lines for the MC and solid lines for data; red for the MPW fitter results and black for the RAT results.

was at (-186.0,254.0,-4999.9) mm, comparing the MPW results from the MC and data. The plot shows that when the source was close to the AV bottom, the performance of the energy reconstruction is still good.

### 5.3.4.3 Energy Resolutions

As mentioned in Sect. 5.3.1.1, the  $^{16}\text{N}$  source can be considered as an electron source with a known spatial distribution. The  $\gamma$ -photons emitted from the source interact with the detector materials via different processes and produce electrons with various energies. Fig. 5.26 shows the spectra of electron energies derived from the simulations of the  $^{16}\text{N}$  central run 107055. It shows the contributions from three processes: Compton scattering, pair production, and photoelectric absorption. Among these contributions, Compton scattering is dominant, while photoelectric absorption is negligible. The  $\gamma$ -photons transfer energies to electrons, while the energy reconstruction for SNO+ is based on electron equivalent energy (unit: MeVee), so the source energy must be mapped to electron equivalent energy [189].

Following the methods described in Refs. [176, 189], a map that relates the number of Cherenkov photons to the electron energy is created by simulating electron events with different energies at the detector center, as shown in Fig. 5.27(a). By looking up the map and applying linear interpolation, the number of the photons created from the  $^{16}\text{N}$  source

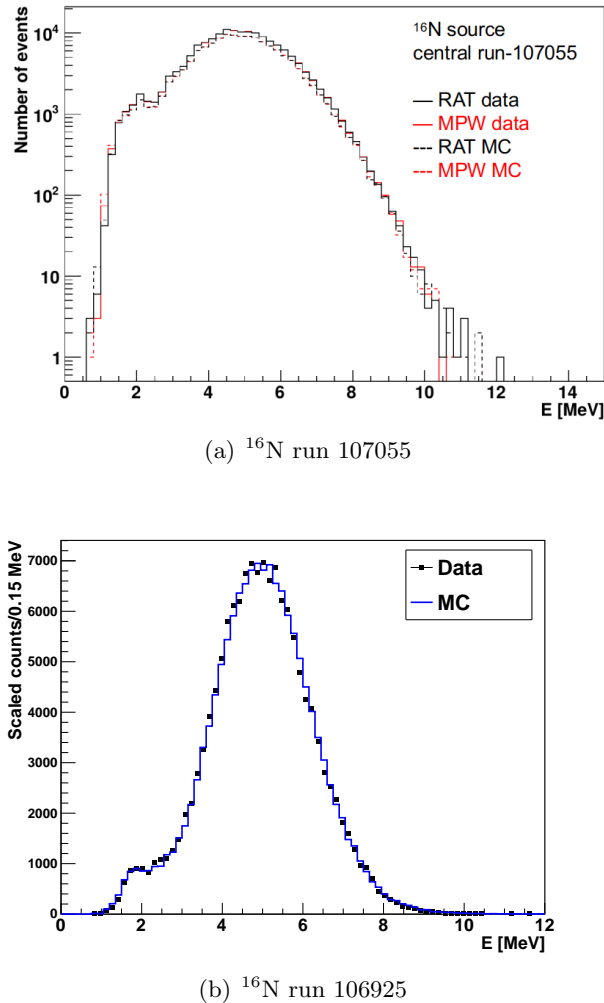


Figure 5.25: Reconstructed energy spectra from the  $^{16}\text{N}$  central run 107055 (upper) and 106925 (lower). For run 107055 (upper), the MPW fitter results and the RAT results are also compared. Dashed lines for the MC and solid lines for data; red for the MPW fitter results and black for the RAT results. For run 106925 (lower), the reconstructed data (black dots) are compared to the MC (blue line), both being MPW fitter results.

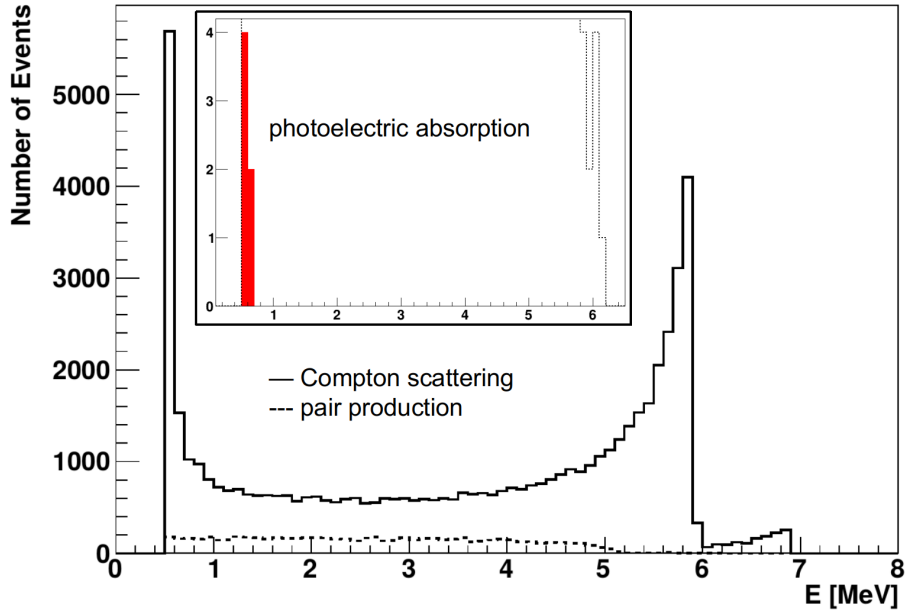


Figure 5.26: Simulated electron energy spectra for different processes, extracted from  $10^5$  MC simulations of  $^{16}\text{N}$  central run 107055. Contributions from three processes: Compton scattering, pair production, and photoelectric absorption are shown.

can be converted into an effective or apparent electron energy spectrum ( $P_{\text{source}}(T_e)$ ) [176]. Fig. 5.27(b) shows the effective electron spectrum of  $^{16}\text{N}$  central run 107055.

To obtain the energy reconstruction resolutions, the reconstructed energy spectrum  $P(T_{\text{eff}})$  is fitted with the energy resolution function defined as [176]:

$$P(T_{\text{eff}}) = N \int P_{\text{source}}(T_e) \frac{1}{\sqrt{2\pi}\sigma_E} \exp \left[ -\frac{[(1 + \delta_E)T_{\text{eff}} - T_e]^2}{2\sigma_E^2} \right], \quad (5.14)$$

where the predicted apparent energy spectrum,  $P_{\text{source}}(T_e)$ , is convolved with a Gaussian resolution function. In the Gaussian function,  $\sigma_E$  is the detector resolution and  $\sigma_E = b\sqrt{T_{\text{eff}}}$ , where  $b$  is the energy resolution parameter and  $\delta_E$  is the energy scale parameter.  $P_{\text{source}}(T_e)$  is the apparent energy spectrum.

Before fitting the reconstructed energy spectrum with the energy resolution function, the following cuts were applied (on both the data and MC):

- the position FoM cut  $\text{scaleLogL} > 10$  and the energy FOM cuts mentioned in the previous sections, i.e.  $0 < G_{\text{test}} < 1.9$ ,  $U_{\text{test}} < 0.95$  and  $-11 < Z_{\text{factor}} < 1$ ;



Figure 5.27: Converting number of photons to effective electron spectrum. (a): A 2D map relates the energies of the simulated electrons to the number of Cherenkov photons. (b): Effective electron spectrum of  $^{16}\text{N}$  central run 107055.

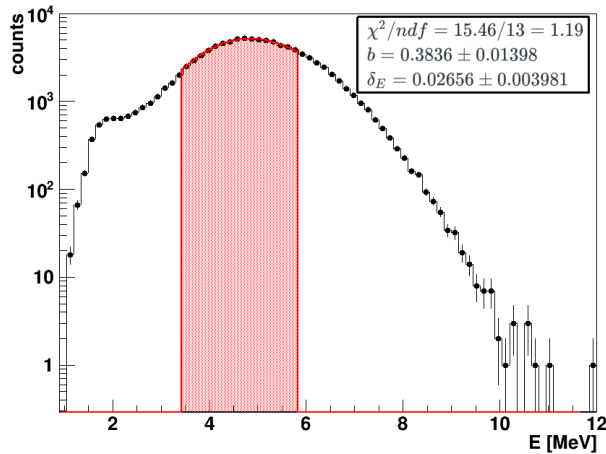


Figure 5.28: The reconstructed energy spectrum of central run 107055 data, fitted with the resolution function (red).

- cuts  $\text{NHit} > 5$ ,  $\text{ITR} > 0.55$  and  $-0.12 < \beta_{14} < 0.95$ , used to remove instrumental backgrounds;
- a conditional distance cut,  $|\vec{X}_{fit} - \vec{X}_{src}| > 700$  mm was suggested by Refs. [190, 176] to remove shadow effects when the events are close to the source container. The conditional cut is applied as follows: an event reconstructed within the 700 mm proximity to the source is retained only if its direction  $\vec{u}_{fit}$  is within  $45^\circ$  of the vector from the source to its vertex, i.e., if  $\sqrt{2}/2 < \vec{u}_{true} \cdot \vec{u}_{fit} < 1$ .

A fit range of [3.5, 6.0] MeV was suggested by Ref. [176] to avoid including poorly reconstructed events due to the trigger inefficiency. Fig. 5.28 shows the energy resolution function fitted with the reconstructed energy spectrum of the  $^{16}\text{N}$  central run 107055 data, after applying the cuts mentioned above.

For all the internal scans, Fig. 5.29 and Fig. 5.30 show the energy scale ( $\delta_E$ ) and energy resolution ( $b$ ) as a function of the source manipulator's radial position. Both the data and MC are shown.

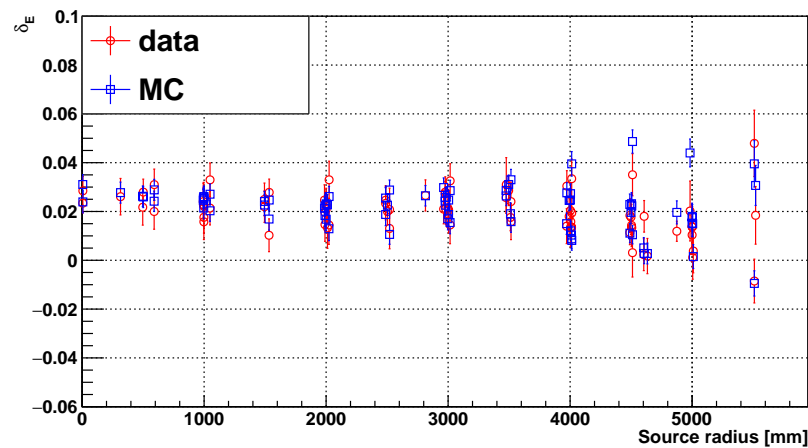


Figure 5.29: Fitted energy scales ( $\delta_E$ ) as a function of the source manipulator's radial position. Red circles for data and blue squares for the MC.

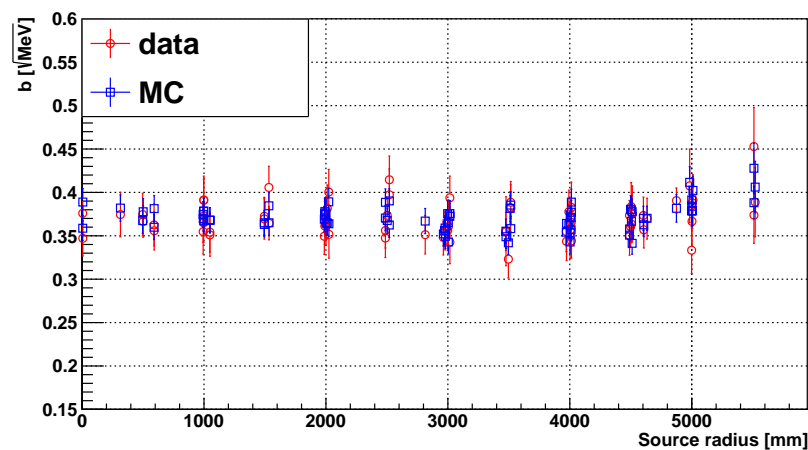


Figure 5.30: Fitted energy resolutions ( $b$ ) as a function of the source manipulator's radial position. Red circles for data and blue squares for the MC.

### 5.3.4.4 Energy Uncertainties

By comparing the differences between data and MC, the uncertainties of the energy scale  $\delta_E$  and resolution  $b$  are calculated as:

$$\Delta_\delta^2 = (\delta_{data} - \delta_{MC})^2 + \text{Error}_{\delta,data}^2 + \text{Error}_{\delta,MC}^2 , \quad (5.15)$$

where  $\delta = b$  or  $\delta_E$ , and  $\Delta_b = \sqrt{\Delta_b^2}$  since the resolution is always positive; while  $\Delta_{\delta_E} = \pm\sqrt{\Delta_{\delta_E}^2}$ . The fit errors in data and MC were also included in the uncertainties. Taking the  $^{16}\text{N}$  scan runs within  $r < 6$  m, the averaged uncertainties are:  $\overline{\Delta_{\delta_E}} = 0.0107$  and  $\overline{\Delta_b} = 0.0369$ . For the  $^{16}\text{N}$  scan runs within  $r < 5.5$  m, which is the fiducial volume of the solar neutrino analysis mentioned in Chapter 6,  $\overline{\Delta_{\delta_E}} = 0.0100$  and  $\overline{\Delta_b} = 0.0320$ .

To apply the energy scale systematics, the reconstructed energy  $E_{fit}$  is smeared by  $E'_{fit} = (1 \pm \Delta_{\delta_E}) E_{fit}$ , where the “+” sign is for scaling up the energy while “−” is for scaling down. Fig. 5.31 shows the effects of smearing the energy scales on the reconstructed energy spectrum of the  $^{16}\text{N}$  central run 107055 MC (the unsmeared data spectrum is also compared). It is obvious that scaling up the  $E_{fit}$  widens the  $E_{fit}$  spectrum while scaling down the  $E_{fit}$  narrows the spectrum.

To apply the energy resolution systematics, the spectrum of the reconstructed energy  $E_{fit}$  is convolved with an additional Gaussian resolution function  $\text{Gaus}(0, \sigma_{\text{smear}})$ , where  $\sigma_{\text{smear}} = \sqrt{E_{fit}} \sqrt{(1 + \Delta_b)^2 - 1}$ . To smear the  $E_{fit}$  event by event,  $E_{\text{smear}}$  is randomly sampled from  $\text{Gaus}(0, \sigma_{\text{smear}})$ , and then  $E'_{fit} = E_{fit} + E_{\text{smear}}$ . Fig. 5.32 shows the effects of smearing the energy resolution on the  $E_{fit}$  spectrum of the  $^{16}\text{N}$  central run 107055 MC (the unsmeared data spectrum is compared). It is obvious that smearing with the additional resolution coming from the uncertainties in  $b$  widens the  $E_{fit}$  spectrum. Similar to the case of position resolutions, because there is no unfolding procedure to improve or narrow the energy resolution, this energy resolution systematic is also one-sided [186]. Therefore, symmetric uncertainties with different signs were taken in the analyses in Chapter 6.

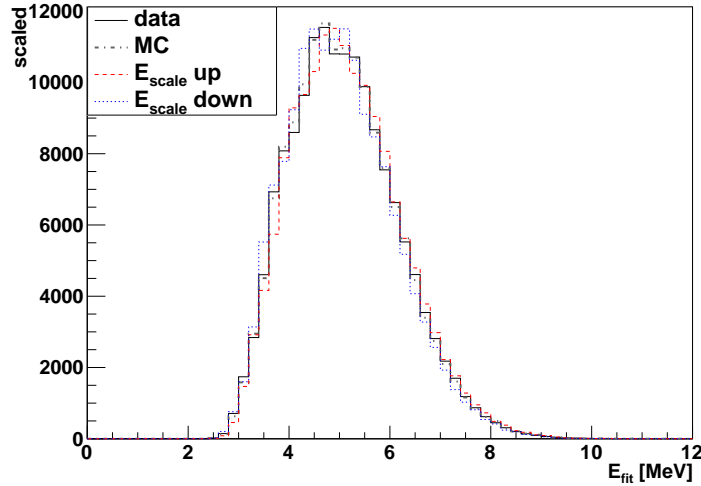


Figure 5.31: Smeared reconstructed energy spectrum of  $^{16}\text{N}$  central run 107055 MC by energy scales. The solid black line is for data and the gray dash-dot line is for unsmeared MC; the red dash line is for scaling up the  $E_{\text{fit}}$  in MC; the blue dot line is for scaling down the  $E_{\text{fit}}$  in MC. Histograms are normalized to the total counts of the data.

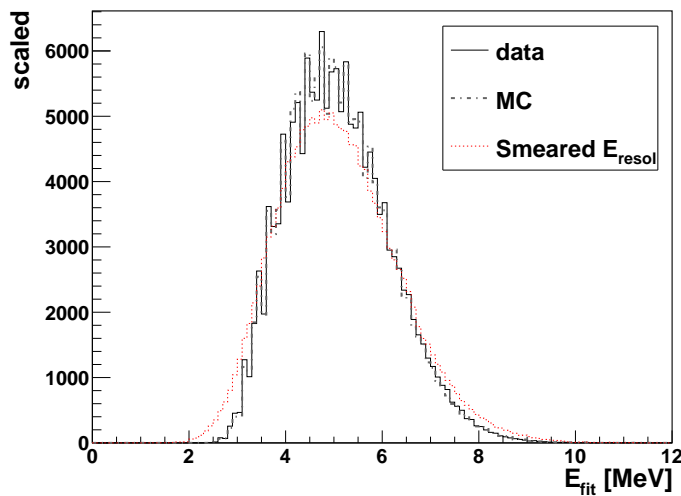


Figure 5.32: Smeared reconstructed energy spectrum of  $^{16}\text{N}$  central run 107055 MC by the energy resolution. The red dash line is for smearing the  $E_{\text{fit}}$  with  $\text{Gaus}(E_{\text{fit}}, \sigma)$ . Histograms are normalized to the total counts of the data.

## Chapter 6

# Solar Neutrino Analysis in the SNO+ Water Phase

The SNO+ water phase data were taken from May 2017 to July 2019, of which the period from May 2017 to October 2018 constitutes the first stage. During this stage, several calibration runs were taken, including  $^{16}\text{N}$  calibration scans and laserball scans. During the period from October 2018 to July 2019, over 20 tonnes of LAB (without PPO) was filled into the detector and formed a layer extending down the neck to a level slightly below the neck base. With the nitrogen cover gas on the top of the AV, the dataset taken during this period is called the “low background dataset”. The main analyses of this chapter are based on this low background dataset. The dataset was processed by the data cleaning procedure, and 4838 runs were used, which summed up a total live time of 190.33 days.

In this chapter, I applied the `MPW fitter` described in Chapter 4 to reconstruct the event vertex and direction both for the data and for run-by-run MC simulations. The run-by-run simulations simulated the full detector conditions for each specific run. The reconstructed event vertex and direction were used as inputs to the `energy fitter`, the classifiers, and the high level cuts. This reconstruction framework differs from the official SNO+ reconstruction (`RAT water fitter`), and therefore provides an alternative analysis of the detector data yielding helpful information, especially in relation to the assessment of the systematic uncertainties associated with reconstruction.

First, a small volume of the open dataset of 2017 was used to test the MPW results, and the results yielded by the `RAT water fitter` were compared. Subsequently, I analyzed the low background dataset, using sub-datasets of the run-by-run MC simulations to evaluate the ability to separate the solar  $\nu_e$  signals from the background. The Toolkit for Multivariate Data Analysis with ROOT (TMVA) package [191, 192] was trained and tested on the MC simulations to obtain optimized discriminants. These optimized discriminants were applied to the whole dataset to remove the backgrounds.

The outputs from the data were fitted to obtain the number of signal events and the background events. Ensemble tests were performed on fake datasets to check the fit pull and bias. The systematics obtained from the  $^{16}\text{N}$  calibration in Chapter 5 were applied to the results. Finally, the solar  $\nu_e$  interaction rates and the  $^8\text{B}$  solar neutrino flux were evaluated.

## 6.1 Backgrounds

### 6.1.1 Internal backgrounds

Most background events are due to natural radioactive isotopes inside or around the detector, such as isotopes in the detection medium, detector walls, ropes, the PMTs, and the other materials. The major isotopes in the water phase are:  $^{238}\text{U}$ ,  $^{232}\text{Th}$ ,  $^{40}\text{K}$ , and  $^{222}\text{Rn}$ . These have been monitored by *in-situ* and *ex-situ* measurements and analyses.

The ubiquitous  $^{238}\text{U}$  and  $^{232}\text{Th}$  isotopes decay sequentially and form decay chains. The target levels in the SNO+ water phase are  $3.5 \times 10^{-14}$  gram  $^{238}\text{U}$  in per gram water ( $\text{gU/gH}_2\text{O}$ ) and  $3.5 \times 10^{-14}$  gTh/gH<sub>2</sub>O [176]. The rates of the background events caused by the decays from specific isotopes, especially the  $\beta$ -decays of  $^{214}\text{Bi}$  (from the  $^{238}\text{U}$  decay chain) and  $^{208}\text{Tl}$  (from the  $^{232}\text{Th}$  decay chain), were carefully calculated and were put into the simulations. In this chapter, the simulated background events from the  $^{214}\text{Bi}$  and the  $^{208}\text{Tl}$   $\beta$ -decays were used to develop a multivariable analysis to select (discriminate) solar neutrino events from the background events.

### 6.1.2 External backgrounds

As mentioned in Sect. 3.1, due to the great depth of the SNO+ detector underground, the event rate of cosmogenic backgrounds induced by cosmic muons is low. Nevertheless, there certainly are some muon events and muon-induced events. There are also instrumental backgrounds, such as the flashers from the PMTs, noise from PMT channels, etc. In order to remove these external backgrounds, a set of data cleaning cuts are applied to the actual data by using the analysis mask. In the following analyses, the data cleaning cuts were always applied to the actual data.

## 6.2 Solar Neutrino Analysis in Open Dataset

The open dataset was taken in 2017 at the beginning of the water phase from run 100000 to run 100399, an interval providing a live time of 16.607 days. This open dataset was used to compare the reconstructed events furnished by the **MPW fitter** against those from the **RAT water fitter**.

In the SNO+ water phase, solar  $\nu_e$ s are measured via elastic scattering:  $\nu_e + e^- \rightarrow \nu_e + e^-$  ( $\nu + e^-$  ES, see Sect. 2.2.1). The observable quantity is the solar angle  $\theta_{\text{sun}}$ , the direction of the event relative to the Sun’s location, which is defined as:

$$\cos \theta_{\text{sun}} \equiv \vec{u}_{\text{event}} \cdot \frac{\vec{X}_{\text{event}} - \vec{X}_{\text{sun}}}{|\vec{X}_{\text{event}} - \vec{X}_{\text{sun}}|}, \quad (6.1)$$

where  $\vec{X}_{\text{sun}}$  is taken as the Sun’s location relative to the SNOLAB location since the whole lab can be treated as a point regarding the long distance to the Sun.

For the open dataset, the data cleaning mask and high level cuts

- $\text{ITR} > 0.55$ ,
- $-0.12 < \beta_{14} < 0.95$ ,

were applied to the data (as mentioned in Sect. 5.2). These cuts were suggested by the collaboration, based on earlier experience for removing instrumental backgrounds [176].

Firstly, all of the solar neutrino candidate events found by the **Rat water fitter** were refitted by the **MPW fitter**. The results are compared in Table 6.1. For each event, their

Table 6.1: Candidate events in the open dataset. Comparison of the fits for candidate events furnished by different fitters.

Fitter	Run	GTID	$z - 0.108(\text{m})$	$R(\text{m})$	$(R/R_{av})^3$	$\cos \theta_{\text{sun}}$	SNO+ Day
Rat	100093	11108354	3.49	3.57	0.21	-0.954	2683.92
MPW	–	–	3.43	3.52	0.20	-0.906	–
Rat	100207	5079885	-2.61	4.60	0.45	0.816	2687.04
MPW	–	–	-3.63	<b>7.61</b>	2.03	<b>0.656</b>	–
Rat	100632	7882360	1.77	3.19	0.15	0.937	2696.93
MPW	–	–	1.67	3.11	0.14	0.911	–
Rat	100663	15767175	-4.33	4.96	0.56	0.978	2698.18
MPW	–	–	-4.45	5.07	0.60	0.980	–
Rat	100915	169700	-1.00	5.10	0.61	0.341	2701.23
MPW	–	–	-1.08	5.08	0.61	0.337	–

Table 6.2: Candidate events in the open dataset found by the MPW fitter.

Run	GTID	$E_{fit}$ (MeV)	$z - 0.108$ (m)	$R$ (m)	$(R/R_{av})^3$	$\cos \theta_{\text{sun}}$
100093	11108354	5.83	3.43	3.52	0.20	-0.907
100632	7882360	6.18	1.67	3.11	0.14	0.915
100663	15767175	6.18	-4.45	5.07	0.60	0.981
100915	169700	5.68	-1.07	5.08	0.61	0.339
100984	8621621	5.70	0.76	4.75	0.502	-0.648
101075	11673714	5.67	4.43	5.18	0.64	0.587

hit PMT distributions, as well as the reconstructed positions and directions from the two fitters, are compared in Fig. 6.1.

From the proximity of the colored points (Fig. 6.1) it can be seen that, for the candidate events, the results from the MPW are largely consistent with those from RAT, although (not apparent from the figure) the MPW fitter disfavored one event in run 100207 (with GTID=5079885), placing its position outside the AV, and the  $\cos \theta_{\text{sun}}$  becomes smaller and is further away from +1. For this event, the *posFOM* of the RAT position fitter is  $scaleLogL = 10.41$ , while the MPW is  $scaleLogL = 11.60$ , both for 35 selected PMTs ( $\text{NHits}_{\text{selected}} = 35$ ). So for this event, the MPW fitter has a better position reconstruction quality than the RAT.

In addition to refitting the candidate events found by the RAT, the MPW fitter can be (and was) used directly to search for candidate events, with the result shown in Table 6.2. Evidently, the MPW fitter obtained a different set of candidate events, albeit overlapping with

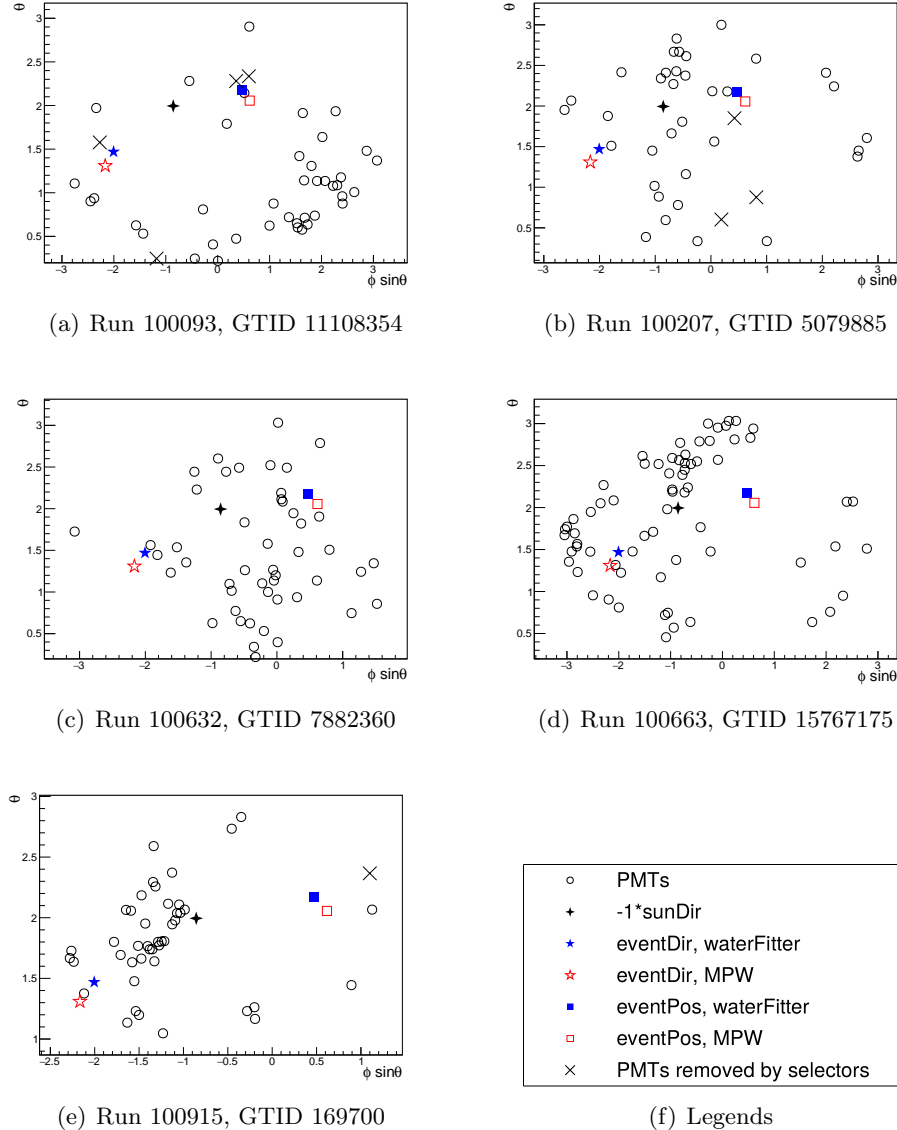


Figure 6.1: Reconstruction results for the candidate events, projected onto PMT sinusoidal maps. Black circles stand for the hit PMTs used by the fitter; crosses stand for the hit PMTs removed by the selectors; blue full star stands for the event direction fitted by the **Rat water fitter**; red open star stands for the direction fitted by the **MPW fitter**; full double diamond stands for the solar direction times -1; blue full square stands for the event position fitted by the **Rat water fitter**; open square stands for the position fitted by the **MPW fitter**.

the set provided by the **RAT** fitter, and so it provides an alternative analysis of the solar neutrinos.

### 6.3 Likelihood Fits for Solar Neutrino Candidate Events

For this section, I focus on the 190.33 live-day low background dataset taken in the second stage of the water phase, with nitrogen cover gas at the top of the neck isolating the newly-filled LAB from lab air. A maximum likelihood fit method for counting the number of the candidate solar neutrino events ( $N_{sig}$ ) and background events ( $N_{bkg}$ ) in a dataset is discussed. To check the method, the dataset from run 200004 to 203602 was used. This dataset has a live time of 92.54 days, about half of the whole 190.33 live-day dataset, so it is denoted as the “half-dataset”. The actual data and the run-by-run MC simulations of this half-dataset were used for testing the analyses in this section and the next.

Before the analysis, the following “beforehand cuts” were applied:

- $\text{NHits} > 20$ ,
- $R'_{fit} < 5500 \text{ mm}$ ,
- $\text{ITR} > 0.55$ ,
- $-0.12 < \beta_{14} < 0.95$ .

Here  $\text{NHits} > 20$  is a reconstruction threshold set for the solar neutrino analysis, which means that only the events with  $\text{NHits} > 20$  were reconstructed by the **MPW fitter**. The  $R'_{fit}$  is the magnitude of the reconstructed event position  $\vec{X}_{fit}$  after the AV coordinate correction:

$$R'_{fit} \equiv \sqrt{x_{fit}^2 + y_{fit}^2 + (z_{fit} - 108)^2},$$

(the 108 mm offset in  $z$  was discussed in Chapter 3 and Chapter 4.). The cut on  $R'_{fit}$  defines a fiducial volume of 5500 mm for solar neutrino analysis. Finally, the high level cuts ITR and  $\beta_{14}$  cuts were mentioned previously.

### 6.3.1 Maximum Likelihood Fit

To prepare for the fit, the values of the solar angle,  $\cos \theta_{\text{sun}}$  from the data were filled into a histogram covering a range of  $[-1,1]$  with 40 bins. For each bin, the observed event count ( $n_{\text{obs}}$ ) was considered as a sum of solar  $\nu_e$  and background events. The count in each bin was assumed to follow a Poisson distribution:  $\text{Poisson}(n_{\text{obs}}, N_{\text{bkg}} P_{\text{bkg}} + N_{\text{sig}} P_{\text{ES}}(E))$ , where  $P_{\text{bkg}}$  and  $P_{\text{ES}}(E)$  are the assumed distributions of background events and solar  $\nu_e$  events respectively.

For background events, a uniform distribution of  $\cos \theta_{\text{sun}}$  was assumed. On the other hand,  $\cos \theta_{\text{sun}}$  distributions for solar  $\nu_e$  events were extracted from the realistic run simulations after applying the beforehand cuts, as shown in Fig. 6.2.

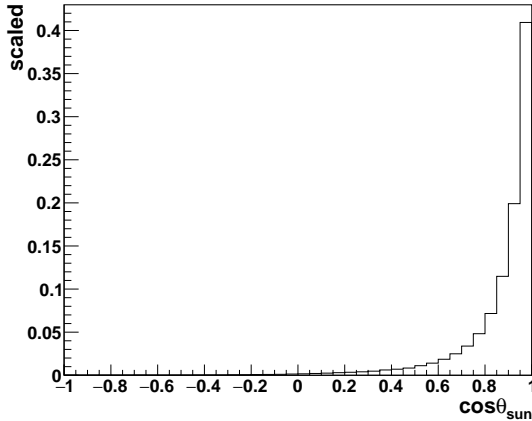


Figure 6.2: The  $\cos \theta_{\text{sun}}$  distribution for solar  $\nu_e$  events extracted from the simulations, which is scaled (so as to have an integral of 1) to obtain a probability density function.

Adding up each bin  $i$  and taking  $N_{\text{bkg}}$  and  $N_{\text{sig}}$  as the free parameters for fitting, the maximum likelihood function was built as [17]:

$$-2 \ln \lambda(N_{\text{sig}}, N_{\text{bkg}}) = 2 \sum_{i=0}^{N_{\text{bins}}} [\mu_i(N_{\text{sig}}, N_{\text{bkg}}) - n_i + n_i \ln \frac{n_i}{\mu_i(N_{\text{sig}}, N_{\text{bkg}})}] , \quad (6.2)$$

where  $\mu_i(N_{\text{sig}}, N_{\text{bkg}})$  is the expected number of events in each bin

$$\mu_i(N_{\text{sig}}, N_{\text{bkg}}) = N_{\text{sig}} \cdot P_{\text{ES}}^i(E^i) + N_{\text{bkg}} \cdot \frac{1}{N_{\text{bins}}} ,$$

and  $N_{\text{bins}}$  is the total number of the bins, usually taken as 40 (for a bin width of 0.05

covering -1 to 1). The calculation of Eqn. 6.2 includes the cases when the bin contains zero ( $n_i = 0$ ).

Fitting the data with  $(N_{bkg}, N_{sig})$  by maximizing the quantity  $-2 \ln \lambda$ , the best fit for  $N_{bkg}$  and  $N_{sig}$  was obtained. In the next section, an ensemble test based on fake datasets was applied to test the fit performances.

### 6.3.2 Ensemble Test

To check the uncertainty of the Poisson fit, a method similar to that of Ref. [190] was used. 5000 fake datasets were generated from the run-by-run MC simulations of the 92.54 live-day half-dataset (runs 200004 to 203602). The “beforehand cuts” had been applied to these simulations.

The number of background events in a fake dataset,  $N_{bkg}^f$ , was assumed to be twice the event number in the  $-1 < \cos \theta_{\text{sun}} < 0$  region, while the number of signal events  $N_{sig}^f = N_{total}^f - N_{bkg}^f$ . These numbers were determined from the actual data, rather than the simulations. Fig. 6.3 shows the actual data of the half-dataset, after the data-cleaning cuts and beforehand cuts. Reading from the actual data, it found  $N_{bkg}^f = 38$  and then  $N_{sig}^f = 109 - N_{bkg}^f = 71$ . To do the ensemble test, for each fake dataset, two random numbers:  $N_{sig}^r$  and  $N_{bkg}^r$  were generated by the `ROOT TRandom3` random number generator class. Each of the two random numbers followed the random Poisson distribution:  $e^{-\mu} \mu^{Nr} / Nr!$ , where  $\mu = 71$  or  $38$ , and thus they fluctuated around  $N_{sig}^f$  or  $N_{bkg}^f$ .

To create the fake datasets, from the solar  $\nu_e$  MC simulations,  $N_{sig}^r$  events that passed the cuts were randomly selected; similarly, from the merged background simulations,  $N_{bkg}^r$  events were randomly selected. These randomly selected events were merged into a fake dataset, and their values of  $E_{fit}$  and  $\cos \theta_{\text{sun}}$  were recorded. By repeating the random selection, an ensemble of fake datasets was created. Each fake dataset was fitted with the maximum likelihood function described in Sect. 6.3.1. Fig. 6.4 shows an example of the fit results from a random fake dataset.

The fit pull and the fit bias were defined by [190]:

$$\text{bias} = \frac{N_{sig} - N_{sig}^r}{N_{sig}} , \quad (6.3)$$

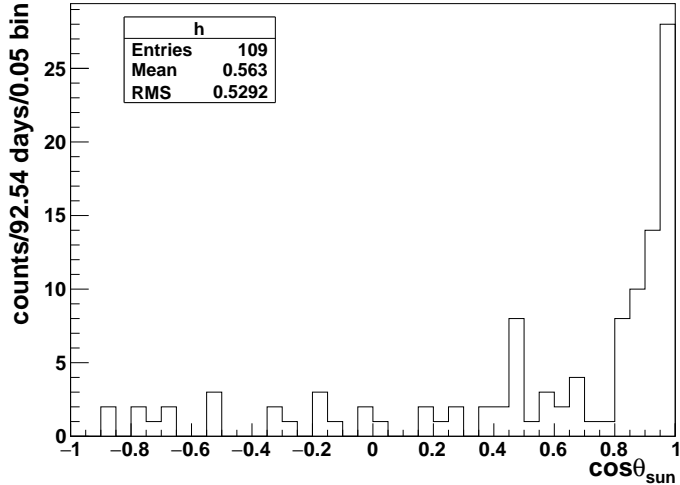


Figure 6.3: Real data from run 200004 to 203602 (half-dataset), after the beforehand cuts. The number of counts in the  $-1 < \cos \theta_{\text{sun}} < 0$  region is 19.

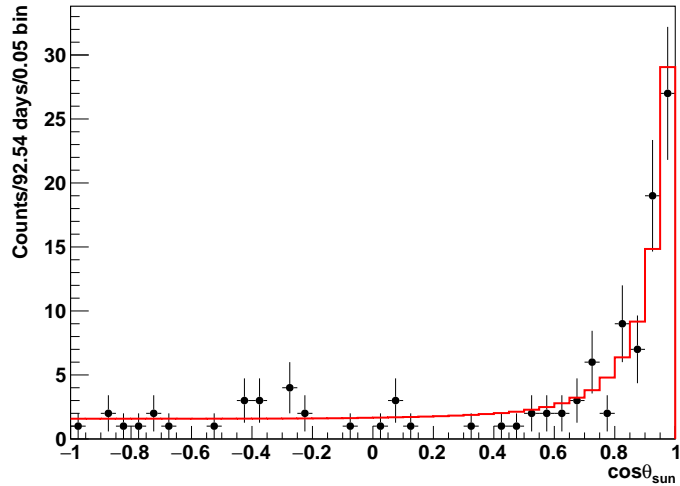


Figure 6.4: An example of the  $\cos \theta_{\text{sun}}$  distribution from a fake dataset fitted with  $(N_{\text{sig}}, N_{\text{bkg}})$ . The black dots are data points and the red line shows the fit. For  $N_{\text{sig}}^r = 73$  and  $N_{\text{bkg}}^r = 44$ , the fit results are  $N_{\text{sig}} = 73.42 \pm 9.42$  and  $N_{\text{bkg}} = 43.58 \pm 7.73$ , with a  $\chi^2/\text{ndf} = 60.19/40 = 1.50$ .

$$\text{pull} = \frac{N_{\text{sig}} - N_{\text{sig}}^r}{\sigma_{\text{sig}}} , \quad (6.4)$$

where  $N_{\text{sig}}$  is the fitted number of signal events,  $\sigma_{\text{sig}}$  is the statistical uncertainty of  $N_{\text{sig}}$ ;

$N_{sig}^r$  is used as the true number of signal events in the fake dataset.

Fig. 6.5 and Fig. 6.6 show the fit pull and bias respectively. The histograms were fitted with Gaussians. For the fitted number of signal events, the Gaussian mean of the fit biases is  $-0.0044 \pm 0.0008$  for 5000 fake datasets while the Gaussian mean of the fit pulls is  $-0.026 \pm 0.006$ . These pulls and biases will be applied on the data. Fig. 6.7 shows the distribution of  $-2 \ln L$  (the log likelihood is calculated according to Eqn. 6.2) returned by the best fit result ( $-2 \ln L_{best}$ ) for each fake dataset. The distribution,  $f(-2 \ln L_{best})$ , follows the asymptotic  $\chi^2$  PDF with a degree of 40 and is used to compute the  $p$ -values [17]. For a best-fit set  $(N_{sig}^i, N_{bkg}^i)$  with a value of  $-2 \ln L_{best}^i$ , the  $p$ -value is calculated as

$$p = \int_{-2 \ln L_{best}^i}^{-2 \ln L_{best}^{max}} f(-2 \ln L_{best}) d(-2 \ln L_{best}).$$

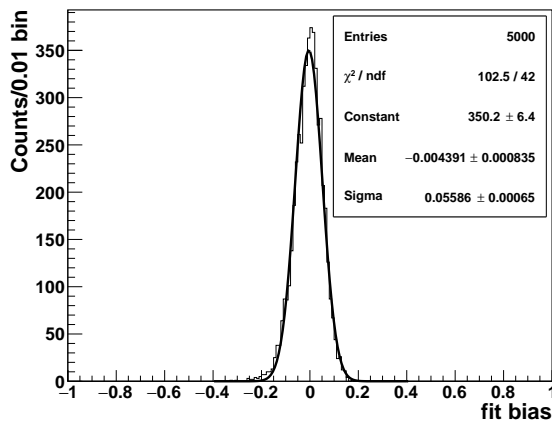


Figure 6.5:  $N_{sig}$  fit biases for 5000 fake datasets.

### 6.3.3 Signal-background Discrimination Based on TMVA

To further reduce the background events, in addition to the “beforehand” cuts mentioned in the previous section, the cuts applied on the position and energy FoMs, as well as the  $kldiv$ , were also considered here. The FoM cuts suggested by the collaboration <sup>1</sup> are [193]:

- $-11 < Z_{factor} < 1$ ,

---

<sup>1</sup>These cuts are mainly based on the  $^{16}\text{N}$  analyses. Suggested by the collaboration, there is also a cut on the quantity of position error calculated by the **Rat water fitter**, with position error  $< 525$  mm. However, this quantity was not calculated by the **MPW fitter**, so it was not included here.

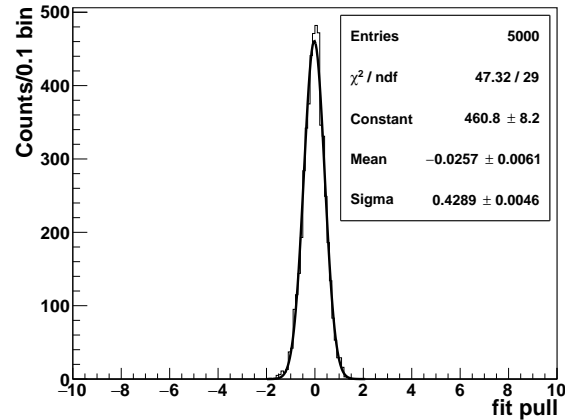


Figure 6.6:  $N_{sig}$  fit pulls for 5000 fake datasets.

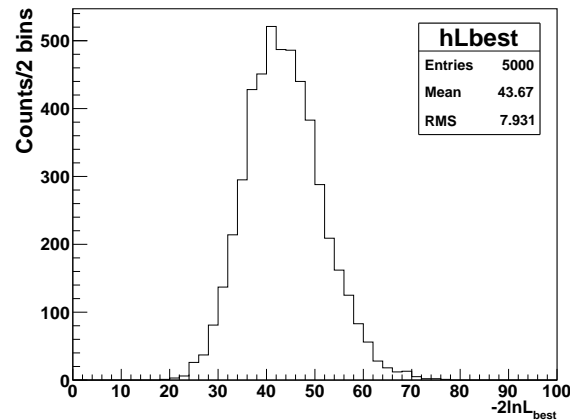


Figure 6.7: The  $-2 \ln L$  distribution of the best fit results from the 5000 fake datasets.

- $\text{scaleLogL} > 10.85$ ,
- $0 < G_{\text{test}} < 1.9$ ,
- $U_{\text{test}} < 0.95$ ,
- $\text{ITR} > 0.55$ ,
- $-0.12 < \beta_{14} < 0.95$ .

These cuts are denoted as “default cuts”.

To optimize the cuts on the FoM, the TMVA package was used. The run-by-run simulations of the solar neutrinos (as signals) and various backgrounds were used to train the machine learning methods in the TMVA. All these variables were used as inputs for training the signal-background discrimination.

For the MC dataset, two types of background isotopes,  $^{208}\text{Tl}$  and  $^{214}\text{Bi}$  were simulated in different detector regions. In this study, the background events simulated in the inner AV (internal backgrounds), inside the AV, and in the external water region were checked. The solar  $\nu_e$  events simulated in the inner AV were used as signals. Table 6.3 summarizes the types of simulations used in this study.

Table 6.3: Datasets of MC simulations.

Simulations	Simulated positions in the detector
$^{208}\text{Tl}$	inner AV (internal $^{208}\text{Tl}$ )
	AV ( $^{208}\text{Tl}$ AV)
	external water (external $^{208}\text{Tl}$ )
$^{214}\text{Bi}$	inner AV (internal $^{214}\text{Bi}$ )
	AV ( $^{214}\text{Bi}$ AV)
	external water (external $^{214}\text{Bi}$ )
Solar $\nu_e$	inner AV (internal $\nu_e$ )
	AV
	external water (external $\nu_e$ )

Different types of the simulations were merged into a mixed dataset. The simulated solar  $\nu_e$  events are tagged as signals and mixed with  $^{214}\text{Bi}$  and  $^{208}\text{Tl}$  background events. The total dataset was divided into training and testing sets.

Fig. 6.8 shows the energy spectrum of simulated internal events with their fitted positions inside the 5.5-m fiducial volume, i.e., with a radial cut of  $R'_{fit} < 5.5$  m.

From the simulations of the half-dataset, runs from run 200004 to 202516 were taken as the training set (about 67 live days and 72.4% of the half-dataset), and the balance (run 202517 to 203602, 27.6%) were taken as the testing set<sup>2</sup>. The machine learning algorithms in the TMVA train the weights of the input variables by using the training set, while they apply the trained weights to the testing set for validations of the signal-background

<sup>2</sup>For a more unbiased analysis, a bootstrap method [194] that randomly separates the training and testing datasets can be used, but it was not applied here.

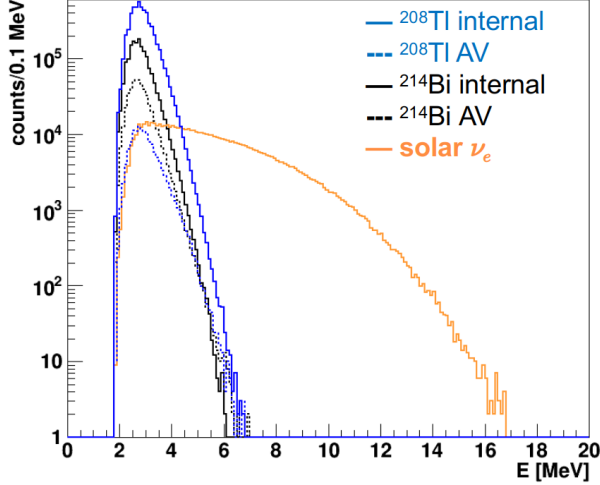


Figure 6.8: Energy spectrum of events from different simulations in the half-dataset:  $^{214}\text{Bi}$  (black),  $^{208}\text{Tl}$  (blue) and solar  $\nu_e$  (orange). Solid lines show the internal events and dotted lines show the AV events.

separation. Once the weights of the input variables were obtained, they were applied to the actual data. Three ranges of  $E_{fit}$  were tested:  $4 < E_{fit} < 15$  MeV,  $5 < E_{fit} < 15$  MeV ( $E > 5$  MeV region), and  $4 < E_{fit} < 5$  MeV (low energy region). Table 6.4 lists the ratios of the signal event count ( $N_{sig}$ ) to the background event count ( $N_{bkg}$ ) for the different energy regions, after application of these beforehand cuts. In the low energy region  $4 < E_{fit} < 5$  MeV background events are dominant, while for  $E_{fit} > 5$  MeV background events are significantly reduced.

Table 6.4: Ratios of the signal event numbers to the background event numbers.

energy region (MeV)	$N_{sig}$	$N_{bkg}$	$N_{sig}/N_{bkg}$
$4 < E_{fit} < 15$	434830	166280	2.6
$5 < E_{fit} < 15$	317205	6359	49.9
$4 < E_{fit} < 5$	117625	159921	0.73

Three machine-learning algorithms/classification methods implemented in the TMVA package were applied to the training and testing datasets: the Fisher discriminants/linear discriminant analysis (Fisher/LD), the Boosted Decision Tree (BDT), and the Artificial Neural Networks Multilayer Perceptron (ANN-MLP, or MLP in short) [192].

The Fisher discriminant  $y_{F_i}(i)$  for classifying event  $i$  is defined by [191]:

$$y_{F_i}(i) = F_0 + \sum_{k=1}^{n_{params}} F_k x_k(i), \quad (6.5)$$

where  $n_{params}$  is the number of input variables, and the Fisher coefficient  $F_k$  is given by:

$$F_k = \frac{\sqrt{N_S N_B}}{N_S + N_B} \sum_{l=1}^{n_{params}} 1/W_{kl}(\bar{x}_{S,l} - \bar{x}_{B,l}), \quad (6.6)$$

where  $N_{S(B)}$  are the number of signal (background) events in the training sample;  $\bar{x}_{S(B),l}$  are the means of input variables for signal (background); and  $W_{kl}$  is the covariance matrix [191].

Considering both the CPU time and machine learning performances, the settings in the TMVA methods were optimized as follows. The BDT method was set by: (1) using the adaptive boosting (AdaBoost) algorithm; (2) training 400 trees with a maximum depth of 3; and (3) using Gini index for the decision tree.

The MLP method was set with: (1) using sigmoid function as the activate function; and (2) using neural networks with 4 hidden layers and 200 training cycles. Detailed descriptions of these settings can be found in Ref. [192].

Eight variables were used as the TMVA inputs: ITR,  $\beta_{14}$ ,  $E_{fit}$ ,  $G_{test}$ ,  $U_{test}$ ,  $scaleLogL$ ,  $Z_{factor}$  and  $\vec{u} \cdot \vec{R}'$ . Among them, the beforehand cuts had been applied to the ITR and  $\beta_{14}$ , and the  $E_{fit}$  had been selected for different regions, as mentioned previously. NHits and  $\theta_{ij}$  were not used for they are considered redundant: NHits is correlated with the event energy, while  $\theta_{ij}$  is anticorrelated with  $\beta_{14}$ .

Using the  $4 < E < 15$  MeV training dataset as an example, the distributions of these variables are shown in Fig. 6.9. The differences in distributions between the signal inputs (black solid lines) and background inputs (red dotted lines) can be observed.

The output signal/background distributions on the test sub-dataset are shown in Fig. 6.10. As one of the essential TMVA outputs, the background rejection versus signal efficiency curve is denoted as a receiver operating characteristic (ROC) curve, which is usually used to test the performance of a machine learning classifier. The integral of the ROC curve, named “area under the curve” (AUC), is often used to summarize the quality of a ROC

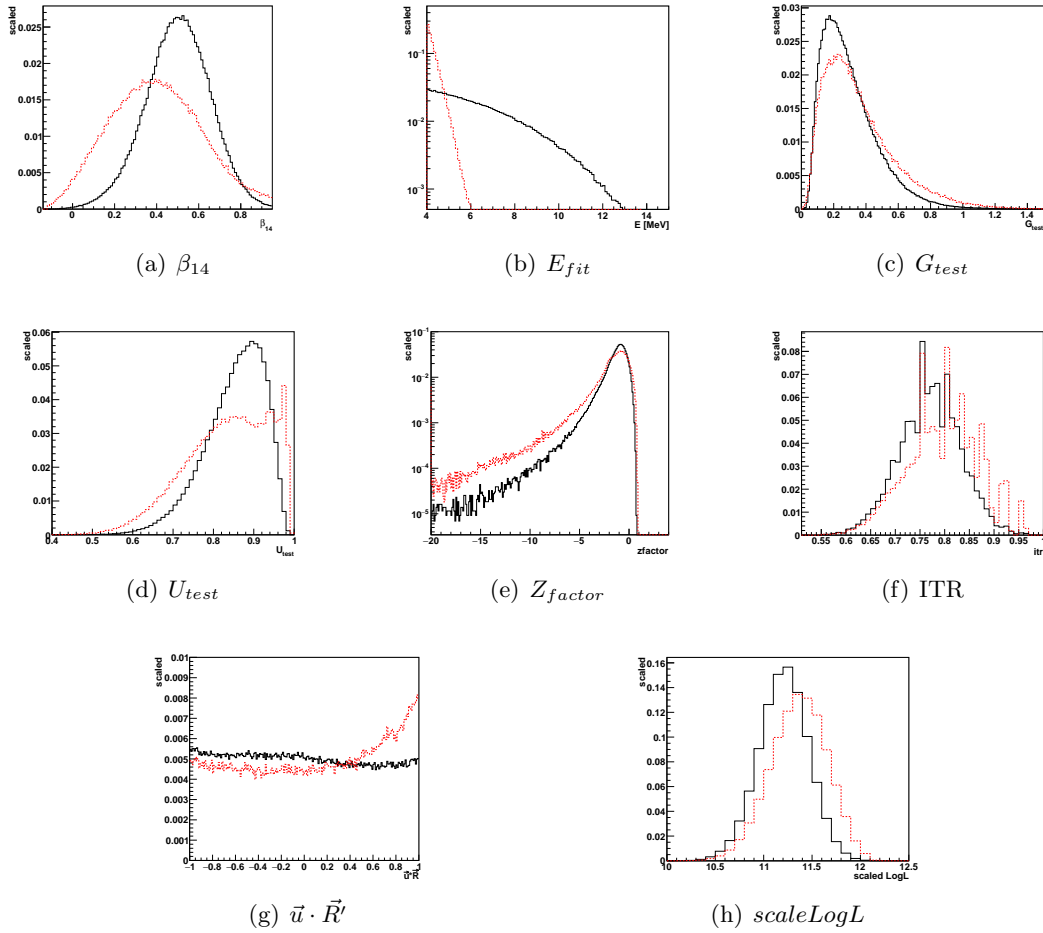


Figure 6.9: Multiple variables as the inputs for the TMVA analysis, for the  $4 < E < 15$  MeV dataset. The distributions of the backgrounds are shown in dotted red lines while the signals are shown in solid black lines. The distributions are normalized to their integrals.

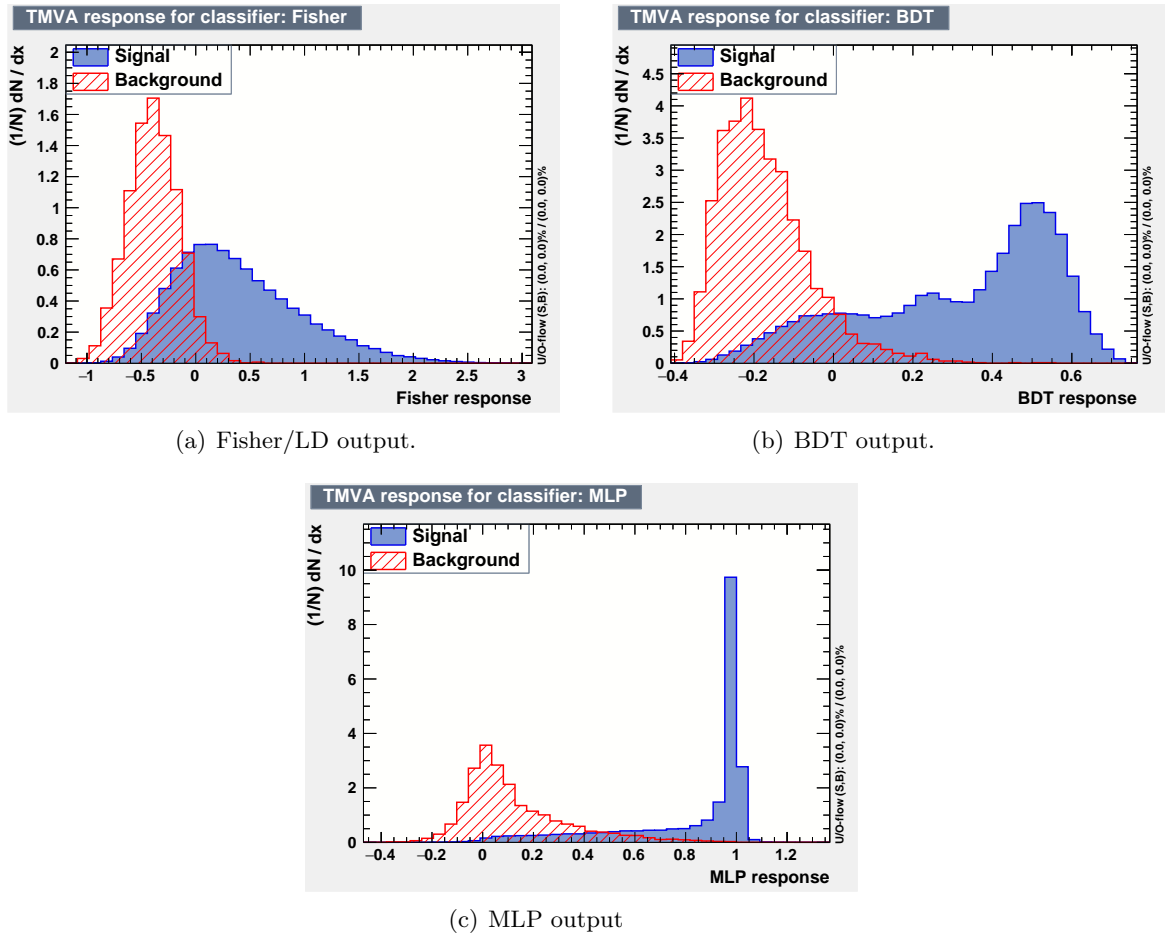


Figure 6.10: TMVA outputs for signal/background separations by the Fisher (a), BDT (b) and MLP (c) methods, for the  $5 < E < 15$  MeV testing dataset.

curve [194]. Fig. 6.11 shows the ROC curves for three different methods and for the testing datasets with different energy regions.

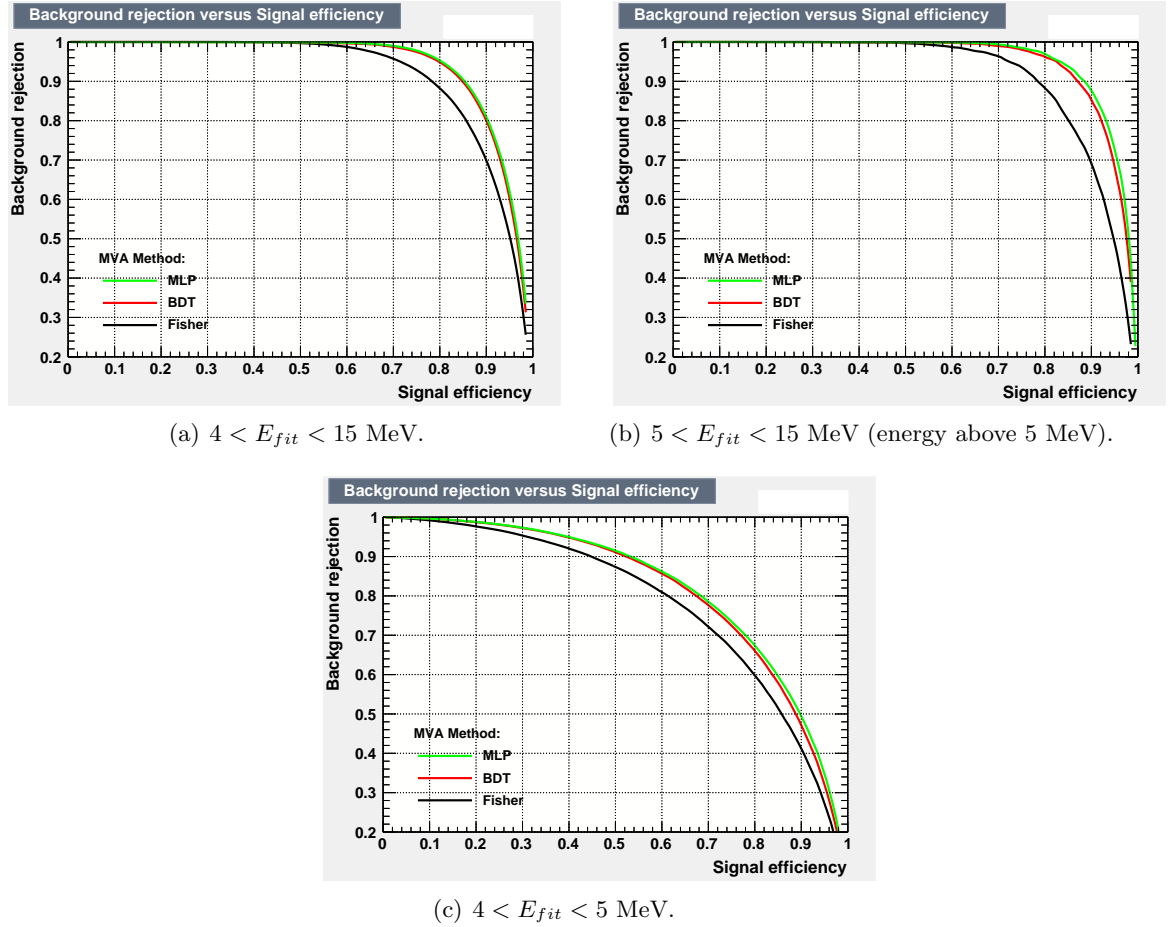


Figure 6.11: TMVA outputs (ROC) for signal/background separations by different methods, for the  $4 < E < 15$  MeV,  $5 < E < 15$  MeV, and  $4 < E < 5$  MeV testing dataset.

Typical CPU times ( $t_{CPU}$ ) to train each algorithm for chosen energy regions are listed in Table 6.5.

The testing results in Table 6.5 show that the Fisher/LD output gives the worst AUC. The BDT and MLP outputs are close to each other while the MLP gives the largest AUC values. However, the MLP was the most expensive method in terms of CPU usage. All three methods are less successful in separating signals from backgrounds in the lower energy region.

The distributions of  $\cos \theta_{\text{sun}}$  were used to show the performance of the solar  $\nu_e$  event

Table 6.5: Testing results from different TMVA methods.

Method	AUC	$t_{\text{CPU}}$ (second/ $10^6$ events)
$4 < E_{fit} < 15 \text{ MeV}$		
Fisher/LD	0.917	0.81
BDT	0.941	249.53
MLP	0.943	1370.02
$5 < E_{fit} < 15 \text{ MeV}$		
Fisher/LD	0.915	0.93
BDT	0.952	269.71
MLP	0.958	1450.90
$4 < E_{fit} < 5 \text{ MeV}$		
Fisher/LD	0.783	0.84
BDT	0.817	280.1
MLP	0.823	1337.9

selection and background event discrimination. Here I applied the BDT and the MLP method on the test sub-dataset. For the real dataset from run 200004 to 207718, the trained weights and variables from the BDT and the MLP methods were applied event by event, and then the discriminator responses,  $D_{\text{BDT}}$  and  $D_{\text{MLP}}$  were calculated by the TMVA respectively. The optimized cuts for the  $D_{\text{BDT}}$  and  $D_{\text{MLP}}$  were obtained by maximizing the *statistical significance*  $S/\sqrt{S+B}$ , where  $S$  is the number of the signal events and  $B$  is the number of the background events. As shown in Fig. 6.13 and Fig. 6.12, for the case of 71 solar  $\nu_e$  events ( $S = 71$ ) and 38 background events ( $B = 38$ ) (these two numbers were derived from the half dataset), the optimized cuts of  $D_{\text{BDT}} > -0.0578$  and  $D_{\text{MLP}} > 0.3476$  were found by the TMVA. Similarly, for the  $\nu_\mu$  case, the optimized cuts of  $D_{\text{BDT}} > -0.0752$  and  $D_{\text{MLP}} > 0.4585$  were found. These cuts were applied to the whole dataset to select the solar neutrino signal events and remove the backgrounds as well.

### 6.3.4 TMVA Outputs

The trained weights were applied to both the simulations and the actual data from the 92.54 live-day half-dataset. Fig. 6.14 shows the results provided by the BDT and MLP selections for the  $4 < E < 15 \text{ MeV}$  region. The BDT selection classifies about 80.8% of the total data as background events while the MLP classifies about 76.17% as background. Rather flat distributions for  $\cos \theta_{\text{sun}}$  are apparent in the plots. Since background events are

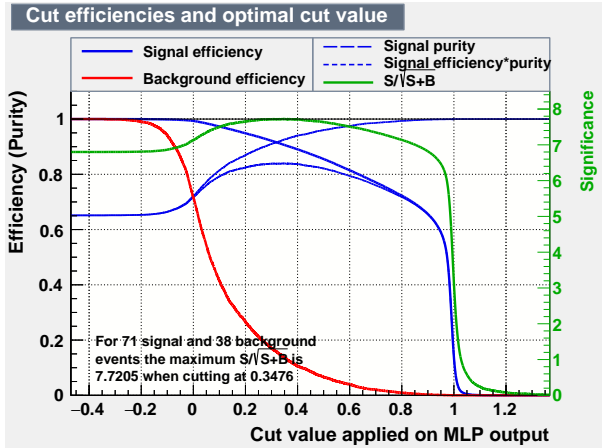


Figure 6.12: MLP cut efficiency, with  $5 < E_{fit} < 15$  MeV.

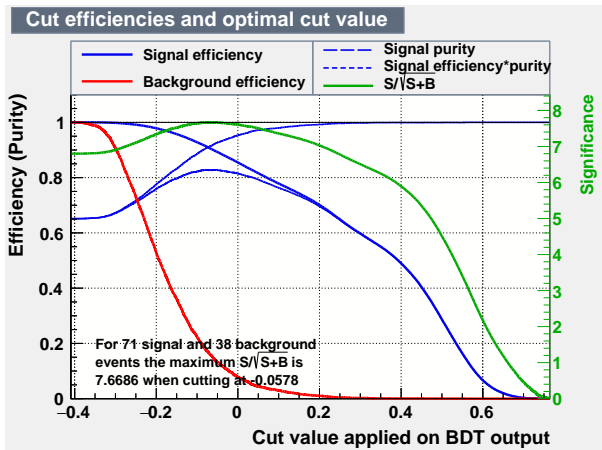


Figure 6.13: BDT cut efficiency, with  $5 < E_{fit} < 15$  MeV.

predominant in the  $4 < E < 5$  MeV region, the analyses to follow will focus only on the  $5 < E < 15$  MeV region.

To test the outputs, the same fake datasets mentioned in Sect. 6.3.2 were used. Fig. 6.15 shows the MLP output distributions of the  $\cos \theta_{\text{sun}}$  for one random fake dataset, for event energy range  $5 < E_{fit} < 15$  MeV. The output after the default cuts is also shown here as a comparison. For this fake dataset, the true number of signal and background events are:  $N_{sig}^{\text{true}} = 68$  and  $N_{bkg}^{\text{true}} = 46$ , while the MLP outputs are  $N_{sig}^{\text{MLP}} = 70$  and  $N_{bkg}^{\text{MLP}} = 44$ . Then the selection ratios of the MLP-selected event count to the true event count are  $N_{sig}^{\text{MLP}}/N_{sig}^{\text{true}} = 1.029$  for signal and  $N_{bkg}^{\text{MLP}}/N_{bkg}^{\text{true}} = 0.9565$  for background.

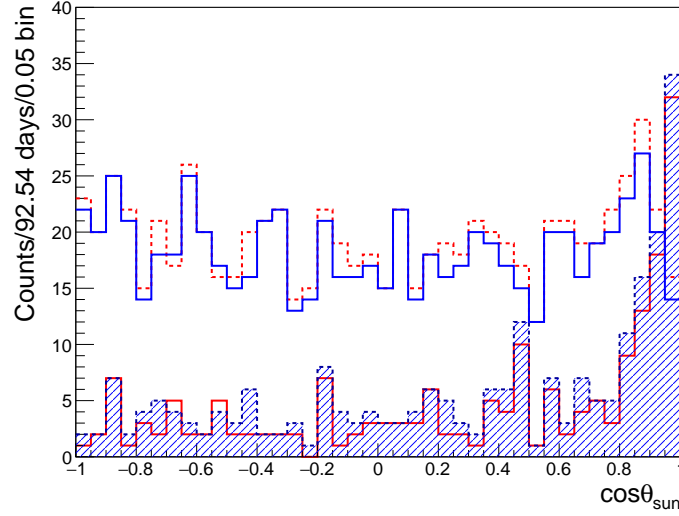


Figure 6.14: BDT and MLP outputs for  $\cos \theta_{\text{sun}}$ , in the  $4 < E_{\text{fit}} < 15$  MeV energy range. The solid red line shows the BDT-selected candidate solar  $\nu_e$  events, while the blue shaded histogram shows the MLP-selected ones. The dotted red line is for BDT-selected backgrounds, while the solid blue line is for the MLP-selected backgrounds.

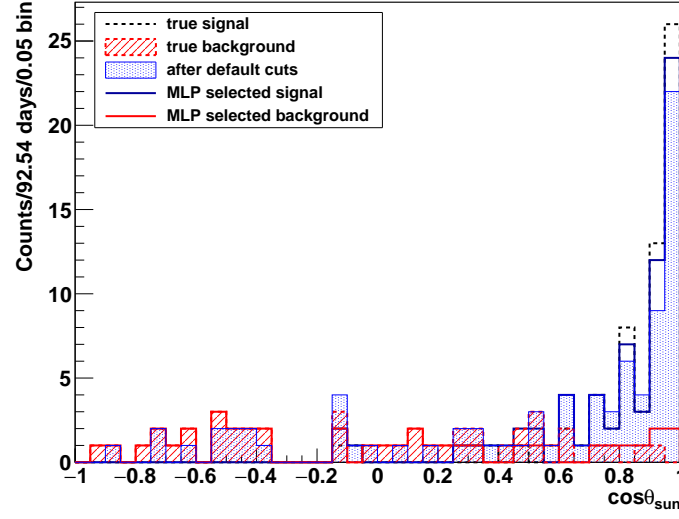


Figure 6.15: MLP outputs from one random fake dataset, with  $5 < E_{\text{fit}} < 15$  MeV. The dashed black line and the shaded red histogram are for the true signal and background events, respectively; the solid black line and the solid red line are for the MLP output of the signal and background events, respectively. Finally, the results after the default cuts are shown in the blue shaded area.

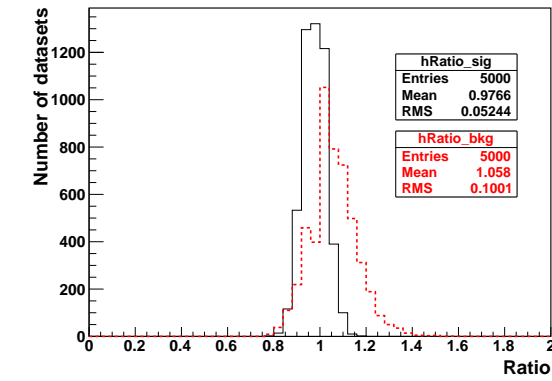
As shown in Fig. 6.16, applying the TMVA BDT and MLP selections to each of the 5000 fake datasets, the selection ratios were found to be  $N_{sig}^{\text{MLP}}/N_{sig}^{\text{true}} = 0.9802 \pm 0.05059$  for signal events, and  $N_{bkg}^{\text{MLP}}/N_{bkg}^{\text{true}} = 1.050 \pm 0.09587$  for background events (using the histogram mean and root mean square). For the MLP case, the ratios are  $N_{sig}^{\text{BDT}}/N_{sig}^{\text{true}} = 0.9766 \pm 0.05244$  and  $N_{bkg}^{\text{BDT}}/N_{bkg}^{\text{true}} = 1.058 \pm 0.1001$ . All these ratios fluctuate around 1.0, thus the TMVA selections are reasonable. To count for the systematic uncertainties from the MLP selection, Here the systematic uncertainties from the MLP selection are counted as  $0.9802 + 0.05059 = 1.031$  and  $0.9802 - 0.05059 = 0.9296$ . These two ratios were applied to the solar  $\nu_e$  MC simulations for evaluating the systematics in the flux scales, which will be discussed in Sect. 6.3.8.

### 6.3.5 Discussions of TMVA Results

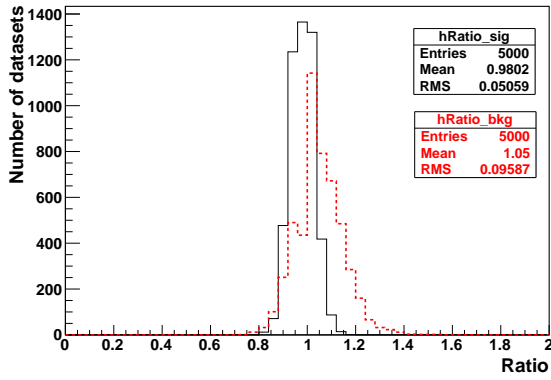
Further studies show that the underestimation of the signal and the overestimation of the background shown in Fig. 6.16 can be reduced by training the TMVA methods with different MC datasets, rather than using a merged MC dataset here. Training the TMVA methods with distinct MC datasets of the internal and external backgrounds separately can be especially useful, since the distributions of a few variables ( $\vec{u} \cdot \vec{R}'$ ,  $\beta_{14}$ ,  $U_{test}$ ,  $G_{test}$  and  $Z_{factor}$ ) are different in the cases of the internal and external backgrounds, as show in Fig. 6.17. Also, different types of background isotopes (such as  $^{208}\text{Tl}$  and  $^{214}\text{Bi}$ ) have different distributions of the input variables. Different MC datasets can be prepared for the TMVA training, and the TMVA outputs can be improved by applying the trained weights from different MC datasets separately. However, this procedure is complicated and not included in this thesis.

Removing the input variables with small differences observed in the distributions of signal and background can boost the TMVA training speed (for example, the ITR shown in Fig. ??). However, the changes in the BDT and MLP outputs are small, since these two methods can put fewer weights on such variables.

The TMVA methods optimize the cuts on more variables (FoMs) and make more stringent cuts to reduce the background events compared to the beforehand cuts. A more stringent radial cut (or tighter FV) can be applied on the low energy region  $4 < E_{fit} < 5$  MeV



(a) BDT.



(b) MLP.

Figure 6.16: Event count ratios from TMVA outputs on 5000 fake datasets, with  $5 < E_{fit} < 15$  MeV. The top is for the BDT results and the bottom is for the MLP results. The black histogram is the distribution of the signal ratios, and the dashed red histogram is the distribution of the background ratios.

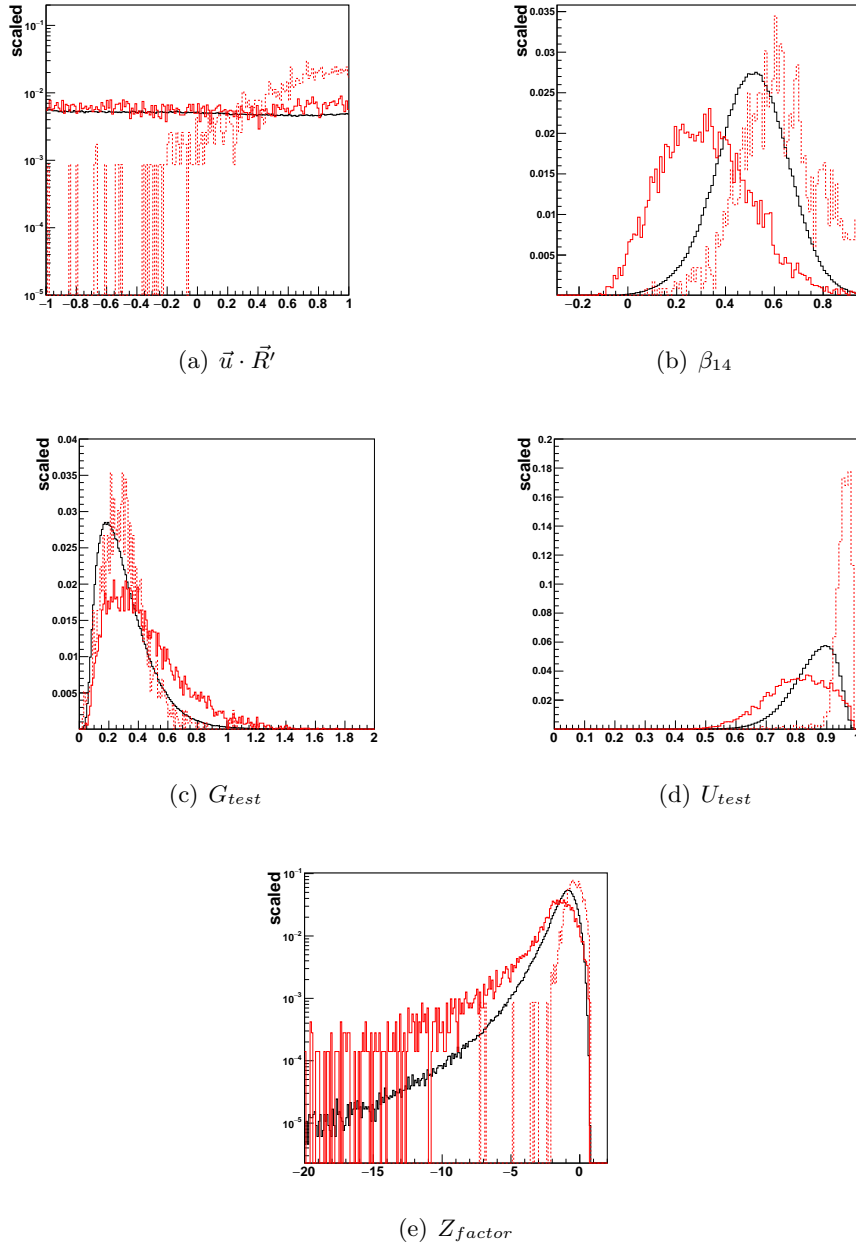


Figure 6.17: The distributions of six variables from the simulated internal and external  $^{208}\text{Tl}$  backgrounds, with  $5 < E_{fit} < 15$  MeV. The solar  $\nu_e$  signal distributions are also compared. Here the “external backgrounds” include the AV and external water backgrounds. The distributions of the internal (external) backgrounds are shown in solid (dashed) red lines, while the solar  $\nu_e$  signals are shown in solid black lines. The distributions are normalized to their integrals.

to eliminate further background events, which dominate in that region. However, tighter cuts can also eliminate the signal events.

Other multivariate analysis packages, such as `StatPatternRecognition` (SPR) [195] developed for high energy physics, can also be considered as an alternative tool or as a reference for results comparisons.

### 6.3.6 Fitting Whole Low Background Dataset

To combine the analyses in the previous two sections, the TMVA selection methods were applied to the actual data of the 190.33 live-day whole dataset, and then a maximum likelihood fit was applied to the selected data.

For the whole dataset, the TMVA methods were applied to the whole MC datasets of the solar  $\nu_e$  simulations as well as the background simulations<sup>3</sup>. Similarly, the training subset used 70.25% of the whole dataset (run 200004 to 205296), while the testing subset used the rest 29.75% (run 205297 to 207718). The trained BDT and MLP weights were applied to the whole dataset.

In the region of  $5 < E_{fit} < 15$  MeV, the outputs from the BDT and MLP were fitted to obtain  $N_{sig}$  and  $N_{bkg}$ . Fig. 6.18(a) and 6.18(b) show their results respectively. For comparison, the results from applying the default cuts are shown in Fig. 6.18(c). The fit results are summarized in Table 6.6.

Table 6.6: Fit results for the whole dataset ( $5 < E < 15$  MeV).

Methods	$N_{sig}$	$N_{bkg}$	$R_{sig}$	$R_{bkg}$	$p$ -value
BDT	$124.1 \pm 12.15$	$39.94 \pm 7.966$	$0.9381 \pm 0.09186$	$0.3020 \pm 0.06024$	0.1417
MLP	$126.1 \pm 12.23$	$40.94 \pm 8.022$	$0.9532 \pm 0.09245$	$0.3096 \pm 0.06066$	0.1179
Default	$119.33 \pm 11.96$	$42.67 \pm 8.15$	$0.90 \pm 0.09$	$0.32 \pm 0.06$	0.19

Results from the three methodologies are consistent with each other. The estimated background rate in the [5,15] MeV energy region is about  $\frac{1}{3}$  of the signal rate, which indicates that a low background measurement is achieved for the solar neutrino analysis with the energy down to 5 MeV. For the sake of simplicity, since the output from the BDT selection gives a better  $p$ -value, the analyses to follow will use only the BDT selector.

<sup>3</sup>The simulations of solar  $\nu_\mu$  were also trained with the background simulations separately to calculate the detected  $\nu_\mu$  from the oscillated solar neutrino flux mentioned in next section

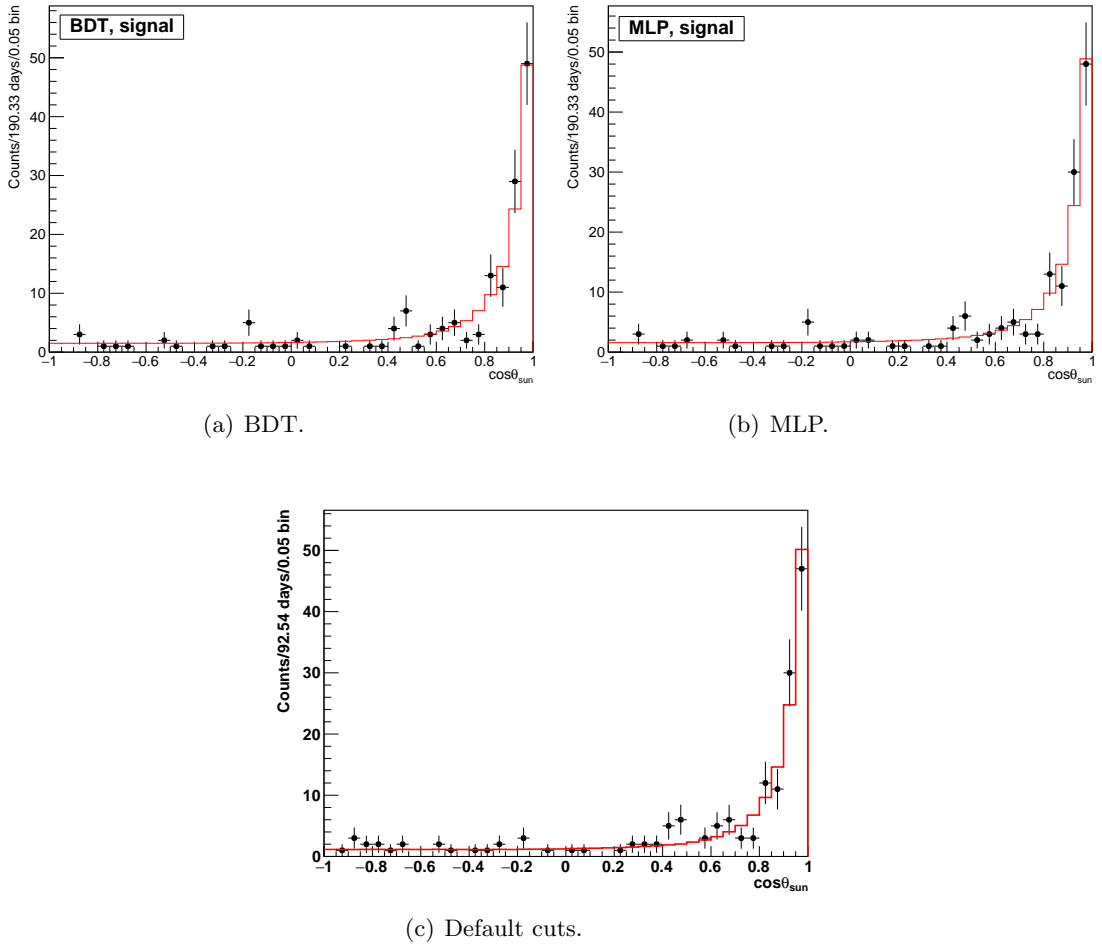


Figure 6.18: Poisson fit results for the  $5 < E_{\text{fit}} < 15$  MeV range, from the outputs of BDT (a), MLP (b), and default cuts (c).

### 6.3.7 Evaluating ${}^8\text{B}$ Solar Neutrino Flux

A program called **PSelmaa** (Physics interpretation Sun-Earth Large Mixing Angle Adiabatic Approximation) was implemented in **RAT** [196]. The software uses the BS05(OP) SSM model. It assumes the normal mass hierarchy, and it applies the MSW effects due to the Sun (see Chapter 2) but neglects the MSW effects due to the Earth (i.e., the regeneration of coherence in the Earth). Fig. 6.19 shows the survival probability curve as a function of energy (in 0.1 MeV intervals) taken from the **PSelmaa** (as SNO+ can not discriminate  $\nu_\mu$  and  $\nu_\tau$ , only the  $\nu_\mu$  MC is included in  $P_{e\alpha}$ ).

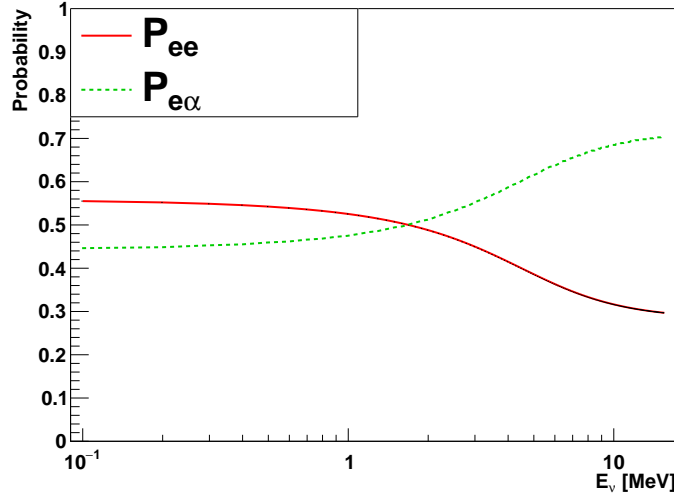


Figure 6.19: The MSW survival probability curves as functions of MC energy. The  $P_{ee}$  is in solid red line and  $P_{e\alpha}(= 1 - P_{ee})$  is in dashed green line.

In order to enlarge the MC datasets for analysis, the MC simulations of solar neutrinos were produced much larger than the expected numbers. The number of simulated solar  $\nu_e$  events is 1700 times the nominal (flux scale =  $\frac{1}{1700}$ ); while the number of solar  $\nu_\mu$  events is 9600 times the nominal (flux scale =  $\frac{1}{9600}$ ). The two flux scale factors are prescribed according to the ratio of the ES cross-sections:  $\sigma^{ES}(\nu_e + e^-)/\sigma^{ES}(\nu_{\mu,\tau} + e^-) \approx 6.5$ , as mentioned in Sect. 2.2.1. A nominal  ${}^8\text{B}$  solar  $\nu_e$  flux  $\Phi_{MC}^{total} = 5.46 \times 10^6 \text{ cm}^{-2}\text{s}^{-1}$  from the SSM prediction (see Refs. [17, 197]) is used by the simulation.

Since it is impossible for the SNO+ detector to discriminate between  $\nu_\mu$  and  $\nu_\tau$  by detecting the elastic scattering events,  $\nu_\tau$  is not generated separately [186]. Therefore, the generated solar  $\nu_\mu$  events are considered as a combination of  $\nu_\mu$  and  $\nu_\tau$  ( $\nu_\mu \approx \nu_{\mu,\tau}$ ) in the solar neutrino flux. In addition, due to the data cleaning procedure, the actual live time of the data is slightly shorter than the raw live time used by the MC simulations. To compare the MC with the data, a live time fraction was applied to the MC:  $f_{\text{live time}} = \frac{t_{\text{data live time}}}{t_{\text{MC run time}}} = \frac{190.33 \text{ days}}{198.17 \text{ days}} = 0.96$ . Similarly, assuming a sacrifice of 1.2% from the data cleaning cuts on the data<sup>4</sup>, a scale factor  $f_{\text{dataClean}} = (1 - \frac{1.2}{100}) = 0.988$  was applied to the MC simulations. Accordingly the numbers of MC-generated  $\nu_e$  and  $\nu_\mu$  events are scaled by  $f_{\text{live time}}$  and

<sup>4</sup>This sacrifice was determined by the collaboration in 2017 and was used in Refs. [186]. However, this value needs to be updated for the dataset used here.

flux scale, then weighted by the oscillation probabilities  $P_{ee}$  and  $P_{e\alpha} = 1 - P_{ee}$ . Applying these weighting parameters as well as the BDT selections to the MC histograms, the MC  $\cos \theta_{\text{sun}}$  distributions in the energy region  $5 < E_{\text{fit}} < 15$  MeV are shown (with and without oscillations) in Fig. 6.20.

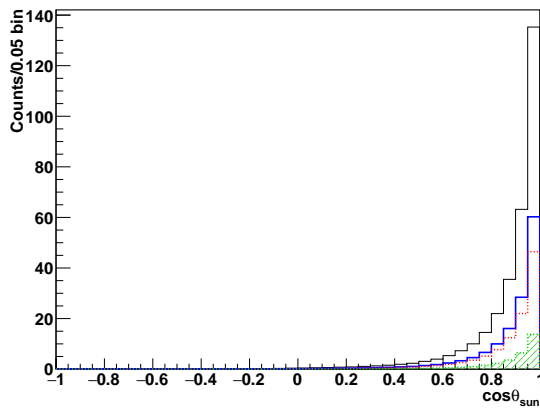


Figure 6.20: The MC  $\cos \theta_{\text{sun}}$  distributions used as PDFs for the flux calculations, for  $5 < E_{\text{fit}} < 15$  MeV after the BDT selections. The black histogram is the  $\nu_e$  flux without oscillation, denoted  $\text{PDF}(\nu_e, \text{without oscillation})$ . This histogram is used for fitting the elastic scattering flux. The histogram in dashed red line is the  $\nu_e$  flux and the green shaded histogram is the  $\nu_\mu$  flux, both including the oscillation. These two histograms were combined to form the total flux including the oscillation, which is given by the blue line and is denoted by  $\text{PDF}(\nu_e + \nu_\mu, \text{oscillated})$ . This (blue) histogram is used for fitting the total flux.

Reading from the above histograms, the expected event count for  $\nu_e$  without the oscillation is  $N_{\nu_e} = 314.679$ . Assuming a flux of  $\nu_\mu$ , the expected number of  $\nu_\mu$  is  $N_{\nu_\mu} = 49.2741$ , then  $N_{\nu_e}/N_{\nu_\mu} \approx 6.4$ , which is consistent with the ratio of the cross-sections mentioned before. Including the oscillations, the expected event counts for  $\nu_e$  and  $\nu_\mu$  are  $N_{\nu_e}^{\text{osci}} = 109.494$  and  $N_{\nu_\mu}^{\text{osci}} = 32.0757$  respectively, and the combined event count is  $N_{\nu_e+\nu_\mu}^{\text{osci}} = 141.569$ .

To fit for the total  ${}^8\text{B}$  neutrino flux, the fit parameter used here is the flux scale  $f_s^{\text{tot}}$ , which is interpreted as the fraction of the observed  ${}^8\text{B}$  flux to the expected flux. Using the same method in Sect. 6.3.1, and in the Eqn. 6.2, replacing the  $N_{\text{sig}}$  with  $N_{\text{sig}} = f_s^{\text{tot}} \cdot N_{\nu_e+\nu_\mu}^{\text{osci}}$  (where the estimated  $N_{\nu_e+\nu_\mu}^{\text{osci}} = 141.57$ ), and then fitting the  $f_s^{\text{tot}}$  and the  $N_{\text{bkg}}$  with the  $\text{PDF}(\nu_e + \nu_\mu, \text{oscillated})$ . The fit results are  $f_s^{\text{tot}} = 0.8462 \pm 0.08398$  (corresponding to  $N_{\text{sig}} = 119.8 \pm 11.89$  events) and  $N_{\text{bkg}} = 38.20 \pm 7.731$  events, with a  $p$ -value of 0.1470.

Fig. 6.21 shows the fit spectrum.

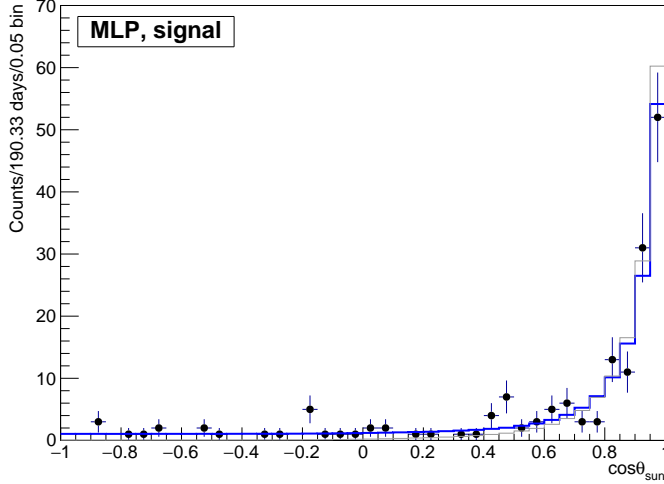


Figure 6.21: A fit on the total  ${}^8\text{B}$  flux. The black dots are the data points and the blue histogram is the fit.

To fit for the  ${}^8\text{B}$  flux corresponding to an observed flux of ES interactions, the same procedure was used, while the fit parameter was changed to  $N_{sig} = f_s N_{\nu_e}$  ( $= 314.68$ ) and the PDF was changed to  $\text{PDF}(\nu_e, \text{without oscillation})$ . As shown in Fig. 6.22, the fit results are  $f_s^{ES} = 0.3798 \pm 0.03772$  (corresponding to  $N_{sig} = 119.5 \pm 11.62$  events) and  $N_{bkg} = 38.48 \pm 7.751$  events, with a  $p$ -value = 0.140.

The  $N_{sig}$  and  $N_{bkg}$  values obtained here by fitting the flux fractions are consistent with the values obtained in Sect. 6.3.6.

With the nominal  ${}^8\text{B}$  solar neutrino flux  $\Phi_{MC}^{total}$ , the estimated total flux is:

$$\Phi^{total}({}^8\text{B}) = f_s^{tot} \cdot \Phi_{MC}^{total} = (4.62 \pm 0.459(\text{stat.})) \times 10^6 \text{ cm}^{-2}\text{s}^{-1}, \quad (6.7)$$

and the estimated elastic scattering flux is:

$$\Phi^{ES} = f_s^{ES} \cdot \Phi_{MC}^{total} = (2.074 \pm 0.2061(\text{stat.})) \times 10^6 \text{ cm}^{-2}\text{s}^{-1}. \quad (6.8)$$

The next section will evaluate the systematic uncertainties of the flux fractions.

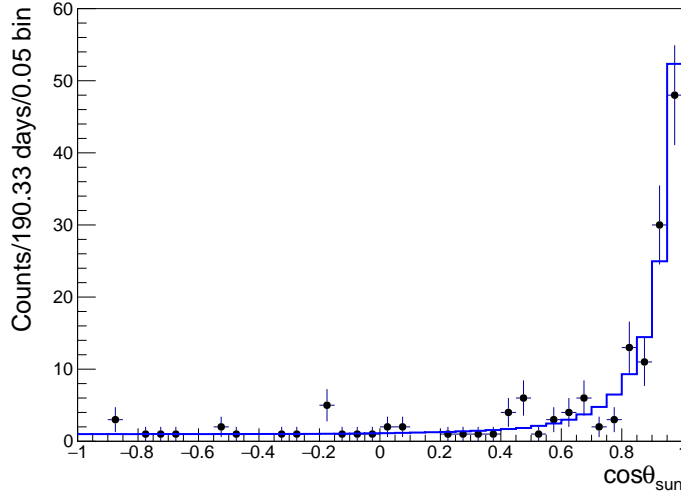


Figure 6.22: Fitting with the spectrum of elastic scattering. The black dots are the data points and the blue histogram is the fit.

### 6.3.8 Systematics Evaluation

In Chapter 5, the reconstruction systematics of the event position, direction, and energy were obtained. The quantities of position scale, position shifts, direction resolution,  $\beta_{14}$  shifts, energy scale ( $E_{scale}$ ) and energy resolution ( $E_{resol}$ ) were used to evaluate the systematic uncertainties of the solar neutrino analysis. Table 6.7 summarizes these systematics and their applications to transform the reconstructed results. In this thesis, only the systematics mentioned below were taken into account, and these systematics are considered uncorrelated.

Note that the position shifts were applied to the  $x_{fit}$ ,  $y_{fit}$ , and  $z_{fit}$  respectively, while the position scales were applied simultaneously to the position vector:

$$\vec{X}'_{fit} = ((1 + \Delta x^\pm)x_{fit}, (1 + \Delta y^\pm)y_{fit}, (1 + \Delta z^\pm)z_{fit}) .$$

For  $\delta_\theta$ , since there is no physical meaning to the case that  $|\cos \theta_{\text{sun}}| > 1$ , a procedure following Ref. [176] was performed: if the transformation causes  $\cos \theta_{\text{sun}} > 1$ , the smeared value is reset to 0.999; on the other hand, the  $\cos \theta_{\text{sun}} < -1$  case happens more frequently and is considered to be a consequence of mis-reconstruction. In this case, a random value is chosen by uniformly sampling on the range [-1,1].

Table 6.7: Systematics for the solar  $\nu_e$  analysis in the water phase. See Sect. 5.3.1.2, 5.3.2.2, 5.3.3 and 5.3.4.4 for details. The positive and negative values of a quantity  $Q$  are denoted as  $Q^+$  and  $Q^-$ , respectively.

Systematics	values ( $Q^+/Q^-$ )	transformation
$x$ shift ( $\Delta x^\pm$ )	+6.48/-5.98 mm	$x_{fit} + \Delta x^\pm$
$y$ shift ( $\Delta y^\pm$ )	+6.13/-4.11 mm	$y_{fit} + \Delta y^\pm$
$z$ shift ( $\Delta z^\pm$ )	+6.71/-4.82 mm	$z_{fit} + \Delta z^\pm$
$x$ resolution ( $\sigma_x$ )	113.6 mm	$x_{fit} + Gaus(0, \sigma_x)$
$y$ resolution ( $\sigma_y$ )	90.99 mm	$y_{fit} + Gaus(0, \sigma_y)$
$z$ resolution ( $\sigma_z$ )	145.56 mm	$z_{fit} + Gaus(0, \sigma_z)$
$x$ scale ( $\delta_x^\pm$ )	+0.07%/-0.06%	$(1 + \delta_x^\pm)x_{fit}$
$y$ scale ( $\delta_y^\pm$ )	+0.02%/-0.07%	$(1 + \delta_y^\pm)y_{fit}$
$z$ scale ( $\delta_z^\pm$ )	+0.08%/-0.01%	$(1 + \delta_z^\pm)z_{fit}$
$r'$ scale ( $\delta_{r'}^\pm$ )	$\sqrt{\sum_{i=1}^3 (\frac{\partial r'}{\partial x_i})^2 (\delta_{x_i}^\pm)^2}$	$(1 \pm \delta_{r'}^\pm/100)r'$
direction resolution ( $\delta_\theta^\pm$ )	+0.013/-0.101	$1 + (\cos \theta_{\text{sun}} - 1)/(1 + \delta_\theta^\pm)$
$E_{scale}$ ( $\Delta_{\delta_E}$ )	1.0%	$(1 \pm \Delta_{\delta_E})E_{fit}$
$E_{resol}$ ( $\Delta_b$ )	$0.037 \sqrt{\text{MeV}}$	$E_{fit} + Gaus(0, \sigma_{smear})$ , $\sigma_{smear} = \sqrt{E_{fit}} \sqrt{(1 + \Delta_b)^2 - 1}$
–	–	$\beta_{14} + \Delta \beta_{14}^\pm$
$\beta_{14}$ shift ( $\Delta \beta_{14}^\pm$ )	+0.010/-0.036	

To evaluate the systematics of the solar neutrino analysis, the systematic transformations in Table 6.7 were applied to the reconstructed quantities in MC simulations independently. The reconstructed quantities after the transformations are called “smeared” values. The smeared values of an event can affect whether the event will pass the cuts: the smeared positions of an event affect whether the event can pass the fiducial volume cut and then affect the results after the position cuts; the smeared energies affect the results after the energy cuts and the smeared  $\beta_{14}$  affect the results after the  $\beta_{14}$  cuts. Thus, for the solar  $\nu_e$  and  $\nu_\mu$  simulations, the shape of the  $\cos \theta_{\text{sun}}$  distribution used as the PDF will be changed by the smeared values. In addition, the  $\delta_\theta$  transformation changes the PDF shape directly. Finally, the spectrum of the data was re-fit with the smeared PDFs to obtain the smeared physics quantity (specifically, the flux ratio  $f_s$  mentioned in the previous section), and the differences between the original value and the smeared value are used as the systematics of the physics quantity.

To obtain the smeared PDFs, first, only the cuts  $5 < E_{fit} < 15$  MeV (for selecting energy region),  $\text{NHits} > 20$  (reconstruction threshold) and  $\text{ITR} > 0.55$  (determined from

the instrumental noises and its systematic uncertainty was not considered) were applied to the MC simulations of the solar  $\nu_e$  and  $\nu_\mu$ . Then the systematic transformations were applied one by one and event by event. For the transformations, the positive (“smearing up”) and negative (“smearing down”) values were applied, respectively. After the transformation, the whole beforehand cut was applied. Lastly, the TMVA BDT selection was applied. For a specific smeared quantity, the final output of the MC  $\cos \theta_{\text{sun}}$  spectrum was used as the smeared PDF for that quantity. For example, if  $E_{fit}$  is smeared by scaling up, i.e.  $E'_{fit} = (1 + \Delta_{\delta_E})E_{fit}$ , then the outputs of the  $\cos \theta_{\text{sun}}$  after the beforehand cut and TMVA BDT selection is used as the “energy scale-up PDF”.

Fig. 6.23 shows the effects of smearing the direction parameter, energy scale, and energy resolution on the MC PDF. The original MC PDF is shown as black solid line histograms, overlaid by the smeared histograms.

Applying the systematic transformation in Table 6.7 to the MC ES PDF, and then refitting the data with the smeared PDFs for each quantity, the smeared values of the flux fractions ( $f'_s$ ) were found. The systematics of the  $f_s$  are calculated by  $\Delta f_s = f'_s - f_s$ . These results are listed in Table 6.8. To summarise, the systematic uncertainties from the smeared  $\beta_{14}$  are negligible, while those resulting from smearing the position, direction, and energy result in more significant uncertainties.

Table 6.8: Systematics for the fitted flux scale  $f_s$ .

Systematics	$\Delta f_s (+/-)$
$x$ shift	+0.001891/-0.001962
$y$ shift	+0.001888/-0.001955
$z$ shift	+0.002071/-0.001818
$x$ resolution	+0.0001450/-0.0001450
$y$ resolution	+0.00009800/-0.00009800
$z$ resolution	+0.0001290/-0.0001290
$r'$ scale	+0.001423/-0.001237
position scale	+0.000583/-0.00306
direction resolution ( $\delta_\theta$ )	+0.01676/-0.004034
$E_{scale}$ ( $\Delta_{\delta_E}$ )	+0.01456/-0.01752
$E_{resol}$ ( $\Delta_b$ )	+0.003363/-0.003363
$\beta_{14}$ shifts	+0.003968/-0.003285

Using the quadrature sum ( $\sigma_{tot}^2 = \sum_i \sigma_i^2$ ) which assumes that all the systematic variables

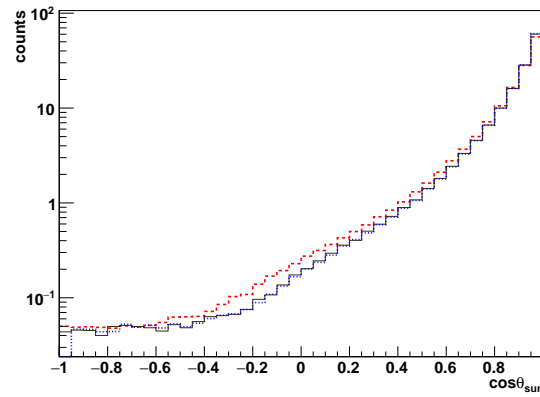
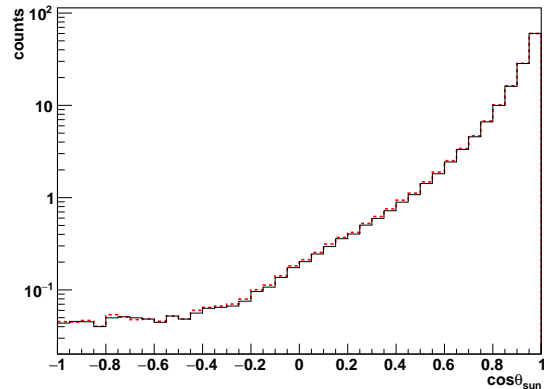
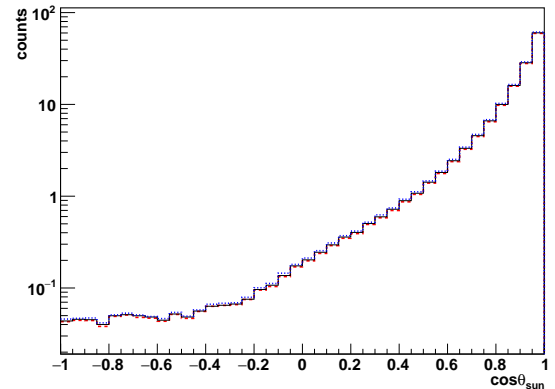
(a) Smearing direction parameter  $\delta_\theta$ .(b) Smearing energy resolution  $\Delta_b$ .(c) Smearing energy scale  $\Delta_{\delta_E}$ .

Figure 6.23: Smearing effects on the  $\cos\theta_{\text{sun}}$ . The histogram with a solid black line is the PDF before smearing. The dotted blue histogram is for smearing up the quantity (i.e., taking the positive values) and the dashed red is for smearing down (i.e., taking the positive values).

are independent, the total systematic uncertainty of the total flux fraction  $f_s^{tot}$  is expected to be:  $(f_s^{tot})_{-0.01917}^{+0.02311}$ . Using the same procedure to evaluate the systematics of the elastic scattering flux fraction  $f_s^{ES}$  gives  $(f_s^{ES})_{-0.008324}^{+0.009676}$ .

### 6.3.9 Summary of Results

With the systematic uncertainties of the flux fractions obtained from the previous section, the total flux is:

$$\Phi_{fit}^{total}(^8\text{B}) = f_s \cdot \Phi_{MC}^{total} = (4.62 \pm 0.459(stat.)_{-0.105}^{+0.126}(syst.)) \times 10^6 \text{ cm}^{-2}\text{s}^{-1}, \quad (6.9)$$

while the ES flux is:

$$\Phi_{ES} = f_s \cdot \Phi_{MC}^{total} = (2.07 \pm 0.206(stat.)_{-0.0455}^{+0.0528}(syst.)) \times 10^6 \text{ cm}^{-2}\text{s}^{-1}. \quad (6.10)$$

A quadratic total uncertainty  $\sigma_{tot}$  is calculated by combining the larger uncertainties in statistics and systematics:

$$\sigma_{tot} = \sqrt{\sigma_{stat,large}^2 + \sigma_{sys,large}^2}. \quad (6.11)$$

Fig. 6.24 shows a comparison of the  $\Phi_{ES}$  results given here to recent measurements from SNO+ [1], Super-K [45] and Borexino [49]. The energy regions for the analyses, the start and end dates of the data-taking, and the live time are also shown in the figure.

To combine the results from different experiments, an unconstrained average value  $\hat{\theta}$  and its uncertainty  $\sigma_{\hat{\theta}}$  are calculated by [17, 198]:

$$\hat{\theta} = \sum_{i=1}^N \left( \frac{x_i}{\sigma_i^2} \right) \Bigg/ \sum_{i=1}^N \left( \frac{1}{\sigma_i^2} \right), \quad (6.12)$$

$$\sigma_{\hat{\theta}} = \left[ \sum_{i=1}^N \left( \frac{1}{\sigma_i^2} \right) \right]^{-\frac{1}{2}}, \quad (6.13)$$

where  $x_i$  is the measured  $\Phi_{ES}$  value from each experiment, and the  $\sigma_i$  is the total uncertainty  $\sigma_{tot}$  calculated from each experiment.

Combined with the results from other experiments, the average results are listed in Table 6.9. The  $\Phi_{ES}$  result from this thesis is combined with the SNO+ 2018 result and

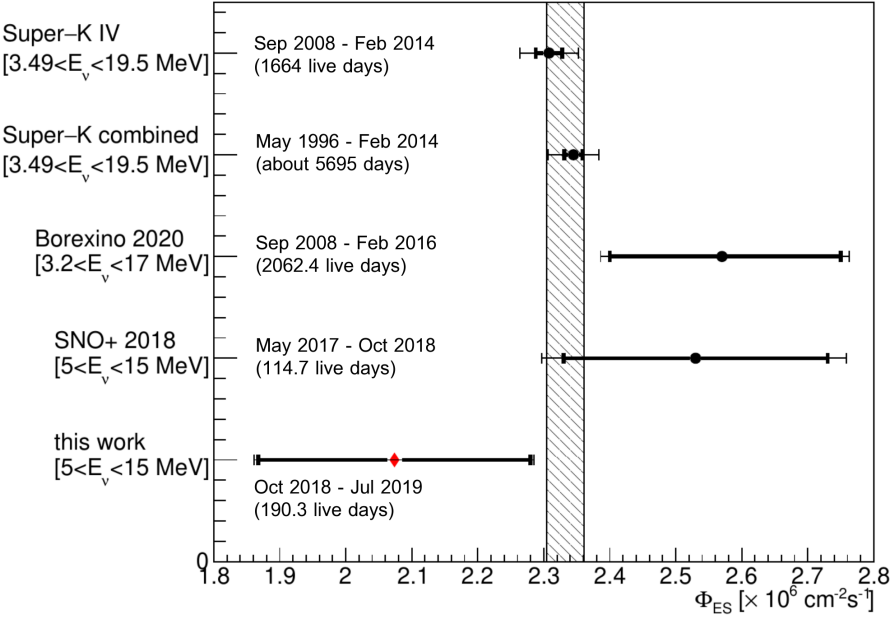


Figure 6.24: A comparison of the ES fluxes measured recently by three independent experiments: SNO+ 2018 published data (SNO+ 2018) [1], Super-K phase-IV measurement (Super-K IV) and the combined four phases measurement (Super-K combined) [45], and the Borexino measurements published in 2020 (Borexino 2020) [49]. The thick error bars include the statistical errors and the thin ones are quadratic errors including both the statistical and systematical errors. The shaded band is for the unconstrained average value and uncertainty of all the results:  $\hat{\theta} \pm 1\sigma_{\hat{\theta}}$ .

then with all the other experiments' results. The average result without this work is shown in the same plot. All the three average results are consistent with each other.

From the average result including all the experiments mentioned, the region of  $\hat{\theta} \pm 1\sigma_{\hat{\theta},tot}$  is plotted as the shaded band in Fig. 6.24.

### 6.3.10 Limitations of this Study

This study focuses on measuring solar neutrinos in the energy region [5,15] MeV with a fiducial volume of 5.5 m.

As listed in Table 6.3, I only used the  $^{208}\text{Tl}$  and  $^{214}\text{Bi}$  backgrounds simulated in three detector components. The other sources of backgrounds were not included, such as the radio-isotopes in AV ropes and PMTs (etc.) and cosmic muon induced isotopes. A more comprehensive study would be required if one wished to simulate and account for all possible

Table 6.9: Average results.

Combinations	$\Phi_{ES} (\times 10^6 \text{ cm}^{-2}\text{s}^{-1})$
not including this work	$2.338 \pm 0.02868$
this work and SNO+ 2018	$2.281 \pm 0.1572$
all	$2.333 \pm 0.02843$

background events.

To fit the background events, I assumed a flat distribution of  $\cos \theta_{\text{sun}}$ . A more realistic distribution could be investigated to more properly describe the backgrounds. Furthermore, background levels might vary over time, so a more detailed analysis including different time intervals would increase confidence that the present results are representative.

The evaluation here of systematic uncertainties is not comprehensive. In particular, uncertainties intrinsic to the solar neutrino model used by the MC simulations to “produce” solar neutrinos and apply oscillations are *not included* here. The uncertainties in the SSM model as well as the neutrino flavor transformation parameters can affect the MC simulations. In addition, the energy calibration used to mitigate the difference between data and simulations is not applied. This procedure can reduce the uncertainties from the energy reconstructions.

Since the dataset used here has a very low level of background events, it is possible to probe the energy region down to 3.5 MeV, enabling the study of the solar neutrinos in a lower energy region. However, since the reconstruction threshold was set as  $\text{NHits} > 20$ , that analysis is not included in the thesis. It may be worthwhile to investigate the data with a lower NHit threshold down to  $\text{NHits} > 6$ , and to apply a proper TMVA method selection for reducing the backgrounds in the lower energy region.

# Chapter 7

## Conclusions

In this thesis, a reconstruction algorithm framework (the Multi-Path Fitter) was developed for multiple SNO+ physics phases. For the SNO+ detector with a diameter of 12 m, it achieves position resolutions of 300 mm for the water phase and 70 mm for the scintillator phase. The position biases are within 100 mm for both phases. This framework has been applied to the SNO+ water phase and partial-fill phase analysis, and it has potentials to be applied in the scintillator phase and tellurium phase. This thesis used the fitter for analyzing the  ${}^8\text{B}$  solar neutrinos during the water phase. The fitter was also used by the SNO+ collaboration as the prime vertex fitter for the physics analyses during the partial-fill phase.

For the water phase, the reconstruction uncertainties in event position, direction and energy were determined by analyzing the data and simulations of  ${}^{16}\text{N}$  source calibrations. For a fiducial volume of 5.5 m, the position biases between the data and simulations in the  $(x, y, z)$  axes are all within  $\pm 10$  mm; the fractional energy scale uncertainty is 1.0%, and the fractional uncertainty on the energy resolution at kinetic energy  $T_e$  is  $0.037\sqrt{T_e/\text{MeV}}$ .

By utilizing the water phase reconstruction, this thesis provides an alternative analysis for the  ${}^8\text{B}$  solar neutrino measurement during the SNO+ water phase. By looking at the low background dataset for 190.33 live days, a  ${}^8\text{B}$  solar neutrino rate of  $0.90 \pm 0.09$  events/(kt·day) with a background rate of  $0.29 \pm 0.06$  events/(kt·day) in the energy region [5,15] MeV were obtained. As the energy threshold is pushed down to 5 MeV, this background rate is significantly low for the solar neutrino measurement in a water Cherenkov

detector.

The result also gives an estimated  ${}^8\text{B}$  solar neutrino flux as:

$\Phi_{^8\text{B}} = (4.62 \pm 0.459(\text{stats.})^{+0.126}_{-0.105}(\text{syst.})) \times 10^6 \text{ cm}^{-2}\text{s}^{-1}$ , while the elastic scattering flux is measured as:

$$\Phi_{\text{ES}} = (2.07 \pm 0.206(\text{stats.})^{+0.0528}_{-0.0455}(\text{syst.})) \times 10^6 \text{ cm}^{-2}\text{s}^{-1}.$$

The  $\Phi_{\text{ES}}$  result given here is consistent with the recent measurements from the Super-Kamiokande and Borexino experiments.

# Bibliography

- [1] M. Anderson, S. Andringa, S. Asahi, M. Askins, D. Auty, N. Barros, D. Bartlett, F. Barão, R. Bayes, E. Beier, *et al.*, “Measurement of the  ${}^8\text{B}$  solar neutrino flux in SNO+ with very low backgrounds,” *Physical Review D*, vol. 99, no. 1, p. 012012, 2019.
- [2] SNO+ Collaboration, “SNO+ director’s review documentation,” *SNO+ Internal Document*, 2021.
- [3] A. Hallin, “Fitting partial fill data from december 2014,” *SNO+ Internal Document, docDB-2888-v3.*, 2014.
- [4] D. Auty and A. Hallin, “Partial water fitter,” *SNO+ Internal Document, docDB-2965-v2.*, 2015.
- [5] K. Singh, “Wavelength shifter: Carbostyryl 124,” *SNO+ Internal Document, docDB-3351-v2.*, 2015.
- [6] K. Singh, “Wavelength shifter in water phase of SNO+,” *SNO+ Internal Document, docDB-3869-v2.*, 2015.
- [7] K. Singh, “Multipath fitter processor,” *SNO+ Internal Document, docDB-3849-v1.*, 2016.
- [8] J. Hu and J. Tseng, “Updates on the multipath water fitter 2018,” *SNO+ Internal Document, docDB-4936-v2.*, 2018.
- [9] J. Leite-Lopes, “Weak interaction physics: from its origin to the electroweak model,” tech. rep., SCAN-9607019, 1996.

- [10] H. Bethe and R. Peierls, “The “neutrino”,” *Nature*, vol. 133, no. 3362, pp. 532–532, 1934.
- [11] F. Reines, C. Cowan Jr, F. Harrison, A. McGuire, and H. Kruse, “Detection of the free antineutrino,” *Physical Review*, vol. 117, no. 1, p. 159, 1960.
- [12] G. Danby, J. M. Gaillard, K. Goulian, L. M. Lederman, N. Mistry, M. Schwartz, and J. Steinberger, “Observation of high-energy neutrino reactions and the existence of two kinds of neutrinos,” *Physical Review Letters*, vol. 9, no. 1, p. 36, 1962.
- [13] K. Kodama, N. Ushida, C. Andreopoulos, N. Saoulidou, G. Tzanakos, P. Yager, B. Baller, D. Boehnlein, W. Freeman, B. Lundberg, *et al.*, “Observation of tau neutrino interactions,” *Physics Letters B*, vol. 504, no. 3, pp. 218–224, 2001.
- [14] D. Decamp, B. Deschizeaux, J.-P. Lees, M.-N. Minard, J. Crespo, M. Delfino, E. Fernandez, M. Martinez, R. Miquel, M. Mir, *et al.*, “Determination of the number of light neutrino species,” *Physics Letters B*, vol. 231, no. 4, pp. 519–529, 1989.
- [15] C. Giunti and C. W. Kim, *Fundamentals of neutrino physics and astrophysics*. Oxford university press, 2007.
- [16] E. Antonio, *State Of The Art Of Neutrino Physics: A Tutorial For Graduate Students And Young Researchers*, vol. 28. World Scientific, 2018.
- [17] Particle Data Group, P. Zyla, R. Barnett, J. Beringer, O. Dahl, D. Dwyer, D. Groom, C.-J. Lin, K. Lugovsky, E. Pianori, *et al.*, “Review of particle physics,” *Progress of Theoretical and Experimental Physics*, vol. 2020, no. 8, p. 083C01, 2020.
- [18] K. McFarland, “Neutrino interactions,” in *Neutrinos in Particle Physics, Astrophysics and Cosmology*, pp. 79–104, CRC Press, 2008.
- [19] Z. Xing and S. Zhou, *Neutrinos in particle physics, astronomy and cosmology*. Springer Science & Business Media, 2011.
- [20] Y. Suzuki, “The sun, neutrinos and Super-Kamiokande,” *Proceedings of the Japan Academy, Series B*, vol. 96, no. 6, pp. 204–233, 2020.

- [21] E. Akhmedov, “Quantum mechanics aspects and subtleties of neutrino oscillations,” *arXiv preprint arXiv:1901.05232*, 2019.
- [22] Y. Fukuda, T. Hayakawa, E. Ichihara, K. Inoue, K. Ishihara, H. Ishino, Y. Itow, T. Kajita, J. Kameda, S. Kasuga, *et al.*, “Evidence for oscillation of atmospheric neutrinos,” *Physical Review Letters*, vol. 81, no. 8, p. 1562, 1998.
- [23] Wikipedia, *CP violation*, 2020 (accessed Mar 15, 2020). <https://en.wikipedia.org/wiki/CPViolation>.
- [24] I. J. Aitchison and A. J. Hey, *Gauge theories in particle physics: A practical introduction, Volume 2: Non-Abelian Gauge theories: QCD and the electroweak theory*, vol. 2. CRC Press, 2012.
- [25] S. Abe, T. Ebihara, S. Enomoto, K. Furuno, Y. Gando, K. Ichimura, H. Ikeda, K. Inoue, Y. Kibe, Y. Kishimoto, *et al.*, “Precision measurement of neutrino oscillation parameters with KamLAND,” *Physical Review Letters*, vol. 100, no. 22, p. 221803, 2008.
- [26] K. Abe, C. Bronner, Y. Haga, Y. Hayato, M. Ikeda, K. Iyogi, J. Kameda, Y. Kato, Y. Kishimoto, L. Marti, *et al.*, “Atmospheric neutrino oscillation analysis with external constraints in Super-Kamiokande I-IV,” *Physical Review D*, vol. 97, no. 7, p. 072001, 2018.
- [27] F. P. An, A. Balantekin, H. Band, M. Bishai, S. Blyth, D. Cao, G. Cao, J. Cao, W. Cen, Y. Chan, *et al.*, “Measurement of electron antineutrino oscillation based on 1230 days of operation of the Daya Bay experiment,” *Physical Review D*, vol. 95, no. 7, p. 072006, 2017.
- [28] X. Qian and J.-C. Peng, “Physics with reactor neutrinos,” *Reports on Progress in Physics*, vol. 82, no. 3, p. 036201, 2019.
- [29] K. Abe, R. Akutsu, A. Ali, C. Alt, C. Andreopoulos, L. Anthony, M. Antonova, S. Aoki, A. Ariga, Y. Asada, *et al.*, “Constraint on the matter-antimatter symmetry-violating phase in neutrinooscillations,” *arXiv preprint arXiv:1910.03887*, 2019.

- [30] A. Y. Smirnov, “Solar neutrinos: Oscillations or no-oscillations?,” *arXiv preprint arXiv:1609.02386*, 2016.
- [31] A. Y. Smirnov, “The MSW effect and matter effects in neutrino oscillations,” *Physica Scripta*, vol. 2005, no. T121, p. 57, 2005.
- [32] M. Fukugita and T. Yanagida, *Physics of Neutrinos: and Application to Astrophysics*. Springer Science & Business Media, 2013.
- [33] H. A. Bethe, “Energy production in stars,” *Physical Review*, vol. 55, no. 5, p. 434, 1939.
- [34] W. C. Haxton, R. Hamish Robertson, and A. M. Serenelli, “Solar neutrinos: status and prospects,” *Annual Review of Astronomy and Astrophysics*, vol. 51, pp. 21–61, 2013.
- [35] L. Oberauer, A. Ianni, and A. Serenelli, *Solar Neutrino Physics: The Interplay Between Particle Physics and Astronomy*. John Wiley & Sons, 2020.
- [36] J. W. F. Valle and J. Romao, *Neutrinos in high energy and astroparticle physics*. John Wiley & Sons, 2015.
- [37] F. Suekane, *Neutrino oscillations: a practical guide to basics and applications*, vol. 898. Springer, 2015.
- [38] J. N. Bahcall, “Solar neutrinos. I. theoretical,” *Physical Review Letters*, vol. 12, no. 11, p. 300, 1964.
- [39] R. Davis Jr, “Solar neutrinos. II. experimental,” *Physical Review Letters*, vol. 12, no. 11, p. 303, 1964.
- [40] R. Davis Jr, D. S. Harmer, and K. C. Hoffman, “Search for neutrinos from the sun,” *Physical Review Letters*, vol. 20, no. 21, p. 1205, 1968.
- [41] V. N. Gavrin, “The russian-american gallium experiment SAGE,” *UFN*, vol. 181, p. 0975, 2011.

- [42] W. Hampel, J. Handt, G. Heusser, J. Kiko, T. Kirsten, M. Laubenstein, E. Pernicka, W. Rau, M. Wojcik, Y. Zakharov, *et al.*, “GALLEX solar neutrino observations: Results for GALLEX IV,” *Physics Letters B*, vol. 447, no. 1-2, pp. 127–133, 1999.
- [43] K. Zuber, *Neutrino physics*. CRC press, 2020.
- [44] Super Kamiokande, “Solar neutrinos,” 2020 (accessed 1-Jan-2020). <http://www-sk.icrr.u-tokyo.ac.jp/sk/sk/solar-e.html>.
- [45] K. Abe, Y. Haga, Y. Hayato, M. Ikeda, K. Iyogi, J. Kameda, Y. Kishimoto, L. Marti, M. Miura, S. Moriyama, *et al.*, “Solar neutrino measurements in Super-Kamiokande-IV,” *Physical Review D*, vol. 94, no. 5, p. 052010, 2016.
- [46] Q. R. Ahmad, R. Allen, T. Andersen, J. Anglin, J. Barton, E. Beier, M. Bercovitch, J. Bigu, S. Biller, R. Black, *et al.*, “Direct evidence for neutrino flavor transformation from neutral-current interactions in the Sudbury Neutrino Observatory,” *Physical review letters*, vol. 89, no. 1, p. 011301, 2002.
- [47] B. Aharmim, S. Ahmed, A. Anthony, N. Barros, E. Beier, A. Bellerive, B. Beltran, M. Bergevin, S. Biller, K. Boudjemline, *et al.*, “Combined analysis of all three phases of solar neutrino data from the Sudbury Neutrino Observatory,” *Physical Review C*, vol. 88, no. 2, p. 025501, 2013.
- [48] A. Gando, Y. Gando, K. Ichimura, H. Ikeda, K. Inoue, Y. Kibe, Y. Kishimoto, M. Koga, Y. Minekawa, T. Mitsui, *et al.*, “Constraints on  $\theta_{13}$  from a three-flavor oscillation analysis of reactor antineutrinos at KamLAND,” *Physical Review D*, vol. 83, no. 5, p. 052002, 2011.
- [49] M. Agostini, K. Altenmüller, S. Appel, V. Atroshchenko, Z. Bagdasarian, D. Basilico, G. Bellini, J. Benziger, D. Bick, D. Bravo, *et al.*, “Improved measurement of b-8 solar neutrinos with 1.5 kt·y of Borexino exposure,” *Physical Review D*, vol. 101, no. 6, p. 062001, 2020.

- [50] M. Agostini, K. Altenmüller, S. Appel, D. Jeschke, B. Neumair, L. Oberauer, L. Papp, S. Schönert, F. von Feilitzsch, V. Atroshchenko, *et al.*, “Comprehensive measurement of pp-chain solar neutrinos,” *Nature*, vol. 562, no. 7728, pp. 505–510, 2018.
- [51] Borexino Collaboration *et al.*, “Experimental evidence of neutrinos produced in the CNO fusion cycle in the sun,” *Nature*, vol. 587, no. 7835, pp. 577–582, 2020.
- [52] G. D. O. Gann, “Everything under the sun: A review of solar neutrinos,” in *AIP Conference Proceedings*, vol. 1666, p. 090003, AIP Publishing LLC, 2015.
- [53] S. Davini, M. Agostini, S. Appel, G. Bellini, J. Benziger, D. Bick, G. Bonfini, D. Bravo, B. Caccianiga, F. Calaprice, *et al.*, “CNO and pep solar neutrino measurements and perspectives in Borexino,” vol. 675, no. 1, p. 012040, 2016.
- [54] S. Vagnozzi, K. Freese, and T. H. Zurbuchen, “Solar models in light of new high metallicity measurements from solar wind data,” *The Astrophysical Journal*, vol. 839, no. 1, p. 55, 2017.
- [55] D. G. Cerdeno, J. H. Davis, M. Fairbairn, and A. C. Vincent, “CNO neutrino grand prix: The race to solve the solar metallicity problem,” *Journal of Cosmology and Astroparticle Physics*, vol. 2018, no. 04, p. 037, 2018.
- [56] Hyper-Kamiokande Collaboration, “Bringing neutrino research to the next level,” 2021 (accessed 1-Jan-2021). <http://www.hyper-k.org/en/overview.html>.
- [57] T. Yano, “Solar neutrino physics at Hyper-Kamiokande,” in *36th International Cosmic Ray Conference (ICRC2019)*, vol. 36, p. 1037, 2019.
- [58] DUNE Collaboration, “An international experiment for neutrino science,” 2021 (accessed 1-Jan-2021). <https://www.dunescience.org/>.
- [59] F. Capozzi, S. W. Li, G. Zhu, and J. F. Beacom, “Dune as the next-generation solar neutrino experiment,” *Physical review letters*, vol. 123, no. 13, p. 131803, 2019.
- [60] M. Askins, Z. Bagdasarian, N. Barros, E. Beier, E. Blucher, R. Bonventre, E. Bourret, E. Callaghan, J. Caravaca, M. Diwan, *et al.*, “Theia: an advanced optical neutrino detector,” *The European Physical Journal C*, vol. 80, no. 5, pp. 1–31, 2020.

- [61] A. Giaz, “Status and perspectives of the JUNO experiment,” *arXiv preprint arXiv:1804.03575*, 2018.
- [62] J. F. Beacom, S. Chen, J. Cheng, S. N. Dousttimotlagh, Y. Gao, G. Gong, H. Gong, L. Guo, R. Han, H.-J. He, *et al.*, “Physics prospects of the jinping neutrino experiment,” *Chinese physics C*, vol. 41, no. 2, p. 023002, 2017.
- [63] M. Wurm, LAGUNA-LENA Working Group, *et al.*, “Studying neutrino properties in the future lena experiment,” *Nuclear Physics B-Proceedings Supplements*, vol. 237, pp. 314–316, 2013.
- [64] L. Baudis, A. Ferella, A. Kish, A. Manalaysay, T. M. Undagoitia, and M. Schumann, “Neutrino physics with multi-ton scale liquid xenon detectors,” *Journal of cosmology and astroparticle physics*, vol. 2014, no. 01, p. 044, 2014.
- [65] J. Aalbers, F. Agostini, M. Alfonsi, F. Amaro, C. Amsler, E. Aprile, L. Arazi, F. Arneodo, P. Barrow, L. Baudis, *et al.*, “Darwin: towards the ultimate dark matter detector,” *Journal of Cosmology and Astroparticle Physics*, vol. 2016, no. 11, p. 017, 2016.
- [66] J. Aalbers, F. Agostini, S. A. Maouloud, M. Alfonsi, L. Althueser, F. Amaro, J. Angevaare, V. C. Antochi, B. Antunovic, E. Aprile, *et al.*, “Solar neutrino detection sensitivity in darwin via electron scattering,” *The European Physical Journal C*, vol. 80, no. 12, pp. 1–10, 2020.
- [67] N. Aghanim, Y. Akrami, M. Ashdown, J. Aumont, C. Baccigalupi, M. Ballardini, A. Banday, R. Barreiro, N. Bartolo, S. Basak, *et al.*, “Planck 2018 results-vi. cosmological parameters,” *Astronomy & Astrophysics*, vol. 641, p. A6, 2020.
- [68] C. Dvorkin, M. Gerbino, D. Alonso, N. Battaglia, S. Bird, A. D. Rivero, A. Font-Ribera, G. Fuller, M. Lattanzi, M. Loverde, *et al.*, “Neutrino mass from cosmology: Probing physics beyond the standard model,” *arXiv preprint arXiv:1903.03689*, 2019.
- [69] J. Lesgourgues, G. Mangano, G. Miele, and S. Pastor, *Neutrino cosmology*. Cambridge University Press, 2013.

- [70] M. Aker, K. Altenmüller, M. Arenz, M. Babutzka, J. Barrett, S. Bauer, M. Beck, A. Beglarian, J. Behrens, T. Bergmann, *et al.*, “Improved upper limit on the neutrino mass from a direct kinematic method by katrin,” *Physical review letters*, vol. 123, no. 22, p. 221802, 2019.
- [71] W. H. Furry, “On transition probabilities in double beta-disintegration,” *Physical Review*, vol. 56, no. 12, p. 1184, 1939.
- [72] W. Haxton, G. Stephenson Jr, and D. Strottman, “Double beta decay and the majorana mass of the electron neutrino,” *Physical Review Letters*, vol. 47, no. 3, p. 153, 1981.
- [73] B. Povh, K. Rith, and F. Zetsche, *Particles and nuclei*, vol. 1. Springer, 2008.
- [74] B. R. Martin and G. Shaw, *Nuclear and particle physics: an introduction*. John Wiley & Sons, 2019.
- [75] E. Akhmedov, “Majorana neutrinos and other majorana particles: Theory and experiment,” *arXiv preprint arXiv:1412.3320*, 2014.
- [76] E. Majorana and L. Maiani, *A symmetric theory of electrons and positrons*. Springer, 2006.
- [77] M. J. Dolinski, A. W. Poon, and W. Rodejohann, “Neutrinoless double-beta decay: status and prospects,” *Annual Review of Nuclear and Particle Science*, vol. 69, pp. 219–251, 2019.
- [78] V. Albanese, R. Alves, M. Anderson, S. Andringa, L. Anselmo, E. Arushanova, S. Asahi, M. Askins, D. Auty, A. Back, *et al.*, “The SNO+ Experiment,” *Journal of Instrumentation*, vol. 16, no. 08, p. P08059, 2021.
- [79] A. Gando, Y. Gando, T. Hachiya, A. Hayashi, S. Hayashida, H. Ikeda, K. Inoue, K. Ishidohiro, Y. Karino, M. Koga, *et al.*, “Search for majorana neutrinos near the inverted mass hierarchy region with KamLAND-Zen,” *Physical Review Letters*, vol. 117, no. 8, p. 082503, 2016.

- [80] C. Alduino, F. Alessandria, K. Alfonso, E. Andreotti, C. Arnaboldi, F. Avignone III, O. Azzolini, M. Balata, I. Bandac, T. Banks, *et al.*, “First results from CUORE: A search for lepton number violation via  $0\nu\beta\beta$  decay of te-130,” *Physical review letters*, vol. 120, no. 13, p. 132501, 2018.
- [81] M. Agostini, G. Araujo, A. Bakalyarov, M. Balata, I. Barabanov, L. Baudis, C. Bauer, E. Bellotti, S. Belogurov, A. Bettini, *et al.*, “Final results of GERDA on the search for neutrinoless double- $\beta$  decay,” *Physical Review Letters*, vol. 125, no. 25, p. 252502, 2020.
- [82] SNOLAB, “SNOLAB user’s handbook,” 2006 (accessed 1-Jan-2020). [http://snolab2008.snolab.ca/snolab\\_users\\_handbook\\_rev02.pdf](http://snolab2008.snolab.ca/snolab_users_handbook_rev02.pdf).
- [83] “Muons,” 2001 (accessed 19-July-2019). [https://cosmic.lbl.gov/SKliewer/Cosmic\\_Rays/Muons.htm](https://cosmic.lbl.gov/SKliewer/Cosmic_Rays/Muons.htm).
- [84] J. Waterfield, *Optical Calibration System for SNO+ and Sensitivity to Neutrinoless Double-beta Decay*. PhD thesis, University of Sussex, 2017.
- [85] S. Andringa, E. Arushanova, S. Asahi, M. Askins, D. Auty, A. Back, Z. Barnard, N. Barros, E. Beier, A. Bialek, *et al.*, “Current status and future prospects of the SNO+,” *Advances in High Energy Physics*, vol. 2016, 2016.
- [86] M. Stringer, *Sensitivity of SNO+ to Supernova Neutrinos*. PhD thesis, University of Sussex, 2019.
- [87] P. G. Jones, *Background Rejection for the Neutrinoless Double Beta Decay Experiment SNO+*. PhD thesis, University of Oxford, 2011.
- [88] M. Anderson, S. Andringa, E. Arushanova, S. Asahi, M. Askins, D. Auty, A. Back, Z. Barnard, N. Barros, D. Bartlett, *et al.*, “Search for invisible modes of nucleon decay in water with the SNO+ detector,” *Physical Review D*, vol. 99, no. 3, p. 032008, 2019.
- [89] M. Anderson, S. Andringa, M. Askins, D. Auty, N. Barros, F. Barão, R. Bayes, E. Beier, A. Bialek, S. Biller, *et al.*, “Measurement of neutron-proton capture in the SNO+ water phase,” *Physical Review C*, vol. 102, no. 1, p. 014002, 2020.

- [90] M. Anderson, S. Andringa, M. Askins, D. Auty, F. Barão, N. Barros, R. Bayes, E. Beier, A. Bialek, S. Biller, *et al.*, “Optical calibration of the SNO+ detector in the water phase with deployed sources,” *arXiv preprint arXiv:2106.03951*, 2021.
- [91] J. Paton, “Neutrinoless double beta decay in the SNO+ experiment,” in *Prospects in Neutrino Physics (NuPhys2018) London, United Kingdom, December 19-21, 2018*, 2020.
- [92] J. D. Jackson, *Classical Electrodynamics*. John Wiley & Sons, 2007.
- [93] L. D. Landau, J. Bell, M. Kearsley, L. Pitaevskii, E. Lifshitz, and J. Sykes, *Electrodynamics of Continuous Media*, vol. 8. elsevier, 2013.
- [94] H. W. C. Tseung and N. Tolich, “Ellipsometric measurements of the refractive indices of linear alkylbenzene and ej-301 scintillators from 210 to 1000 nm,” *Physica Scripta*, vol. 84, no. 3, p. 035701, 2011.
- [95] W. R. Leo, *Techniques for Nuclear and Particle Physics Experiments: a How-to Approach*. Springer Science & Business Media, 2012.
- [96] T. Kaptanoglu, *Reactor Antineutrinos in the SNO+ Water Phase and Detector R&D for Large-Scale Neutrino Detectors*. PhD thesis, University of Pennsylvania, 2020.
- [97] G. F. Knoll, *Radiation Detection and Measurement*. John Wiley & Sons, 2010.
- [98] J. Birks and F. Firk, “The theory and practice of scintillation counting,” *Physics Today*, vol. 18, p. 60, 1965.
- [99] B. Von Krosigk, *Measurement of Proton and  $\alpha$  Particle Quenching in LAB Based Scintillators and Determination of Spectral Sensitivities to Supernova Neutrinos in the SNO+ Detector*. PhD thesis, Technische Universitaet Dresden, 2015.
- [100] A. Sörensen, *Temperature Quenching in LAB Based Liquid Scintillator and Muon-induced Backgrounds in the SNO+ Experiment*. PhD thesis, Technische Universitaet Dresden, 2016.

- [101] J. Dunger, *Topological and Time Based Event Classification for Neutrinoless Double Beta Decay in Liquid Scintillator*. PhD thesis, University of Oxford, 2018.
- [102] D. A. McQuarrie and J. D. Simon, *Physical chemistry: a molecular approach*, vol. 1. University science books Sausalito, CA, 1997.
- [103] SNO+ Collaboration, M. Anderson, S. Andringa, L. Anselmo, E. Arushanova, S. Asahi, M. Askins, D. Auty, A. Back, Z. Barnard, *et al.*, “Development, characterisation, and deployment of the SNO+ liquid scintillator,” *arXiv preprint arXiv:2011.12924*, 2020.
- [104] J. B. Birks, “Scintillations from organic crystals: specific fluorescence and relative response to different radiations,” *Proceedings of the Physical Society. Section A*, vol. 64, no. 10, p. 874, 1951.
- [105] PerkinElmer, “Liquid scintillation cocktails,” 1998-2021 (accessed 20-Dec-2019).  
<https://www.perkinelmer.com/en-ca/lab-products-and-services/application-support-knowledgebase/radiometric/liquid-scintillation-cocktails.html>.
- [106] X. Dai, E. Rollin, A. Bellerive, C. Hargrove, D. Sinclair, C. Mifflin, and F. Zhang, “Wavelength shifters for water cherenkov detectors,” *Nuclear Instruments and Methods in Physics Research Section A: Accelerators, Spectrometers, Detectors and Associated Equipment*, vol. 589, no. 2, pp. 290–295, 2008.
- [107] *Wavelength shifter*, 2020 (accessed Mar 30, 2020). [https://en.wikipedia.org/wiki/Wavelength\\_shifter](https://en.wikipedia.org/wiki/Wavelength_shifter).
- [108] J. Alonso, N. Barros, M. Bergevin, A. Bernstein, L. Bignell, E. Blucher, F. Calaprice, J. Conrad, F. Descamps, M. Diwan, *et al.*, “Advanced scintillator detector concept (ASDC): a concept paper on the physics potential of water-based liquid scintillator,” *arXiv preprint arXiv:1409.5864*, 2014.
- [109] M. Askins, M. Bergevin, A. Bernstein, S. Dazeley, S. Dye, T. Handler, A. Hatzikoutelis, D. Hellfeld, P. Jaffke, Y. Kamyshkov, *et al.*, “The physics and nuclear non-

- proliferation goals of WATCHMAN: A WAter CHerenkov Monitor for ANtineutrinos,” *arXiv preprint arXiv:1502.01132*, 2015.
- [110] Wikipedia, “Linear alkylbenzene,” 2020 (accessed 1-Jan-2020). [https://en.wikipedia.org/wiki/Linear\\_alkylbenzene](https://en.wikipedia.org/wiki/Linear_alkylbenzene).
- [111] S. W. Wunderly and J. M. Kauffman, “New quench-resistant fluors for liquid scintillation counting,” *International Journal of Radiation Applications and Instrumentation. Part A. Applied Radiation and Isotopes*, vol. 41, no. 9, pp. 809–815, 1990.
- [112] Y. Xing-Chen, Y. Bo-Xiang, Z. Xiang, Z. Li, D. Ya-Yun, L. Meng-Chao, D. Xue-Feng, Z. Xuan, J. Quan-Lin, Z. Li, *et al.*, “Preliminary study of light yield dependence on LAB liquid scintillator composition,” *Chinese Physics C*, vol. 39, no. 9, p. 096003, 2015.
- [113] T. Kaptanoglu, M. Luo, and J. Klein, “Cherenkov and scintillation light separation using wavelength in LAB based liquid scintillator,” *Journal of Instrumentation*, vol. 14, no. 05, p. T05001, 2019.
- [114] V. Novikov, “Scintillator development for SNO+,” *SNO+ Internal Document (2009)*.
- [115] S. Grullon, “Light yield and scintillation decay time constants of te-loaded liquid scintillator for the sno+ experiment,” in *Proceedings of the 26th International Conference on Neutrino Physics and Astrophysics (Neutrino’14)*, 2014.
- [116] S. D. Biller, E. J. Leming, and J. L. Paton, “Slow fluors for highly effective separation of cherenkov light in liquid scintillators,” *arXiv preprint arXiv:2001.10825*, 2020.
- [117] A. LaTorre, “New measurements for the timing spectrum of electrons and alphas in LAB + PPO,” *SNO+ Internal Document, docDB-4081-v1.*, 2016.
- [118] T. Kaptanoglu, “Measurements of light yield and timing of 0.5 g/l LAB + PPO,” *SNO+ Internal Document, docDB-5997-v1.*, 2019.
- [119] T. Kaptanoglu, “Penn light yield measurements of Te+DDA samples,” *SNO+ Internal Document, docDB-5124-v2.*, 2018.

- [120] J.-S. Wang, “Bipo analysis using partial fill data,” *SNO+ Internal Document, docDB-5950-v3.*, 2019.
- [121] M. Smiley, “Berkeleyalphabeta recoordination dec 2020 for partial fill,” *SNO+ Internal Document, docDB-6754-v1.*, 2020.
- [122] H. O’Keeffe, V. Lozza, and M. Chen, “LAB backgrounds expected numbers,” *SNO+ Internal Document, docDB-507-v42.*, 2010-2021.
- [123] SNO+ Tellurium Loading Working Group, “Te loading,” *SNO+ Internal Document, planned to be submitted.*
- [124] S. Biller, S. Manecki, S. Collaboration, *et al.*, “A new technique to load 130te in liquid scintillator for neutrinoless double beta decay experiments,” in *Journal of Physics: Conference Series*, vol. 888, p. 012084, IOP Publishing, 2017.
- [125] S. Biller, “DDA synthesis model,” *SNO+ Internal Document, docDB-5364-v3.*, 2018.
- [126] S. Biller, “DDA vs SOP,” *SNO+ Internal Document, docDB-5437-v1.*, 2018.
- [127] Hamamatsu-Photonics, “Photomultiplier tube r580,” 2020 (accessed 1-Jan-2020).  
[www.hamamatsu.com/eu/en/product/type/R580/index.html](http://www.hamamatsu.com/eu/en/product/type/R580/index.html).
- [128] CAEN, “DT5751 - CAEN - tools for discovery.,” 2020 (accessed 1-Jan-2020). [www.caen.it/products/dt5751](http://www.caen.it/products/dt5751).
- [129] CAEN, “CoMPASS multiparametric DAQ software for physics applications,” 2020 (accessed 1-Jan-2020). <https://www.caen.it/products/compass/>.
- [130] National Nuclear Data Center, 2019 (accessed Oct 30, 2019). <https://www.nndc.bnl.gov/>.
- [131] B. Von Krosigk, M. Chen, S. Hans, A. Junghans, T. Kögler, C. Kraus, L. Kuckert, X. Liu, R. Nolte, H. M. O’Keeffe, *et al.*, “Measurement of *alpha*-particle quenching in lab based scintillator in independent small-scale experiments,” *The European Physical Journal C*, vol. 76, no. 3, pp. 1–13, 2016.

- [132] J. Boger, R. Hahn, J. Rowley, A. Carter, B. Hollebone, D. Kessler, I. Blevis, F. Dalnoki-Veress, A. DeKok, J. Farine, *et al.*, “The Sudbury Neutrino Observatory,” *Nuclear Instruments and Methods in Physics Research Section A: Accelerators, Spectrometers, Detectors and Associated Equipment*, vol. 449, no. 1-2, pp. 172–207, 2000.
- [133] K. Hamamatsu Photonics, “Photomultiplier tubes: Basics and applications, 2007,” 2018.
- [134] G. O. Gann, “Dealing with time in RAT,” *SNO+ Internal Document, docDB-481-v2.*, 2010.
- [135] R. Bonventre, *Neutron Multiplicity in Atmospheric Neutrino Events at the Sudbury Neutrino Observatory*. PhD thesis, University of Pennsylvania, 2014.
- [136] J. Rumleskie, *SNO+ Sensitivities to Pre-supernova and Supernova Neutrinos*. PhD thesis, Laurentian University of Sudbury, 2021.
- [137] J. M. Walker, *Study of Invisible Mode Nucleon Decay in the SNO+ Detector*. PhD thesis, University of Liverpool, 2016.
- [138] K. Singh, P. Gorel, A. Hallin, C. Krauss, and Z. Petriw, “Underwater photometry system of the SNO+ experiment,” in *Journal of Physics: Conference Series*, vol. 1342, p. 012130, IOP Publishing, 2020.
- [139] M. R. Dragowsky, *Sudbury Neutrino Observatory Energy Calibration using Gamma-ray Sources*. PhD thesis, Oregon State University, 1999.
- [140] M. Dragowsky, A. Hamer, Y. Chan, R. Deal, E. Earle, W. Frati, E. Gaudette, A. Hallin, C. Hearns, J. Hewett, *et al.*, “The  $^{16}\text{N}$  calibration source for the Sudbury Neutrino Observatory,” *Nuclear Instruments and Methods in Physics Research Section A: Accelerators, Spectrometers, Detectors and Associated Equipment*, vol. 481, no. 1-3, pp. 284–296, 2002.
- [141] A. S. Hamer, *Energy Calibration of SNO for Measurement of the Charged-current Neutrino Reaction*. PhD thesis, Queen’s University, 2001.

- [142] R. F. MacLellan, *The Energy Calibration for the Solar Neutrino Analysis of all Three Phases of the Sudbury Neutrino Observatory*. PhD thesis, Queen's University, 2009.
- [143] M. Mottram, "N16 source update," *SNO+ Internal Document, docDB-1769-v1.*, 2013.
- [144] Z. Barnard, "Update to N16 geometry," *SNO+ Internal Document, docDB-4414-v1.*, 2017.
- [145] R. Bayes, "Analysis of N16 scan," *SNO+ Internal Document, docDB-4482-v2.*, 2017.
- [146] S. Agostinelli, J. Allison, K. a. Amako, J. Apostolakis, H. Araujo, P. Arce, M. Asai, D. Axen, S. Banerjee, G. . Barrand, *et al.*, "Geant4—a simulation toolkit," *Nuclear instruments and methods in physics research section A: Accelerators, Spectrometers, Detectors and Associated Equipment*, vol. 506, no. 3, pp. 250–303, 2003.
- [147] R. Brun, F. Rademakers, P. Canal, *et al.*, "Root: An object oriented data analysis framework, 2007," *See Also <http://root.cern.ch>.*
- [148] *RAT Overview*, 2020 (accessed Mar 15, 2020). <https://rat.readthedocs.io/en/latest/overview.html>.
- [149] G. Horton-Smith *et al.*, "Introduction to GLG4sim," 2006.
- [150] T. Caldwell, "Simulation of noble liquid detectors using rat," in *AARM Meeting at Fermilab*, 2014.
- [151] J. Dittmer and M. Meyer, "Topological track reconstruction with the SNO+ experiment," *SNO+ Internal Document, docDB-5749-v1.*, 2019.
- [152] M. G. Boulay, *Direct Evidence for Weak Flavour Mixing with the Sudbury Neutrino Observatory*. PhD thesis, Queen's University, 2004.
- [153] C. Jillings, R. Ford, A. Hallin, P. Harvey, R. MacLeod, H. Mak, P. Skensved, and R. Stevenson, "The photomultiplier tube testing facility for the Sudbury Neutrino Observatory," *Nuclear Instruments and Methods in Physics Research Section A: Accelerators, Spectrometers, Detectors and Associated Equipment*, vol. 373, no. 3, pp. 421–429, 1996.

- [154] P. Gregory, *Bayesian Logical Data Analysis for the Physical Sciences: A Comparative Approach with Mathematica® Support*. Cambridge University Press, 2005.
- [155] W. H. Press, S. A. Teukolsky, W. T. Vetterling, and B. P. Flannery, *Numerical Recipes 3rd Edition: The Art of Scientific Computing*. Cambridge university press, 2007.
- [156] E. Turner, “A water scattering scaling factor for rat,” *SNO+ Internal Document, docDB-5864-v2.*, 2019.
- [157] I. T. Coulter, *Modelling and Reconstruction of Events in SNO+ Related to Future Searches for Lepton and Baryon Number Violation*. PhD thesis, University of Oxford, 2013.
- [158] F. Barao and J. Maneira, “Group velocity measurement, plot for approval,” *SNO+ Internal Document, docDB-5071-v1.*, 2017.
- [159] P. Skensved and B. Robertson, “Miscellaneous effects,” *SNO Technical Report, SNO-STR-90-28.*, 1990.
- [160] S. J. Brice, *Monte Carlo and Analysis Techniques for the Sudbury Neutrino Observatory*. PhD thesis, University of Oxford, 1996.
- [161] L. Lebanowski, “Improved mode cut,” *SNO+ Internal Document, docDB-5488-v1.*, 2019.
- [162] P. Mekarski, *Electron Antineutrinos in the Water Phase of the SNO+ Experiment*. PhD thesis, University of Alberta, 2018.
- [163] E. Leming, “LAB + PPO timing measurements at Oxford,” *SNO+ Internal Document, docDB-6161-v1.*, 2019.
- [164] E. Leming, “Oxford LAB + PPO timing and light yield measurements,” *SNO+ Internal Document, docDB-6179-v1.*, 2019.
- [165] J. Hu, “Partial fitter re-coordination with various PPO concentrations based on Oxford measurements,” *SNO+ Internal Document, docDB-6186-v2.*, 2020.

- [166] J. Hu, “Test the PPO concentration effect on the partial fitter reconstruction,” *SNO+ Internal Document, docDB-6230-v1.*, 2020.
- [167] J. Hu, “Use multipath fitter to fit water level,” *SNO+ Internal Document, docDB-6062-v1.*, 2019.
- [168] E. Leming and J.-S. Wang, “Partial fill time residuals,” *SNO+ Internal Document, docDB-5957-v1.*, 2019.
- [169] I. Morton-Blake, “Partial fill: Bipo214 time residuals + energy data/mc comparison,” *SNO+ Internal Document, docDB-6796-v1.*, 2021.
- [170] Wikipedia, *JSON*, 2020 (accessed Mar 15, 2020). <https://en.wikipedia.org/wiki/JSON>.
- [171] B. A. Moffat, *The Optical Calibration of the Sudbury Neutrino Observatory*. PhD thesis, Queen’s University, 2001.
- [172] M. Mottram, “Note on RSP fitter,” *SNO+ Internal Document, docDB-3939-v1.*, 2016.
- [173] K. Majumdar, “Functional form energy reconstruction,” *SNO+ Internal Document, docDB-2782-v2.*, 2016.
- [174] M. Mottram, “Updated functional form energy reconstruction: Energyrthetafunctional,” *SNO+ Internal Document, docDB-3488-v1.*, 2015.
- [175] L. Lebanowski, “Water reconstruction errors and fom,” *SNO+ Internal Document, docDB-6190-v2.*, 2020.
- [176] Water Physics Group, “Water physics unidoc,” *SNO+ Internal Document*, 2021.
- [177] M. Mottram, “Energy reconstruction in partial scintillator fill,” *SNO+ Internal Document, docDB-3133-v1.*, 2015.
- [178] Y. Zhang, “Performance of Qenergy based on Q,” *SNO+ Internal Document, docDB-6065-v1.*, 2019.

- [179] J. Hu, “Updates on the multipath fitter and partial energy,” *SNO+ Internal Document, docDB-5765-v1.*, 2019.
- [180] J. Hu, “Switch the charge-ratio partial energy fitter to nhit-ratio,” *SNO+ Internal Document, docDB-6495-v1.*, 2020.
- [181] M. Anderson, “Water phase ml fitter: status and updates, direction fitter,” *Canadian AI Conference 2020 - Talk*.
- [182] M. Anderson, “Deep learning to reconstruct particle interaction properties for the SNO+ neutrino physics experiment,” *Canadian AI Conference 2020 - Talk*.
- [183] M. Anderson, “Status and updates on neural network fitter,” *SNO+ Internal Document, docDB-6298-v1.*, 2020.
- [184] J. Klein, “Leta high level cuts (including QPDT and ITR),” *SNO+ Internal Document, docDB-2512-v1.*, 2014.
- [185] J. A. Dunmore, *The Separation of CC and NC Events in the Sudbury Neutrino Observatory*. PhD thesis, University of Oxford, 2004.
- [186] E. Marzec, *Measurement Of  ${}^8B$  Solar Neutrinos in the SNO+ Water Phase and a Model of Vacuum-Enhanced Neutrino Mixing*. PhD thesis, 2019.
- [187] P.-L. Drouin, *Three-phase Extraction of the Electron Neutrino Survival Probability at the Sudbury Neutrino Observatory*. PhD thesis, Carleton University, 2012.
- [188] R. Bayes and B. Krar, “ $\beta_{14}$  discrepancy in SNO+,” *SNO+ Internal Document, docDB-6613-v2.*, 2020.
- [189] M. Askins, *Search for Invisible Neutron Decay in SNO+ Water Phase*. PhD thesis, University of California Davis, 2018.
- [190] LETA Working Group, “Low energy threshold analysis (leta) unidoc v. 0.1,” *SNO+ Internal Document, docDB-4322-v1.*, 2017.
- [191] TMVA, 2020 (accessed Mar 30, 2020). <https://root.cern.ch/tmva>.

- [192] K. Albertsson, S. Gleyzer, A. Hoecker, L. Moneta, P. Speckmayer, J. Stelzer, J. Therhaag, E. von Toerne, H. Voss, and S. Wunsch, “Tmva 4,” *arXiv preprint physics/0703039*, 2007.
- [193] M. Askins, “Water phase figures of merit selection,” *SNO+ Internal Document, docDB-6560-v1.*, 2020.
- [194] K. P. Murphy, *Machine learning: a probabilistic perspective*. MIT press, 2012.
- [195] *StatPatternRecognition and Machine Learning in HEP*, 2020 (accessed Mar 30, 2020).  
<http://www.hep.caltech.edu/~narsky/spr.html>.
- [196] F. Shaker, “PSelmaa a solar neutrino tool,” *SNO+ Internal Document, docDB-6013-v1.*, 2019.
- [197] N. Vinyoles, A. M. Serenelli, F. L. Villante, S. Basu, J. Bergström, M. Gonzalez-Garcia, M. Maltoni, C. Peña-Garay, and N. Song, “A new generation of standard solar models,” *The Astrophysical Journal*, vol. 835, no. 2, p. 202, 2017.
- [198] O. Behnke, K. Kröninger, G. Schott, and T. Schörner-Sadenius, *Data analysis in high energy physics: a practical guide to statistical methods*. John Wiley & Sons, 2013.
- [199] ROOT, *TDecompQRH Class Reference*, 2020 (accessed Mar 15, 2020). <https://root.cern.ch/doc/master/classTDecompQRH.html>.

## Appendix A

# Details for the Multi-Path Fitter

### A.1 Create a Random Vertex

This section is derived from P. G. Jones and I. Coutler’s early work on the SNO+ reconstruction algorithms [87, 157], and K. Singh’s work on the `MultiPath` processor [7].

To create a random vertex, four random seeds are generated from the uniform distribution function: `RandFlat` in Class Library for High Energy Physics library (CLHEP).

One random seed is used for generating the time of the vertex:  $t$  is a random variable following a uniform distribution in a range of [100, 300] ns, say,  $t \sim U(100, 300)$  ns.

Three random seeds are used for generating the position of the trial vertex:  $\text{ran0} \sim U(0, 1)$ ,  $\text{ran1} \sim U(-1, 1)$  and  $\text{ran2Pi} \sim U(0, 2\pi)$ .

Let  $r = \sqrt[3]{\text{ran0}} * 8390$  mm<sup>1</sup>,  $\phi = \text{ran2Pi}$ ,  $\cos \theta = \text{ran1}$  and  $\sin \theta = \sqrt{1 - \cos^2 \theta}$ , then the trial position can be built in Cartesian coordinate system:

$$\vec{x}_{trial} = (r \sin \theta \cos \phi, r \sin \theta \sin \phi, r \cos \theta) .$$

This procedure ensures that a proper random position is generated inside a sphere with a radius of 8.39 m.

For the trial direction, two random seeds are used. Each follows a uniform distribution:  $\text{ranPi} \sim U(0, \pi)$  and  $\text{ran2Pi} \sim U(0, 2\pi)$ . Then the trial direction is built as:  $\vec{u}_0 = (\cos \phi \sin \theta, \sin \phi \sin \theta, \cos \theta)$ , with zenith angle  $\theta = \text{ranPi}$  and azimuth angle  $\phi = \text{ran2Pi}$ .

---

<sup>1</sup> $r_{PSUP} = 8390$  mm is the radius of the PSUP.

Note that here the `ranPi` and `ran2Pi` are generated independently for the trial direction and they are not related to the vertex case.

## A.2 Levenberg-Marquardt Method

This section is derived from Ref. [155]. Levenberg-Marquardt (MRQ) method is a common routine for non-linear fitting. Let  $\mathbf{a} = [a_0, a_1, \dots, a_{M-1}]^T$  be an  $M$ -dimensional vector with  $M$  unknown parameters to be fit, for example,  $\mathbf{a}$  is an event vertex with 4 parameters:  $\mathbf{a} = [x, y, z, t]^T$ .

A  $\chi^2$  merit function with the unknown parameter vector  $\mathbf{a}$  can be built and by minimizing the function, the best-fit  $\mathbf{a}$  can be found.

The  $\chi^2(\mathbf{a})$  can be approximately expanded into a quadratic form of Taylor-series:

$$\chi^2(\mathbf{a}) \simeq \gamma - \mathbf{d} \cdot \mathbf{a} + \frac{1}{2} \mathbf{a} \cdot \mathbf{D} \cdot \mathbf{a}, \quad (\text{A.1})$$

where  $\gamma$  is a  $M$ -dimension constant vector around  $\mathbf{a}$ ,  $\mathbf{d}$  is a  $M$ -dimension vector and  $\mathbf{D}$  is a  $M \times M$  Hessian matrix.

To find a  $\mathbf{a}_{min}$  so that a  $\min \chi^2(\mathbf{a}_{min})$  is reached, in computing science we usually use iteration steps:

$$\mathbf{a}_{min} = \mathbf{a}_{cur} + D^{-1}[-\nabla \chi^2(\mathbf{a}_{cur})], \quad (\text{A.2})$$

where  $\mathbf{a}_{cur}$  is the current trial value of  $\mathbf{a}$  and we assume matrix  $\mathbf{D}$  is invertible. The  $\mathbf{a}_{cur}$  thus jumps onto  $\mathbf{a}_{min}$ .

According to the definition of a  $\chi^2$  merit function, it can be written out explicitly as:

$$\chi^2(\mathbf{a}) = \sum_{i=0}^{N-1} \left[ \frac{y_i - y(x_i | \mathbf{a})}{\sigma_i} \right]^2, \quad (\text{A.3})$$

and with the same Taylor expansion, the quadratic form is written as:

$$\chi^2(\mathbf{a}) \approx \chi^2(\mathbf{a}_{cur}) + \sum_k \frac{\partial \chi^2(\mathbf{a}_{cur})}{\partial \alpha_k} \delta \alpha_k + \frac{1}{2} \sum_{kl} \frac{\partial^2 \chi^2(\mathbf{a}_{cur})}{\partial \alpha_k \partial \alpha_l} \delta \alpha_k \delta \alpha_l, \quad (\text{A.4})$$

where the first derivatives are:

$$\frac{\partial \chi^2}{\partial a_k} = -2 \sum_{i=0}^{N-1} \left[ \frac{y_i - y(x_i | \mathbf{a})}{\sigma_i} \right] \frac{\partial y(x_i | \mathbf{a})}{\partial a_k}, \quad k = 0, 1, \dots, M-1, \quad (\text{A.5})$$

and the second derivatives are:

$$\frac{\partial^2 \chi^2}{\partial a_k \partial a_l} = 2 \sum_{i=0}^{N-1} \left\{ \frac{\partial y(x_i | \mathbf{a})}{\partial a_k} \frac{\partial y(x_i | \mathbf{a})}{\partial a_l} - [y_i - y(x_i | a)] \frac{\partial^2 y(x_i | \mathbf{a})}{\partial a_k \partial a_l} \right\}, k = 0, 1, \dots, M-1. \quad (\text{A.6})$$

Let  $\beta_k \equiv -\frac{1}{2} \frac{\partial \chi^2}{\partial a_k}$ ,  $\alpha_{kl} \equiv \frac{1}{2} \frac{\partial^2 \chi^2}{\partial a_k \partial a_l}$ , then the factor of 2 is removed. The  $\alpha_{kl}$  is defined as the curvature matrix and  $\alpha = \frac{1}{2} \mathbf{D}$ , which implies that it is the half of the Hessian matrix.

From A.2, we have:  $D(\mathbf{a}_{min} - \mathbf{a}_{cur}) = [-\nabla \chi^2(\mathbf{a}_{cur})]$ , which gives  $2\alpha \delta \mathbf{a} = 2\beta$ . The A.2 is now transformed into a systems of linear equations:

$$\sum_{l=0}^{M-1} \alpha_{kl} \delta a_l = \beta_k, \quad (\text{A.7})$$

where  $\delta a_l$  is a varying amount added to the current value of parameter for the next iteration.

The main task now is to calculate  $\alpha_{kl}$  and  $\beta_k$  and then solve for  $\delta a_l$  in A.7. Once  $\delta a_l$  is solved, we can vary the current trial or approximate values of  $\mathbf{a}_{cur}$  and let it go close to or reach the  $\mathbf{a}_{min}$ .

If we consider the method of steepest descent:  $\mathbf{a}_{next} = \mathbf{a}_{cur} - \text{const} \cdot \nabla \chi^2(\mathbf{a}_{cur})$ , where const is a constant, then the  $\delta a_l$  is solved by:

$$\delta a_l = \text{const} \cdot \beta_l, \quad (\text{A.8})$$

where no Hessian matrix is needed.

In the MRQ method, in order to solve for  $\delta a_l$ , the detailed calculation of  $\mathbf{D}^{-1}$  in A.2 and the simplified calculation of steepest descent in A.8 are combined and a smooth transition between A.2 and A.8 is considered.

In A.8, the const describes the distance or magnitude of how far the parameter should go along the gradient  $\beta_l$ . From dimensional analysis, since  $\beta_k \equiv -\frac{1}{2} \frac{\partial \chi^2}{\partial a_k}$  and  $\chi^2$  is a non-dimensional number,  $[\beta_l] = [1/a_l]$ . Then from A.8,  $[\text{const}] = [a_l^2]$ . The const has the same dimension to the term  $1/\alpha_{ll} = 1/(\frac{1}{2} \frac{\partial^2 \chi^2}{\partial a_l \partial a_l})$ , i.e., the diagonal elements in the curvature matrix. A bridge between A.2 and A.8 is thus built. The diagonal elements in the curvature matrix can control the magnitude of the const, tells how far the parameter should go along the gradient.

Then A.8 can be written as:

$$\delta a_l = \frac{1}{\lambda \alpha_{ll}} \beta_l \text{ or } \lambda \alpha_{ll} \delta a_l = \beta_l, \quad (\text{A.9})$$

where  $\alpha_{ll}$  is written in a form of  $\alpha_{ll} = \sum_{i=0}^{N-1} \frac{1}{\sigma_i^2} \left[ \frac{\partial y(x_i|\mathbf{a})}{\partial a_l} \frac{\partial y(x_i|\mathbf{a})}{\partial a_l} \right]$  to ensure that  $\alpha_{ll}$  is always positive; a fudge factor  $\lambda$  can be set to  $\lambda \gg 1$  to avoid the case when the value of const is taken too large.

Compare A.7 and A.9, if define a new curvature matrix  $\alpha'$  as  $\alpha'_{jj} \equiv (1 + \lambda)\alpha_{jj}$  (for diagonal elements) and  $\alpha'_{jk} \equiv \alpha_{jk}$  ( $j \neq k$ ) (for non-diagonal elements), these two equations can be combined into one:

$$\sum_{l=0}^{M-1} \alpha'_{kl} \delta a_l = \beta_k . \quad (\text{A.10})$$

From the definition of  $\alpha'$ , if  $\lambda$  takes a large value,  $\alpha'$  is dominated by diagonal elements, then A.10 is close to A.9; while if  $\lambda \rightarrow 0$ , A.10 is close to A.7.

The algorithm of the MRQ method requires a reasonable start value (first guess) of the fitting parameter  $\mathbf{a}$  and a reasonable preset value of  $\lambda$  (usually take  $\lambda = 0.001$ ). The iteration loop of the algorithm is: calculate the value of  $\chi^2(\mathbf{a})$ , solve for  $\delta \mathbf{a}$  from A.10 and then calculate  $\chi^2(\mathbf{a} + \delta \mathbf{a})$ . During this loop, the algorithm checks whether  $\chi^2(\mathbf{a} + \delta \mathbf{a}) \geq \chi^2(\mathbf{a})$ , if it is,  $\lambda$  is increased by  $\lambda = 10 \cdot \lambda$ ; if not,  $\lambda$  is decreased by  $\lambda = 0.1 \cdot \lambda$ .

The iteration loop is terminated when the change amount of the  $\chi^2$  is negligible: if the loop calculates several  $\chi^2$  values which are close to each other within a fit tolerance (**fTolerance**):  $|\chi^2_{current} - \chi^2_{previous}| < \text{fTolerance}$ , the algorithm will consider the  $\chi^2$  is minimized with a set of best-fit parameters. Here the termination condition of iterating the  $\chi^2$  value to convergence to the machine accuracy or to the roundoff limit is not used, since  $\chi^2$  is a statistical quantity rather than a solution of an equation. It is not statistical meaningful to vary the value of  $\mathbf{a}$  to vary  $\chi^2$  by a small amount  $\ll 1$ .

Once the minimum is reached,  $\lambda$  is set to 0 and then the estimated covariance matrix of the standard errors in the fitted  $\mathbf{a}$  can be calculated as:  $C \equiv \alpha^{-1}$ .

The MRQ method is the core algorithm in the **MP fitter** framework for likelihood fitting. A few fitter setting parameters relating to the method can be optimized in practice. These parameters are:

- **fTolerance**: the fit tolerance, which is set as  $|\chi^2_{current} - \chi^2_{previous}| < \text{fTolerance}$ .
- **nGood**: the number of good fits. The maximum number of the “good fits” required to be a valid result. This is to avoid the case when the MRQ minimizer finds a local

minima instead of a global minima.

- **fMaxIter**: the maximum iteration. The allowed maximum number for looping the MRQ minimizer.
- **nStart**: the maximum number of start positions. If the start value does not give a valid result, the fitter will try another random start value. **nStart** is the maximum number of the start value the fitter is allowed to try.

Table. A.1 shows the optimized values of the fitter setting parameters for different phases.

Table A.1: Optimized fitter setting parameters for different physics phases.

SNO+ phase	fTolerance	nGood	fMaxIter	nStart
water phase	0.001	6	500	250
partial-fill phase	0.001	4	100	250
scintillator phase	0.001	4	100	250

A trade-off between the accuracy & precision of the reconstructed results and the CPU time is considered. If increasing the **fTolerance** while decreasing the number of **nGood**, **fMaxIter** and **nStart**, the CPU time will decrease at costs of the fitter accuracy & precision, and vice versa.

### A.3 Calculations of Derivatives of Likelihood Functions

The MRQ method requires the derivatives of the likelihood function. These derivatives can be calculated analytically in explicit mathematical forms.

The position difference is defined as  $\vec{X}_{\text{diffCh}} = \vec{X}_0 - \vec{X}_{\text{pmt}}$ . Then the *TOF* for the prompt Cherenkov light is  $t_{\text{Ch}} = |\vec{X}_{\text{diffCh}}|/v_g$  and  $\mathcal{L}_{\text{Ch}} = \mathcal{L}(t_{\text{Ch}})$ .

Then it comes out for the water vertex case,

$$\frac{\partial \mathcal{L}}{\partial t_0} = \frac{d\mathcal{L}_{\text{Ch}}}{dt_{\text{Ch}}} , \quad (\text{A.11})$$

$$\frac{\partial \mathcal{L}}{\partial x} = \frac{\partial \mathcal{L}_{\text{Ch}}}{\partial t_{\text{Ch}}} \frac{dt_{\text{Ch}}}{dx} = -\frac{d\mathcal{L}_{\text{Ch}}}{dt_{\text{Ch}}} \frac{X_{\text{diffCh}}}{|\vec{X}_{\text{diffCh}}| \cdot v_g} , \quad (\text{A.12})$$

$$\frac{\partial \mathcal{L}}{\partial y} = -\frac{d\mathcal{L}_{\text{Ch}}}{dt_{\text{Ch}}} \frac{Y_{\text{diffCh}}}{|\vec{X}_{\text{diffCh}}| \cdot v_g}, \quad (\text{A.13})$$

$$\frac{\partial \mathcal{L}}{\partial z} = -\frac{d\mathcal{L}_{\text{Ch}}}{dt_{\text{Ch}}} \frac{Z_{\text{diffCh}}}{|\vec{X}_{\text{diffCh}}| \cdot v_g}, \quad (\text{A.14})$$

where the derivative  $\frac{d\mathcal{L}_{\text{Ch}}}{dt_{\text{Ch}}}$  can be calculated numerically from the timing PDF saved as a binned histogram.

For the water direction case,

$$\frac{\partial \mathcal{L}}{\partial \theta} = \frac{d\mathcal{L}_{\text{Ch}}}{d \cos \theta_{\text{Ch}}} \frac{d \cos \theta_{\text{Ch}}}{d \theta} = \frac{d\mathcal{L}_{\text{Ch}}}{d \cos \theta_{\text{Ch}}} \frac{d \vec{u}_0}{d \theta} \cdot \frac{\vec{X}_{\text{diffCh}}}{|\vec{X}_{\text{diffCh}}|}, \quad (\text{A.15})$$

where  $d\vec{u}_0/d\theta = (\cos \phi \cos \theta, \sin \phi \cos \theta, -\sin \theta)$  and

$$\frac{\partial \mathcal{L}}{\partial \phi} = \frac{d\mathcal{L}_{\text{Ch}}}{d \cos \theta_{\text{Ch}}} \frac{d \cos \theta_{\text{Ch}}}{d \phi} = \frac{d\mathcal{L}_{\text{Ch}}}{d \cos \theta_{\text{Ch}}} \frac{d \vec{u}_0}{d \phi} \cdot \frac{\vec{X}_{\text{diffCh}}}{|\vec{X}_{\text{diffCh}}|}, \quad (\text{A.16})$$

where  $d\vec{u}_0/d\phi = (-\sin \phi \sin \theta, \cos \phi \sin \theta, 0)$ . The derivative  $\frac{d\mathcal{L}_{\text{Ch}}}{d \cos \theta_{\text{Ch}}}$  can be calculated numerically from the PMT angular response PDF saved as a binned histogram.

## A.4 Inversion of Hessian Matrix

Matrix inversion is a frequent calculation when applying the MRQ method. In the **MP fitter**, the inversion of a  $2 \times 2$  Hessian matrix (usually used for direction reconstruction with two parameters) is calculated directly. For the higher dimension matrix, usually the  $4 \times 4$  matrix for vertex reconstruction, a **SDecompQRH** class is called for calculating the inversion matrix by using QR decomposition method [155]. This class was introduced by Jeff Tseng and it was modified from the ROOT **TDecompQRH** class [199]. Compared to the ROOT version, its **Solve()** function was slightly modified for solving the matrix equation  $Ax = b$ , where  $A = QR$  is composed of an orthogonal matrix  $Q$  and an upper triangular matrix  $R$ . If the diagonal element in  $R$  is too small, instead of returning failure, the modified algorithm simply sets the corresponding  $x$  component to be 0. This allows an optimization for the MRQ method to continue in frequent cases when the matrix is singular.

## A.5 Likelihood Surfaces

Fig. A.1 shows vertex likelihood surfaces produced by the MRQ method in the **MP water fitter**, for a typical  $^{16}\text{N}$  event (central run-100934, event GTID = 61836), projected on  $X - Y$ ,  $Y - Z$  and  $X - Z$  planes. A clear global maxima gives the reconstructed vertex:  $\vec{X}_{fit} = (-211.958, 503.399, 275.990)$  mm and  $t_{fit} = 217.039$  ns. Fig. A.2 shows the likelihood surface projected on  $x, y, z, t$ -axis respectively (i.e., the best-fit  $\ln \mathcal{L}$  values as functions of the trial  $x, y, z, t$  values). Each of these one dimensional curves show a global maximum. Fig. A.3 shows the derivatives of the best-fit  $\ln \mathcal{L}$  with respect to the trial  $x, y, z$  and  $t$  values. The analytical derivatives mostly match with the numerical derivatives used by the fitter. The best-fit parameters were obtained when the  $\frac{\partial \ln \mathcal{L}}{\partial x^i} = 0$  ( $x^i = x, y, z, t$ ), or the best-fit points are at  $(x_{trial}^i, \frac{\partial \ln \mathcal{L}}{\partial x_{trial}^i}) = (x_{best}^i, 0)$  ( $x^i = x, y, z, t$ ). It also shows clearly that all the derivative curves pass through the best-fit points almost linearly.

## A.6 Detailed Light Path Calculations in the Partial Fitter

The following algorithm shows the detailed calculations in the **MP partial fitter** for evaluating the light path in the scintillator regions. Each check steps are marked by number and if-conditions are marked by Latin letters (a, b or c).

---

First check the ray-sphere intersection (Eqn. 4.15):

If  $\Delta > 0$ ,

(step. 1a) if  $|\vec{x}_0| < r_{AV}$  (and  $a_+ > 0 > a_-$ ), check the ray-plane intersection:

(2a-a) if  $a_3 > 0$ , the ray-vector hits the interface plane:

(3a-a-a) if  $z_0 < Z_{split}$  and  $a_3 < a_+$ :  $d_{sp,AV} = a_+ - a_3$ , see Fig. A.4 (a).

(3a-a-b) if  $z_0 \geq Z_{split}$ :

(4a-a-b-a) if  $a_3 < a_+$ :  $d_{sp,AV} = a_3$ , see Fig. A.4 (b).

(4a-a-b-b) if  $a_3 \geq a_+$ :  $d_{sp,AV} = a_+$ , see Fig. A.4 (c).

(2a-b) if  $a_3 \leq 0$ :

(3a-b) if  $z_0 > Z_{split}$ :  $d_{sp,AV} = a_+$ , see Fig. A.4 (d).

(step. 1b) if  $|\vec{x}_0| \geq r_{AV}$  (and  $a_+ > a_- > 0$ ), calculate the z position of the intersection point:  $z_{\pm} = z_0 + a_{\pm} \cdot (z_{PMT} - z_0) / |\vec{X}_{PMT} - \vec{X}_0|$ :

(1-b-a) if  $z_- \geq Z_{split}$  and  $z_+ \geq Z_{split}$ :  $d_{sp,AV} = a_+ - a_-$ , see Fig. A.4 (e).

(1-b-b) if  $z_- < Z_{split}$  and  $z_+ > Z_{split}$  and  $a_3 > 0$ :  $d_{sp,AV} = a_+ - a_3$ , see Fig. A.4 (f).

(1-b-c) if  $z_- > Z_{split}$  and  $z_+ < Z_{split}$  and  $a_3 > 0$ :  $d_{sp,AV} = a_3 - a_-$ , see Fig. A.4 (g).

---

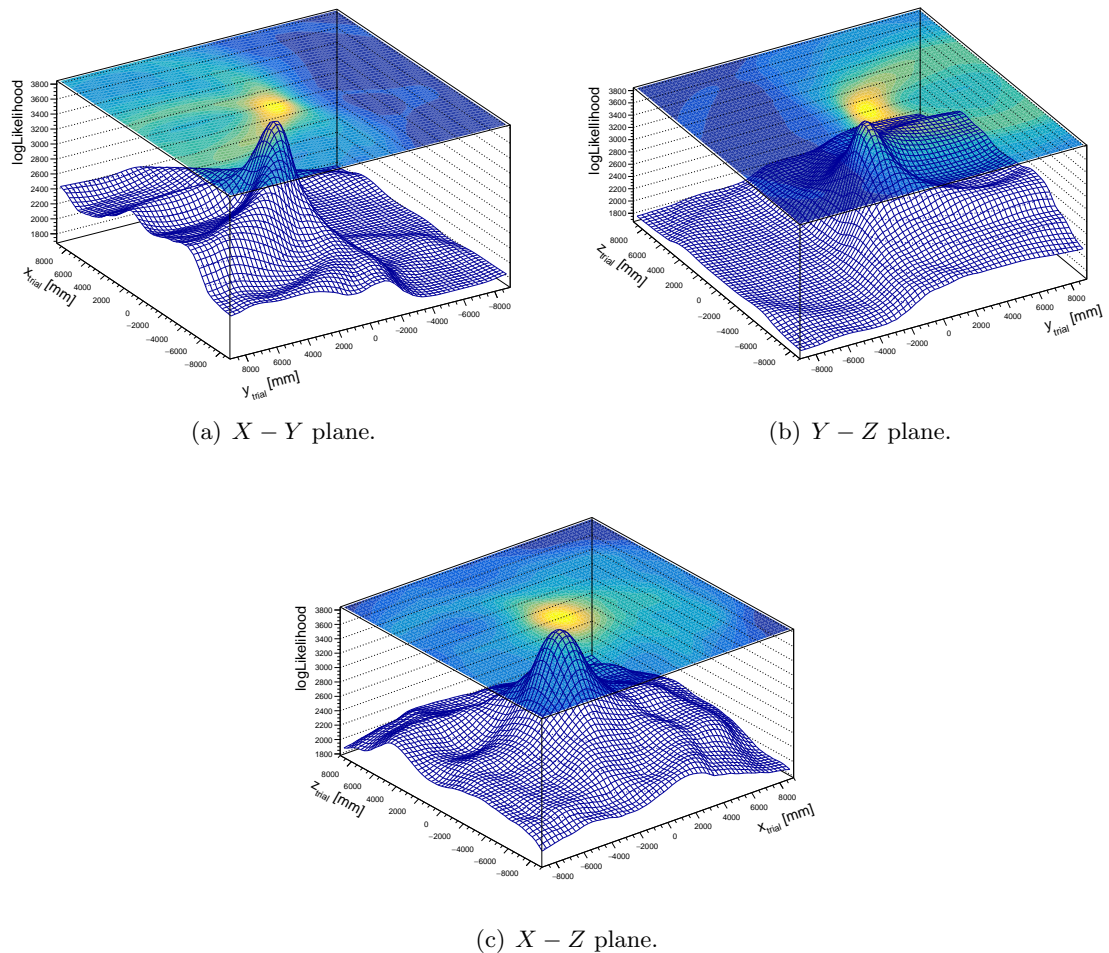


Figure A.1: Likelihood surface of an  $^{16}\text{N}$  event projected on  $X - Y$ ,  $Y - Z$ ,  $X - Z$  planes. A clear global maxima is reached for the fitted vertex.

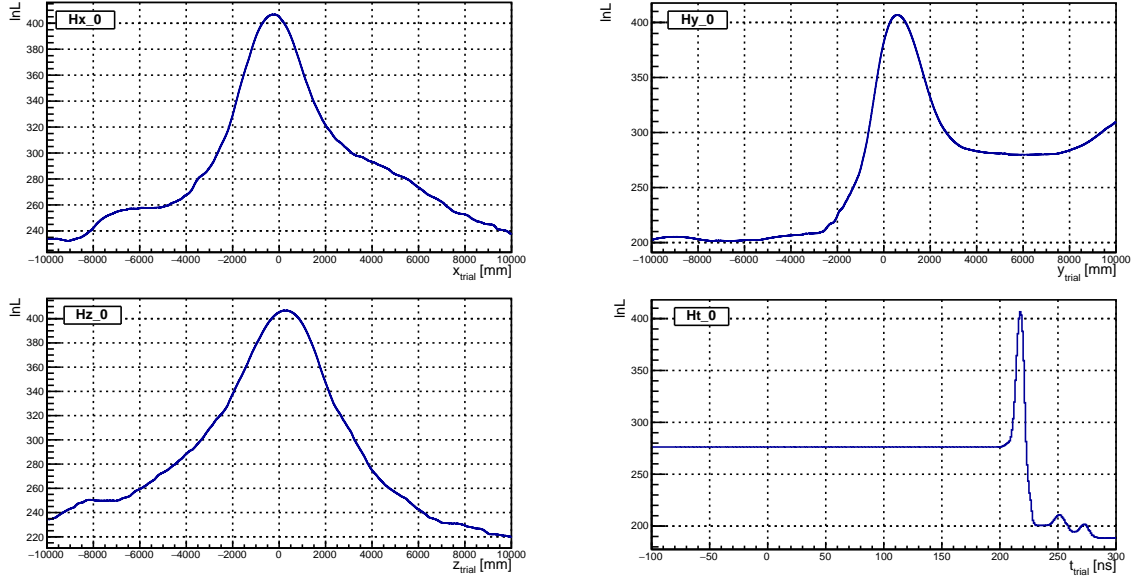


Figure A.2: Likelihood surface of an  $^{16}\text{N}$  event projected on  $x, y, z, t$ -axis respectively.

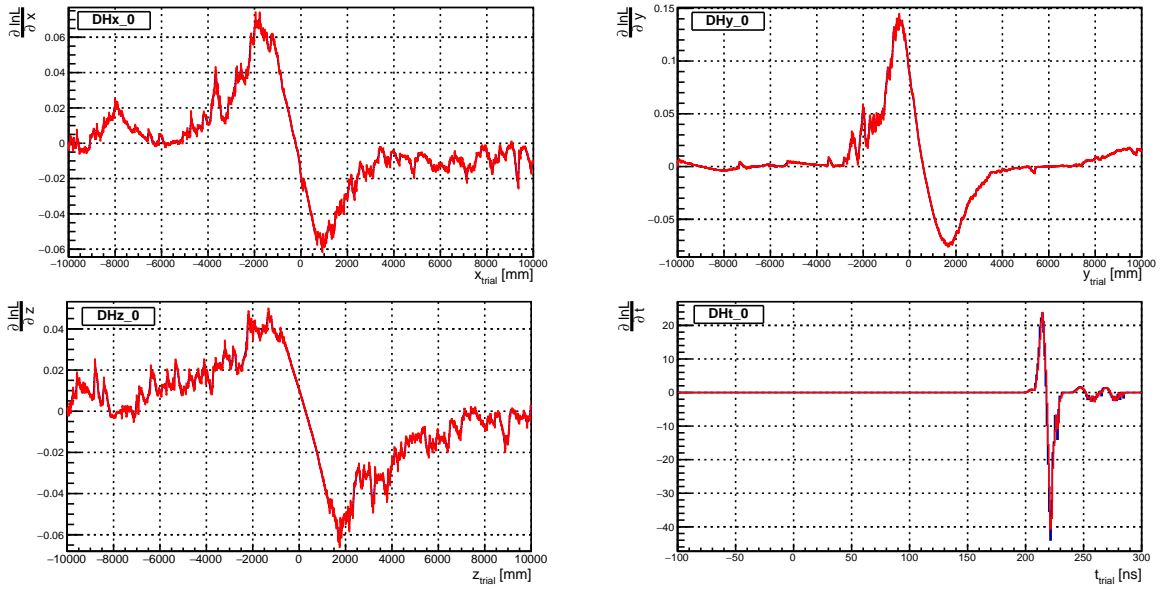


Figure A.3: Derivatives of the best-fit  $\ln \mathcal{L}$  of an  $^{16}\text{N}$  event projected on  $x, y, z, t$ -axis respectively. The analytical derivatives (blue) are overlaid with numerical derivatives (red). They mostly match with each other.

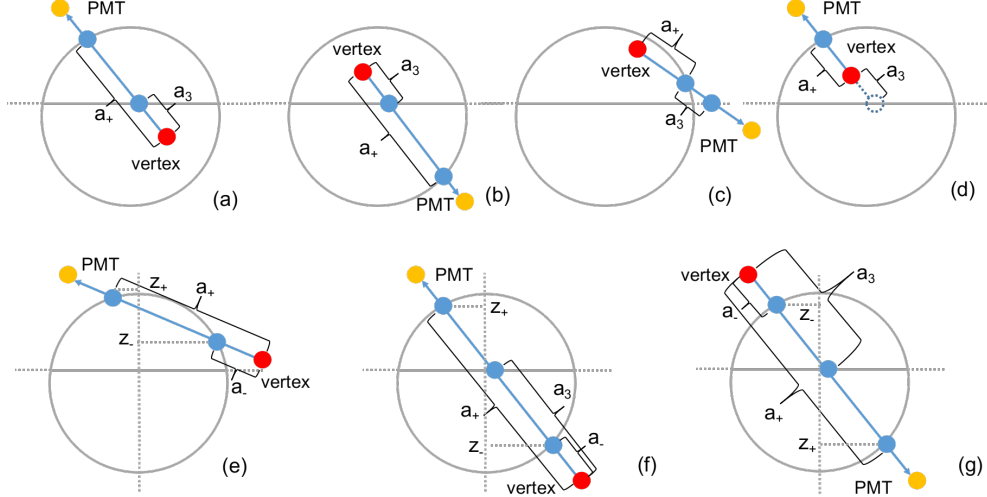


Figure A.4: Layouts for the scintillator light paths inside the AV sphere.

---

First check the ray-cylinder intersection (Eqn. 4.15):

If  $\Delta_{neck} > 0$ ,

(step. 1a) if  $a'_+ a'_- < 0$  (event position is inside the cylinder), check the z position of the intersection point on neck,  $z_+ = z_0 + a'_+ u_z$ :

(2a-a) if  $6108 < z_+ < 8390$  mm (in the valid neck region), then check the AV sphere:

(3a-a-a) if  $|\vec{X}_0| \geq r_{AV}$ :  $d_{sp,neck} = a'_+$ , see Fig. A.5 (a).

(3a-a-b) if  $|\vec{X}_0| < r_{AV}$  and  $a'_+ a'_- < 0$ :  $d_{sp,neck} = a'_+ - a'_-$ , the light ray first hits the sphere inside the cylinder and then hits the cylinder, see Fig. A.5 (b).

(2a-b) if  $z_+ < 6108$  mm:

(3a-b) if  $|\vec{X}_0| \geq r_{AV}$  and  $6108 < z_0 < 8390$  mm:

(4a-b) if  $a'_+ > a'_- > 0$ :  $d_{sp,neck} = a'_-$ , see Fig. A.5 (c).

(step. 1b) if  $a'_+ > a'_- > 0$  (event position is outside the cylinder), check the z position of the intersection point on neck,  $z'_\pm = z_0 + a'_\pm \cdot u_z$ :

(2b-a) if  $6108 < z'_\pm < 8390$  mm, check the AV intersection:

(3b-a-a) if  $a_\pm$  do not exit (never passes through AV),  $d_{sp,neck} = a'_+ - a'_-$ , see Fig. A.5 (d).

(3b-a-b) if  $a'_+ > a'_- > 0$ , evaluate the z positions of the ray-sphere intersection points  $z_\pm = z_0 + a_\pm \cdot u_z$ :

(4b-a-a) if  $z_\pm \geq 6108$  mm:  $d_{sp,neck} = a'_+ - a'_- - (a'_+ - a'_-)$ , see Fig. A.5 (e). The path inside the sphere is subtracted to avoid duplicated calculation.

(4b-a-b) if  $z_+ < 6108$  and  $6108 < z_- < 8390$  mm:

(5b-a-b-a) if  $a'_+ > a'_- > 0$ :  $d_{sp,neck} = a'_- - a'_+$ , see Fig. A.5 (f).

(5b-a-b-b) if  $z_- < 6108$  and  $6108 < z_+ < 8390$  mm:

in this case, either the event position is inside the sphere ( $a'_+ a'_- < 0$ ), shown in Fig. A.5 (g), or outside the sphere ( $a'_+ a'_- < 0$ ), shown in Fig. A.5 (h)), the path in neck is same:  $d_{sp,neck} = a'_+ - a'_+$ .

---

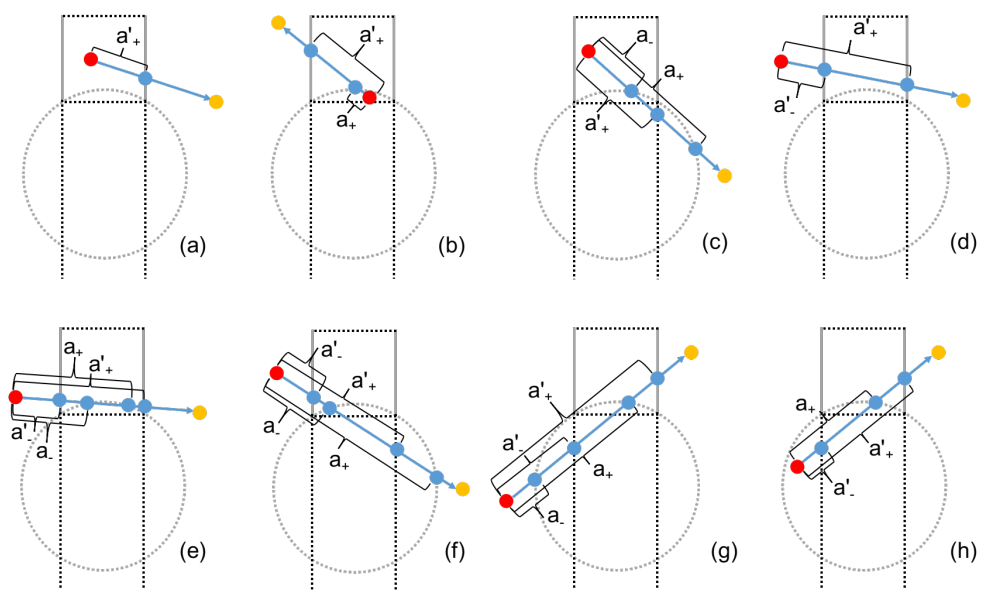


Figure A.5: Layouts of the scintillator light paths inside the neck cylinder.

## Appendix B

# Information for $^{16}\text{N}$ Scan Runs

### B.1 $^{16}\text{N}$ Source Positions in the Scan Runs

The tables below show the  $^{16}\text{N}$  runs used in this thesis. Table B.1 to B.3 are the internal scans inside the AV along the detector  $z$ -axis,  $y$ -axis and  $x$ -axis respectively. Table B.4 shows the runs when the source was at the detector corner. Table B.5 shows the external scans.

Table B.1:  $^{16}\text{N}$  internal  $z$ -axis scan runs ( $Z$  scans). The last 3 scans were inside the AV neck (neck runs).

run number	nominal source position [mm]		
	$x$	$y$	$z$
100934	-186.0	256.0	1.0
106923	-186.0	254.0	-5501.2
106925	-186.0	254.0	-4999.899
106930	-186.0	254.0	-4500.2
106942	-186.0	254.0	-4001.0
106944	-186.0	254.0	-3501.399
106946	-186.0	254.0	-2999.7
106948	-186.0	254.0	-2500.399
106950	-186.0	254.0	-1998.499
106952	-186.0	254.0	-1499.5
106954	-186.0	254.0	-1000.099
106956	-186.0	254.0	-499.6
106958	-186.0	254.0	0.401
106960	-186.0	254.0	500.8
106962	-186.0	254.0	1000.3
106964	-186.0	254.0	1500.9
106967	-186.0	254.0	2000.001
106969	-186.0	254.0	2500.3
106971	-186.0	254.0	3000.3
106973	-186.0	254.0	3500.9
106975	-186.0	254.0	4000.5
106977	-186.0	254.0	4500.4
106979	-185.037	247.24	4973.567
107049	-121.599	81.021	6496.04
107051	-123.099	126.177	6997.52
107053	-124.4	153.386	7499.79

Table B.2:  $^{16}\text{N}$  internal  $y$ -axis scan runs ( $Y$  scans).

run number	nominal source position [mm]		
	$x$	$y$	$z$
106992	-5.995	-0.201	-1.107
106994	-7.761	-998.068	0.159
106996	-7.084	-2000.578	-0.716
106998	-5.491	-2998.017	-4.196
107000	-3.774	-3992.167	-7.374
107002	-1.624	-4999.882	-12.012
107004	-1.745	5002.057	-9.897
107006	-3.967	3973.021	-7.359
107008	-5.984	2980.035	-3.441
107010	-7.952	1986.669	-1.714
107012	-9.242	994.183	0.553
107014	-9.867	496.858	0.269
107016	-8.414	1494.71	0.634
107018	-6.835	2487.539	-1.126
107026	-4.949	3496.338	-5.971
107028	-2.539	4505.371	-7.453
107030	-7.711	-501.268	0.126
107033	-7.534	-1494.927	-0.096
107035	-6.349	-2487.912	-1.434
107043	-4.366	-3475.769	-6.019
107045	-2.799	-4498.62	-10.213
107047	-1.898	-4874.53	-11.077

Table B.3:  $^{16}\text{N}$  internal  $x$ -axis scan runs ( $X$  scans).

run number	nominal source position [mm]		
	$x$	$y$	$z$
107055	-5.283	-0.209	-1.057
107075	-4999.043	2.46	-9.899
107077	-4002.525	5.269	-7.364
107079	-3004.229	8.101	-2.54
107081	-2000.155	10.637	-0.361
107083	-992.994	11.641	0.024
107085	998.133	10.897	-0.044
107087	2011.103	9.874	0.057
107091	4003.323	4.378	-5.974
107093	5004.868	2.262	-7.547
107095	4503.445	3.278	-7.0
107110	-4489.301	3.918	-10.545
107116	3511.147	5.742	-2.578
107118	2502.805	8.681	-2.803
107120	-3476.709	6.643	-4.886

Table B.4:  $^{16}\text{N}$  corner scan runs.

run number	nominal source position [mm]		
	<i>x</i>	<i>y</i>	<i>z</i>
106981	-186.0	254.0	5500.9
106985	-186.0	254.0	5999.8
107058	-8.765	996.891	0.172
107060	-7.518	1990.663	-0.445
107062	-7.794	-997.865	0.155
107064	-7.083	-1990.651	-0.744
107089	3003.718	7.258	-0.69
107098	2091.016	6.312	2099.444
107020	-5.399	1991.04	1988.97
107022	-9.92	2776.47	-2839.41
107024	-10.44	3227.32	-3324.9
107037	-8.377	-2832.33	-2839.69
107039	-9.284	-3137.21	-3212.18
107041	-4.719	-2099.25	2110.71
107100	2824.56	13.507	-2840.13
107102	3245.74	13.681	-3264.76
107104	-3250.29	13.438	-3264.7
107106	-2834.05	13.893	-2839.43
107108	-2109.28	6.613	2098.57
107112	-2771.9	16.196	-4773.96
107114	2771.1	15.596	-4773.27

Table B.5:  $^{16}\text{N}$  external scan runs.

run number	nominal source position [mm]		
	<i>x</i>	<i>y</i>	<i>z</i>
111211	-5861.0	-2524.0	-1.62
111213	-5861.0	-2524.0	-5000.525
111215	-5861.0	-2524.0	-4000.021
111217	-5861.0	-2524.0	-3000.151
111219	-5861.0	-2524.0	-1999.248
111221	-5861.0	-2524.0	-998.923
111223	-5861.0	-2524.0	1000.798
111225	-5861.0	-2524.0	2000.597
111228	-5861.0	-2524.0	3000.734
111230	-5861.0	-2524.0	4000.977
111232	-5861.0	-2524.0	5000.86
111234	-5861.0	-2524.0	4498.167
111236	-5861.0	-2524.0	3498.838
111238	-5861.0	-2524.0	2498.641
111240	-5861.0	-2524.0	1498.713
111242	-5861.0	-2524.0	-1501.717
111244	-5861.0	-2524.0	-2500.89
111246	-5861.0	-2524.0	-3500.764
111248	-5861.0	-2524.0	-4500.812

## Appendix C

# Bi-Po Analysis

### C.1 Uranium chain and Bi-Po Analysis

A flowchart for picking up the Bi-Po event pairs is listed in Fig. C.1. The algorithm is based on Ref. [120].

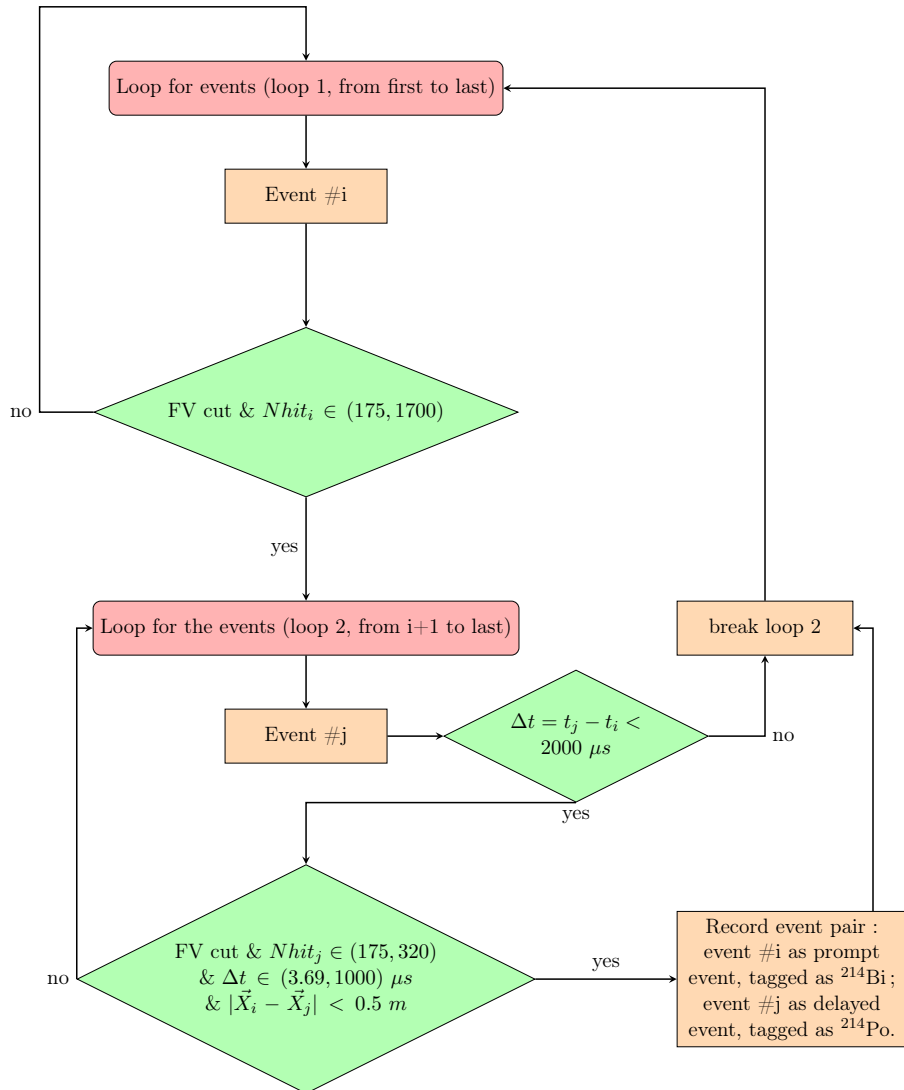


Figure C.1: A flow chart for Bi-Po tagging.